Interplay of Symmetry and Topology in 2D Non-Centrosymmetric Superconductors Illustrated in 1H Transition Metal Dichalcogenides

A DISSERTATION
SUBMITTED TO THE FACULTY OF THE GRADUATE SCHOOL
OF THE UNIVERSITY OF MINNESOTA
BY

Daniel Shaffer

IN PARTIAL FULFILLMENT OF THE REQUIREMENTS
FOR THE DEGREE OF
DOCTOR OF PHILOSOPHY

Fiona J. Burnell, Adviser

August 2020

Acknowledgements

It goes without saying that I could not finish this dissertation without the support of many people. First of all, I of course would like to thank my advisor Fiona Burnell and my co-advisor Rafael Fernandes for their guidance throughout the program, in particular for forcing me to improve my scientific communication skills (which still need much work as this dissertation will attest). I am also thankful to many faculty members from whom I learned a lot inside and outside of the classroom, in particular Andrey Chubukov and Alex Kamenev who (along with Fiona and Rafael) taught me the tools of the trade and that no picture can replace a real calculation, and Boris Shklovskii who taught all of us that pictures are worth more than a thousand equations. Particular thanks go to Andrey, Turan Birol and Vlad Pribiag who agreed to be on my dissertation committee.

Many friends and colleagues have also helped me throughout the program and affected my thinking on many subjects in physics and beyond, sometimes perhaps without knowing. I am grateful to Jian Kang and Ruiqi Xing for helping me understand RG early on, Menxing Ye for catching an embarrassing mistake that would undermine this whole dissertation, Mike Sammon for asking that one time in the stats class what phases of matter are (among other questions), Alex Hamill and Brett Heischmidt for providing some nice experimental data and figures in the last chapter of this dissertation, and Kexin Wang and Bo Xiong for going through parts of Fradkin's book with me. Less specifically but no less importantly, I would also like to thank Mitia Chichinadze, Saumitran Kasturirangan, Dan Phan, Amartya Saha, Yiming Wu, Xuzhe Ying, and many others. I learned a lot from our conversations. Thank you to Mitia and Saumit in particular for providing great entertainment in the office.

Finally, and most importantly, I would like to thank my family. Though I talk with them all the time, I feel like I don't get enough opportunities to express my gratitude for all that they have done, and they have helped me more than they know. I deeply appreciate the support of my parents, Leonid and Olga, and my brother. It is regretful that due to the current pandemic I am not able to thank them in person. And of course I must thank my wife, Maria Bakhtsiyarava, without whose support in this past month I am convinced I would not be able to finish this dissertation, and who has made my life so much brighter.

Dedication

In memoriam: Dusia, Valeriy, and Valentina

Abstract

The subject of this dissertation is at the intersection of two major fields of condensed matter physics: unconventional superconductivity (SC) and topological phases of matter. Both conventional and unconventional superconductors exhibit similar qualitative behavior: they pass currents with zero resistance and expel magnetic fields, both effects due to formation of a Cooper pair condensate. Broadly, an unconventional superconductor is simply one that is not described by the textbook Bardeen-Cooper-Schrieffer theory. There are at least three things that can make a superconductor unconventional: the pairing mechanism, the symmetry of the Cooper pair, and topology. In many unconventional superconductors the paring mechanism is thought to arise due to the 2D nature of the material that can exhibit strong quantum fluctuations. Unconventional pairing can lead to spin-triplet Cooper pairs with a non-zero orbital momentum, or even a non-zero total momentum, in which case they can realize the so-called pair density wave (PDW). Since magnetic fields align spins that can only form spin-triplet states, one possibility for realizing unconventional superconductors is to look for superconductors that survive in large magnetic fields. This is well-known to occur in systems with strong spin-orbit coupling (SOC) that is also well-known to lead to possible topological phases and topological superconductors in particular, which exhibit Majorana edge modes that may one day be useful for building a quantum computer.

All of these elements come together in a family of monolayer materials with strong SOC known as the 1H transition metal dichalcogenides (TMDs) that have recently been found to be superconducting. The thesis of this dissertation is that they can indeed host interesting unconventional and topological SC phases. To show this, in Chapter 2 we analyze the possible symmetry breaking instabilities using the parquet renormalization group that has been successfully used in other unconventional superconductors. We find that Coulomb interactions can lead to unconventional SC and PDW. In Chapter 3, we explain what makes phases in general topological, and how the topology is restricted by their symmetry. In Chapter 4, we combine the results of the two previous chapter to study 1H-TMDs in a mean-field theory, and find unconventional topological phases. In Chapter 5 we study the PDW phase in more detail, and in Chapter 6 we conclude by looking at recent experimental data that indeed suggests that 1H-$NbSe_2$ may be an unconventional superconductor, but perhaps not the one we anticipated in theory.

Contents

List of Tables

List of Figures

List of Symbols

Latin

$\mathbf{A}^{(\alpha)}(\mathbf{p}), A_{\eta\tau}(\mathbf{p})$	Berry connection/vector potential
a	lattice constant
$\mathbf{B}$	magnetic field
$\mathbf{b}$	magnetic field in units of $g_L\mu_B$
$\mathcal{C}$	particle-hole symmetry
$c^\dagger_{\mathbf{p}\eta\tau}, c_{\mathbf{p}\eta\tau}$	creation/annihilation operators in SOC basis
$D^{(\ell\mu)}_{\eta\zeta}$	$(\ell\mu)$ irrep gap function coefficient in SC and PDW channels
$d^\dagger_{\mathbf{p}\eta\alpha}, d_{\mathbf{p}\eta\beta}$	creation/annihilation operators in spin basis
E	energy
$E_{\eta\tau}(\mathbf{p})$	BdG spectrum
$\mathbf{E}$	electric field

Greek

α	spin index
α_R	Rashba spin-orbit coupling parameter
β	spin index, inverse temperature
β_I, β_η	Ising spin-orbit coupling parameter
Γ	the Gamma point
$\Gamma^{(0)}$	fourth order GL free energy coefficient
$\gamma^{(\ell\mu)}$	SC channel in RG belonging to $(\ell\mu)$ irrep
$\Delta_{\eta\zeta}(\mathbf{p})$	SC and PDW gap functions with pocket indices
$\Delta_{\eta\tau}(\mathbf{p})$	SC gap function on τ (inner/outer) Fermi surface on η pocket
δ	Kronecker delta/additional spin index
$\epsilon_\eta(\mathbf{p})$	η pocket dispersion without SOC

$\boldsymbol{\mathcal{E}}$	shear strain field	$\varepsilon_{\eta\zeta}$	Levi-Civita symbol
$F_{\eta\zeta}(i\omega, \mathbf{p})$	anomalous Green's function	ε	dimensionless strain parameter
$\mathbf{F}^{(\alpha)}(\mathbf{p})$	Berry curvature vector	ζ	pocket index, zeta function, field scaling parameter in RG
$\mathcal{F}$	free energy	η	pocket index
$G_{\eta\zeta}(i\omega, \mathbf{p})$	Green's function	$\Theta^{(\ell\mu)}_{\eta\zeta}(\theta)$	Chebyshev harmonics in the $(\ell\mu)$ irrep
$\mathcal{G}_{\eta\zeta}(i\omega, \mathbf{p})$	Green's function in Nambu space	θ	angle
$g^{(\ell\mu)}_{\eta'\zeta';\eta\zeta}$	coupling constants for $(\ell\mu)$ SC and PDW channels	ϑ	magnetic field angle
$g^{(\ell\mu)}_{\eta\zeta}$	coupling constants for $(\ell\mu)$ SC channels	$\kappa^{(\ell\mu)}$	PDW channel in RG belonging to $(\ell\mu)$ irrep
g_L	Landé g-factor	Λ	high energy cutoff
$\mathbf{g}_\eta$	SOC vector	$\lambda_I p_F^3$	Ising SOC parameter at Γ point
H	Hamiltonian	λ	additional Pauli matrix label
$\mathcal{H}, \mathcal{H}^{(BdG)}$	first-quantized/BdG Hamiltonian	μ	labels Pauli matrices σ^μ with $\mu = 0, x, y, z$
$h^{(\ell\mu)}_{\eta\zeta}$	coupling constants for $(\ell\mu)$ PDW channels	μ_B	Bohr magneton
i	imaginary number	μ_η	chemical potential at η pocket
j	integer or x, y, z	$\hat{\mu}$	mismatch detuning parameter between Γ and K pockets
j_I	source term in the action	ν	additional Pauli matrix label
$\mathcal{K}$	complex conjugation	$\xi_{\eta\tau}$	dispersion with SOC
$\mathbf{k}$	momentum	$\Pi_{\eta\tau}(\mathbf{p})$	pairing susceptibility or particle-particle bubble
$\mathbf{L}$	angular momentum	$\varpi(x)$	$-\log\frac{1.13\Lambda}{T} + \mathrm{Re}\left[\psi\left(\frac{1}{2} + \frac{ix}{4\pi T}\right) - \psi\left(\frac{1}{2}\right)\right]$
L	Lagrangian	ρ	CDW order parameter

ℓ	irrep label, orbital angular momentum, loop current order	ϱ	RG rescaling parameter
$(\ell\mu)$	channel label indicating D_{3h} irrep and spin-singlet/triplet components	$\Sigma^{(\ell\mu)}_{\eta\zeta}(\mathbf{p})$	irrep basis functions $\Theta^{(\ell\mu)}_{\eta\zeta}(\theta)\sigma^\mu i\sigma^y$
$M_j, \mathcal{M}_j$	reflection in plane perpendicular to $j = x, y, z$	σ^μ	Pauli matrices including $\sigma^0 = 1$
m, m_η	effective mass at η pocket	$\boldsymbol{\sigma}$	vector of Pauli matrices $(\sigma^x, \sigma^y, \sigma^z)$
$N_{\eta\tau}$	density of states of τ Fermi surface at η pocket	ς^μ	additional Pauli matrices in Nambu indices
$N_{M\mathbb{Z}}$	mirror Chern number invariant	τ^μ	additional Pauli matrices
n	integer	τ	SOC index for inner/outer SOC split Fermi surfaces
$\mathcal{O}$	operator in the action	υ	additional SOC index
$\mathbf{p}$	momentum	$\lvert\Upsilon_{\eta\tau}(\mathbf{p})\rangle$	four component eigenvector of BdG Hamiltonian
p_F	Fermi momentum	ϕ	complex phases
$Q^{(\ell\mu)}_{\eta\tau}$	projected irrep basis functions	χ	SC susceptibility in GL free energy
$\mathbf{q}$	momentum	$\Psi_{\mathbf{p}\eta\alpha}$	Nambu spinor
$\mathcal{S}$	chiral symmetry	$\psi_{\mathbf{p}}$	spinor
$\mathbf{S}$	spin operator	$\psi(x)$	the digamma function
S	action	ω	Matsubara frequency
s_j	generic RG coupling constants		
$T, \mathcal{T}$	temperature or time reversal symmetry		
T_c	critical temperature		
$\mathbb{T}$	torus		
$\mathbf{T}$	solid torus		

t	RG time, tight binding hopping
$U^{\alpha}_{\eta\tau}(\mathbf{p})$	unitary transformation from spin to SOC basis
$[U_{\eta\zeta}(\mathbf{p},\mathbf{k})]^{\alpha'\beta'}_{\alpha\beta}$	interactions keeping momenta fixed or exchanged
$u^{(\ell\mu)}_{\eta\zeta}$	coupling constants for U interactions
$u_{\alpha}(\mathbf{p}), u_{\eta\tau}(\mathbf{p})$	Nambu eigenspinor component
$\lvert u_{\alpha}(p)\rangle$	Bloch eigenstates
$V^{\eta'\zeta';\alpha'\beta'}_{\eta\zeta;\alpha\beta}(\mathbf{p},\mathbf{k})$	pairing interactions in spin basis
$\tilde{V}^{\zeta\upsilon}_{\eta\tau}(\mathbf{p};\mathbf{k})$	projected pairing interactions in SOC basis
$\mathbf{v}$	velocity
$v_{\alpha}(\mathbf{p}), v_{\eta\tau}(\mathbf{p})$	Nambu eigenspinor component
$W^{(\mu)}_{\eta\zeta;\tau}(\mathbf{p})$	Pauli matrix projection on corresponding Fermi surfaces
w	trigonal warping parameter
x	coordinate
y	coordinate
$\mathcal{Z}$	partition function
Z	atomic number/quasiparticle renormalization
$\mathbb{Z}$	the integers
$\mathbb{Z}_2$	the integers modulo 2
z	coordinate

Chapter 1

Introduction

The leitmotif of this dissertation, as of much contemporary condensed matter physics, is the interplay between symmetry and topology, in particular the symmetry and topology of ground states of many-body systems that characterize phases of matter. Both notions of phases and topology are intimately connected with the notion of adiabatic transformations of the system which allows us to say that two states or two systems are in the *same* phase: what we mean is precisely that we can adiabatically transform one system into the other by tuning some physical parameter (we say that the systems are adiabatically connected). This is not just a theoretical consideration, but in fact a practical one. When we change the parameter by an infinitesimal amount, the statement that the system responds adiabatically means that the new state of the system is for all practical purposes indistinguishable from the old state. In other words, no experiment could tell the new state from the old. It is a matter of self-consistency to declare all states that we cannot distinguish to describe the same phase of matter.

In reality we can of course experimentally distinguish many different phases of matter, which means that if we try to adiabatically connect them we must fail: if we change the tuning parameter by an infinitesimal amount, the system responds dramatically and something (any property of the system that we can measure) changes by a finite amount, i.e. discontinuously. More precisely, there is a non-analyticity in some measurable quantity. This necessarily happens if the measured quantity is discrete and so cannot change continuously, and consequently such quantities allow us to classify phases.

The paradigmatic example of a discrete quantity which we can use to classify phases is symmetry. A state of a system will always either have a symmetry or not, with no possibility in between. This is of course Landau's classification of phases with spontaneously broken symmetries, and which explains almost all familiar examples like water and ice. It should be emphasized that to some

degree the possibility of spontaneous symmetry breaking is surprising: it means that the ground state of the system has a different symmetry than the system itself, an example of emergent behavior when many particles are put together to produce something that was not there before, in this case an order that breaks a symmetry. The reason is that the symmetric state becomes unstable at the phase transition, which as we will see can be understood as a consequence of renormalization processes.

It is now well-known that other discrete quantities besides symmetry, generally referred to as topological invariants, can be used to characterize phases of matter. The first and best known example is the quantum Hall effect in which the topological invariant is the Chern number that counts the number of occupied Landau levels (which are discrete and have the same symmetry) and which changes discontinuously as the filling changes. The topology in this case is determined by adiabatic transformations: a topologically trivial state is defined to be one that can be adiabatically connected to a state that is a simple product state of single particle states (the atomic limit). It is another example of emergent behavior when many particles are put together. Note that non-trivial topology may, in principle, coincide with symmetry breaking when it develops, so the notion of topological phases is complementary and not orthogonal to symmetry breaking phases.

Which phases of matter can occur in a system depends strongly on its dimensionality. Of course most systems of interest are 3D, but some thin film systems can be effectively 2D, some like graphene essentially truly 2D (interfaces in heterostructure can also sometimes effectively form their own system, like the 2D electron gas), and wire systems can be essentially 1D. Dimensionality is well-known to affect many system properties, including their topology: the QHE, for example, occurs only in 2D systems. In general 2D systems are particularly interesting from a topological point of view because in 2D one can count how many times a path of a particle winds around a fixed reference point. This leads among other things to the possibility of non-fermionic nor bosonic statistics (i.e. anyons), the lack of chaos in dynamical systems, and the Mermin-Wagner theorem that states that no spontaneous breaking of continuous symmetries is possible in 2D at non-zero temperature, which means that corresponding phase transitions are often topological (of BKT type, i.e. proceeding by vortex proliferation).[1]

Symmetry and topology also generally interact with each other (as we will see in Chapter 3). Symmetry can have two general effects on topology: it can force topology to be trivial, as in the case of the QHE that requires time reversal symmetry (TRS) to be broken; or it may allow us to define new

[1] Other dimensions have similar interesting topologies, but not for particle like objects: in 3D for example particle paths around fixed points are all equivalent (contractible), but loop-like objects do have a 'winding' number similar to the one in 2D (related to the fact that the corresponding homotopy group of 2D spheres in 3D space is not trivial).

topological phases that would be impossible without it. In the latter case, this is because symmetry may restrict the adiabatic transformations we are allowed to make to the system while staying in the same phase. The corresponding phases are called symmetry-protected topological (SPT) phases for that reason, with the best known example possibly being the topological insulators or the quantum spin Hall effect (QSHE) protected by TRS and spin-rotation symmetry respectively.

Since the QHE has been understood in terms of the Berry connection and the Chern number [14, 161, 170], the topological classification has been extended to include gaped phases with antiunitary symmetry using the tenfold way [10, 132, 99], gapless (including nodal) phases with anti-unitary symmetries in [105, 197], as can topological defects [169]. Antiunitary symmetries are not the only possible symmetries, and more recently recently the classification has been extended to include crystalline symmetries like mirror symmetries and rotations, both for fully gapped [29, 38] and gapless phases [28, 158, 167]. Such phases are called *crystalline* topological phases to distinguish them from other SPTs. A good review of all these classifications is in [30]. The experimental hallmark of the topological phases are end/edge/surface modes (in 1/2/3D respectively) resulting from the bulk-boundary correspondence.[2] For example, 2D nodal phases protected by anti-unitary symmetries exhibit flat band edge modes [144, 151, 145, 82]. The flatness is not in general guaranteed for crystalline phases, as seen for example in 3D crystalline topological insulators, where they are referred to as drumhead states [15, 23, 156].

The classifications naturally include topological superconductors such as chiral [130] and helical [128] superconducting (SC) phases that exhibit Majorana edge modes (a pedagogical review of TSC is [143]). As we will see in Chapter 2, SC phases, which break a $U(1)$ symmetry[3], are in a sense another example of a symmetry protected phase.[4] The SC instability in which a Cooper condensate forms from electrons paired on opposite side of the Fermi surface (thereby destroying it) is only guaranteed to exist when the spectrum of the system is symmetric under momentum reversal $\mathbf{p} \to -\mathbf{p}$, which can be a consequence of TRS or inversion symmetry of the system. If the momentum-reversal symmetry is broken to a sufficient degree, the SC phase becomes unstable, but it can survive if the symmetry is only weakly broken, a situation we will also be interested in below.

[2] Though we will not consider them, crystalline symmetries also naturally result in the recently introduced higher-order topological invariants characterized by hinge states (corner states in 2D and 3D and edge states in 3D) [149, 172, 182, 79, 126].

[3] Note that it is not the *gauge* symmetry associated with charge conservation as sometimes stated [56].

[4] SC can be considered to be a topological phase [49], and it is well known to be characterized by off-diagonal long range order (ODLRO), with off-diagonal meaning that it is non-local. Relatedly, regular metallic Fermi surfaces have been understood as symmetry protected gapless topological phases [66, 177] protected by the $U(1)$ symmetry broken by SC. Luttinger's theorem stating that the area/volume in momentum space enclosed by the Fermi surface (which is the total electron density of the system) is fixed under renormalization can also be understood as a topological statement.

Often, new non-uniform phases can occur in proximity of the phase transition, in which the order parameter acquires a small momentum (thus breaking translational symmetry). Non-uniform SC phases of this kind are also known as Fulde-Ferrel-Larkin-Ovchinikov (FFLO) phases [53, 87], which we will consider in Chapter 4 (see also [104] for an overview). Another interesting possibility is that a non-uniform SC with large pairing momentum develops spontaneously, in which case it is referred to as a pair-density wave (PDW), a possibility we will explore in Chapter 5.

Given the considerations above, what kind of system would we want to consider if we are interested in topological phases? There are many possibilities (some discussed in reviews cited above). A 2D system might be interesting as we mentioned, especially if it is superconducting. Symmetry is also important: we want the system to be symmetric (so it has interesting topology) but not too symmetric (otherwise the topology is trivial). A hint as to what is not too symmetric is that spin-orbit coupling (SOC) is now well-established to sometimes lead to topological phases. SOC is itself a consequence of the absence of inversion symmetry, and systems that lack inversion are referred to as non-centrosymmetric. Non-centrosymmetric systems in general have garnered some attention in 3D materials like $CePt_3Si$ and other similar heavy fermion systems, and UTe_2 and some other uranium based superconductors. A good reference is [13], and a good review is in [163]. One of the main interests is the search for topological phase, and there are for example recent claims of chiral superconductivity in UTe_2 [71]. Lack of inversion symmetry has been considered in 2D as well (and much earlier), but until recently mostly in thin film systems with Rashba SOC induced by the substrate (and not intrinsic to the system), which was one of the earliest studied non-centrosymmetric systems [42, 54]. In that case FFLO is well-known to occur in presence of an in-plane magnetic field [42, 41, 3, 85, 107].

A class of non-centrosymmetric 2D materials with strong intrinsic Dresselhaus type SOC has more recently been produced using molecular beam epitaxy (MBE) and exfoliating bulk samples, namely the 1H transition metal dichalcogenides (TMDs). We will describe them in more detail inSection 1.2, and a general overview of TMDs is provided in [103]. Moreover, they have been observed to be superconducting in large in-plane magnetic fields that indicates the presence of strong SOC [22, 191, 168, 188, 98, 133, 187, 174, 157, 40, 122, 164], making them a good contender for realizing interesting topological SC phases.

The thesis of this dissertation is that they can indeed realize several such phases, at least theoretically. In particular, we will find that in additional to the nodal topological SC phase found by [62] in 1H-$NbSe_2$ in high in-plane magnetic fields, a crystalline nodal topological SC phase exists protected by a mirror symmetry when Rashba SOC is added to the system (as we generically expect due to

substrate effects), provided the in-plane magnetic field is aligned along certain symmetry directions. That phase can additionally host Bogolyubov Fermi surfaces. We also find a chiral SC phase in the limit of strong Rashba SOC (which is known for the case without Dresselhaus SOC [85, 127]). We also find that PDW phases are possible. As we will see in Chapter 6, the experimental reality is more complicated than the theory, but it offers potentially even more interesting possibilities.

1.1 Outline of this Dissertation and Methods Overview

After discussing the band structure of 1H-TMDs in Section 1.2 that will be the model material throughout the dissertation, the general outline of the thesis will roughly follow the logic outlined above. We will first consider the spontaneous symmetry breaking classification of phases from the more modern perspective of the renormalization group analysis (RG) in Chapter 2, with a focus on superconductivity as an instability of the Fermi surface, and apply it to the specific case of 1H-TMDs (in the absence of SOC) in Section 2.2. In Chapter 3 we then present more precisely the notion of symmetry protected topological phases and derive some of the invariants that will be relevant later. We also include a derivation of the $\mathbb{Z}_2$ invariant for time reversal invariant 2D topological insulators both because it illustrates the interaction between symmetry and topology we are interested in, and because I am not aware of this particular derivation appearing elsewhere in the literature (other derivations, of course, are well-known [52, 113]).

We then study the effects of SOC on uniform SC in 1H-TMDs in Chapter 4 (presenting the results of [153]) using a self-consistent mean field analysis. We identify several interesting topological phases mentioned above and below. In Chapter 5 we study the PDW instability that also arises in the RG analysis, which we do mostly neglecting SOC, though we consider its effect in Section 5.3. Those two chapters, along with Section 2.2, contain the main theoretical contribution of this thesis. In Chapter 6, we compare the theory with recent unanticipated experimental results and discuss a possible explanation within a phenomenological framework.

Below we give a more detailed outline, including an overview of the methodology and previous work, as well as our main results.

Methods and Results

Given a model of the normal state of 1H-TMDs (e.g. given in Section 1.2), how do we proceed to identify its phases, in particular the SC phase? Several previous studies have taken different approaches [195, 62, 199, 196, 165, 70, 67, 48, 179, 166, 123, 124, 110, 109, 115, 111]. The most

common approach among these has been to simply assume the standard BCS form of the gap function, i.e. an s-wave spin-singlet order parameter, as done for example in [62, 165, 70, 179, 166]. This is a bit dangerous given that 1H-TMDs have strong SOC and spin is not conserved, so spin-singlet and spin-triplet SC phases always mix, but nevertheless valid conclusions can be drawn even then: for example [62] found a nodal topological phase. Arguments from symmetry can then be used to show that including other terms does not affect the topology of the phase, an approach taken by [48] who also considered an additional f-wave triplet order.

A bit more generally, taking a phenomenological approach one could consider some or all possible symmetry allowed gaps. This is for example the approach in [195], who obtain a phenomenological form of the interactions and solve a self-consistent gap equation for 1H-MoS_2 with Rashba SOC, that has two K pockets in the hexagonal Brillouin zone. [123, 124, 110, 109, 115, 111] take a similar approach to systems with an additional pocket at the Γ point, considering symmetry allowed interactions and then numerically solving the gap equation.

A more rigorous approach is to use RG to identify the leading instabilities of the system, which is the method that we start with in this dissertation. This allows us to rule out some phases allowed phenomenologically, given some reasonable assumptions about the form of the bare interactions. In 1H-TMDs, an RG analysis was performed by [67] for doped 1H-MoS_2, but as we will outline below the systems we consider are more general. In Section 2.1 of Chapter 2, we will first present the general RG procedure for interacting fermionic systems, with the main goal of deriving the flow equations that we will solve for 1H-TMDs in Section 2.2. RG allows us to perform a stability analysis of the symmetric state of the system, which is the more modern approach to spontaneous symmetry breaking is to perform. Experimentally, such a stability analysis amount to for example placing a system in a small external magnetic field to see if it develops a magnetization that remains after the external field is turned off. If it does, we conclude that the system is a ferromagnet. Essentially, we 'tap' the system with the external field to see if it develops a symmetry breaking order (similar to a pencil falling over in the direction it was tapped in). RG is allows us to perform a theoretical analogue of this procedure using quantum field theory. In theory and experiment, the external field induces a response of the system that either shrinks to zero or grows to infinity under RG. In the former case we say the system is at a fixed point of RG, while in the latter we say that there is an instability and a new fixed point corresponding to the ordered state is reached. All phases of matter can be classified as fixed points of RG by this procedure.

The RG analysis is a standard technique and has been applied in many other condensed matter systems, e.g.: high T_c systems like cuprates and pnictides [63, 80, 32, 33, 50, 65] (see [102, 45] for a

review); FeSe [190]; Sr_2RuO_4 [173]; doped [120, 119, 121], bilayer [39] and twisted bilayer graphene [26, 27, 34, 35, 78]; layered oxides [171, 147]; and many other systems. More recently RG has been applied to TMD systems as well, specifically for doped MoS_2 with spin polarized Fermi surfaces located at K points of the hexagonal Brillouin zone [67], and for a system with a similar 'fermiology' to TMDs but with a Γ hole pocket and electron K pockets (which therefore exhibits particle-hole instabilities including magnetism) in [192]. Our work presented in Section 2.2 is the first to apply RG to generic 1H-TMD (and similar) systems that have only hole pockets at Γ and K points [153].

Note that several RG schemes exist, and in Section 2.1 I will be describe the momentum shell (parquet) RG mostly following the standard reference [154]. There are many other good references that go over the RG calculation, including several textbooks [9, 37, 49, 155, 1] and papers [102]. However, I will make several technical amendments to [154] that will be needed for our application. First of all, I will use the coherent state path integral formulation at finite temperature since there is little extra cost (and this allows us to compute T_c in RG), and use a slightly different Feynman diagrams. I will also be more careful about the soft cutoff, following the method standard in non-perturbative RG due to Polchinski [1], which will simplify the tree level analysis and works better for lattice systems. On a lattice it is also more convenient to use a different interaction decomposition (Chebyshev polynomials instead of Legendre polynomials). We will emphasize throughout that RG is a *stability* analysis of the system.

The main technical difference from [154] is that I will include band and spin indices. This will lead to the main technical result in Section 2.2: that a singlet SC instability is possible with purely repulsive interactions due to pair hopping between the Γ and K pockets, similar to the $s^{\pm}$ state considered in [171, 65]; as well as a triplet superconducting instability that is possible due to the topology of the K pockets (a mechanism very different from one considered in [67]), promoted by an exchange interaction.[5] To the best of my knowledge, this is the first time a triplet SC phase was found in RG in TMD-like systems, but a similar phase was found in some models in doped graphene [57] and considered phenomenologically in doped MoS_2 [131, 195]; more recently it was found in bilayer TMDs in [75].

In addition, we find that singlet and triplet PDW instabilities are possible, in case of repulsive interactions only if either an Umklapp process (taking a K, K pair to a $\Gamma, -K$ pair) or a process exchanging Γ and $\pm K$ is sufficiently strong, respectively realizing a singlet or a triplet PDW instability. Note that PDW has also already been considered in 1H-TMDs with repulsive interactions,

[5] Note that if we think of total momentum measured from the Γ point, the exchange process is in equivalent to backscattering that underlies the Kohn-Luttinger mechanism.

specifically in systems with the structure of doped 1H-MoS_2 that do not have a Γ pocket [67, 176]. The latter refers to a PDW with a small pairing momentum that is more analogous to the standard FFLO. [67] invoke the Kohn-Luttinger mechanism [83] (a two-loop RG calculation in 2D [102]), which may be relevant at very low temperatures and which we do not consider. In our model no PDW arises from repulsive interaction in the absence of the Γ pocket.

To include SOC in our analysis of uniform SC, we switch to a mean-field analysis, using interactions we found in the RG analysis. In order to study their topology, we will first discuss symmetry protected topological phases more broadly in Chapter 3, focusing on the topological invariants that we will later use, which includes invariants for 2D crystalline nodal phases protected by a mirror symmetry. In Chapter 3 we therefore begin with an overview of the 1D two-level system with mirror symmetry that, when extended into 2D, will lead to the phase that we later find in Chapter 4. Since we also find a chiral phase, we present a general procedure for computing the Berry curvature in SC systems and discuss the Chern number. We also present a derivation of the Chern number (following [161]) that we then extend to a derivation of the Fu-Kane [52] (or Kane-Mele [76, 77, 113]) $\mathbb{Z}_2$ invariant as a case study of the interplay between symmetry and topology. Though the result is well-known, to the best of my knowledge the latter derivation has not been presented in the same approach elsewhere in the literature.

In Chapter 4 we present a self-consistent mean field analysis of superconductivity in metallic 1H-TMD systems with strong SOC and/or magnetic field, focusing on systems with a Γ pocket like 1H-$NbSe_2$. This is the main result reported in our work in [153]. Note that no previous studies cited above simultaneously considered Ising and Rashba SOC with an in-plane magnetic field (as mentioned, Rashba SOC with and without in-plane magnetic fields has been considered previously), and all express the gap function in terms of spin-singlet and spin-triplet components that are mixed due to the SOC. We find it more convenient to work in a basis in which the Hamiltonian (and therefore the Green's function that enters the gap equation) is diagonal. We refer to the corresponding basis the SOC basis, which is also known as the helical or band basis in non-centrosymmetric literature ([13, 163] provide good overviews). Working in the spin basis is of course equally valid (especially for weak SOC), and has been used to study non-centrosymmetric systems besides TMDs for example in [51, 55]. It is more common, however, to work in the SOC basis, as done already by Gor'kov and Rashba in [54] who pointed out the possibility of spin-singlet and spin-triplet mixing, and more recently in [138, 136, 135, 137, 141, 146, 85, 184]. In the limit of strong SOC or magnetic field, it greatly simplifies the analysis as we can consider pairing between inner and outer Fermi surfaces only.

Using the SOC basis, in Chapter 4 we confirm the previous result of [62] who showed the existence of a nodal topological phase in presence of a strong in-plane magnetic field protected by the TR-like symmetry $\tilde{\mathcal{T}}$. However, we find that these nodes are generically lifted by Rashba SOC unless the magnetic field is oriented along one of the Γ-K directions, in which case a *crystalline* nodal topological phase is realized, protected by a vertical mirror symmetry. We show this first by simply projecting the gap function into the SOC basis, which has a simple physical interpretation base on symmetry properties of spin under reflection. We then go over the solutions of the linearized gap equation in for various parameter values and present a phase diagram, confirming the existence of the nodal phases. In the presence of both Rashba and magnetic field, the nodes in the crystalline phase are shifted from zero energy, resulting in small Bogolyubov Fermi surfaces (which have recently been considered in [7, 194, 20, 106, 167]). The nodes are likely brought back to zero energy in the FFLO phase that is expected to be realized due to the asymmetry, but we do not study the FFLO self-consistently. Finally, we find that in addition to the nodal phase, a chiral SC phase that spontaneously breaks TRS is realized in the absence of a magnetic field and at large Rashba SOC (relative to Ising SOC), assuming the triplet instability we found in Chapter 2 is the leading instability in the absence of SOC. Similar phases of different physical origin have been found in doped MoS_2 [67] and doped graphene [200, 120]. We confirm the topological nature of both the chiral and the nodal phases using an analysis following the general one presented in Chapter 3.

Next, in Chapter 5 we consider the PDW instability we also find in RG. The PDW phase is similar to the FFLO [87, 53] phase and both are examples of inhomogeneous SC with an order parameter $\Delta \sim e^{i\mathbf{r}\cdot\mathbf{Q}}$, with $\mathbf{Q}$ being the total momentum of the Cooper pairs. Unlike FFLO, however, PDW emerges spontaneously in a material with no external fields breaking time reversal symmetry (TRS).[6] PDW has been invoked to explain some aspects the pseudogap regime in cuprates like the observed charge density wave (CDW) order, which as we will see can be induced by the PDW (see [8] for a review, which also covers PDW more generally in other systems). More recently it has also been proposed to exist in halos of vortices of uniform superconductors [181] and in the vicinity of the $\nu = 5/2$ fractional quantum hall state [142]. Even more recently, there is a claim of observation of PDW on the surface of bulk 2H-$NbSe_2$ [97].

Unlike the uniform SC phases, the PDW is not guaranteed by any intrinsic symmetry of the system, and in particular is suppressed by trigonal warping at K pockets (see Figure 1.2). After a general phenomenological Ginzburg-Landau discussion, we therefore perform a self-consistent stability analysis accounting for detuning from perfect nesting, including the trigonal warping and

[6] Some authors consider FFLO to be a special case of PDW.

miss-match between the Γ and K pockets. This identifies the range of detuning parameters for which PDW remains a viable instability. We further analyze whether the PDW is of FF or LO type is realized, meaning one or both of K and $-K$ pairing momentum PDWs are present respectively, the former therefore spontaneously breaking TRS. Paring between Γ and K pockets (which we find is needed for repulsive interactions to stabilize the PDW instability) turns out to favor FF-type PDW.

Finally, in Chapter 6, we look at a recent experiment on few-layer 1H-$NbSe_2$ reported in [58], who found a twofold anisotropic response to an in-plane magnetic field rotated around the sample (a very similar experiment and result was also reported in [186]; one of the samples in their case was a monolayer). This is not consistent with any of the solutions we find in Chapter 4 (which suggests the anisotropy should be sixfold if Rashba SOC is present), which may be due to the presence of strain that we have ignored in our analysis.By symmetry, we find that both the horizontal mirror symmetry and the three-fold rotation symmetry must be broken to a two-fold symmetry by some fields other than the magnetic field (possibly by Rashba SOC and strain respectively). Using a phenomenological model (generalizing [160]), we argue that the most plausible explanation is a proximity and mixing between the usual s-wave singlet SC instability and either a p-wave triplet or d-wave singlet SC instability.[7]

1.2 Non-Centrosymmetric 1H-TMDs

In this section we will present the lattice and a model of the band structure of 1H-TMDs including SOC, establishing the notation that we will refer to throughout the dissertation. We will also include symmetry breaking terms like Rashba SOC and in-plane magnetic field that are of interest both theoretically and experimentally.

Although TMDs have several possible lattice structures, we are mostly interested in the 1H structure since it breaks inversion symmetry (see Figure 1.1). The H stands for hexagonal, while the 1 indicates the number of layers in a unit cell (one for a monolayer). The parent bulk compounds are 2H-TMDs in which the inversion symmetry is restored and relates neighboring layers within a single unit cell (in some references the monolayers are also referred to as '2H' as a result). All of the structures are made of a layer of transition metals (in a triangular lattice for the 1H structures) sandwiched between two layers of chalcogen atoms, which are atoms in the oxygen family. Common examples are MoS_2 (which is an insulator but can become metallic when doped by electrostatic gating), TaS_2, and $NbSe_2$. The latter are metals and will be the main examples we consider.

[7] More accurately, between A_1' irrep of D_{3h} and one of the 2D irreps E' or E''.

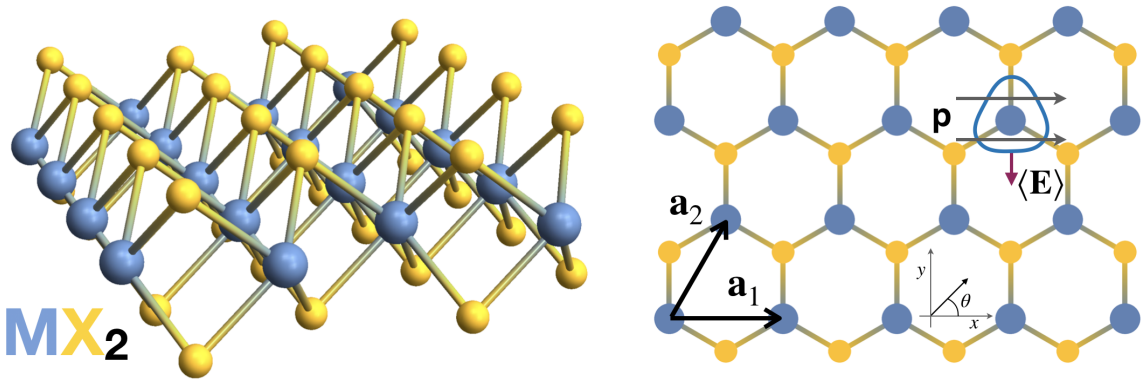

Figure 1.1: Lattice structure of 1H-TMDs MX_2 where M is a metal and X is a chalcogen. Basis lattice vectors $\mathbf{a}_1$ and $\mathbf{a}_1$ are also shown. The figure also illustrates how the absence of inversion symmetry results in SOC: an electron in a Bloch plane-wave state with momentum $\mathbf{p}$ going in the $\hat{\mathbf{x}}$ direction is in a superposition of states that pass on top and bottom of a given nucleus (the paths are indicated with gray arrows), which sees a different nuclear electric field (an equipotential of the field is shown). The Bloch wave therefore sees an effective average electric field $\langle \mathbf{E} \rangle$ pointing in the $-\hat{\mathbf{y}}$ direction. In the electron's rest frame, it therefore sees a magnetic field $\mathbf{B} \propto \mathbf{p} \times \langle \mathbf{E} \rangle$ that point out of the page, which is the Ising SOC.

The main property of these materials that we are interested in is SOC. To see how it arises due to the lack of inversion symmetry, recall that it is a relativistic effect due to the relative motion of the electrons and the nuclei in the system. An electron moving with velocity $\mathbf{v}$ relative to a nucleus with electric field $\mathbf{E}$ will in its own rest frame see a magnetic field $\mathbf{B} = -\mathbf{v} \times \mathbf{E} \propto \mathbf{p} \times \mathbf{E}$ (in Gaussian units with $c = 1$). The magnetic field couples to the electron's spin through the usual Zeeman coupling, $H_{SOC} = -\boldsymbol{\mu} \cdot \mathbf{B} \propto \mathbf{S} \cdot \mathbf{p} \times \mathbf{E}$ where $\mathbf{S}$ is the spin of the electron. If the electric field of the nucleus is taken to be $\mathbf{E} \propto \frac{Z\mathbf{r}}{r}^3$ where Z is the atomic number, after averaging we get the standard SOC term $H_{SOC} \propto \frac{Z^4}{a_0^3} \mathbf{L} \cdot \mathbf{S}$ where a_0 is the Bohr radius and $\mathbf{L} = \mathbf{r} \times \mathbf{p}$ is the angular momentum (see, e.g., [86]). This shows also why the presence of heavy transition metals is important, as it greatly enhances the SOC. Note that the SOC can be thought of as an effective magnetic field $\mathbf{g}(\mathbf{p})$ that is an odd function of momentum. This means it preserves time reversal symmetry (TRS), but it breaks spin rotation symmetry (i.e. spin is not conserved, since electrons with different spins have different energies).

In a crystal lattice, however, the electrons we are interested in are in fully delocalized Bloch states and not bound to the nucleus. If the Bloch wave is propagating with momentum $\mathbf{p}$, it is in an equal superposition of states of electrons that pass a given nucleus on the left and on the right (in 2D). As a result, the SOC needs to be averaged over all the states (formally this can be done using perturbation theory). In a centrosymmetric system, this average vanishes for all momenta due to

the inversion symmetry: for any path the electron takes passing at $\mathbf{r}$, there is a path where it passes at $-\mathbf{r}$ though an equal nuclear electric field that contributes the exact opposite effect. In a non-centrosymmetric system, the nuclear field is distorted (e.g. due to electron bonds with neighboring nuclei), and so the SOC effect doest cancel between the two paths. We can also think of the net SOC effect as being due to an average electric field (averaged over the direction perpendicular to the motion of the Bloch wave), which we can see is non-zero from Figure 1.1.

Symmetry places additional constrains on the form of SOC in 1H-TMDs, which have D_{3h} point group symmetry. The Brillouin zone is hexagonal and we take one of the K points to lie along the x axis. As we saw the field $\mathbf{g}(\mathbf{p})$ must be odd due to TRS. D_{3h} contains a three-fold rotation symmetry C_3, which leads to $\mathbf{g}(\mathbf{p}) \propto \cos 3\theta$ with θ the angle of the momentum $\mathbf{p}$ measured from the x axis. The h in D_{3h} means that it also has a horizontal mirror symmetry M_z, with the reflection plane being the xy plane. Note that under reflection, spin components parallel to the mirror flip, while perpendicular components stay the same, a fact that will be important at several instances in this thesis. In this case, the mirror symmetry means that spins have to point out of the plane, and as a result

$$\mathbf{g}(\mathbf{p}) = \lambda_I p_x (p_x^2 - 3p_y^2)\hat{\mathbf{z}} = \lambda_I p_F^3 \cos 3\theta \hat{\mathbf{z}} \tag{1.1}$$

where λ_I is a constant and p_F is the Fermi momentum (we will mostly be interested in Fermi surface physics). Importantly, note that the SOC vanishes along the Γ-M lines by symmetry (not just for the leading order term). This is a form of Dresselhaus SOC which is well known. All possible forms of SOC have been tabulated for all non-centrosymmetric point groups, e.g. in [163].

1.2.1 Band Structure and $\mathbf{k} \cdot \mathbf{p}$ Model

Another important aspect of 1H-TMDs is their band structure. Technically, only a single energy band (split into two by SOC) crosses the Fermi level (see Figure 1.2), and it is predominantly composed of d-orbital electrons originating from the transition metal. Heuristically, we can therefore think of 1H-TMD monolayers as a metallic layer sandwiched between two insulators, with all the transport happening in the metallic layer. Importantly, there are disconnected hole pockets centered at the two non-identical K points (with $K' = -K$) in all metallic 1H-TMDs systems like doped MoS_2, and an additional hole pocket at the Γ point in intrinsically metallic monolayers like $NbSe_2$ and TaS_2 (see Figure 4.1). Various first-principles studies like bulk (and more recently monolayer) DFT calculations and monolayer tight-binding models suggest that the Γ pocket is composed predominantly from d_{z^2}

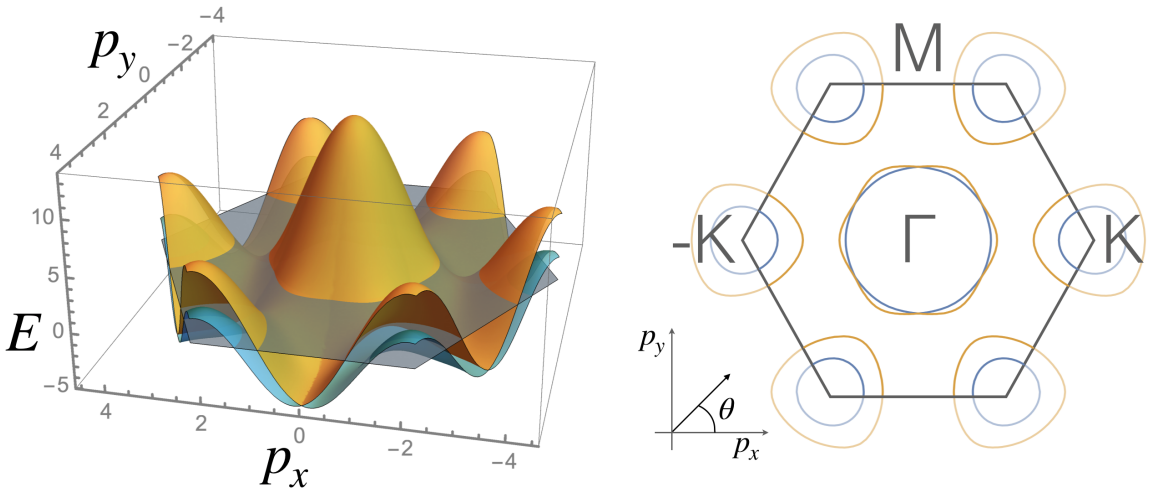

Figure 1.2: Cartoon band structure (left) and Fermi surfaces (right) of metallic 1H-TMDs (doped insulating 1H-TMDs are similar, but typically have no Γ pocket), with Fermi level at $E = 0$, obtained using a tight-binding model with parameters summarized in Appendix A (no attempt at fitting the real band structure has been made, and the Ising SOC is much larger than in real systems to illustrate the splitting). Note the spin degeneracy along Γ-M lines.

orbitals (onsite to leading order in a tight-binding model), while $\pm K$ pockets are predominantly $d_{x^2-y^2} + d_{xy}$ in character (mostly arising from nearest-neighbor hopping in a tight-binding) [73, 96, 123, 110, 184].

For systems with K pockets only, a valley index $\epsilon = \pm 1$ corresponding to the ϵK point is often introduced by analogy with graphene. To account for the Γ pocket, we introduce a generalized valley index $\eta = 0, \pm 1$ corresponding to ηK points, with $0K = \Gamma$ by convention (it will occasionally be necessary to introduce a second valley index, for which we will useζ). For clarity, we will sometimes interchangeably use $\eta = \Gamma, \pm K$. An important point is that $3K$ is equivalent to Γ (i.e. it is an Umklapp momentum), which means that the η valley index is defined modulo 3. The form of SOC we obtained above is an expansion about the Γ point,

$$\mathbf{g}_\Gamma(\mathbf{p}) = \lambda_I p_F^3 \cos 3\theta \hat{\mathbf{z}} \tag{1.2}$$

with p_F and θ measured from the Γ point. To obtain the SOC at the K points, we restrict this form to the K points (keeping only the leading order):

$$\mathbf{g}_{\pm K}(\mathbf{p}) = \pm \beta_I \hat{\mathbf{z}} \tag{1.3}$$

where the SOC is simply constant at the pocket and in that sense even more analogous to an out-of-plane magnetic field. The authors who originally considered it in MoS_2 were reminded of the Ising model, and so SOC of this form has been dubbed Ising SOC [98] (which is what the I stands for in the subscripts). We thus arrive at the effective $(\mathbf{k}\cdot\mathbf{p})$ model of the normal state of 1H-TMDs:

$$H = \sum_{\mathbf{p}\eta\alpha\beta} d^\dagger_{\mathbf{p}\eta\alpha} \left[\epsilon_\eta(\mathbf{p}) + \mathbf{g}_\eta(\mathbf{p})\cdot\boldsymbol{\sigma}\right]_{\alpha\beta} d_{\mathbf{p}\eta\beta} \tag{1.4}$$

where $d_{\mathbf{p}\eta\alpha}$ are annihilation operators for electrons at the ηK pocket with momentum $\mathbf{p}$ measured from the ηK point with spin $\alpha = \pm 1$ for spin up and down respectively (quantized along the out-of-plane z axis), and

$$\epsilon_\eta(\mathbf{p}) = -\frac{p^2}{2m_\eta} - \mu_\eta \tag{1.5}$$

is the dispersion in the absence of SOC, with m_η, μ_η being the corresponding effective mass and chemical potentials that may not be equal between different pockets. $\boldsymbol{\sigma} = (\sigma^x, \sigma^y, \sigma^z)$ is a vector of Pauli matrices. To give a sense of scale, the band width in metallic 1H TMDs is typically on the order of 1 eV, while the Ising SOC is estimated to be around $\lambda_I p_F \sim$35 meV at Γ and 75 meV at K points in monolayer DFT calculation [184] (see also [189, 96, 84, 110]), with an average SOC reported around 40 meV in 1H-$NbSe_2$ [187, 40]. Taking $\mu = -0.4$ eV gives $m = p_F^2/2\mu \approx m_0$ where m_0 is the electron rest mass when the wavenumber corresponding to the Fermi momentum is $p_F/\hbar = 0.45$ Å^{-1} [18], which matches reasonably well the Fermi surfaces found in the first-principle calculation (see Figure 4.1(a)). Note that because Ising SOC vanishes along the Γ-M lines where spin is therefore degenerate, the Fermi surfaces at the Γ pocket intersect along those lines.

1.2.2 Symmetry Breaking Perturbations

In addition to the intrinsic SOC, we will consider symmetry breaking terms in the Hamiltonian. These in general correspond to some symmetry breaking fields (e.g. electric, magnetic, or strain fields), which are conveniently categorized using irreducible representations (irrep) of the D_{3h} point group (actually it will later be convenient to think of a system with D_{6h} point group symmetry in the absence of any SOC, with Ising SOC being a symmetry breaking field braking it down to D_{3h}). Recall that a representation is (from a mathematical point of view) a map $\rho : G \to GL(V)$ from the symmetry group G to the group of linear transformations (i.e. matrices) $GL(V)$ of a certain vector space V; physically, the vectors of that vector space are the symmetry breaking fields, and

often the space itself is also referred to as the representation. The point is that the fields are acted upon by the symmetry group and transform using matrices (that represent the group). In general the symmetry can map some vector components into each other, but some components are never mapped into each other. The vector space can thus be broken into irreducible pieces that do not transform into each other and only stay within their irreducible subspace of smaller dimension (in 2D point groups, the dimension is always $1, 2$ or 3). A representation restricted to these irreducible N-dimensional subspaces is called an irrep of dimension N and the corresponding fields are said to transform according to that irrep. Typically a field belonging to a single irrep will only break some of the point group symmetries, reducing it to a point group that is a subgroup of the original one. Table 1.1 lists all the irreps of D_{3h} (that we label with ℓ by analogy with orbital angular momentum that labels irreps of $SO(2)$) and the corresponding physical fields/functions of cartesian coordinates belonging to those irreps, as well as the reduced point groups.

$\ell(D_{3h})$	Cartesian	Field	Subgroup
$A_1^{'}$	$1, \cos 3\theta$	NA	NA
$A_2^{'}$	$R_z, \sin 3\theta$	B_z	C_{3h}
$A_1^{''}$	$z \sin 3\theta$	B_z with E_z	D_3
$A_2^{''}$	z	E_z or Rashba SOC	C_{3v}
$E^{'}$	x, $x^2 - y^2$ y, $2xy$	$\mathcal{E}_x$ $\mathcal{E}_y$	C_s (C_{2v})
$E^{''}$	R_x, xz R_y, yz	B_y $-B_x$	C_s (C_2)

Table 1.1: Irreducible representations (irreps) of the D_{3h} point group symmetry, functions of Cartesian coordinates (including rotations R_j) and physical fields that transform according to these irreps, and the reduced point groups in the presence of the fields (groups in parentheses have non-canonical orientations). E_j and B_j are components of electric and magnetic fields, $\mathcal{E}_j$ are components of the shear strain tensor (or electric field). Note that the E' and E'' irreps are 2D, and the irrep fields have two components that we list in columns.

We will mostly consider magnetic fields and Rashba SOC as the symmetry breaking fields. Rashba SOC [21] transforms according to the A_2'' irrep and breaks the horizontal mirror symmetry (as well as two-fold rotations, so the reduced group is no longer dihedral). Physically, this is usually due to the fact that 2D samples are on a substrate, but it can also be tuned by perpendicular electric fields. In either case the SOC arises due to the same effective magnetic field seen in the rest frame of the electron, but in this case due to (nuclear or external) electric fields that point (on average) in

the z direction. Repeating the SOC calculation we did above with $\mathbf{E} = E\hat{\mathbf{z}}$, we find that

$$\mathbf{g}_R(\mathbf{p}) = \alpha_R(p_y\hat{\mathbf{x}} - p_x\hat{\mathbf{y}}) \tag{1.6}$$

with the Rashba SOC parameter α_R (so the energy scale associated with Rashba is $\alpha_R p_F$). This results in spins aligning in a circulating patter around the Fermi surface. Note that since Rashba SOC does not vanish along Γ-M lines, the spin degeneracy at those points is lifted, and the Fermi surfaces at the Γ pocket split and no longer intersect. For simplicity we assume the Rashba parameter is equal on all pockets. As mentioned above, 2D non-centrosymmetric superconductors with Rashba SOC have been well-studied, in part since it is expected to occur even in thin film systems without any intrinsic SOC (e.g. [54, 127, 85, 140, 137, 148]).

It is also well-known that SOC in 2D materials makes the superconducting state particularly robust agains in-plane magnetic fields (which belongs to the E'' irrep) [51]. Indeed, the Pauli limit has been seen to be exceeded in multiple experiments on superconducting 1H-TMDs [22, 191, 168, 188, 98, 133, 187, 174, 157, 40, 122, 164], with Ising SOC being invoked as the explanation in [98, 133, 187, 40, 70, 51]. This is because the orbital limiting (i.e. vortex proliferation) is absent for an in-plane field, while the paramagnetic Pauli (or Chandrasekhar-Clogston [24, 36]) limiting that typically results from Cooper pair breaking in conventional s-wave spin-singlet BCS superconductors due to spin alignment with the external field is absent due to SOC (in simple terms because spin is not conserved, and Cooper pairs always have singlet components). The external field adds a Zeeman term to the Hamiltonian

$$H_Z = \sum_{\mathbf{p}\eta\alpha\beta} d^\dagger_{\mathbf{p}\eta\alpha} \left[\mathbf{b}\cdot\boldsymbol{\sigma}\right]_{\alpha\beta} d_{\mathbf{p}\eta\beta} \tag{1.7}$$

where $\mathbf{b} = \frac{1}{2} g_L \mu_B \mathbf{B}$ is the magnetic field in units of the Bohr magneton μ_B times the Landé g-factor g_L. As we will see in Chapter 4, the fact that the Pauli limit is exceeded is best understood in terms of electrons with a given momentum $\mathbf{p}$ seeing an effective magnetic field that is a combination of both the external magnetic field and the effective magnetic field due to SOC with the total normal state Hamiltonian given by

$$H = \sum_{\mathbf{p}\eta\alpha\beta} d^\dagger_{\mathbf{p}\eta\alpha} \left[\epsilon_\eta(\mathbf{p}) + \boldsymbol{\beta}_\eta(\mathbf{p})\cdot\boldsymbol{\sigma}\right]_{\alpha\beta} d_{\mathbf{p}\eta\beta} \tag{1.8}$$

where

$$\boldsymbol{\beta}_\eta(\mathbf{p}) = \mathbf{g}_\eta(\mathbf{p}) + \mathbf{g}_R(\mathbf{p}) + \mathbf{b} \tag{1.9}$$

As a result, when the magnetic field is applied the spins tilt in its direction but do not fully align with it, and some spin-singlet pairing remains possible. Note that the spin degeneracy is again lifted along the Γ-M lines (even without Rashba SOC) and the Γ Fermi surfaces split. An alternative (though less likely) explanation would invoke spin-triplet interactions, which as we will see may be possible in these systems (in that case the Pauli limit does not apply even in the absence of SOC). Again for a sense of magnitude of the parameters, $\alpha_R p_F$ was estimated to be about 0.8 meV in gated MoS_2 in [98], while a magnetic field $b = 0.5$ meV corresponds to about 8.3 T. In other words, we expect these to be much smaller than the Ising SOC, but possible comparable or larger than the size of the SC gap (which vanishes at the phase transition and estimated to be about 2 meV at zero temperature in [58]).

That superconductivity remains possible in large magnetic fields in itself offers interesting possibilities for unconventional SC phases. Besides breaking the point group symmetries (including importantly the vertical mirror symmetry), the in-plane magnetic field breaks TRS. In the absence of Rashba SOC, however, it does not break the product of TRS and the vertical mirror symmetry $\tilde{\mathcal{T}} = \mathcal{T} M_z$ (where $\mathcal{T} = i\sigma^y \mathcal{K}$ is TRS and $\mathcal{K}$ is complex conjugation), which acts as a TR-like symmetry (we will define what that means more precisely in Chapter 3). This is another important reason why SC can be seen above the Pauli limit: as a result of this symmetry, the Fermi surfaces remain symmetry under momentum reversal $\mathbf{p} \to -\mathbf{p}$ (as has also been pointed out in [48]). As we will emphasize in Chapter 2, the momentum reversal symmetry of the Fermi surfaces (more precisely the whole band structure) is a fundamental reason why SC is possible. As we will see in Chapter 4, the TR-like symmetry also protects nodes in a nodal topological superconducting phase that was first noted in [62], who were motivated by the experiments cited above.

When both Rashba SOC and in-plane magnetic field are present together, no TR-like symmetry exists, which means that in general both the nodes and the superconductivity lose their protection. It will turn out that the nodes disappear immediately except for one case: we will show in Chapter 4 that if the the magnetic field oriented along one of the Γ-K directions two pairs of the original six pairs of nodes remain and are protected by a horizontal mirror symmetry $\mathcal{M}_x = i\sigma^x$ that alone is not broken. The SC phase itself is more robust than the nodes and remains stable as long as the symmetry breaking is not too strong. Note that the shifting of the Fermi surfaces is well-known to

occur in the same situation with no Ising SOC [42, 41, 3, 85, 107], resulting in FFLO phases (the effect is not unique to SC phases [178]). The question of when a phase 'protected' by a symmetry can survive when that symmetry is broken will arise also when we study pairing instabilities *within* the K pocket in Chapter 5 (another reason the pocket structure is interesting in TMDs), which results in a pair density wave (PDW) phase with Cooper pairs with a large total momentum.

The SOC Basis

For later reference throughout this dissertation, note that the total Hamiltonian is diagonalized by operators

$$c_{\mathbf{p}\eta\tau} = U^{\alpha}_{\eta\tau}(\mathbf{p}) d_{\mathbf{p}\eta\tau} \tag{1.10}$$

where the index $\tau = \pm$ labels inner and outer Fermi surfaces respectively. The unitary transformation is

$$U^{\alpha}_{\eta\tau}(\mathbf{p}) = \frac{1}{\sqrt{2}} \sqrt{1 + \frac{\tau\alpha\beta_{\eta z}(\mathbf{p})}{\beta_{\eta}(\mathbf{p})}} \left(\tau e^{-i\phi_{\eta}}\right)^{\frac{1+\alpha}{2}} \tag{1.11}$$

where

$$e^{i\phi_{\eta}(\mathbf{p})} = \frac{\beta_{\eta x} + i\beta_{\eta y}}{|\beta_{\eta x} + i\beta_{\eta y}|} = \frac{\alpha_R p_y + b_x + i(-\alpha_R p_x + b_y)}{\sqrt{(\alpha_R p_y + b_x)^2 + (\alpha_R p_x - b_y)^2}}, \tag{1.12}$$

with $\beta_{\eta} = |\boldsymbol{\beta}_{\eta}(\mathbf{p})|$ (which plays the role of a magnetic field). We will refer to this as the SOC basis (also referred to as band or helical basis in non-centrosymmetric literature), though note that we also include the magnetic field in it. The normal state dispersions (i.e.eigenvalues of the Hamiltonian) are

$$\xi_{\eta\tau}(\mathbf{p}) = \epsilon_{\eta}(\mathbf{p}) + \tau \left|\boldsymbol{\beta}_{\eta}(\mathbf{p})\right| \equiv \epsilon_{\eta}(\mathbf{p}) + \tau\beta_{\eta}(\mathbf{p}) \tag{1.13}$$

with the Fermi surfaces determined by $\xi_{\eta\tau}(\mathbf{p}) = 0$.

Chapter 2

The Renormalization Group

In this chapter we review the renormalization group (RG) technique for fermionic many-body systems in Section 2.1. RG allows us to obtain an effective action for low-energy modes of the system by successively integrating out high-energy modes, and to identify any instabilities of the system that correspond to symmetry breaking phases, in particular superconducting phases that we are most interested in. We then apply RG to transition metal dichalcogenides in Section 2.2. As explained in the introduction, we generally follow the standard reference [154], amending where necessary for our purposes. The analysis in Section 2.2 is the first theoretical contribution of this dissertation, part of which appeared in [153].

2.1 Renormalization Group

RG is essentially a stability analysis of many body systems that allows us to understand symmetry breaking phases of matter as instabilities of symmetric but unstable states. This is closely related to the way we test phases in experiment in which symmetry breaking perturbations are introduced to probe the system. For example, we can send a particle (or beam) into the system and see what comes out, or apply an external field to see if the system will order. The path integral formalism using coherent states was in part developed to theoretically study precisely this situation and allows us to add symmetry breaking terms to the path integral [37], and which we therefore use in RG. To emphasize this connection with experiment, we recall the linear response theory in Section 2.1.1, which naturally leads to the concept of an effective action and renormalization (including in particular RG) that we introduce in Section 2.1.2. From there the analysis follows the standard path: we consider the Gaussian (and Fermi liquid) fixed points (which represent the symmetric state) in Section 2.1.3, including corrections to interactions at leading order (tree level).

Going to next order in Section 2.1.4 we find that the symmetric fixed points are unstable to various interaction channels, in particular the pairing channel we are most interested in. We derive the RG flow for the interactions in that subsection. Finally, in Section 2.1.5 we will see that the instability indicates formation of bound states that become the relevant degrees of freedom at a new fixed point. We show that an equivalent approach is to introduce an external bound state (as a symmetry breaking perturbation or vertex) and see if the system orders in response by computing the RG vertex flow. The external vertex and internal interaction RG flows give equivalent results, and we use both in the next section Section 2.2.

2.1.1 Linear Response of a System: The Green's Function

There are many references that cover the formalism that we present here, including the diagrammatic technique that we will be using [9, 37, 74, 49, 100, 46, 92, 2]. In this formalism, as in usual statistical mechanics, the system is described by the partition function

$$\mathcal{Z} = \int e^{-S[d,\bar{d}]} \mathcal{D}\bar{d}\mathcal{D}d \tag{2.1}$$

S is the action of the system that is a functional of the fields (which are themselves functions) and where d is a fermionic field expressed in terms of Grassmann variables. We will work in momentum space and take $d_{\mathbf{p}\eta\alpha}$ as in Section 1.2 with η a pocket/band index and $\alpha = \uparrow, \downarrow = \pm 1$ the spin index, and the momentum $\mathbf{p}$ is measured from the pocket center. The action for such systems can quite generally be written as (in imaginary time formalism accounting for finite temperature)

$$S[d_{\mathbf{p}\eta\alpha}, \bar{d}_{\mathbf{p}\eta\alpha}] \equiv S[d, \bar{d}] = \int_0^\beta L[d_{\mathbf{p}\eta\alpha}, \bar{d}_{\mathbf{p}\eta\alpha}] d\tau \tag{2.2}$$

with imaginary time τ integrated up to $\beta = 1/T$ (taking the Boltzmann constant to be 1), where the Lagrangian is

$$L[d_{\mathbf{p}\eta\alpha}, \bar{d}_{\mathbf{p}\eta\alpha}] = \sum_{\mathbf{p}\eta\alpha} \bar{d}_{\mathbf{p}\eta\alpha} \partial_\tau d_{\mathbf{p}\eta\alpha} + H[d_{\mathbf{p}\eta\alpha}, \bar{d}_{\mathbf{p}\eta\alpha}] \tag{2.3}$$

with Hamiltonian

$$H[d_{\mathbf{p}\eta\alpha}, \bar{d}_{\mathbf{p}\eta\alpha}] = \sum_{\mathbf{p}\eta\alpha\beta} \bar{d}_{\mathbf{p}\eta\alpha} \left[\mathcal{H}_\eta(\mathbf{p})\right]_{\alpha\beta} d_{\mathbf{p}\eta\beta} + \\ + \sum_{\substack{\mathbf{p},\mathbf{k},\mathbf{q} \\ \eta\eta'\zeta\zeta'\alpha\beta\alpha'\beta'}} V_{\eta\zeta;\alpha\beta}^{\eta'\zeta';\alpha'\beta'}(\mathbf{p},\mathbf{k},\mathbf{q}) \bar{d}_{\mathbf{p}+\mathbf{q},\eta'\alpha'} \bar{d}_{\mathbf{k}-\mathbf{q},\zeta'\beta'} d_{\mathbf{p}\eta\beta} d_{\mathbf{k}\eta\beta} \tag{2.4}$$

where α', β, β' are additional spin indices and η', ζ, ζ' are additional pocket indices, and V are the interactions. Again quite generally,

$$\mathcal{H}_\eta(\mathbf{p}) = \epsilon_\eta(\mathbf{p}) + \boldsymbol{\beta}_\eta(\mathbf{p}) \cdot \boldsymbol{\sigma} \tag{2.5}$$

that can include spin orbit coupling and magnetic field. We can Fourier transform the fields $d_{\mathbf{p}\eta\alpha}(\tau) \to d_{\mathbf{p}\eta\alpha}(\omega)$ which amounts to replacing $\partial_\tau \to i\omega$ in the Berry phase part of the Lagrangian. Since at finite temperature the Lagrangian is periodic with period β, the frequencies are restricted to be fermionic Matsubara frequencies, $\omega_n = (2n+1)\pi T$ for integer n, and the integral is replaced with a sum $\int d\tau \to T\sum_n$. For simplicity, we will assume that the interactions are frequency independent, so the action is

$$S[d, \bar{d}] = T \sum_{n\mathbf{p}\eta\alpha} \bar{d}_{\mathbf{p}\eta\alpha} \left[-i\omega + \mathcal{H}_\eta(\mathbf{p})\right]_{\alpha\beta} d_{\mathbf{p}\eta\beta} + S_I[d, \bar{d}] \tag{2.6}$$

where

$$S_I[d, \bar{d}] = T^3 \sum_{\substack{n_1,n_2,n_3,\mathbf{p},\mathbf{k},\mathbf{q} \\ \eta\eta'\zeta\zeta'\alpha\beta\alpha'\beta'}} V_{\eta\zeta;\alpha\beta}^{\eta'\zeta';\alpha'\beta'}(\mathbf{p},\mathbf{k},\mathbf{q}) \bar{d}_{\mathbf{p}+\mathbf{q},\eta'\alpha'} \bar{d}_{\mathbf{k}-\mathbf{q},\zeta'\beta'} d_{\mathbf{p}\eta\beta} d_{\mathbf{k}\eta\alpha} \tag{2.7}$$

We will generally assume that the interactions conserve energy, momentum and spin. Note the factor of T^3 in the interactions is because as a result there are only three Matsubara sums involved (which will be important for scaling later).

We now introduce an auxiliary source term of the form (we will consider other forms, but this one will turn out to be the most important)

$$S_j[d, \bar{d}, j, \bar{j}] = \sum_I \left(\bar{j}_I d_I + \bar{d}_I j_I\right) \tag{2.8}$$

where j is the 'generalized force' or current source Grassmann variable that is fixed and I, J are

multi-indices including $\mathbf{p}, \eta, \alpha$. The total partition function is then

$$\mathcal{Z}[j,\bar{j}] = \left\langle e^{\sum_I (\bar{j}_I d_I + \bar{d}_I j_I)} \right\rangle = \mathcal{Z}_0^{-1} \int e^{-S[d,\bar{d}]} e^{\sum_I (\bar{j}_I d_I + \bar{d}_I j_I)} \mathcal{D}d\mathcal{D}\bar{d} \tag{2.9}$$

The linear response of the system here is the expectation value of d, which is

$$\langle d_I \rangle = \mathcal{Z}^{-1}[j,\bar{j}] \int d_I e^{-S[d,\bar{d}]} e^{\sum_I (\bar{j}_I d_I + \bar{d}_I j_I)} \mathcal{D}d\mathcal{D}\bar{d} = \frac{\delta \log \mathcal{Z}[j,\bar{j}]}{\delta \bar{j}_I} \tag{2.10}$$

Recall that this is how all thermodynamic quantities are computed in ordinary statistical mechanics. Here the 'force' j_I creates an expectation value for a single particle state, so we can think of S_j as adding a particle to the system. In general, for a small force j we expect the response to be linear, i.e. $\langle d_I \rangle \propto j_I$, and we therefore define the susceptibility as $\langle d_I \rangle = \chi_{IJ} j_J$, where

$$\chi_{IJ} = -\left. \frac{\delta^2 \log \mathcal{Z}[\bar{j},j]}{\delta j_J \delta \bar{j}_I} \right|_{j=0} \tag{2.11}$$

where $j = 0$ means all of j_I and $\bar{j}_I$ are set to zero. But this is nothing but

$$-\frac{\delta^2 \log \mathcal{Z}[\bar{j},j]}{\delta j_J \delta \bar{j}_I} = \mathcal{Z}_0^{-1} \int d_I e^{-S[d,\bar{d}]} e^{\sum_I (\bar{j}_I d_I \bar{d}_J + \bar{d}_I j_I)} \mathcal{D}d\mathcal{D}\bar{d} = \left\langle d_I \bar{d}_J \right\rangle = G_{IJ} \tag{2.12}$$

which is the definition of the Green's function of the system. This is the central object of the diagrammatic theory where it is represented as a line with an arrow, Figure 2.1:

$$G_{IJ} = -\left\langle d_I \bar{d}_J \right\rangle \tag{2.13}$$

or more explicitly

$$G_{\eta\zeta;\alpha\beta}(i\omega_n, \mathbf{p}; i\omega'_{n'}, \mathbf{k}) = -\left\langle \bar{d}_{\mathbf{p}\eta\alpha}(\omega_n) d_{\mathbf{k}\zeta\beta}(\omega'_{n'}) \right\rangle \tag{2.14}$$

It is therefore the (linear response) susceptibility to introducing a single particle into the system, which can be considered an instance of the fluctuation-dissipation theorem. Note that being an expectation value of the ground state wave function, it contains a very small fraction of the information about the whole wave function, but generally we can deduce the symmetry of the phase from the symmetry of the Green's function.

In the context of the stability analysis what we are after is to see whether an infinitesimal j results in a finite response, which corresponds to an *infinite* value of the Green's function, i.e. its poles. The

Figure 2.1: Diagrammatic representation of the Green's function, also called a propagator or two-point correlation function.

poles of the Green's functions are dispersions of the resonant modes of the system. In general poles can appear in higher-order correlation functions as well, e.g. if we introduced a vertex representing a bosonic field that couples quadratically to the fermions that we will study below. It turns out, however, that we do not need to add more fields to compute higher order correlation functions, because $\mathcal{Z}[j, \bar{j}]$ (or rather its logarithm) in fact contains all of them: it is the moment-generating function (MFG) from which all correlations can be obtained by differentiation as

$$\left.\frac{\delta^{2N} \log \mathcal{Z}[\bar{j}, j]}{\delta j_{I_1} \ldots \delta j_{I_M} \delta \bar{j}_{J_1} \ldots \delta \bar{j}_{J_N}}\right|_{j=0} = \left\langle d_{J_N} \ldots d_{J_1} \bar{d}_{I_1} \ldots \bar{d}_{I_M} \right\rangle \tag{2.15}$$

Note that terms with odd numbers of fields typically vanish so $M+N$ should be even, but in general the expectation value may not vanish even when $M \neq N$.

The main problem is that for a general form of the action, we do not know how to compute the average. We only really know how to do Gaussian integrals, i.e. for the non-interacting part of the action quadratic in the fields:

$$S_0[d, \bar{d}] = T \sum_{n \mathbf{p} \eta \alpha} \bar{d}_{\mathbf{p}\eta\alpha} \left[-i\omega_n + \mathcal{H}_\eta(\mathbf{p})\right]_{\alpha\beta} d_{\mathbf{p}\eta\beta} \tag{2.16}$$

In principle we may need to further diagonalize the single-particle $\mathcal{H}_\eta(\mathbf{p})$. We will call its eigenvalues $\xi_{\eta\tau}(\mathbf{p})$ with τ labeling the energy bands. A bit more generally, and for later use, we can also include additional order parameters like the superconducting gap function in the quadratic part of the action, which we can write as

$$S_0[d, \bar{d}] = \sum_{IJ} \bar{d}_I \mathcal{G}^{-1}_{IJ} d_J \tag{2.17}$$

where we allow $d_I = \bar{d}_{\mathbf{p}\eta\alpha}$, for which we can evaluate the partition function by doing the (Berezin)

integral

$$\begin{aligned}\mathcal{Z}[\bar{j},j] &= \mathcal{Z}_0^{-1}\int e^{-\sum_{IJ}\bar{d}_I\mathcal{G}_{IJ}^{-1}d_J}e^{\sum_I\left(\bar{j}_Id_I+\bar{d}_Ij_I\right)}\mathcal{D}d\mathcal{D}\bar{d}\\ &= \mathcal{Z}_0^{-1}\det\left[\mathcal{G}^{-1}\right]\ e^{-\sum_{IJ}\bar{j}_I\mathcal{G}_{IJ}j_J}\end{aligned} \tag{2.18}$$

In particular,

$$\langle d_Id_J\rangle = \frac{\delta^2\log\mathcal{Z}[\bar{j},j]}{\delta j_J\delta\bar{j}_I} = -\mathcal{G}_{IJ} \tag{2.19}$$

where we include the possibility that the Green's function

$$\mathcal{G}_{IJ} = \begin{pmatrix} G_{IJ} & F_{IJ} \\ F_{IJ}^\dagger & -G_{JI}\end{pmatrix} \tag{2.20}$$

includes anomalous components

$$F_{\eta\zeta;\alpha\beta}(i\omega_n,\mathbf{p};i\omega'_{n'},\mathbf{k}) = -\left\langle d_{\mathbf{p}\eta\alpha}(\omega_n)d_{\mathbf{k}\zeta\beta}(\omega'_{n'})\right\rangle \tag{2.21}$$

Comparing (2.17) with (2.16), we have

$$G_{\eta\zeta;\alpha\beta}(i\omega_n,\mathbf{p};i\omega'_{n'},\mathbf{k}) \equiv \left[G_\eta(i\omega_n,\mathbf{p})\right]_{\alpha\beta}\delta_{nn'}\delta_{\mathbf{pk}}\delta_{\eta\zeta} = \left[\frac{\delta_{\omega\omega'}\delta_{\mathbf{pk}}\delta_{\eta\zeta}}{i\omega-\mathcal{H}_\eta(\mathbf{p})}\right]_{\alpha\beta} \tag{2.22}$$

with poles $i\omega_n$ equal to the eigenvalues of the Hamiltonian (the anomalous Green's function vanishes in this case).

Although this is the only case we can do, note that since we know the generating function, we can obtain *all* correlation functions by simple differentiation combined with induction, which yields Wick's theorem:

Theorem 2.1 (Wick's Theorem for Fermions)
For Gaussian distributions (i.e. S_0 quadratic in the fields),

$$\langle d_1\dots d_N\rangle = \sum_{p\in P_N^2}\operatorname{sgn}p\prod_{\{I,J\}\in p}\langle d_Id_J\rangle = -\sum_{p\in P_N^2}\operatorname{sgn}p\prod_{\{I,J\}\in p}\mathcal{G}_{IJ} \tag{2.23}$$

where fermionic[1] fields d_I with multi-index I can be either $d_{\mathbf{p}\eta\alpha}$ or $\bar{d}_{\mathbf{p}\eta\alpha}$, P_N^2 are all possible pairings

[1]For bosons, the same theorem applies but with $\operatorname{sgn}p$ replaced by 1.

p of $\{1,\dots N\}$, i.e. distinct partitions of $\{1,\dots N\}$ into pairs, and $\operatorname{sgn} p$ is the sign of the pairing (i.e. the parity of the number of pair-wise permutations required to obtain the order of pairs in p). Note that the result is zero if N is odd. □

For a proof of this theorem see [37, 74, 46].

The importance of the theorem lies in the following observation. The total action is

$$\mathcal{Z} = \int e^{-S_0[d,\bar{d}]} e^{-S_I[d,\bar{d}]} \mathcal{D}d\ \mathcal{D}\bar{d} = \mathcal{Z}_0 \left\langle e^{-S_I[d,\bar{d}]} \right\rangle_0 \tag{2.24}$$

where $\mathcal{Z}_0$ is the partition function without interactions. But we can always expand the exponential $e^{-S_I[d,\bar{d}]}$ using Taylor series, and then use the cumulant expansion

$$\left\langle e^X \right\rangle = e^{\sum_{n=1}^{\infty} \kappa_n[X]} = e^{\langle X\rangle + \mathrm{Var}[X]/2 + \dots} \tag{2.25}$$

which implicitly defines the cumulants $\kappa_n[X]$, with $\kappa_1[X] = \langle X\rangle$, $\langle X\rangle = \mathrm{Var}[X]$ the variance of X, etc. Since the cumulants are in this case linear combinations of correlation functions, we can compute the partition function with a general action using Wick's theorem. Diagrammatically, the cumulant expansion is just the linked-cluster theorem that states that corrections to the action can be computed in terms of connected Feynman diagrams only that represent the correlation functions [155, 37]. To get the response of the system we can similarly compute the total Green's function as $\left\langle d_I \bar{d}_J e^{-S_I[d,\bar{d}]} \right\rangle_0$ in a similar fashion, which yields the diagrammatic expansion of the total Green's function in terms of the 'bare' Green's function $G^{(0)}$ for the system in the absence of interactions.

2.1.2 Effective Action and Renormalization

For a many body system there is generally going to be an energy scale above which no new response is going to be generated, which we will call Λ. The standard approach is to restrict the integration inside the action to $\xi < \Lambda$. This is the hard cutoff often used in RG. Looking ahead, however, and as discussed in [155], at some point in RG with Fermi surfaces the hard cutoff becomes inconvenient because the momentum cutoff $p_\Lambda(\theta)$ (which can depend on the angle) defines an annular region that does not map into the same region in the rescaling step in RG which we will discuss presently. To circumvent this issue, a soft cutoff $\theta_\Lambda(\xi)$ needs to be introduced as

$$S_0[d,\bar{d};\theta_\Lambda] = T \sum_{n\mathbf{p}\eta\alpha} \theta_\Lambda^{-1}(\mathbf{p}) \bar{d}_{\mathbf{p}\eta\alpha} \left[-i\omega_n + \mathcal{H}_\eta(\mathbf{p})\right]_{\alpha\beta} d_{\mathbf{p}\eta\beta} \tag{2.26}$$

This is a common way the cutoff is implemented in non-perturbative or functional RG [1]. The exact form of θ_Λ does not matter, but it is roughly 1 for $\xi < \Lambda$, and vanishes smoothly for $\xi > \Lambda$. Note that we do not introduce a cutoff in S_I. Also note that it is the *inverse* of θ_Λ that enters in S_0; as a result, when θ_Λ is small, S_0 is large, and e^{-S_0} is very small and does not contribute to the path integral.

The soft cutoff has a more physical interpretation. Note that the bare Green's function corresponding to (2.26) is

$$G_{\eta\zeta;\alpha\beta}(i\omega_n, \mathbf{p}; i\omega'_{n'}, \mathbf{k}) \equiv [G_\eta(i\omega_n, \mathbf{p})]_{\alpha\beta} \delta_{nn'}\delta_{\mathbf{pk}}\delta_{\eta\zeta} = \left[\frac{\delta_{nn'}\delta_{\mathbf{pk}}\delta_{\eta\zeta}\theta_\Lambda}{i\omega_n - \mathcal{H}_\eta(\mathbf{p})}\right]_{\alpha\beta} \tag{2.27}$$

so the soft cutoff plays the role of the renormalization factor or quasiparticle weight Z from Landau's Fermi liquid theory (which we are partially building towards). In fact, the linear response approach outlined here parallels closely the original formulation by Landau, who considered the change of the system's energy as a single particle was added to it, which can be interpreted as the energy of a different object called the quasiparticle.

More generally, the probing particle will interact with some but not all of the system. In a fermionic system, these are typically states close to the Fermi level. In order to take this into account, we want to split the system into the low energy part (close to the Fermi level) that we care about, and the high energy part that we do not care about. To do this we want to split the modes into low and high energy modes with the cutoff splitting into

$$\theta_\Lambda = \theta_\Lambda^> + \theta_\Lambda^< \tag{2.28}$$

where $\theta_\Lambda^< = \theta_{\Lambda-\delta\Lambda}$ has the same form as the original cutoff. Note, however, that there is no sharp distinction between low and high energy modes when using a soft cutoff (which requires a modification to the RG procedure as it is described in [155]). The trick is to define $d = d_< + d_>$ using the Gaussian identity (omitting an irrelevant constant Jacobian; see section 2.2 in [1, Chapter 2] for a proof)

$$\mathcal{D}d\,\mathcal{D}\bar{d}\; e^{-S_0[d,\bar{d};\theta_\Lambda]} \propto \mathcal{D}d_<\mathcal{D}\bar{d}_<\mathcal{D}d_>\mathcal{D}\bar{d}_> e^{-S_0[d_<,\bar{d}_<;\theta_\Lambda^<]} e^{-S_0\left[d_>,\bar{d}_>;\theta_\Lambda^>\right]} \tag{2.29}$$

which implicitly defines the low and high energy modes. We can then define the *effective* low energy

action via (omitting $\bar{d}$ in the argument of the action for clarity)

$$\mathcal{Z} = \int e^{-S[d_<,d_>]} \mathcal{D}\bar{d}_< \mathcal{D}d_< \mathcal{D}\bar{d}_> \mathcal{D}d_> = \int e^{-S_{eff}[d_<]} \mathcal{D}\bar{d}_< \mathcal{D}d_< \tag{2.30}$$

i.e.

$$e^{-S_{eff}[d_<]} = \int e^{-S[d_<,d_>]} \mathcal{D}\bar{d}_> \mathcal{D}d_> \tag{2.31}$$

In other words, the effective action is obtained from the microscopic action by integrating out the high energy modes. As in (2.24), we make use of the fact that (2.26) is quadratic in the fields, which allows us to use the same Feynman rules to compute the integral. Explicitly, we have

$$S[d_<, d_>] = S_0[d_<; \theta_\Lambda^<] + S_0[d_>; \theta_\Lambda^>] + S_I[d_<, d_>] \tag{2.32}$$

and we have

$$e^{-S_{eff}[d_<]} = e^{-S_0[d_<;\theta_\Lambda^<]} \left\langle e^{-S_I[d_<,d_>]} \right\rangle_> \mathcal{Z}_{0>} \tag{2.33}$$

where

$$\mathcal{Z}_{0>} = \int e^{-S_0[d_>;\theta_\Lambda^>]} \mathcal{D}\bar{d}_> \mathcal{D}d_> \tag{2.34}$$

and the average over high energy modes is defined as

$$\left\langle e^{-S_I[d_<,d_>]} \right\rangle_> = \frac{1}{\mathcal{Z}_{0>}} \int e^{-S_0[d_>;\theta_\Lambda^>]} e^{-S_I[d_<,d_>]} \mathcal{D}\bar{d}_> \mathcal{D}d_> \tag{2.35}$$

We thus have

$$S_{eff} = S_0 + \delta S \tag{2.36}$$

where we again can use the cumulant expansion

$$\delta S = -\sum_{n=1}^{\infty} \kappa_n \left[-S_I[d_<, d_>]\right] \tag{2.37}$$

Since the low energy fields are not integrated out, this has the symbolic form

$$S_{eff} = s_0 + s_2 \bar{d}_< d_< + s_4 \bar{d}_< \bar{d}_< d_< d_< + \cdots = \sum_j s_j \mathcal{O}_j[d_<(\mathbf{p})] \tag{2.38}$$

The operator expansion holds more generally for any form of the action.

The idea of the renormalization *group* is that the renormalization can be done in multiple steps. i.e. high energy modes do not have to be integrated out all at once, but rather removed systematically starting at the highest energy Λ, first integrating out modes within a narrow energy shell of thickness $d\Lambda = \Lambda\left(1 - \frac{1}{\varrho}\right)$ for some rescaling factor $\varrho \gtrapprox 1$.[2] The new effective action thus runs up to energy Λ/ϱ. This is the first step of RG. The second step is to realize that if we redefine the units by rescaling all lengths $x' = x/\varrho$ (equivalently all momenta as $p' = \varrho p$), we end up with an effective action that again runs up to energy Λ, i.e. has the same form as the original action. Quite generally, if the original action has the general form (2.38), after the two RG steps it becomes

$$S'[d_<] = \sum_j s'_j \mathcal{O}_j[d_<(\mathbf{p}'/\varrho)] \tag{2.39}$$

Note that some s_j may have started as zero and new terms in the action can be introduced. The third and final step of RG is to redefine the field as $d'(\mathbf{p}') = d_<(p)/\zeta$, with ζ, which amounts to a new choice of units for the field, typically chosen such that the leading s_j is constant. In the absence of a Fermi surface, this is typically the quadratic kinetic energy term. In the presence of a Fermi surface, the correct choice amounts to keeping the volume (or area in 2D) inside the Fermi surface fixed, in accordance with Luttinger's theorem (assuming the shape of the Fermi surface is not deformed under RG to the point where its topology changes). For a circular Fermi surface, this means simply keeping the Fermi momentum fixed.

After these three steps,[3] we finally obtain a new action (redefining s'_j)

$$S'[d'] = \sum_j s'_j \mathcal{O}_j[d'_<(\mathbf{p}')] \tag{2.40}$$

At this point we can change the perspective on the renormalization process. Instead of thinking of eliminating the high energy modes, we instead simply think of their cumulative effect on the action of the low energy modes. The cutoff in that perspective is a fixed element of the system that does

[2] In most references, s is used instead of ϱ. We use ϱ to avoid confusion with action parameters.

[3] The group in RG refers to the three steps acting in a similar way a group element acts on the action. This is a bit of a misnomer since the steps in RG do not necessarily have an inverse, and so form a semigroup rather than a group.

not flow under RG, and instead the parameters s_j are renormalized by the high energy modes and are said to flow under RG. Defining the RG 'time' as $dt = \frac{d\Lambda}{\Lambda} = \frac{\varrho-1}{\varrho}$ (i.e. $t = \log \Lambda/E$ with $\Lambda - E$ essentially the energy window within which the high energy modes have been eliminated), we can consider $s_j(t)$ as functions of t. A single iteration of the RG procedure gives

$$s_j' = s_j(t) + ds_j = s_j(t) + \beta_j(s_j)dt \tag{2.41}$$

where we introduce the beta functions

$$\beta_j(s_j) = \frac{ds_j}{dt} \tag{2.42}$$

which define the RG flow equations. As a result, it is not necessary to actually repeat the RG procedure, and instead we can solve a set of differential equations in the limit $t \to \infty$. There are two possible outcomes: some s_j blow up under the flow, in which case the corresponding terms $\mathcal{O}_j$ are called *relevant* in the RG sense; or they do not, in which case they either go to zero and the corresponding $\mathcal{O}_j$ are called *irrelevant*, or approach a constant, with $\mathcal{O}_j$ called *marginal* in that case.

If there are no relevant terms in the action, it approaches a *fixed point* at which all the beta functions vanish. This corresponds to a stable phase of matter (and a saddle point of the action in the sense that under RG the action remains unchanged, $\delta S = 0$). Not all fixed points are stable, however. As a typical example, it is possible that if $s_j = 0$, it remains zero under the RG flow, but blows up when it is positive, so introducing a small δs_j as a perturbation moves the action away from the fixed point, at which point it usually flows to a different, stable, fixed point (in our case there will be a finite number of relevant terms). The RG analysis therefore reduces to identifying the fixed points of the RG flow, and then analyzing their stability for small deviations from the fixed point.

With this conceptual reframing we can thus return to the original motivation for RG, namely the search for the ground state of a many-body system. As discussed in the beginning of the chapter, a natural choice is a state that respects all the symmetries of the system, so we choose an action that is a fixed point of RG that respects all these symmetries. This amounts to some choice of marginal operators $\mathcal{O}_j$. We then ask if this fixed point is stable if small additional operators are added as a perturbation. Note that in general we do not know all possible operators, but typically we consider interaction terms or symmetry breaking terms. If the perturbing term turns out to be relevant, it corresponds to an instability of the state, and the action flows to a different fixed point. The most useful aspect of the RG analysis is that the relevant perturbations provide a hint to what symmetry

is broken, as we will see in the next section.

2.1.3 Gaussian and Fermi Liquid Fixed Points

For the RG analysis of S_0 alone, either a soft or a hard cutoff produce the same result, since the mode elimination step is in either case trivial (see [154] for details). More important is the rescaling step. To see this, we Taylor expand the dispersion

$$\xi_{\eta\tau}(\mathbf{p}) \approx \mu_{\eta\tau} + v_{F\eta\tau}\left(p - p_{F\eta\tau}(\theta)\right) + \ldots \tag{2.43}$$

where $\mu_{\eta\tau}$ is the chemical potential, $p_{F\eta\tau}(\theta)$ is the Fermi momentum (that can be a function of the angle of $\mathbf{p}$ in 2D), and $v_{F\eta\tau}$ is the Fermi velocity. Because in this case we know the ground state (determined by the Fermi distribution), we know that the p linear term needs to be marginal in RG, which is ensured by rescaling the fields c (or d) by $\zeta = \varrho^{\frac{3}{2}}$.[4] The chemical potential is then relevant, while all higher powers of p are irrelevant because n^{th} powers are rescaled by s^{-n} ($s = \frac{1}{1-dt} = 1+dt$), so at the fixed point we roughly have $\mu_{\eta\tau} = v_{F\eta\tau}p_{F\eta\tau}$ (exact for a circular Fermi surface).

The Gaussian fixed point of RG is therefore S_0 with linearized dispersions $\xi_{\eta\tau}(\mathbf{p})$, all higher order terms being irrelevant and so not part of the fixed point. The fixed point is thus characterized by a small set of parameters: p_F, μ and v_F. In general, the chemical potential μ and the Fermi velocity (or equivalently the effective mass) can flow, but the Fermi momentum must be held constant in accord with Luttinger's theorem.

We next consider if the Gaussian fixed point is stable against interactions. For this we compute $\left\langle e^{-S_I[d_<,d_>]}\right\rangle_>$, or rather what we are more interested in, its logarithm

$$-\delta S[d_<,\bar{d}_<] = \log\left\langle e^{-S_I[d_<,d_>]}\right\rangle_>, \tag{2.44}$$

using (2.37). Here we need to assume that the interactions are weak in the sense that the cumulant expansion is an asymptotic series. This is justified from the stability analysis point of view since what we are asking is whether the RG fixed point is stable against small perturbations; the microscopic interactions in the system need not be small as we will discuss later. The leading approximation is

[4] For any dimension. Note that we only rescale the radial component of momentum and we also rescale $T \to T' = sT$ (which is the same as rescaling the frequency ω) to account for a change in energy units.

therefore

$$\begin{aligned}\delta S &\approx \langle S_I[d_<, d_>]\rangle_> = \\ &= \left\langle \sum V_{IJKL}(\bar{d}_{I<} + \bar{d}_{I>})(\bar{d}_{J<} + \bar{d}_{J>})(d_{K<} + d_{K>})(d_{L<} + d_{L>})\right\rangle_> \end{aligned} \tag{2.45}$$

Note again that there is no cutoff in the summation/integration in S_I, only in S_0. This is particularly convenient in a lattice system, since we do not need to worry about periodicity and boundary conditions.

Since we are averaging over the fast modes only, only terms with even number of high energy modes are non-zero, so symbolically we can write without indices

$$\delta S \approx \delta s_0^1 + \delta s_2^1 \bar{d}_< d_< + \delta s_4^1 \bar{d}_< \bar{d}_< d_< d_< \tag{2.46}$$

The first term, δs_0^1, arises when all fields in (2.45) are high energy modes and is just a constant that is absorbed into the normalization of the probability distribution and is of no interest to us. The second term, δs_2^1, is more interesting and comes about when two of the fields are high energy modes (one incoming and one outgoing, i.e. one with a bar and one without). This is the so-called one loop (1L) correction to the single-body Hamiltonian $\mathcal{H}_\eta(\mathbf{p})$ and can for example change the chemical potential and the (effective) mass (the number of loops is essentially the number of interactions involving high energy modes). These are of central interest in the Fermi liquid theory, which aims to relate the relationship between these quantities and interactions, but here we are more interested in whether the interactions themselves are relevant or not. The first correction to the interactions in RG is the δs_4^1 term, which simply amounts to setting all modes in (2.45) to be low energy. This is a zero loop or tree level correction to the interactions.

We can verify moreover that if we expand the interactions in a Taylor series in the radial component of momentum, symbolically

$$V(P) = V_0 + V_1 P + V_2 P^2 + \ldots \tag{2.47}$$

then after rescaling the momenta we have in any dimension

$$V_n' = s^{-n} V_n = (1 - ndt) V_n \tag{2.48}$$

so that the beta function is

$$\frac{dV_n}{dt} = -nV_n \tag{2.49}$$

which is marginal for $n = 0$ and irrelevant (exponentially suppressed) otherwise. So only interactions independent of the radial components of momentum and on the Fermi surface are marginal, and the rest are irrelevant. It should be emphasized that already at the tree level analysis of the interactions we find that the Gaussian fixed point we started with is not a unique fixed point. Rather, there are infinitely many fixed points for any value of the (in principle infinitely many) marginal coupling constants. This 'fixed manifold' corresponds to the Fermi liquid phase, and as Landau already realized it is completely characterized by the coupling constants, effective mass and the Fermi momentum. Much of Fermi liquid theory analyses the relationships between the coupling constants, the effective mass, and other observables like zero sound and compressibility. Details can be found in [92, 2, 102] and in [154, 1] from the RG point of view. Here, we are not as interested in the Fermi liquid phase itself, but rather want to consider it as the symmetric fixed point we discussed above and look for its instabilities.

2.1.4 One-Loop RG Flow for Interactions

Above we found that the interactions at the Fermi liquid fixed point are marginal at tree level. This does not guarantee that the fixed point is stable, since there are infinitely many terms in the cumulant expansion and it is not guaranteed to not diverge once all terms are summed up. We will see that some interactions can become relevant already at one loop order, i.e. the next order approximation:

$$\begin{aligned} \delta S &\approx \langle S_I[d_<, d_>]\rangle_> - \frac{1}{2}\mathrm{Var}_> \left[-S_I[d_<, d_>]\right] = \\ &= \langle S_I[d_<, d_>]\rangle_> - \frac{1}{2}\left(\left\langle S_I^2[d_<, d_>]\right\rangle_> - \langle S_I[d_<, d_>]\rangle_>^2\right) \end{aligned} \tag{2.50}$$

The new term contains combinations of eight fields and we get all possible contractions of pairs of high energy modes:

$$\delta S \approx \delta s_0^1 + \delta s_0^2 + (\delta s_2^1 + \delta s_2^2)\bar{d}_< d_< + (\delta s_4^1 + \delta s_4^2)\bar{d}_<\bar{d}_< d_< d_< + \ldots \tag{2.51}$$

where I am omitting the terms with six and eight fields (which are irrelevant due to the rescaling of the fields), and δs_j^2 correspond to the corrections from the new term. Again, we are not as interested in the δs_0^2 and δs_2^2 terms as the first can be absorbed into the normalization of the path integral and the latter will renormalize the mass. Computing the δs_4^2 term can be done directly using Wick's theorem, keeping four of the fields at high energy. The generic term will be of the form

$$\left(\delta s_4^2\right)_{I'J'K'L'} = \left\langle V_{I'J'KL} V_{IJK'L'} \bar{d}_{I>} \bar{d}_{J>} d_{K>} d_{L>} \right\rangle + \dots \tag{2.52}$$

Note that the interaction V has two low energy indices (primed) and two high energy indices (unprimed) that are kept inside the average since they are functions of momentum of the high energy modes. Wick's theorem turns the expectation values into pairs of Green's functions:

$$\left(\delta s_4^2\right)_{I'J'K'L'} = \sum_{IJKL} V_{I'J'KL} G^{>}_{JK} V_{IJK'L'} G^{>}_{IL} + \dots \tag{2.53}$$

where the summation includes integration over all momenta corresponding to the I, J, K, L indices (constrained by momentum conservation) and the $>$ superscript on the Green's functions indicates that these are propagators for the high energy modes and therefore carry factors of the soft cutoffs $\theta^{>}_{\Lambda}$. In the approach we adopted, this sets the boundaries of integration, which means only the momenta of the Green's functions that lie within a thin momentum shell between p_Λ and $p_{\Lambda - d\Lambda}$ contribute significantly to the integral. We will find that generically, the arguments of the two Green's functions are $G^{>}_{JK}(\mathbf{q}) G^{>}_{IL}(\pm\mathbf{q} + \mathbf{K})$ for some $\mathbf{K}$ determined by the external momenta of the low energy modes, and $\mathbf{q}$ being integrated over all momenta. If $\mathbf{K}$ is not equal to zero, $\int \theta^{>}_{\Lambda}(\mathbf{q}) \theta^{>}_{\Lambda}(\mathbf{q}+\mathbf{K}) [\dots] d\mathbf{q} \propto d\Lambda^2$, as can be concluded from Figure 2.2. When we look at the beta function for the coupling constants, we divide by $d\Lambda$ and take it to zero (i.e. compute the derivative), so all terms with $\mathbf{K} \neq 0$ will vanish to this order. Thus only terms with $\mathbf{K} = 0$ may contribute to the flow, which will be the key observation. Keeping only such terms is the essence of parquet RG (pRG).

So far we considered a generic form of the contraction, but in general it is complicated to keep track of all possible contractions already at one loop. A bookkeeping device is needed, and fortunately, this is precisely what Feynman diagrams are.[5] As an instance of the linked-cluster theorem, the subtraction of $\langle S_I \rangle^2_{>}$ in (2.50) amounts precisely to the statement that we only need to compute the connected Feynman diagrams. There are four topologies of one loop diagrams, shown in Figure 2.3 (five if we count the last diagram with $\mathbf{p}$ and $\mathbf{k}$ exchanged). The external

[5] See Table 8.3 in [37] for a list of the Feynman rules; a slight difference is that I do not assume spin degeneracy here.

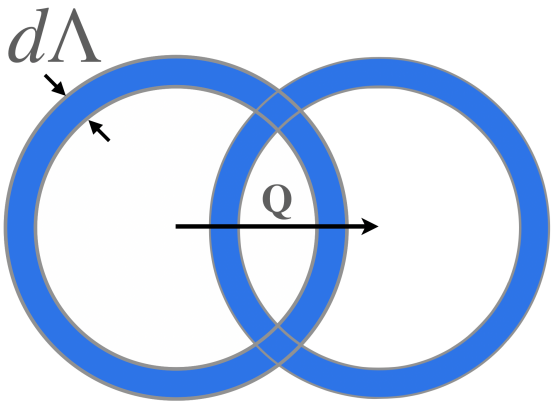

Figure 2.2: Fundamental reason the Fermi liquid is unstable towards pairing instabilities, but mostly stable otherwise: the phase space available for high energy modes in a thin shell defined by $d\Lambda$ has an area $d\Lambda^2$ for $\mathbf{Q} \neq 0$, the intersection of two shifted shells. Only $\mathbf{Q} = 0$, when the shells are perfectly nested, contributes significantly to the RG flow.

lines correspond in this case to the low energy modes, and are to be 'amputated.' Internal lines with arrows correspond to the Green's functions, and the wavy lines to interactions, so indeed each diagram corresponds to a term of the form (2.53). The figure shows the four-momenta $p = (i\omega_n, \mathbf{p})$ etc., from which we can identify the diagrams for which $K = 0$.

Particle-Hole Instabilities

At tree level, there was nothing to distinguish any particular interactions, but at one loop we find that they decouple into three channels. The first case corresponds to $Q = 0$ (and by antisymmetrization $Q = k - p$), in Figure 2.3, which correspond to interactions that do not change the direction of incoming fermions (or exchange them). See top of Figure 2.4. For lack of a better term I refer to them as U type, with action given by

$$S_U[d, \bar{d}] = T^3 \sum_{\substack{nn', \mathbf{p}, \mathbf{k} \\ \eta\zeta\alpha\beta\alpha'\beta'}} [U_{\eta\zeta}(\mathbf{p}, \mathbf{k})]_{\alpha\beta}^{\alpha'\beta'} \, \bar{d}_{\mathbf{p}\eta\alpha'} \bar{d}_{\mathbf{k}\zeta\beta'} d_{\mathbf{k}\zeta\beta} d_{\mathbf{p}\eta\alpha} \tag{2.54}$$

where we can drop some of the indices, as well as one momentum and one Matsubara sum. Here we assume no additional nesting, i.e. that no two pockets are identical, and that there are no large segments of the Fermi surfaces separated by the same transfer momentum; otherwise additional instabilities are possible. We only keep the $Q = 0$ terms: note that in the diagrammatic technique, the correct procedure is to first renormalize the $Q = 0$ diagrams, and only then obtain the $Q = k - p$

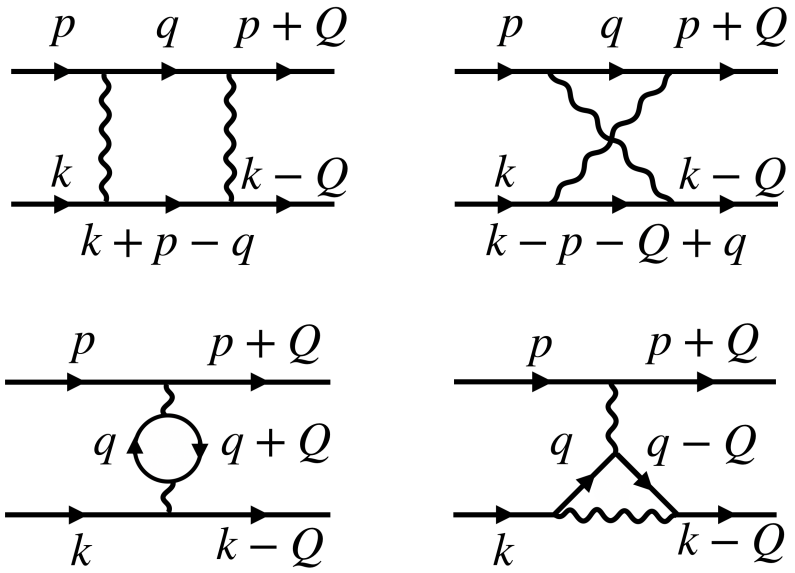

Figure 2.3: The four types of one-loop corrections to interactions (five if we count the last diagram with p and k exchanged and $Q \to -Q$).

by anti-symmetrizing. Checking the phase space condition, we find that the condition that $\mathbf{K} = 0$ in $G^{>}_{IL}(\pm\mathbf{q} + \mathbf{K})$ (one of the internal Green's function inside the integral) holds only for the last two diagrams in Figure 2.3. The structure of the diagrams means that in the rotation invariant, spin conserving case these interactions decouple according to harmonics (in 2D)

$$[U_{\eta\zeta}(\mathbf{p}, \mathbf{k})]^{\alpha'\beta'}_{\alpha\beta} = [U_{\eta\zeta}(\theta, \theta')]^{\alpha'\beta'}_{\alpha\beta} = \sum_{\ell\mu\nu} u^{(\ell\mu\nu)}_{\eta\zeta} \Theta^{(\ell\mu)}_{\eta}(\theta) \Theta^{(\ell\nu)}_{\zeta}(\theta') \sigma^{\mu}_{\alpha\alpha'} \sigma^{\nu}_{\beta\beta'} \tag{2.55}$$

where θ and θ' are angles corresponding to $\mathbf{p}$ and $\mathbf{k}$ respectively, $\ell = 0, 1, 2, \ldots$ labels the harmonics and the $\mu, \nu = 0, x, y, z$ labels the Pauli matrices, including $\sigma^0_{\alpha\beta} = \delta_{\alpha\beta}$ (note that the $\mu = 0$ for all even ℓ, and $\mu \neq 0$ for odd ℓ). In Fermi liquid theory, it is conventional to label the $\mu = \nu = 0$ interactions F and the $\mu = \nu \neq 0$ interactions G, also respectively referred to as charge and spin components of the interactions, as well as density-density and exchange or spin fluctuations interactions as they can be expressed as products of charge and spin density operators [102, 92]. From the latter observation it is cleat that F and G are the only terms that conserve the spin operators $\bar{d}_\alpha \mathbf{S}_{\alpha\beta} d_\beta$. If spin is not conserved, there can be additional Dzhyaloshinkii-Moriya (DM or anti-symmetric exchange) interactions of the form $\mathbf{D} \cdot \boldsymbol{\sigma}_{\alpha\alpha'} \times \boldsymbol{\sigma}_{\beta\beta'}$, e.g. due to SOC (we will in general assume no DM interactions for simplicity). There can then also be spin direction anisotropy in G.

The U interactions are thus characterized by the coupling constants $u_{\eta\zeta}^{(\ell\mu)}$, which we will label u_ℓ for simplicity when omitting indices. If the system is rotationally invariant, note that $U_{\eta\zeta}(\theta,\theta') = U_{\eta\zeta}(\theta-\theta')$ and the harmonics can be expressed in terms of Legendre polynomials $P_\ell(\theta-\theta')$, but on a lattice the interactions can depend on both angles separately. It is then more sensible to expand in 'Chebyshev polynomials' $\Theta^{(\ell_1)}(\theta)\Theta^{(\ell_2)}(\theta')$ with $\Theta^{(\ell)}(\theta) = \cos\ell\theta$ and $\Theta^{(\ell')}(\theta) = \sin\ell\theta$. On a lattice the ℓ index should be instead considered as an irreducible representation (irrep) label of the point (or space) group of the lattice symmetries.

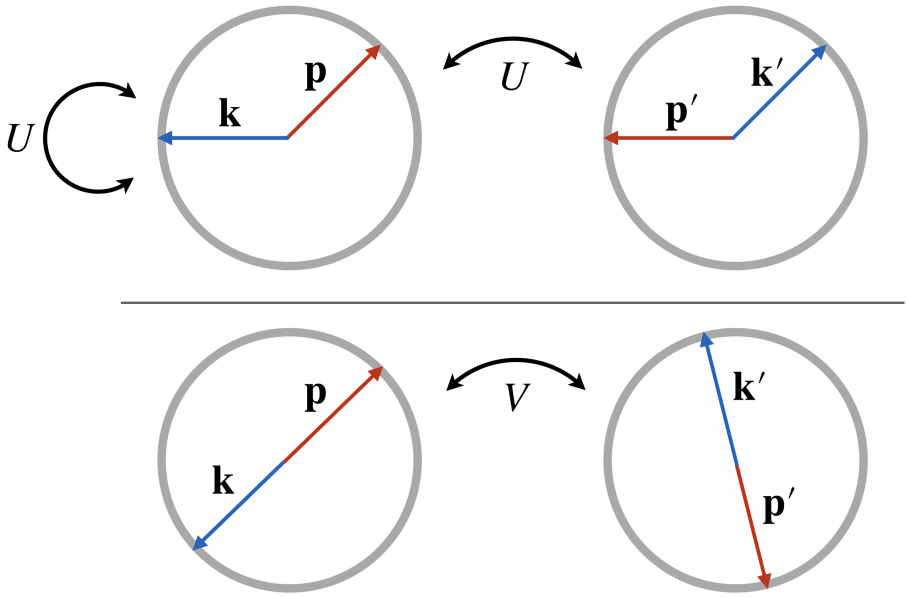

Figure 2.4: U and V type interactions marginal in RG at tree level. U corresponds to processes that do not change the momenta of the interacting particles, at most exchanging them (when renormalization we do not include the exchange process, which is fixed by anti-symmetrization). The V process involves pairs with zero total momentum that can therefore scatter into any other such pair.

We will be mostly interested in a different type of interactions below, but here we briefly outline the one loop correction in RG to the U type interactions. The generic form of the correction is

$$(\delta s_4^2)_{I'J'K'L'} = \sum U_{I'J'KL} G^{>}_{IK}(q) U_{IJK'L'} G^{>}_{LJ}(q) \tag{2.56}$$

Diagrams where the two Green's functions are integrated over q with the same sign of q in the argument are called *particle-hole* diagrams, since in the diagram this means that the fermions are propagating in opposite directions in time. This may be the most clear in the third ('bubble') type of diagrams, but all except for the first (ladder) diagram in Figure 2.3 are particle-hole diagrams. The

ladder diagram is a *particle-particle* diagram. Since the interactions are independent of frequency and momentum magnitude, the only dependence on these is in the Green's functions. We therefore define the (infinitesimal, angle resolved) particle-hole bubble or susceptibility as

$$d\Pi^{ph}_{\eta\zeta}(\theta) = T\sum_{|\mathbf{q}|,\omega} G^{>}_{\eta}(i\omega,\mathbf{q})G^{>}_{\zeta}(i\omega,\mathbf{q}) \tag{2.57}$$

Note that the Green's functions are in general matrices in spin indices, not diagonal if SOC is present, and therefore so is the bubble. Since we are considering the possibility of SOC, the two Green's functions may not be simultaneously diagonalizable for unequal pocket indices, but the matrix elements of $d\Pi^{ph}_{\eta\zeta}(\theta)$ are related by a spin rotation transformation to

$$\begin{aligned} d\Pi^{ph}_{\eta\tau;\zeta\upsilon}(\theta) &= T\sum_{n,|\mathbf{q}|} G^{>}_{\eta\tau}(i\omega_n,\mathbf{q})G^{>}_{\zeta\upsilon}(i\omega_n,\mathbf{q}) = T\sum_{n,|\mathbf{q}|}\frac{\theta^{>}_{\Lambda}(\xi_{\eta\tau}(\mathbf{q}))\theta^{>}_{\Lambda}(\xi_{\zeta\upsilon}(\mathbf{q}))}{(i\omega_n-\xi_{\eta\tau}(\mathbf{q}))(i\omega_n-\xi_{\zeta\upsilon}(\mathbf{q}))} = \\ &= \sum_{|\mathbf{q}|}\frac{n_F\left(\xi_{\eta\tau}(\mathbf{q})\right)-n_F\left(\xi_{\zeta\upsilon}(\mathbf{q})\right)}{\xi_{\eta\tau}(\mathbf{q})-\xi_{\zeta\upsilon}(\mathbf{q})}\theta^{>}_{\Lambda}(\xi_{\eta\tau}(\mathbf{q}))\theta^{>}_{\Lambda}(\xi_{\zeta\upsilon}(\mathbf{q})) = \\ &= -\frac{1}{2}\sum_{|\mathbf{q}|}\frac{\tanh\frac{\beta\xi_{\eta\tau}(\mathbf{q})}{2}-\tanh\frac{\beta\xi_{\zeta\upsilon}(\mathbf{q})}{2}}{\xi_{\eta\tau}(\mathbf{q})-\xi_{\zeta\upsilon}(\mathbf{q})}\theta^{>}_{\Lambda}(\xi_{\eta\tau}(\mathbf{q}))\theta^{>}_{\Lambda}(\xi_{\zeta\upsilon}(\mathbf{q})) \end{aligned} \tag{2.58}$$

where $\tau,\upsilon=\pm$ are the 'pseudospin'/SOC basis indices (see (1.10)), n_F is the Fermi distribution function, and we have evaluated the Matsubara sum. Again because of the cutoff overlaps, the only relevant contribution is from $\xi_{\eta\tau}(\mathbf{q})\approx\xi_{\zeta\upsilon}(\mathbf{q})\approx\pm\Lambda$ if η and ζ are both electron or both hole pockets. Assuming $\Lambda\gg T$ (valid in particular for $T=0$), the two hyperbolic tangents have the same sign and tend to cancel:

$$\begin{aligned} d\Pi^{ph}_{\eta\tau;\zeta\upsilon}(\theta) &\approx -\sum_{|\mathbf{q}|}\frac{e^{-2\beta\Lambda}\left(1-e^{\beta|\xi_{\eta\tau}(\mathbf{q})-\xi_{\zeta\upsilon}(\mathbf{q})|}\right)}{|\xi_{\eta\tau}(\mathbf{q})-\xi_{\zeta\upsilon}(\mathbf{q})|}\theta^{>}_{\Lambda}(\xi_{\eta\tau}(\mathbf{q}))\theta^{>}_{\Lambda}(\xi_{\zeta\upsilon}(\mathbf{q}))\approx \\ &\approx e^{-2\beta\Lambda}\sum_{|\mathbf{q}|}\theta^{>}_{\Lambda}(\xi_{\eta\tau}(\mathbf{q}))\theta^{>}_{\Lambda}(\xi_{\zeta\upsilon}(\mathbf{q}))\approx e^{-2\beta\Lambda}N\ d\Lambda \end{aligned} \tag{2.59}$$

where N is the average density of states (DOS) of the two pockets involved. In particular at $T=0$ the bubble vanishes, which can be deduced analytically by replacing the Matsubara sum with an integral and noting there are two poles in the integrand that lie on the same side of the complex plane. At small temperatures, the bubble does not vanish but it is exponentially suppressed, and only sufficiently strong attractive interactions can result in a relevant flow.

This is markedly different if we instead consider the possibility that one pocket is a hole pocket

and the other is an electron pocket. In that case the main contribution comes from $\xi_{\eta\tau}(\mathbf{q}) \approx -\xi_{\zeta\upsilon}(\mathbf{q}) \approx \pm\Lambda$ for $\eta \neq \zeta$. Since this does not happen for concentric pockets, the interactions involve a momentum transfer, an example of nesting (the momentum $\mathbf{q}$ is measured from the pocket centers). In that case we find instead that the hyperbolic tangents now add together rather than cancel, so

$$d\Pi^{ph}_{\eta\tau;\zeta\upsilon}(\theta) \approx -N\frac{d\Lambda}{\Lambda} = -N\ dt \tag{2.60}$$

Integrating this over the RG time we therefore find that $\Pi^{ph} \propto -Nt = -N\log\frac{\Lambda}{E}$. Note that it diverges as $E \to 0$, which means that the divergence is due to the low energy modes, i.e. this is an infrared divergence in high-energy terminology (or IR instability).

As we will see below for the pairing interactions, the logarithmic divergence of the bubble is indicative of a relevant flow in RG, depending on the sign of the interactions. Here I neglected the spin structure of the interactions, but if we restore it we find that the spin traces involved in the particle-hole diagrams decouple the spin and charge interactions, i.e. they flow independent of each other as claimed. As a result, the U interactions split into two charge and spin *channels* that correspond to so-called spin and charge density wave (SDW and CDW) instabilities. These typically break translational invariance, as well as spin rotation invariance and time reversal symmetry for SDW. These are therefore some of the phases discussed in the introduction of this chapter that can be understood as symmetry breaking instabilities of the Fermi liquid. The particle-hole instabilities require nesting of a particle and a hole pocket, a situation considered for example in [192] for a system very similar to metallic 2H-TMD's, but which is not the case in TMDs that we will consider below. I will therefore assume that no such nesting occurs and the particle-hole channels remain marginal.

Particle-Particle Instability

The second type of marginal interactions (at tree level) corresponds to interactions between fermions with opposite momenta that by momentum conservation scatter into each other (see bottom of Figure 2.4). These are called BCS interactions in [154], but I will call them pairing interactions here. In some situations we will be interested in, it can happen that $\mathbf{p}+\mathbf{p}' = \mathbf{Q}$ for some fixed value $\mathbf{Q}$ for infinitely many values of $\mathbf{p}$ and $\mathbf{p}'$ *on* the Fermi surface, a condition called *nesting* for $\mathbf{Q} \neq 0$. The simplest example of nesting is if the entire Fermi surface is shifted by momentum $\mathbf{Q}$, which of course requires breaking time reversal symmetry. We are mostly interested in $\mathbf{Q} = 0$ that can be

considered as a special case, but for which the term nesting is not used. I use V to label them:

$$S_V[d,\bar{d}] = \frac{T^3}{2} \sum_{\substack{nn',\mathbf{p},\mathbf{k} \\ \eta\zeta\alpha\beta\alpha'\beta'}} V^{\eta'\zeta';\alpha'\beta'}_{\eta\zeta;\alpha\beta}(\mathbf{p};\mathbf{k}) \bar{d}_{\mathbf{k}\eta'\alpha'} \bar{d}_{-\mathbf{k}\zeta'\beta'} d_{-\mathbf{p}\zeta\beta} d_{\mathbf{p}\eta\alpha} \tag{2.61}$$

where again there are only two momenta and frequencies to sum. With the relabeling, the incoming pair has momenta $\pm\mathbf{p}$ and the outgoing pair has momenta $\pm\mathbf{k}$. Note that the band/pocket indices need to satisfy some conditions as a result of momentum conservation.

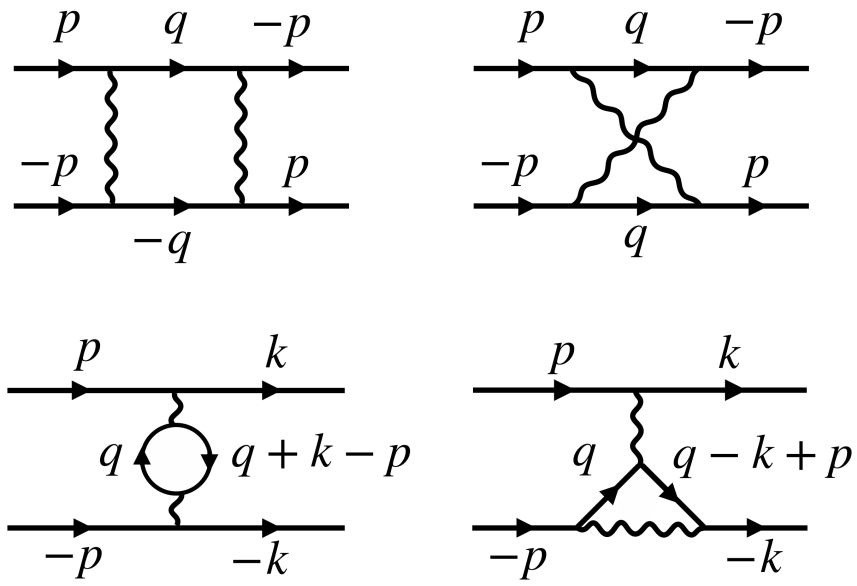

Figure 2.5: Same as Figure 2.3 but with momenta relabeled for pairing interactions.

For the pairing interactions, we relabel the diagram in Figure 2.3 $\mathbf{k} = -\mathbf{p}$ and $\mathbf{Q} = \mathbf{k} - \mathbf{p}$ to get Figure 2.5. Only the particle-particle ladder diagram satisfies the phase space condition that $\mathbf{K} = 0$ in $G^{>}_{IL}(\pm\mathbf{q} + \mathbf{K})$ (one of the internal Green's function inside the integral), and the correction to the action is

$$(\delta s_4^2)_{I'J'K'L'} = \sum V_{I'J'IJ} G^{>}_{IK}(q) V_{KLK'L'} G^{>}_{JL}(-q) \tag{2.62}$$

As in the particle-hole channel, the interactions decompose into channels that we will see flow independently:

$$V^{\eta'\zeta';\alpha'\beta'}_{\eta\zeta;\alpha\beta}(\mathbf{p},\mathbf{k}) = V^{\eta'\zeta';\alpha'\beta'}_{\eta\zeta;\alpha\beta}(\theta,\theta') = \sum_{\ell\mu\nu} g^{(\ell\mu\nu)}_{\eta'\zeta';\eta\zeta} \left[\Sigma^{(\ell\mu)}_{\eta\zeta}(\theta)\right]_{\alpha\beta} \left[\Sigma^{(\ell\nu)*}_{\eta'\zeta'}(\theta')\right]_{\alpha'\beta'} \tag{2.63}$$

where

$$\Sigma^{(\ell\mu)}_{\eta\zeta}(\theta) = \Theta^{(\ell\mu)}_{\eta\zeta}(\theta) i\sigma^y\sigma^\mu \tag{2.64}$$

ℓ is an irrep label that can again be either the orbital angular momentum or label lattice harmonics. Note that the spin index order on the Pauli matrices is different in this case (α' and β are exchanged), which is a choice that will be convenient later. This is the singlet/triplet pairing decomposition of the interactions, as opposed to the charge/spin decomposition we used for U interactions. The $i\sigma^y$ is included in (2.64) so that $\mu = \nu = 0$ interactions correspond to interactions between singlet pairs (i.e. total spin zero), while $\mu = \nu \neq 0$ correspond to interactions between triplet pairs (total spin 1), which we call the singlet and triplet interactions. These are all the terms if interactions conserve spin, since no singlet pair can scatter into a triplet term (nor can components of the spin of the triplet pairs be changed). In principle, $\mu \neq \nu$ terms are also allowed if spin is not conserved by the interactions, which is allowed if SOC is present. They do not lead to new kinds of instabilities, so for simplicity we will only consider interactions with $\mu = \nu$.

In this case we will be more precise and plug in the interactions from Eq. (2.63) to calculate the correction. We then want to see how the coupling constants $g^{(\ell\mu)}_{\eta\zeta;\eta'\zeta'}$ flow (we assume spin conserving interactions). The pocket indices fix inner and outer legs of the diagram and we sum over all possible pockets for the internal legs that we label η'' and ζ'' (see Figure 2.6). The correction will therefore be proportional to squares of other coupling constants:

$$dg^{(\ell\mu)}_{\eta\zeta;\eta'\zeta'} \propto g^{(\ell\mu)}_{\eta\zeta;\eta''\zeta''} g^{(\ell\mu)}_{\eta''\zeta'';\eta'\zeta'} \tag{2.65}$$

with implicit summation over indices on the RHS that are not on the LHS. The full correction corresponding to the particular coupling constant is to the action is

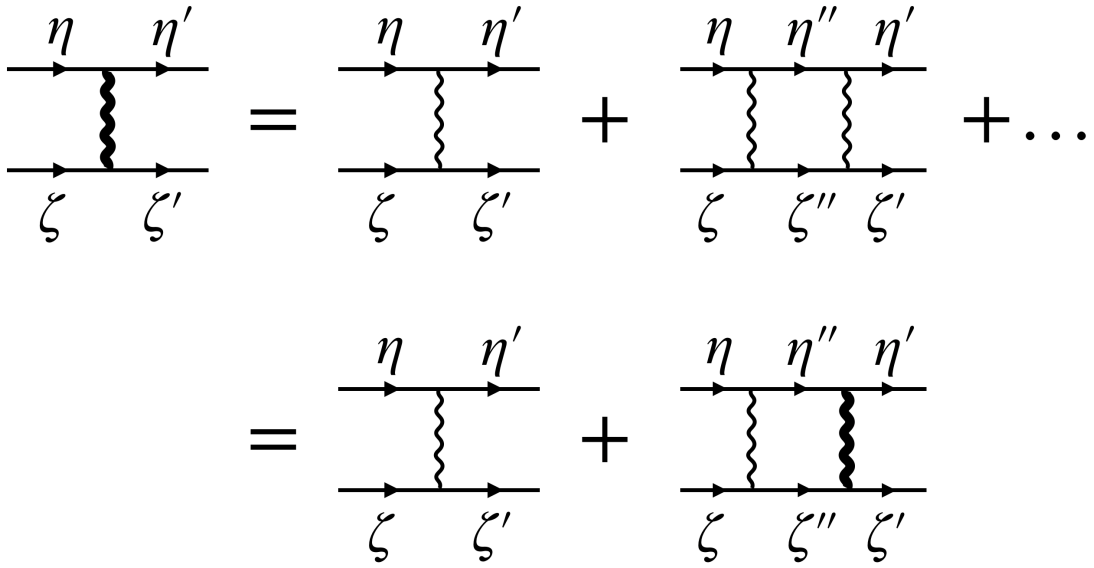

Figure 2.6: The ladder series of diagrams with band indices (only one loop order is shown). Thick wavy line represents renormalized interactions. Iterating the equation allows summing all the ladder diagrams and yields the Dyson equation, shown in the second line.

$$
\begin{aligned}
\delta S^{(\ell\mu)}_{\substack{\eta\zeta;\eta'\zeta' \\ \alpha\beta\alpha'\beta'}} &= \bar{d}_{\mathbf{k}\eta'\alpha'<}\bar{d}_{-\mathbf{k}\zeta'\beta'<}d_{-\mathbf{p}\zeta\beta<}d_{\mathbf{p}\eta\alpha<}T\sum g^{(\ell\mu)}_{\eta\zeta;\eta''\zeta''}\left[\Sigma^{(\ell\mu)}_{\eta\zeta}(\theta)\right]_{\alpha\beta}\left[\Sigma^{(\ell\mu)*}_{\eta''\zeta''}(\theta'')\right]_{\gamma\delta}\left[G^{>}_{\eta''}(q)\right]_{\gamma\gamma'} \\
&\quad \times g^{(\ell\mu)}_{\eta''\zeta'';\eta'\zeta'}\left[\Sigma^{(\ell\mu)}_{\eta''\zeta''}(\theta'')\right]_{\gamma'\delta'}\left[\Sigma^{(\ell\mu)*}_{\eta'\zeta'}(\theta')\right]_{\alpha'\beta'}\left[G^{>}_{\zeta''}(-q)\right]_{\delta\delta'} = \\
&= \left[\Sigma^{(\ell\mu)}_{\eta\zeta}(\theta)\right]_{\alpha\beta}\left[\Sigma^{(\ell\mu)*}_{\eta'\zeta'}(\theta')\right]_{\alpha'\beta'}\bar{d}_{\mathbf{k}\eta'\alpha'<}\bar{d}_{-\mathbf{k}\zeta'\beta'<}d_{-\mathbf{p}\zeta\beta<}d_{\mathbf{p}\eta\alpha<}\times \\
&\quad \times T\sum g^{(\ell\mu)}_{\eta\zeta;\eta''\zeta''}g^{(\ell\mu)}_{\eta''\zeta'';\eta'\zeta'}\left[\Sigma^{(\ell\mu)*}_{\eta''\zeta''}(\theta'')\right]_{\gamma\delta}\left[G^{>}_{\eta''}(q)\right]_{\gamma\gamma'}\left[\Sigma^{(\ell\mu)}_{\eta''\zeta''}(\theta'')\right]_{\gamma'\delta'}\left[G^{>}_{\zeta''}(-q)\right]_{\delta\delta'} = \\
&= \left[\Sigma^{(\ell\mu)*}_{\eta\zeta}(\theta)\right]_{\alpha\beta}\left[\Sigma^{(\ell\mu)}_{\eta'\zeta'}(\theta')\right]_{\alpha'\beta'}\bar{d}_{\mathbf{k}\eta'\alpha'<}\bar{d}_{-\mathbf{k}\zeta'\beta'<}d_{-\mathbf{p}\zeta\beta<}d_{\mathbf{p}\eta\alpha<}\times \\
&\quad \times T\sum g^{(\ell\mu)}_{\eta\zeta;\eta''\zeta''}g^{(\ell\mu)}_{\eta''\zeta'';\eta'\zeta'}\mathrm{Tr}\left[\Sigma^{(\ell\mu)\dagger}_{\eta''\zeta''}(\theta'')G^{>}_{\eta''}(q)\Sigma^{(\ell\mu)}_{\eta''\zeta''}(\theta'')G^{>T}_{\zeta''}(-q)\right] \qquad (2.66)
\end{aligned}
$$

where the sum is over indices absent on the LHS as well as q that includes the frequency and the associated angle θ''; in particular, γ, γ', δ, and δ' are internal spin indices. The trace is over the spin indices. The complexity of the expressions illustrates the advantage of the diagrammatic technique for keeping track of indices, e.g. the spin indices are summarized in Figure 2.7. Writing out the full term is however helpful to justify why we chose the singlet/triplet decomposition of interactions in (2.63), which is forced upon us by the RG: this is the only way we can factor out

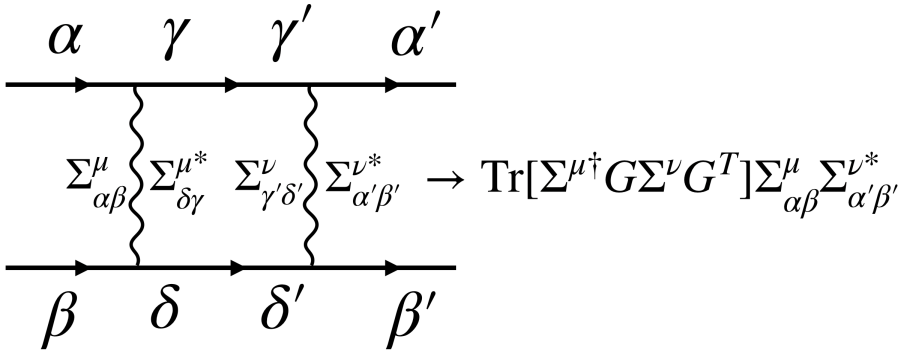

Figure 2.7: The one-loop ladder diagram with spin indices written out corresponding to Eq. (2.66).

$\left[\Sigma^{(\ell\mu)\dagger}_{\eta\zeta}(\theta)\right]_{\alpha\beta}\left[\Sigma^{(\ell\mu)}_{\eta'\zeta'}(\theta')\right]_{\alpha'\beta'}$ from the sum and obtain interaction with the same spin structure.

Matching the coupling constants, we thus find that

$$dg^{(\ell\mu)}_{\eta\zeta;\eta'\zeta'} = g^{(\ell\mu)}_{\eta\zeta;\eta''\zeta''}g^{(\ell\mu)}_{\eta''\zeta'';\eta'\zeta'}d\bar{\Pi}^{(\ell\mu)pp}_{\eta''\zeta''} \tag{2.67}$$

from which we get the beta function

$$\dot{g}^{(\ell\mu)}_{\eta\zeta;\eta'\zeta'} = \frac{dg^{(\ell\mu)}_{\eta\zeta;\eta'\zeta'}}{dt} = g^{(\ell\mu)}_{\eta\zeta;\eta''\zeta''}g^{(\ell\mu)}_{\eta''\zeta'';\eta'\zeta'}\frac{d\bar{\Pi}^{(\ell\mu)pp}_{\eta''\zeta''}}{dt} \tag{2.68}$$

where we defined the dot to indicate differentiation with respect to the RG time t, and introduced the (infinitesimal, angle averaged) particle-particle bubble or pairing susceptibility

$$d\bar{\Pi}^{(\ell\mu)pp}_{\eta''\zeta''} = T\sum \mathrm{Tr}\left[\Sigma^{(\ell\mu)\dagger}_{\eta''\zeta''}(\theta'')G^{>}_{\eta''}(q)\Sigma^{(\ell\mu)}_{\eta''\zeta''}(\theta'')G^{>T}_{\zeta''}(-q)\right] \tag{2.69}$$

The structure of the bubble explains why we do not need to consider interactions with multiple irrep or orbital indices ℓ: assuming the band structure itself respects the symmetry of the system, the Green's functions always belong to the trivial representation. For example in a rotationally invariant system, the Green's function is independent of the angle θ''. As a result, the sums

$$T\sum \mathrm{Tr}\left[\Sigma^{(\ell\mu)\dagger}_{\eta''\zeta''}(\theta'')G^{>}_{\eta''}(q)\Sigma^{(\ell'\mu)}_{\eta''\zeta''}(\theta'')G^{>T}_{\zeta''}(-q)\right] = 0 \tag{2.70}$$

if $\ell \neq \ell'$ by the choice of $\Sigma^{(\ell\mu)}$. Similarly, if we assume the system has spin-rotation symmetry, the

Green's functions are proportional to the identity matrix in spin indices, and we end up with

$$\mathrm{Tr}\left[\Sigma^{(\ell\mu)\dagger}_{\eta''\zeta''}(\theta'')\Sigma^{(\ell\nu)}_{\eta''\zeta''}(\theta'')\right] \propto \mathrm{Tr}\left[\sigma^{\mu}\sigma^{\nu}\right] = 2\delta_{\mu\nu} \tag{2.71}$$

Note that in this case the singlet and each of the three triplets interactions decouple in the flow equation. Spin rotation moreover forces each of the triplets to be degenerate, i.e. $g^{(\ell x)}_{\eta\zeta;\eta'\zeta'} = g^{(\ell y)}_{\eta\zeta;\eta'\zeta'} = g^{(\ell z)}_{\eta\zeta;\eta'\zeta'}$. The three triplets therefore constitute a single triplet channel. If spin is not conserved, the Green's functions are not proportional to the identity, which both lifts the degeneracy of the triplets and can mix them with the singlet channel.

In principle we can add SOC in the RG analysis, but here we will only consider the case where the Green's functions are proportional to the identity in spin indices. In this case,

$$d\bar{\Pi}^{(\ell\mu)pp}_{\eta\zeta} = 2\int_0^{2\pi} \left|\Theta^{(\ell\mu)}_{\eta\zeta}(\theta)\right|^2 d\Pi^{pp}_{\eta\zeta}(\theta)\frac{d\theta}{2\pi} \tag{2.72}$$

where

$$d\Pi^{pp}_{\eta\zeta}(\theta) = T\sum_{\omega,|\mathbf{q}|} G^{>}_{\eta}(q)G^{>}_{\zeta}(-q) \tag{2.73}$$

is the angle resolved (infinitesimal) particle-particle bubble (note the factor of two due to the trace). The Green's functions are simply

$$G^{>}_{\eta}(q) = \frac{\theta^{>}_{\Lambda}(\varepsilon_{\eta}(\mathbf{q}))}{i\omega_n - \varepsilon_{\eta}(\mathbf{q})} \tag{2.74}$$

so that

$$\begin{aligned} d\Pi^{pp}_{\eta\zeta}(\theta) &= T\sum_{n,|\mathbf{q}|} \frac{\theta^{>}_{\Lambda}(\varepsilon_{\eta}(\mathbf{q}))\theta^{>}_{\Lambda}(\varepsilon_{\zeta}(-\mathbf{q}))}{(i\omega_n - \varepsilon_{\eta}(\mathbf{q}))(-i\omega_n - \varepsilon_{\zeta}(-\mathbf{q}))} = \\ &= -\sum_{|\mathbf{q}|} \frac{n_F\left(\varepsilon_{\eta}(\mathbf{q})\right) - n_F\left(-\varepsilon_{\zeta}(-\mathbf{q})\right)}{\varepsilon_{\eta}(\mathbf{q}) + \varepsilon_{\zeta}(-\mathbf{q})}\theta^{>}_{\Lambda}(\varepsilon_{\eta}(\mathbf{q}))\theta^{>}_{\Lambda}(\varepsilon_{\zeta}(\mathbf{q})) = \\ &= -\frac{1}{2}\sum_{|\mathbf{q}|} \frac{\tanh\frac{\beta\varepsilon_{\eta}(\mathbf{q})}{2} + \tanh\frac{\beta\varepsilon_{\zeta}(\mathbf{q})}{2}}{\varepsilon_{\eta}(\mathbf{q}) + \varepsilon_{\zeta}(\mathbf{q})}\theta^{>}_{\Lambda}(\varepsilon_{\eta}(\mathbf{q}))\theta^{>}_{\Lambda}(\varepsilon_{\zeta}(\mathbf{q})) \end{aligned} \tag{2.75}$$

There are two cases: either $\varepsilon_{\eta}(\mathbf{q}) = \varepsilon_{\zeta}(\mathbf{q}) = \Lambda$ at the same $\mathbf{q}$, or they do not. In the latter case, the

particle-particle bubble vanishes. In the former, we have

$$d\Pi^{pp}_{\eta\zeta}(\theta) = -\frac{\tanh\frac{\beta\Lambda}{2}}{2\Lambda}\sum_{|\mathbf{q}|}\theta^{>}_{\Lambda}(\varepsilon_\eta(\mathbf{q}))\theta^{>}_{\Lambda}(\varepsilon_\zeta(\mathbf{q})) \tag{2.76}$$

To account for a possible difference in DOS's on the η and ζ pockets, note that

$$\varepsilon_\eta(\mathbf{q}) + \varepsilon_\zeta(\mathbf{q}) = \frac{|\mathbf{q}|^2}{2m_\eta} + \frac{|\mathbf{q}|^2}{2m_\zeta} - \mu_\eta - \mu_\zeta = \frac{|\mathbf{q}|^2}{M_{\eta\zeta}} - \mu_\eta - \mu_\zeta \tag{2.77}$$

with the reduced mass $M_{\eta\zeta} = \frac{2m_\eta m_\zeta}{m_\eta + m_\zeta}$, so that the effective DOS is $\frac{M_{\eta\zeta}}{\pi} = \frac{2N_\eta N_\zeta}{N_\eta + N_\zeta}$ where N_η is the DOS of the η pocket. We finally have

$$d\Pi^{pp}_{\eta\zeta}(\theta) \approx -\frac{2N_\eta N_\zeta}{N_\eta + N_\zeta}\frac{\tanh\frac{\beta\Lambda}{2}}{2\Lambda}d\Lambda = -\frac{N_\eta N_\zeta}{N_\eta + N_\zeta}\tanh\frac{\beta\Lambda}{2}\,dt \tag{2.78}$$

Assuming the DOS are isotropic, we have

$$d\bar{\Pi}^{(\ell\mu)pp}_{\eta\zeta} = d\bar{\Pi}^{pp}_{\eta\zeta} = -\frac{2N_\eta N_\zeta}{N_\eta + N_\zeta}\tanh\frac{\beta\Lambda}{2}\,dt \tag{2.79}$$

(if DOS's are not isotropic, the expression is roughly correct for an average DOS, but note that we cannot in general drop the ℓ and μ indices). Finally, we define

$$\tilde{g}^{(\ell\mu)}_{\eta\zeta;\eta'\zeta'} = \sqrt{\frac{2N_\eta N_\zeta}{N_\eta + N_\zeta}}\sqrt{\frac{2N_{\eta'} N_{\zeta'}}{N_{\eta'} + N_{\zeta'}}}\,g^{(\ell\mu)}_{\eta\zeta;\eta'\zeta'} \tag{2.80}$$

to obtain the one loop RG flow equation for the pairing interactions:

$$\dot{\tilde{g}}^{(\ell\mu)}_{\eta\zeta;\eta'\zeta'} = -\tanh\frac{\beta\Lambda}{2}\;\tilde{g}^{(\ell\mu)}_{\eta\zeta;\eta''\zeta''}\tilde{g}^{(\ell\mu)}_{\eta''\zeta'';\eta'\zeta'} \tag{2.81}$$

Example 2.1 (Single Band Case: the BCS Instability and T_c)
In general, (2.81) is a matrix equation that for multiple band systems requires 'diagonalizing' in the pocket indices. It is instructive to consider the single band case, for which the RG flow equation (2.81) is particularly simple:

$$\dot{\tilde{g}}^{(\ell\mu)} = -\tanh\frac{\Lambda}{2T}\left(\tilde{g}^{(\ell\mu)}\right)^2 \tag{2.82}$$

Note that we are also rescaling the temperature $T \to \varrho T = (1 + dt)T$ at each RG step, so it is also

flowing as

$$\dot{T} = T \tag{2.83}$$

so in terms of the 'lab' units $T = T_0 e^t$, so the flow equation for $\tilde{g}^{(\ell\mu)}$ becomes[6]

$$\dot{\tilde{g}}^{(\ell\mu)} = -\tanh\left[\frac{\Lambda}{2T_0}e^{-t}\right]\left(\tilde{g}^{(\ell\mu)}\right)^2 \tag{2.84}$$

The flow equation has a formal solution

$$\tilde{g}^{(\ell\mu)}(t) = \frac{\tilde{g}_0^{(\ell\mu)}}{1 + \tilde{g}_0^{(\ell\mu)}\int_0^t \tanh\left[\frac{\Lambda}{2T_0}e^{-t'}\right]dt'} \tag{2.85}$$

Considering first the $T = 0$ limit, the flow is simply

$$\dot{\tilde{g}}^{(\ell\mu)} = -\left(\tilde{g}^{(\ell\mu)}\right)^2 \tag{2.86}$$

If $\tilde{g}^{(\ell\mu)} \geq 0$ (repulsive), then it will be exponentially suppressed, i.e. it is irrelevant in the RG sense(a result due to [114]). If $\tilde{g}^{(\ell\mu)} < 0$, however, the coupling constant grows and eventually diverges, i.e. it is relevant in the RG sense. The solution is in general

$$\tilde{g}^{(\ell\mu)}(t) = \frac{\tilde{g}_0^{(\ell\mu)}}{1 + \tilde{g}_0^{(\ell\mu)} t} \tag{2.87}$$

which for a negative $\tilde{g}_0^{(\ell\mu)}$ diverges at a *finite* value of $t_c = -\frac{1}{\tilde{g}_0^{(\ell\mu)}}$ with corresponding energy scale $E_c = \Lambda e^{-\frac{1}{\tilde{g}_0^{(\ell\mu)}}}$. Note that the instability happens first for the strongest coupling $g^(\ell\mu)$, and we can ignore the rest since they are finite at t_c. As long as at least one $\tilde{g}_0^{(\ell\mu)}$ is attractive, we thus find that the RG fixed point we considered above is unstable. This is the BCS instability of the Fermi liquid phase. Notice that unlike the particle-hole instability, all that is required is that the Fermi surface is symmetric under momentum inversion $\mathbf{p} \to -\mathbf{p}$.

At finite T, changing the variable to $x = \frac{\Lambda}{T_0}e^{-t}$, we find that the equation for T_c is [162]:

$$\int_0^{\frac{\Lambda}{2T_c}} \frac{\tanh x}{x} dx = -\frac{1}{\tilde{g}_0^{(\ell\mu)}} \tag{2.88}$$

[6]Note that we could have adapted a scheme in which we do not rescale the cutoff at each stage of RG and keep the energy units fixed, in which case the cutoff would flow as $\Lambda = \Lambda_0 e^{-t}$. This results in the same flow.

which is the standard BCS equation for T_c. For $T_c \ll \Lambda$,

$$T_c = \frac{2e^\gamma}{\pi}\Lambda e^{1/\tilde{g}_0^{(\ell\mu)}} \approx 1.13\Lambda e^{1/\tilde{g}_0^{(\ell\mu)}} \tag{2.89}$$

□

which is therefore a valid solution in the weak coupling limit ($\gamma \approx 0.577$ is the Euler-Mascheroni constant).

Observe that since we can integrate the flow equation, we effectively performed a full renormalization, within logarithmic accuracy. This is in part because the diagrams involved are particularly simple, as we have only ladder diagrams. This allows us to compute the correction in RG to all loops iteratively, but note that higher loops add powers of $d\Lambda$ to each diagram, and as a result only the one loop diagram contributes to the beta function within logarithmic accuracy. In the full renormalization calculation, the diagrams being summed are the same but the sums are not restricted to be in a thin shell, i.e. we sum down to zero energy. We can sum all the diagrams using the Dyson equation (see Figure 2.6), and not surprisingly we get exactly

$$g^{(\ell\mu)} = \frac{g_0^{(\ell\mu)}}{1 - g_0^{(\ell\mu)}\Pi^{pp}} \tag{2.90}$$

with

$$\Pi^{pp} = -N\int_0^{\frac{\Lambda}{2T}} \frac{\tanh x}{x} dx \approx -N \log\frac{1.13\Lambda}{T} \tag{2.91}$$

being the full particle-particle bubble that we can obtain from Eq. (2.75) by replacing $\theta_\Lambda^>$ with $\theta_\Lambda^<$. In regular field theory, what we are computing is in fact the four-point or two particle Green's function and what we find is that after renormalizing, it has a pole at which is diverges. Notice the importance of the logarithmic divergence of the susceptibility as $T \to 0$, as it means that there is a pole for an arbitrarily small bare effective attraction. Note that a pole of the four point Green's function determines a dispersion of a two-particle excitation. This means that the instability of the fixed point of RG against pairing interactions is indicating that two-particle excitations are going to appear. This suggest that similarly to adding the $\bar{j}d$ term to study single particle excitations with an auxiliary fermionic field j, we should now add something like $\bar{\Delta}dd$ with an auxiliary *bosonic* field Δ.

2.1.5 Adding Vertices: Hubbard-Stratonovich and a New Fixed Point

Having found that the Fermi liquid fixed point is unstable towards pairing interactions, let us see what symmetry breaking phase (new fixed point) this instability is pointing to. As we saw, the 1L RG essentially forces us to consider interactions of the form

$$\begin{aligned} S_V[d,\bar{d}] &= T^3 \sum_{\substack{\ell,\mu,n,n',\mathbf{p},\mathbf{k} \\ \eta\zeta\eta'\zeta'\alpha\beta\alpha'\beta'}} g^{(\ell\mu)}_{\eta'\zeta';\eta\zeta} \left[\bar{d}_{\mathbf{k}\eta'\alpha'} \left[\Sigma^{(\ell\mu)*}_{\eta'\zeta'}(\theta')\right]_{\alpha'\beta'} \bar{d}_{-\mathbf{k}\zeta'\beta'}\right] \left[d_{-\mathbf{p}\zeta\beta} \left[\Sigma^{(\ell\mu)}_{\eta\zeta}(\theta)\right]_{\alpha\beta} d_{\mathbf{p}\eta\alpha}\right] \\ &= T \sum_{\substack{\ell,\mu,\mathbf{p},\mathbf{k} \\ \eta\zeta\eta'\zeta'}} g^{(\ell\mu)}_{\eta'\zeta';\eta\zeta} \bar{\Phi}^{(\ell\mu)}_{\eta'\zeta'}(\mathbf{k}) \Phi^{(\ell\mu)}_{\eta\zeta}(\mathbf{p}), \end{aligned} \tag{2.92}$$

combining Eq.'s (2.61) and (2.63). The main thing to note is that the interactions split into 'fields' $\Phi^{(\ell\mu)}_{\eta\zeta}(\mathbf{p})$ that only carry incoming or only outgoing indices, in terms of which it is just a quadratic form. Physically, since these are attractive interactions, we expect bound state (i.e. the Cooper pairs) to appear when they diverge, and we expect the many body state of the system to be properly described in terms of these bound states rather than the original single particle states.

We thus want to think of the interaction term as a propagator for these bound states that mediate the interactions. This can be achieved by using the bosonic version of the generating functional identity (2.18) that we used when studying the linear response:

$$\int e^{-\sum_{IJ} \bar{a}_I V^{-1}_{IJ} a_J} e^{\sum_I \left(\bar{\Phi}_I a_I + \bar{a}_I \Phi_I\right)} \frac{\mathcal{D}a\mathcal{D}\bar{a}}{2\pi i} = \frac{e^{-\sum_{IJ} \bar{\Phi}_I V_{IJ} \Phi_J}}{\det\left[V^{-1}\right]} \tag{2.93}$$

with auxiliary complex fields a. The only difference is that the fields are now complex rather than Grassmann numbers, and the determinant is divided by rather than multiplied by on the RHS as a result. Using it in reverse, we can replace $S_V[d,\bar{d}]$ with

$$\begin{aligned} S_V[d,\bar{d},a,\bar{a}] &= \frac{\beta}{2} \sum_{\substack{\ell,\mu,\mathbf{p},\mathbf{k} \\ \eta\zeta\eta'\zeta'}} \left[\bar{\Delta}^{(\ell\mu)}_{\eta'\zeta'}(\mathbf{k})\right]_{\alpha'\beta'} \left[V^{-1}(\mathbf{p};\mathbf{k})\right]^{\eta'\zeta';\alpha'\beta'}_{\eta\zeta;\alpha\beta} \left[\Delta^{(\ell\mu)}_{\eta\zeta}(\mathbf{p})\right]_{\alpha\beta} + \\ &+ \frac{T}{2} \sum_{\substack{\ell,\mu,\mathbf{p} \\ \eta\zeta\alpha\beta}} \left(\left[\Delta^{(\ell\mu)}_{\eta\zeta}(\mathbf{p})\right]_{\alpha\beta} \bar{d}_{\mathbf{p}\eta\alpha} \bar{d}_{-\mathbf{p}\zeta\beta} + c.c.\right) \end{aligned} \tag{2.94}$$

where we introduce the gap functions for the $(\ell\mu)$ channels

$$\Delta^{(\ell\mu)}_{\eta\zeta}(\mathbf{p}) = \Sigma^{(\ell\mu)*}_{\eta\zeta}(\theta) D^{(\ell\mu)}_{\eta\zeta} \tag{2.95}$$

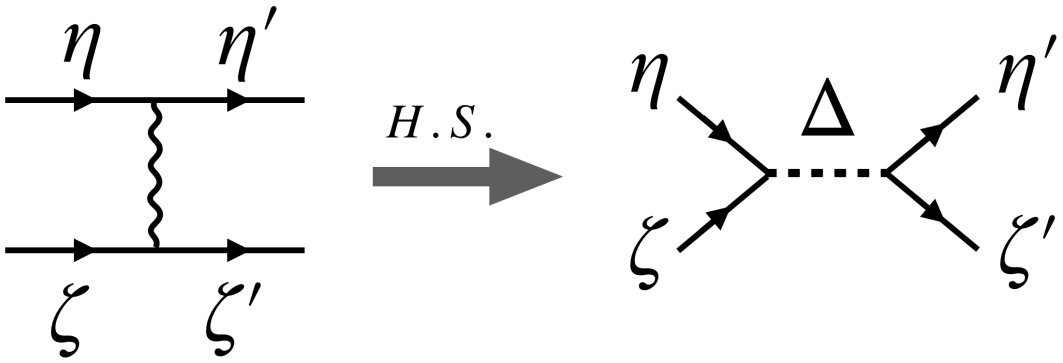

Figure 2.8: Diagrammatic representation of the Hubbard-Stratonovich transformation, in which interactions between fermions are replaced by a bosonic field Δ with a propagator V equal to the original coupling.

with momentum independent coefficients $D^{(\ell\mu)}_{\eta\zeta}$ (the 1/2 is convenient for the BdG formalism, see below). Here $\beta = 1/T$ and the definition of the inverse is

$$\sum \left[V^{-1}(\mathbf{p};\mathbf{q})\right]^{\eta'\zeta';\alpha'\beta'}_{\eta''\zeta'';\alpha''\beta''} V^{\eta''\zeta'';\alpha''\beta''}_{\eta\zeta;\alpha\beta}(\mathbf{q};\mathbf{k}) = \delta_{\eta\eta'}\delta_{\zeta\zeta'}\delta_{\mathbf{kp}}, \tag{2.96}$$

The Hubbard-Stratonovich transformation of S_V thus re-expresses the interactions in terms of boson Δ with propagator V (see Figure 2.8). Notice that it is now quadratic in the fermionic operators, and we can therefore carry out the Gaussian integral to obtain an action just for the new bosonic fields D (or Δ).[7]

Before integrating out the fermions, note that we effectively modified the quadratic part of the fermionic action, which now reads

$$S_0[d,\bar{d}] + S_\Delta[d,\bar{d},\Delta,\bar{\Delta}] = \frac{T}{2}\sum_{n\mathbf{p}\eta\alpha\zeta\beta} \theta_\Lambda^{-1}(\mathbf{p})\bar{\Psi}_{\mathbf{p}\eta\alpha}\left[-i\omega_n + \mathcal{H}^{(BdG)}_{\eta\zeta}(\mathbf{p})\right]_{\alpha\beta}\Psi_{\mathbf{p}\zeta\beta} \tag{2.97}$$

where we introduce the Nambu spinors $\Psi_{\mathbf{p}\eta\alpha} = (d_{\mathbf{p}\eta\alpha}, \bar{d}_{-\mathbf{p}\eta\alpha})^T$ and the Bogolyubov-de Gennes (BdG) Hamiltonian

$$\mathcal{H}^{(BdG)}_{\eta\zeta}(\mathbf{p}) = \begin{pmatrix} \mathcal{H}_\eta(\mathbf{p})\delta_{\eta\zeta} & \Delta_{\eta\zeta}(\mathbf{p}) \\ \Delta^\dagger_{\eta\zeta}(\mathbf{p}) & -\mathcal{H}^T_\zeta(-\mathbf{p})\delta_{\eta\zeta} \end{pmatrix} \tag{2.98}$$

with $\Delta_{\eta\zeta}(\mathbf{p}) = \sum_{\ell\mu}\Delta^{(\ell\mu)}_{\eta\zeta}(\mathbf{p})$. This means that the Green's function now has an anomalous compo-

[7] RG flow of the interactions can actually be analyzed after the Hubbard-Stratonovich transformation, see for example [17].

nent

$$\mathcal{G}_{\eta\zeta}(i\omega_n,\mathbf{p}) = \left(i\omega_n - \mathcal{H}^{(BdG)}(\mathbf{p})\right)^{-1}_{\eta\zeta} = \begin{pmatrix} G_{\eta\zeta}(i\omega_n,\mathbf{p}) & F_{\eta\zeta}(i\omega_n,\mathbf{p}) \\ F^{\dagger}_{\eta\zeta}(i\omega_n,\mathbf{p}) & -G^{T}_{\eta\zeta}(-i\omega_n,-\mathbf{p}) \end{pmatrix} \tag{2.99}$$

Using the special case of the Woodberry matrix identity, $(A+B)^{-1} = A^{-1} - A^{-1}B(A+B)^{-1}$ with $A = \mathcal{H}^{(BdG)}\big|_{\Delta=0}$, we find

$$F_{\eta\zeta}(i\omega_n,\mathbf{p}) = G^{(0)}_{\eta}(i\omega_n,\mathbf{p})\Delta_{\eta\zeta'}(\mathbf{p})G^{T}_{\zeta'\zeta}(-i\omega_n,-\mathbf{p}) \tag{2.100}$$

where $G^{(0)}_{\eta}(i\omega_n,\mathbf{p})$ is the Green's function with $\Delta_{\eta\zeta}(\mathbf{p}) = 0$.[8] Recall that (Eq. (2.21))

$$F_{\eta\zeta;\alpha\beta}(i\omega_n,\mathbf{p}) = -\langle d_{\mathbf{p}\eta\alpha}d_{-\mathbf{p}\zeta\beta}\rangle \approx G^{(0)}_{\eta}(i\omega_n,\mathbf{p})\Delta_{\eta\zeta}(\mathbf{p})G^{(0)T}_{\zeta}(-i\omega_n,-\mathbf{p}) \sim [\Delta_{\eta\zeta}(\mathbf{p})]_{\alpha\beta} \tag{2.101}$$

with $\sim$ indicating that LHS vanishes if the RHS does.

We arrive at an important conclusion that a non-zero value of the bosonic fields Δ, which is called the gap functions, signals a non-zero expectation value of a pair of single particle fields in the ground state. The anomalous Green's function $F = -\langle d_{\mathbf{p}\eta\alpha}d_{-\mathbf{p}\zeta\beta}\rangle$ is therefore an *order parameter* of the superconducting phase that is non-zero inside the phase and zero outside. In this case the type of order is sometimes called the off-diagonal long-range order (ODLRO) (in 2D it is strictly speaking long range only at zero temperature due to the Mermin-Wagner theorem). Note that F is complex, but its overall phase is arbitrary. The fact that the phase is the same for all Cooper pairs indicates that a $U(1)$ symmetry is broken.

Returning now to integrating out the fermions, instead of integrating them all at once, we can again treat (2.97) using RG. An alternative point of view, which gives the same answer, is that we start with the action before the Hubbard-Stratonovich, but introduce an *external* vertex $\Delta\bar{d}\bar{d}$ and compute its RG flow This means adding a new object to the diagrammatics corresponding to the vertex, shown in Figure 2.9. Fortunately, we do not need to do many new calculations. The one loop correction is already in $\langle S_I\rangle_{>}$ and writing out the diagrams we note that they are the same as for the pairing interactions with one interaction line replaced with the anomalous Green's function F (see Figure 2.9). Very generally, we find that the one loop correction is

[8] When only SC or only PDW is present, the BdG Hamiltonian is block diagonal, and the same follows from the 2×2 block matrix inverse formula. One version of that formula is

$$\begin{pmatrix} A & B \\ C & D \end{pmatrix}^{-1} = \begin{pmatrix} A^{-1} + A^{-1}B(D-CA^{-1}B)^{-1}CA^{-1} & -A^{-1}B(D-CA^{-1}B)^{-1} \\ -(D-CA^{-1}B)^{-1}CA^{-1} & (D-CA^{-1}B)^{-1} \end{pmatrix}$$

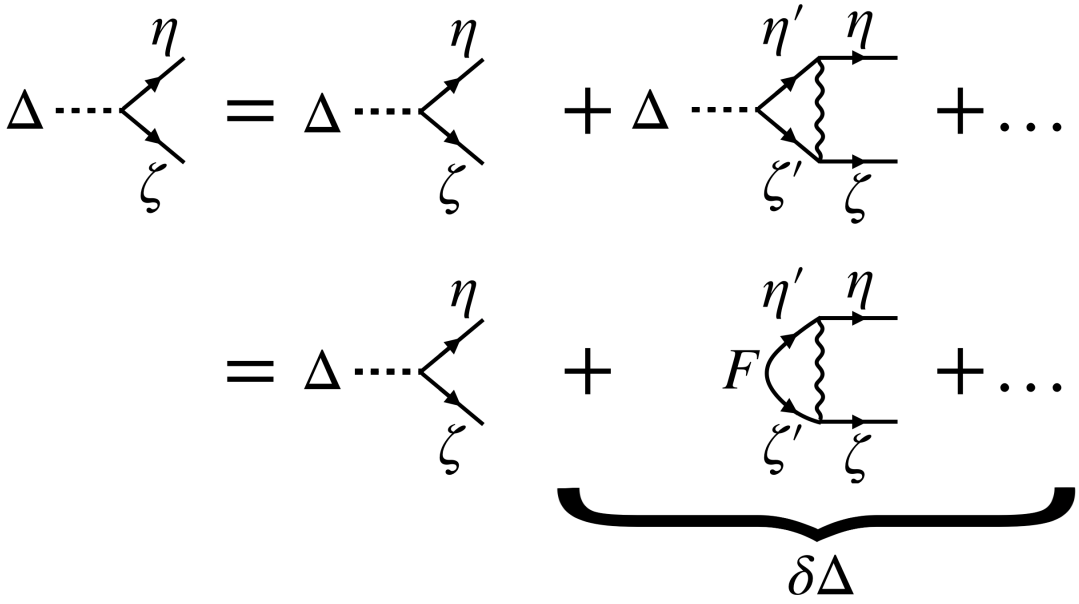

Figure 2.9: The vertex renormalization to one loop. Note that they can be obtained from the renormalization for the interactions by 'collapsing' the left part of the interactions into the vertex.

$$\begin{aligned}[\delta\Delta_{\eta\zeta}(\mathbf{p})]_{\alpha\beta} &= T\sum V^{\eta'\zeta';\alpha'\beta'}_{\eta\zeta;\alpha\beta}(\mathbf{p};\mathbf{k})\,[F_{\eta'\zeta'}(\mathbf{k})]_{\alpha'\beta'} \\ &= T\sum V^{\eta'\zeta';\alpha'\beta'}_{\eta\zeta;\alpha\beta}(\mathbf{p};\mathbf{k})\left[G^{(0)}_{\eta'}(i\omega,\mathbf{k})\Delta_{\eta'\zeta'}(\mathbf{k})G^{T}_{\zeta'}(-i\omega,-\mathbf{k})\right]_{\alpha'\beta'}\end{aligned} \tag{2.102}$$

Considering the case when spin is conserved, we immediately conclude by plugging in (2.63) or simply by comparison with (2.81) that

$$\Delta_{\eta\zeta}(\mathbf{p}) = \sum_{\ell\mu}\Delta^{(\ell\mu)}_{\eta\zeta}(\mathbf{p}) = \Sigma^{(\ell\mu)}_{\eta\zeta}(\theta)D^{(\ell\mu)}_{\eta\zeta} \tag{2.103}$$

where $D^{(\ell\mu)}_{\eta\zeta}$ are complex numbers independent of momentum that flow under RG as

$$\dot{\tilde{D}}^{(\ell\mu)}_{\eta\zeta} = -\tanh\left[\frac{\beta\Lambda}{2}\right]\tilde{g}^{(\ell\mu)}_{\eta\zeta;\eta'\zeta'}\tilde{D}^{(\ell\mu)}_{\eta'\zeta'} \tag{2.104}$$

where

$$\tilde{D}^{(\ell\mu)}_{\eta\zeta} = \sqrt{\frac{2N_\eta N_\zeta}{N_\eta+N_\zeta}}D^{(\ell\mu)}_{\eta\zeta} \tag{2.105}$$

and recall that temperature is flowing as $T = T_0e^t$. This is a matrix equation in pocket indices,

and as long as it has a positive eigenvalue, $D^{(\ell\mu)}_{\eta'\zeta'}$ is relevant in RG. It can be seen that the same $\ell\mu$ channel is selected by both the interactions and the vertex flow, which determines the functional form of the gap function Δ. Thus we conclude the Fermi liquid is unstable to a small perturbation introducing a small Cooper pair condensate. In this case, however, we can completely integrate out the fermions from low energy sector. The new fixed point is obtained by solving the full gap equation, which is just the mean field equation that we will use in Chapter 4.

2.2 RG Analysis of 1H-TMDs and Related Systems

Having developed the RG formalism, we want to apply it to the specific system of interest, the metallic 1H transition metal dichalcogenides (TMDs) like $NbSe_2$. As discussed in Chapter 1, 1H-$NbSe_2$ has three hole pockets centered at $\eta, \zeta = \Gamma, \pm K$. We interchangeably use $\eta = 0, \pm 1$ corresponding to the ηK point, with $0K = \Gamma$. Note that $3K = \Gamma$. By $\mathbf{p}$ and $\mathbf{k}$ we will mean the small momenta measured relative to the pocket centers (so the total momentum is $\mathbf{P} = \mathbf{p} + \eta\mathbf{K}$). Note that the RG analysis depends only on the 'fermiology,' i.e. the Fermi surface structure, and so it applies to any system with a similar Fermi surface structure.

The 1H TMDs have strong SOC as discussed above, but we will not include it in our RG. This can be justified if, as we found above, the RG instability happens at a finite RG 'time' t_c at which the cutoff has been rescaled down to $\Lambda = \Lambda_0 e^{-t_c}$ in lab units. If the rescaled Λ is much larger than the energy scale β_{SOC} associated with the SOC, then the SOC can be safely neglected. If it is not, then in the spirit of the two-step RG approach we can simply keep the channel that grows fastest while neglecting the SOC, and then include SOC in the mean field approximation in Chapter 4 and Chapter 5, for which the rescaled Λ sets the new cutoff. In principle the RG with SOC included is not much more difficult numerically, but since the number of Fermi surfaces then doubles it becomes less tractable analytically. The mean field approach is also more accommodating to studying the suppression of the logarithm in the susceptibility due to symmetry breaking terms, and it is equivalent to the RG calculation when only one instability is present.

The fact that all pockets are hole pockets in TMDs implies that only pairing or particle-particle instabilities of the Fermi surface are possible within logarithmic accuracy (unlike the case considered in [192]). Interestingly, a CDW is nevertheless observed in, e.g. 1H-$NbSe_2$ [117], which is therefore likely to be a high energy phenomenon, i.e. not a Fermi surface instability [11, 73, 72]. It has been argued that the CDW is a result of a structural change (which involves lattice degrees of freedom that we have ignored) [72]. We note that RG has also been done in TMDs with no Γ pocket, e.g.

for doped MoS_2 [67], but the authors had to go to two loops to find an attractive channel (i.e. they considered the Kohn-Luttinger mechanism) which usually gives a low T_c. Here we will show that attraction is possible with entirely repulsive interactions already at one loop even in that system. The analysis is based on [153].

2.2.1 The Interactions

We will carry out the analysis for the general form of the pairing interactions (2.61)-(2.63), but it is instructive to first consider a more physically motivated model of interactions. As we saw in the RG calculation, interactions that depend on the radial component of the momentum are irrelevant in the RG sense. The most local interactions are the on-site density-density interactions $Un_{j\uparrow}n_{i\downarrow}$ where i is the lattice site index and $n_{i\alpha} = \bar{d}_{i\alpha}d_{i\alpha}$; i.e. this is the Hubbard model. In an extended Hubbard model we may in addition consider interactions between nearest neighbors, $Vn_{i\alpha}n_{j\beta}$ (where now all spin combinations are allowed). Recently, it has been proposed that spin fluctuations of the form $J\mathbf{S}_i \cdot \mathbf{S}_i$ with $S_i^j = \bar{d}_{i\alpha}\sigma^j_{\alpha\beta}d_{j\alpha}$ can also be significant [184]. The corresponding interactions in momentum space are nearly isotropic in the small momenta (i.e. expanded around the pocket centers), and higher order harmonics generally carry powers of momentum and are thus expected to be irrelevant in the RG sense. In other words, we expect that the leading interactions are constant in the small momenta.

There are as a result only eight interaction processes allowed by momentum conservation, shown in Figure 2.10. Four of these correspond to interactions between pairs of electrons with zero total momentum and that lead to the superconducting instability: intrapocket density-density g_1 at Γ, interpocket density-density g_2 at $\pm K$, exchange g_3 between $\pm K$, and pair-hopping g_4 between Γ and $\pm K$. The other four are interactions between electrons with a total momentum $\pm 2K = \mp K$: intrapocket h_1 at $\pm K$, interpocket h_2 between Γ and $\pm K$, exchange h_3 between Γ and $\pm K$, and h_4 scattering a pair at Γ and $\pm K$ to a pair at $\mp K$ (the latter is allowed by Umklapp because $3\mathbf{K} = 0$). We also represent the eight processes using Feynman diagrams in Figure 2.11.

Since we already concluded above that only pairing instabilities are possible, we write out the interactions in terms of pair operators:

$$\begin{aligned} H_{\mathrm{SC}} = \sum_{\alpha\beta} (& g_1 \bar{d}_{\mathbf{k}\Gamma\alpha}\bar{d}_{-\mathbf{k}\Gamma\beta}d_{\mathbf{p}\Gamma\beta}d_{-\mathbf{p}\Gamma\alpha} + g_2\bar{d}_{\mathbf{k}K\alpha}\bar{d}_{-\mathbf{k}-K\beta}d_{\mathbf{p}-K\beta}d_{-\mathbf{p}K\alpha} \\ & + g_3\bar{d}_{\mathbf{k}K\alpha}\bar{d}_{-\mathbf{k}-K\beta}d_{\mathbf{p}K\beta}d_{-\mathbf{p}-K\alpha} + g_4\bar{d}_{\mathbf{k}\Gamma\alpha}\bar{d}_{-\mathbf{k}\Gamma\beta}d_{\mathbf{p}K\beta}d_{-\mathbf{p}-K\alpha}) + h.c. \end{aligned} \tag{2.106}$$

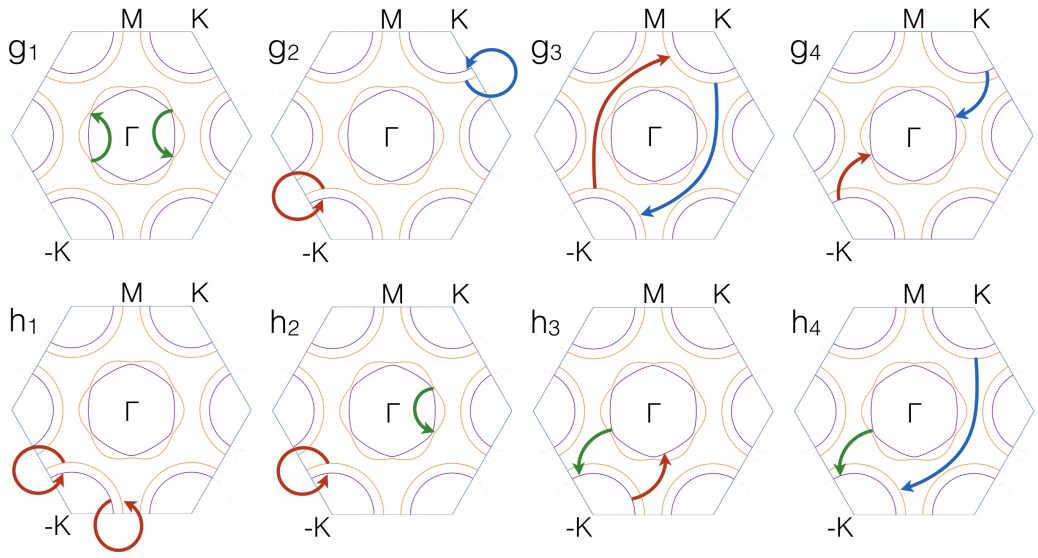

Figure 2.10: Interaction channels g_n and h_n shown in the Brillouin zone. Arrows indicate which pocket the fermions start and end on before and after interacting, with the arrow's head representing an electron creation operator at a momentum $\mathbf{k}$ (relative to the pocket center), and the arrow's end representing an electron annihilation operator at a different momentum $\mathbf{p}$ (relative to the pocket center).

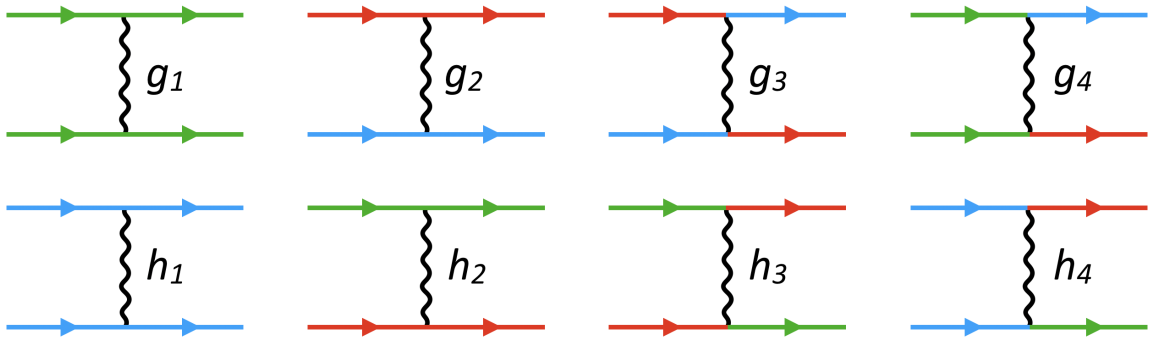

Figure 2.11: Feynman diagrams corresponding to the eight interaction processes in Figure 2.10. Green, blue and red colors correspond to Γ, K and $-K$ pockets respectively.

and

$$H_{\text{PDW}} = \sum_{\alpha\beta}(h_1 \bar{d}_{\mathbf{k}K\alpha}\bar{d}_{-\mathbf{k}K\beta}d_{\mathbf{p}K\beta}d_{-\mathbf{p}K\alpha} + h_2\bar{d}_{\mathbf{k}\Gamma\alpha}\bar{d}_{-\mathbf{k}-K\beta}d_{\mathbf{p}-K\beta}d_{-\mathbf{p}\Gamma\alpha} + h_3\bar{d}_{\mathbf{k}\Gamma\alpha}\bar{d}_{-\mathbf{k}-K\beta}d_{\mathbf{p}\Gamma\beta}d_{-\mathbf{p}\Gamma\alpha} + h_4\bar{d}_{\mathbf{k}K\alpha}\bar{d}_{-\mathbf{k}K\beta}d_{\mathbf{p}\Gamma\beta}d_{-\mathbf{p}-K\alpha}) + h.c. + K \leftrightarrow -K \tag{2.107}$$

Note that because H_{PDW} only involves interactions between pairs with a total momentum $\pm 2K$, the corresponding instability they lead to is a pair density wave (PDW), a pairing instability in which the Cooper pairs have a total momentum $\pm 2K$. Similarly, H_{SC} can only lead to uniform SC.

We assumed furthermore that the interactions originate in the charge channel, i.e. they are all of the form

$$H \sim \delta_{\alpha\alpha'}\delta_{\beta\beta'}\bar{d}_{\mathbf{k}\eta'\alpha'}\bar{d}_{-\mathbf{k}\zeta'\beta'}d_{-\mathbf{p}\zeta\beta}d_{\mathbf{p}\eta\alpha} \tag{2.108}$$

Here we expect only pairing instabilities, based on the general RG analysis, and we therefore need to switch to the singlet/triplet decomposition. To do this we use the completeness relation

$$2\delta_{\alpha\alpha'}\delta_{\beta\beta'} = \sum_{\mu}\left[i\sigma^y\sigma^\mu\right]_{\alpha\beta}\left[(i\sigma^y\sigma^\mu)^\dagger\right]_{\alpha'\beta'} \tag{2.109}$$

Now, for $j = x, y, z$

$$\begin{aligned} \sum_{\mathbf{p}\alpha\beta}\left[i\sigma^y\sigma^j\right]_{\alpha\beta} d_{-\mathbf{p}\Gamma\beta}d_{\mathbf{p}\Gamma\alpha} &= -\sum_{\mathbf{p}\alpha\beta}\left[i\sigma^y\sigma^j\right]_{\alpha\beta} d_{\mathbf{p}\Gamma\alpha}d_{-\mathbf{p}\Gamma\beta} = \\ = -\sum_{\mathbf{p}\alpha\beta}\left[i\sigma^y\sigma^j\right]_{\beta\alpha} d_{-\mathbf{p}\Gamma\beta}d_{\mathbf{p}\Gamma\alpha} &= -\sum_{\mathbf{p}\alpha\beta}\left[i\sigma^y\sigma^j\right]_{\alpha\beta} d_{-\mathbf{p}\Gamma\beta}d_{\mathbf{p}\Gamma\alpha} \to 0 \end{aligned} \tag{2.110}$$

where we relabeled $\mathbf{p} \to -\mathbf{p}$ and $\alpha \leftrightarrow \beta$ going from the first to second line and then used $i\sigma^y\sigma^j = (i\sigma^y\sigma^j)^T$. The arrow indicates that we can take the term to zero after anti-symmetrizing. So the g_1, g_4, h_1 and h_4 interactions are all singlet interactions. In particular this would be the case for a single band system with only the Γ pocket. But we cannot conclude this for g_2 and g_3 (or h_2 and h_3), because under anti-symmetrization they are mapped into each other rather than themselves.

In particular, anti-commutation implies

$$\begin{aligned}
&\delta_{\alpha\alpha'}\delta_{\beta\beta'}\left(g_2\bar{d}_{\mathbf{k}K\alpha'}\bar{d}_{-\mathbf{k}-K\beta'}d_{\mathbf{p}-K\beta}d_{-\mathbf{p}K\alpha}+g_3\bar{d}_{\mathbf{k}K\alpha'}\bar{d}_{-\mathbf{k}-K\beta'}d_{\mathbf{p}K\beta}d_{-\mathbf{p}-K\alpha}\right)= \\
= \quad &\frac{g_2+g_3}{4}(i\sigma^y)_{\alpha\beta}(i\sigma^y)_{\alpha'\beta'}\bar{d}_{-\mathbf{k}-K\beta}d_{\mathbf{p}-K\beta}d_{-\mathbf{p}K\alpha}+ \\
&+\frac{g_2-g_3}{4}\sum_{j=x,y,z}(\sigma^j i\sigma^y)_{\alpha\beta}(\sigma^j i\sigma^y)^*_{\alpha'\beta'}\bar{d}_{\mathbf{k}K\alpha}\bar{d}_{-\mathbf{k}-K\beta}d_{\mathbf{p}-K\beta}d_{-\mathbf{p}K\alpha}
\end{aligned}$$

with the rest of the pocket index combinations then obtained by anti-symmetrizing, and the same for h_2 and h_3. The lesson is that uniform interactions on a triangular lattice with disconnected Fermi surfaces related by momentum inversion lead to triplet interactions. Physically, this is because there is an extra index we can anti-symmetrize in instead of spin (either lattice site or pockets index). Triplet interactions are present already in the extended Hubbard model in the nearest-neighbor density-density interactions, and they were shown to be enhanced by spin fluctuations [184]. In the absence of SOC, triplet interactions could lead to a spin-triplet SC phase, similar to that previously found theoretically in graphene in [57, 200]; more recently it was found in bilayer TMDs in [75] (where again spin fluctuations were argued to stabilize the phase).

Since there are triplet interactions in the system, we need to include such interactions also in the $g_1\ldots$ terms in order to avoid an artificial vanishing of the order parameters. At that stage we may as well consider all possible lattice harmonics of the D_{3h} point group with an arbitrary angular dependance, i.e. take the Hamiltonian in the (2.63) form:

$$H_V=\frac{1}{2}\sum_{\substack{\mathbf{p},\mathbf{k}\\ \eta\zeta\alpha\beta\alpha'\beta'}}V^{\eta'\zeta';\alpha'\beta'}_{\eta\zeta;\alpha\beta}(\mathbf{p};\mathbf{k})\bar{d}_{\mathbf{k}\eta'\alpha'}\bar{d}_{-\mathbf{k}\zeta'\beta'}d_{-\mathbf{p}\zeta\beta}d_{\mathbf{p}\eta\alpha} \tag{2.111}$$

with (reproducing Eq. (2.63))

$$V^{\eta'\zeta';\alpha'\beta'}_{\eta\zeta;\alpha\beta}(\mathbf{p},\mathbf{k})=V^{\eta'\zeta';\alpha'\beta'}_{\eta\zeta;\alpha\beta}(\theta,\theta')=\sum_{\ell\mu\nu}g^{(\ell\mu)}_{\eta'\zeta';\eta\zeta}\left[\Sigma^{(\ell\mu)}_{\eta\zeta}(\theta)\right]_{\alpha\beta}\left[\Sigma^{(\ell\mu)*}_{\eta'\zeta'}(\theta')\right]_{\alpha'\beta'} \tag{2.112}$$

where

$$\Sigma^{(\ell\mu)}_{\eta\zeta}(\theta)=\Theta^{(\ell\mu)}_{\eta\zeta}(\theta)i\sigma^y\sigma^\mu \tag{2.113}$$

are now lattice harmonics for the D_{3h} point group of the 1H-TMDs. The leading harmonics belonging to irreducible representations that correspond to the momentum independent interactions are listed in Table 2.1. These happen to be in the trivial A_1' and the two dimensional E'' irreps. Note that

singlet and triplet terms can belong to the same irreps since D_{3h} is non-centrosymmetric. Since we are ignoring SOC here, however, the point group is effectively D_{6h} and the μ channels will decouple, so we keep that label separately, while ℓ still labels the D_{3h} irrep (note that for 2D irreps, there are two components with an additional label $m = x, y$).

$\ell(D_{3h})$	$\Sigma^{(\ell 0)}_{\eta\eta}$	$\Sigma^{(\ell j)}_{\eta\eta}$
A_1'	$i\sigma^y$	$\sqrt{2}\cos 3\theta_{\mathbf{p}}\sigma^z i\sigma^y$
$E''(m=x)$		$\sqrt{2}\cos 3\theta_{\mathbf{p}}\sigma^x i\sigma^y$
$E''(m=y)$		$\sqrt{2}\cos 3\theta_{\mathbf{p}}\sigma^y i\sigma^y$

$\ell(D_{3h})$	$\Sigma^{(\ell 0)}_{\eta\zeta\neq\eta}$	$\Sigma^{(\ell j)}_{\eta\zeta\neq\eta}$
A_1'	$i\sigma^y$	$\epsilon_{\eta\zeta}\sigma^z i\sigma^y$
$E''(m=x)$		$\epsilon_{\eta\zeta}\sigma^x i\sigma^y$
$E''(m=y)$		$\epsilon_{\eta\zeta}\sigma^y i\sigma^y$

Table 2.1: Leading terms $\Sigma^{(\ell\mu)}_{\eta\zeta}(\mathbf{p})$ for singlet ($\mu = 0$) and triplet ($\mu = j = x, y, z$) interactions in Eq. (2.112) for $\eta = \zeta$ and $\eta \neq \zeta$, where $\epsilon_{\eta\zeta}$ is the Levi-Civita symbol. $\theta_{\mathbf{p}}$ is the angle made by the small momentum $\mathbf{p}$ measured from the K direction. Note that there are no singlet interactions in the E'' irrep in 2D.

As written, the coupling constants $g^{(\ell\mu)}_{\eta\zeta;\eta'\zeta'}$ are somewhat redundant and not very transparent, and it still helps to think in terms of g_1, g_2, g_3, g_4 and h_1, h_2, h_3, h_4 processes. Note also that momentum conservation also implies that $\eta + \zeta = \eta' + \zeta'$ (modulo 3), for example a $K\Gamma \to \Gamma\Gamma$ process is ruled out and some of the $g^{(\ell\mu)}_{\eta\zeta;\eta'\zeta'}$ vanish. We define the $\eta = \zeta$ processes as $g^{(\ell\mu)}_n$ and the $\eta = \zeta \pm 1$ processes as $h^{(\ell\mu)}_n$ with $n = 1, 4$, and 23 as summarized in Table 2.2. In that convention, we then have $g^{(A_1',0)}_n = g_n$ and $h^{(A_1',0)}_n = h_n$ for $n = 1, 4$ but

$$g^{(A_1',0)}_{23} = \frac{g_2 + g_3}{2} \qquad h^{(A_1',0)}_{23} = \frac{h_2 + h_3}{2}$$
$$g^{(A_1',j)}_{23} = g^{(E'',j)}_{23} = \frac{g_2 - g_3}{2} \qquad h^{(A_1',j)}_{23} = h^{(E'',j)}_{23} = \frac{h_2 - h_3}{2} \tag{2.114}$$

with $j = x, y, z$. Note that the general model we consider includes not just these but all possible pairing terms that can come from other contributions.

$g^{(\ell\mu)}_{\eta,-\eta;\zeta,-\zeta}$	$\eta = 0$	$\eta = \pm 1$
$\zeta = 0$	$g_1^{(\ell\mu)}$	$g_4^{(\ell\mu)}$
$\zeta = \pm 1$	$g_4^{(\ell\mu)}$	$g_{23}^{(\ell\mu)}$

$g^{(\ell\mu)}_{\pm 1+\eta,\pm 1-\eta;\pm 1+\zeta,\pm 1-\zeta}$	$\eta = 0$	$\eta = \pm 1$
$\zeta = 0$	$h_1^{(\ell\mu)}$	$h_4^{(\ell\mu)}$
$\zeta = \pm 1$	$h_4^{(\ell\mu)}$	$h_{23}^{(\ell\mu)}$

Table 2.2: Correspondence between coupling constants $g^{(\ell\mu)}_n$ and $g^{(\ell\mu)}_{\eta\zeta;\eta'\zeta'}$. $\eta + \zeta = \eta' + \zeta' = 0$ (left side) correspond to interactions between pairs with total zero momentum that lead to uniform SC, while $\eta + \zeta = \eta' + \zeta' = \pm 2 = \mp 1$ modulo 3 (right side) correspond to interaction between pairs with total momentum $\pm 2K = \mp K$ and lead to PDW with that momentum. $n = 1$ corresponds to intrapocket interactions, $n = 23$ are interpocket interactions (including exchange interactions by antisymmetrization), $g_4^{(\ell\mu)}$ are pair hopping interactions, and $h_4^{(\ell\mu)}$ is the Umklapp process.

For the RG flow, recall that it is convenient to use the dimensionless coupling constants scaled by the DOS $N_\eta = \frac{m_\eta}{4\pi}$ as follows:

$$\tilde{g}_1^{(\ell\mu)} = N_\Gamma g_1^{(\ell\mu)}, \quad \tilde{g}_4^{(\ell\mu)} = \sqrt{N_\Gamma N_K} g_4^{(\ell\mu)}, \quad \tilde{g}_{23}^{(\ell\mu)} = N_K g_{23}^{(\ell\mu)}$$
$$\tilde{h}_1^{(\ell\mu)} = N_K h_1^{(\ell\mu)}, \quad \tilde{h}_4^{(\ell\mu)} = \sqrt{\tfrac{2N_\Gamma N_K^2}{N_\Gamma + N_K}} h_4^{(\ell\mu)}, \quad \tilde{h}_{23}^{(\ell\mu)} = \tfrac{2N_\Gamma N_K}{N_\Gamma + N_K} h_{23}^{(\ell\mu)}$$

On physical grounds, we still expect interactions to decrease in strength with higher harmonics and the corresponding coupling constants to be small.

2.2.2 RG Flow for Interactions

With the interactions in place, we can write out the RG flow for the interactions as given in Eq. (2.81):

$$\dot{\tilde{g}}^{(\ell\mu)}_{\eta\zeta;\eta'\zeta'} = -\tanh\frac{\beta\Lambda}{2}\, \tilde{g}^{(\ell\mu)}_{\eta\zeta;\eta''\zeta''} \tilde{g}^{(\ell\mu)}_{\eta''\zeta'';\eta'\zeta'} \tag{2.115}$$

Note that momentum conservation implies that $\eta + \zeta = \eta' + \zeta' = \eta'' + \zeta''$, which means that the $g_n^{(\ell\mu)}$ and $h_n^{(\ell\mu)}$ decouple into the SC and two PDW channels as expected. Due to the absence of particle-hole logarithm, only ladder diagrams contribute (the pRG is in this case equivalent to RPA). Their flows are thus

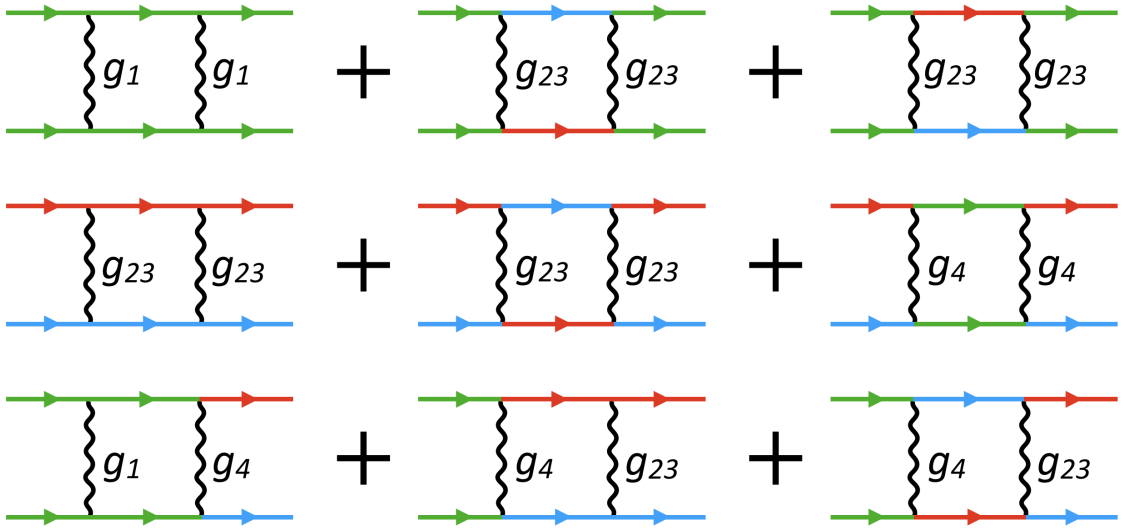

Figure 2.12: The diagrams for one loop corrections to SC interactions in RG. PDW flow is the same with $g \to h$ and momenta on each leg shifted by K or $-K$. Green, blue and red colors correspond to Γ, K and $-K$ pockets respectively.

$$\begin{aligned}
\dot{\tilde{g}}_1^{(\ell\mu)} &= -\tanh\frac{\beta\Lambda}{2}\left[\left(\tilde{g}_1^{(\ell\mu)}\right)^2 + 2\left(\tilde{g}_4^{(\ell\mu)}\right)^2\right] \\
\dot{\tilde{g}}_{23}^{(\ell\mu)} &= -\tanh\frac{\beta\Lambda}{2}\left[2\left(\tilde{g}_{23}^{(\ell\mu)}\right)^2 + \left(\tilde{g}_4^{(\ell\mu)}\right)^2\right] \\
\dot{\tilde{g}}_4^{(\ell\mu)} &= -\tanh\frac{\beta\Lambda}{2}(\tilde{g}_1^{(\ell\mu)} + 2\tilde{g}_{23}^{(\ell\mu)})\tilde{g}_4^{(\ell\mu)}
\end{aligned} \tag{2.116}$$

and

$$\begin{aligned}
\dot{\tilde{h}}_1^{(\ell\mu)} &= -\tanh\frac{\beta\Lambda}{2}\left[\left(\tilde{h}_1^{(\ell\mu)}\right)^2 + 2\left(\tilde{h}_4^{(\ell\mu)}\right)^2\right] \\
\dot{\tilde{h}}_{23}^{(\ell\mu)} &= -\tanh\frac{\beta\Lambda}{2}\left[2\left(\tilde{h}_{23}^{(\ell\mu)}\right)^2 + \left(\tilde{h}_4^{(\ell\mu)}\right)^2\right] \\
\dot{\tilde{h}}_4^{(\ell\mu)} &= -\tanh\frac{\beta\Lambda}{2}(\tilde{h}_1^{(\ell\mu)} + 2\tilde{h}_{23}^{(\ell\mu)})\tilde{h}_4^{(\ell\mu)}
\end{aligned} \tag{2.117}$$

The corresponding diagrams are shown in Figure 2.12. Notice that the SC and the PDW channels are mathematically the same and related by a total momentum shift of K, as are each of the $(\ell\mu)$ channels. It therefore suffices to solve the generic equation

$$\begin{aligned}
\dot{f}_1 &= -f_1^2 - 2f_4^2 \\
\dot{f}_{23} &= -2f_{23}^2 - f_4^2 \\
\dot{f}_4 &= -(f_1 + 2f_{23})\, f_4
\end{aligned} \tag{2.118}$$

Eq. (2.118) has a simple analytical solution, which we can obtain by switching to "cylindrical coordinates"

$$z = 2f_{23} + f_1 \qquad r\cos\theta = f_4 \qquad r\sin\theta = 2f_{23} - f_1 \tag{2.119}$$

The flow equation then becomes

$$\dot{z} = -\frac{z^2}{2} - \frac{r^2}{2}(1 + 7\cos^2\theta) \tag{2.120}$$

$$\dot{r} = -rz \tag{2.121}$$

$$\dot{\theta} = 0 \tag{2.122}$$

We see that one channel, parametrized by θ, is not renormalized. The reason for this will be more clear once we write down the vertex flow equation: there are only two independent order parameters

rather than three, but there is redundancy due to particle-hole symmetry (PHS). The other two channels are easy to decouple into

$$\dot{\gamma}_\pm = \gamma_\pm^2 \tag{2.123}$$

where

$$\gamma_\pm = -\frac{1}{2}\left(z \mp r\sqrt{1+7\cos^2\theta}\right) = \frac{-f_1 - 2f_{23} \pm \sqrt{(f_1-2f_{23})^2 + 8f_4^2}}{2} \tag{2.124}$$

Restoring the indices we thus conclude that the RG channels are

$$\gamma^{(\ell\mu\pm)} = -\frac{\tanh\frac{\beta\Lambda}{2}}{2}\left(\tilde{g}_1^{(\ell\mu)} + 2\tilde{g}_{23}^{(\ell\mu)} \mp \sqrt{\left(\tilde{g}_1^{(\ell\mu)} - 2\tilde{g}_{23}^{(\ell\mu)}\right)^2 + 8\left(\tilde{g}_4^{(\ell\mu)}\right)^2}\right) \tag{2.125}$$

for SC and

$$\kappa^{(\ell\mu\pm)} = -\frac{\tanh\frac{\beta\Lambda}{2}}{2}\left(\tilde{h}_1^{(\ell\mu)} + 2\tilde{h}_{23}^{(\ell\mu)} \mp \sqrt{\left(\tilde{h}_1^{(\ell\mu)} - 2\tilde{h}_{23}^{(\ell\mu)}\right)^2 + 8\left(\tilde{h}_4^{(\ell\mu)}\right)^2}\right) \tag{2.126}$$

for PDW. Note that $\gamma_+ > \gamma_-$, which means that $\gamma^{(\ell\mu+)}$ and $\kappa^{(\ell\mu+)}$ are always more relevant in the RG sense than $\gamma^{(\ell\mu-)}$ and $\kappa^{(\ell\mu-)}$ respectively, and we can therefore drop the latter. We then can drop the $\pm$ index and simply take $\gamma^{(\ell\mu+)} = \gamma^{(\ell\mu)}$ and $\kappa^{(\ell\mu+)} = \gamma^{(\ell\mu)}$. Since we did the calculation at finite temperature, we can also find the critical temperatures of the instabilities from Eq. (2.89):

$$T_c^{(\ell\mu;0)} \approx 1.13\Lambda e^{-1/\gamma_0^{(\ell\mu)}} \tag{2.127}$$

for SC and

$$T_c^{(\ell\mu;\pm 1)} \approx 1.13\Lambda e^{-1/\kappa_0^{(\ell\mu)}} \tag{2.128}$$

for PDW. The $(\ell\mu;\eta)$ indexing indicates the total pairing momentum is ηK; $\gamma_0^{(\ell\mu)}$ and $\kappa_0^{(\ell\mu)}$ are respectively the bare value of $\gamma^{(\ell\mu)}$ and $\kappa^{(\ell\mu)}$. Note that the same T_c is found in the mean-field analysis.

Having found the RG channels, we still want to know when they are relevant, i.e. when are $\gamma^{(\ell\mu\pm)} > 0$ ($\kappa^{(\ell\mu\pm)} > 0$) given the bare values of $\tilde{g}^{(\ell\mu)}$ ($\tilde{h}^{(\ell\mu)}$). For this purpose, it is helpful to interpret the equations for $\gamma^{(\ell\mu\pm)}$ (2.125) geometrically in the parameter space of $\tilde{g}_1^{(\ell\mu)}, \tilde{g}_{23}^{(\ell\mu)}$ and

$\tilde{g}_4^{(\ell\mu)}$ that defines the RG phase diagram shown in Figure 2.13. The yellow half-cone corresponds to $\gamma^{(\mu+)} = 0$: all parameter values inside it are RG irrelevant, while values outside it (e.g. on the cyan cone) are RG relevant (i.e. it is the separatrix). The arrows indicate the flow of the channels under RG; along the yellow cone they flow along straight lines towards the fixed point at the origin. The region outside the yellow cone thus represents the space of coupling constants leading to a Cooper pairing instability. Surfaces of constant $\gamma^{(\ell\mu+)}$ in this phase space correspond to cones like the cyan cone that share the symmetry axis of the yellow cone, shifted along that axis by $\gamma^{(\ell\mu+)}$ (which is thus the distance from the tip of the cone to the origin). The non-renormalized channel corresponds to the azimuthal angle about the symmetry axis of the cones. $\kappa^{(\ell\mu+)}$ has the same phase diagram in the space of $\tilde{h}_1^{(\ell\mu)}$, $\tilde{h}_{23}^{(\ell\mu)}$, and $\tilde{h}_4^{(\ell\mu)}$. To find which instability wins for a given set of bare coupling constants, we can plot the corresponding cones in the same figure, with the outermost cone thus corresponding to the leading instability.

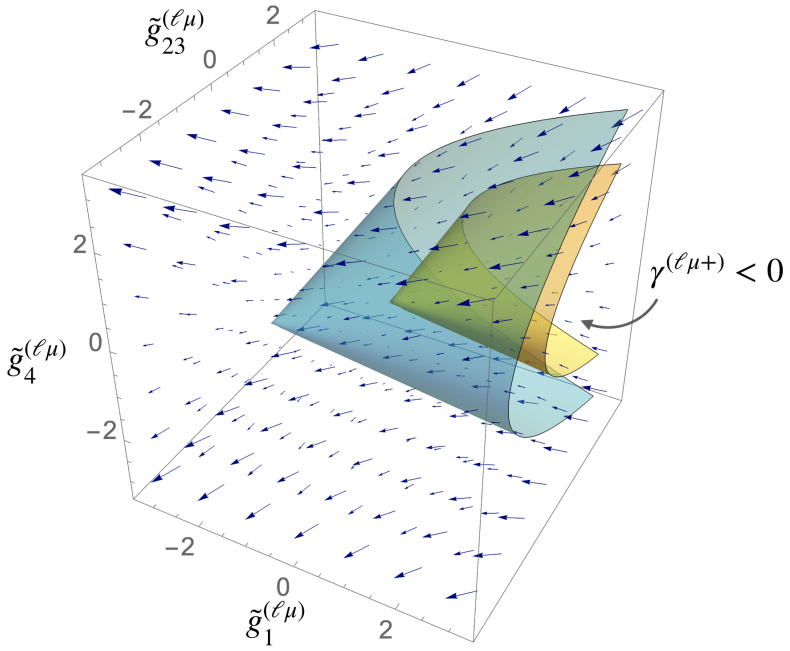

Figure 2.13: SC phase diagram in the parameter space of $\tilde{g}_1^{(\ell\mu)}, \tilde{g}_{23}^{(\ell\mu)}$ and $\tilde{g}_4^{(\ell\mu)}$ showing surfaces $\gamma^{(\ell\mu+)} = 0$ (yellow) and $\gamma^{(\ell\mu+)} > 0$ (cyan). The surfaces are half-cones with a common axis $\tilde{g}_1^{(\ell\mu)} = \tilde{g}_{23}^{(\ell\mu)}$, $\tilde{g}_4^{(\ell\mu)} = 0$ with the distance between the apex and the origin given by $\gamma^{(\ell\mu+)}$. The yellow cone therefore separates superconducting and normal phases. The arrows show the direction of the vector $\left(\dot{\tilde{g}}_1^{(\ell\mu)}, \dot{\tilde{g}}_{23}^{(\ell\mu)}, \dot{\tilde{g}}_4^{(\ell\mu)}\right)$ in (2.116) that show where the coupling constants flow under RG. PDW phase diagram is the same with $g \to h$, $\gamma \to \kappa$. Plotting all the cones for each $(\ell\mu)$ in the same figure, the outermost cone corresponds to the leading instability.

The condition for a given $\gamma^{(\ell\mu+)}$ to be positive is $\tilde{g}_1^{(\ell\mu)} < 0$ *or* $\tilde{g}_{23}^{(\ell\mu)} < 0$ *or* $\left(\tilde{g}_4^{(\ell\mu)}\right)^2 > \tilde{g}_1^{(\ell\mu)}\tilde{g}_{23}^{(\ell\mu)}$ (similarly for PDW). It is instructive to consider what this means for the SC instability with dominant momentum independent interactions. For the singlet $\mu = 0$, the first two conditions simply mean that the interactions are attractive either at the Γ pocket or between the $\pm K$ pockets, as could be the case with electron-phonon interactions. More interestingly, even if these interactions are repulsive, an instability remains possible if the pair hopping (of either sign) is sufficiently strong. This offers a possibility of an effective attraction from purely repulsive interactions, e.g. density-density interactions, similar to the $s^{\pm}$ scenario considered in [171, 65]. Importantly, this is a multi-band effect: a singlet instability from repulsive interactions is impossible in systems without a Γ pocket, for example (except via the Kohn-Luttinger mechanism, as considered in [67]).

For the triplet channels $\mu = j = x, y, z$ with momentum independent interactions at $T = 0$

$$\gamma^{(\ell j+)} = \frac{N_K}{2}\left(-(g_2 - g_3) + |g_2 - g_3|\right) \tag{2.129}$$

for $\ell = A_1'$ or E''. This is positive as long as $g_2 < g_3$. In particular, this can hold for purely repulsive interactions if the exchange interaction g_3 is stronger than g_2. In 2D g_3 (backscattering) is normally a two-loop effect, but in our case because of the structure of the Fermi surface (being disconnected between K and $-K$) backscattering can already be relevant at one-loop and result in a (f-wave) triplet instability. The same conclusion holds for systems without Γ pockets.

The same discussion holds for the PDW instabilities with $g \to h$, $\Gamma \to K \to -K \to \Gamma$. In particular, note that no SC instability can occur from repulsions in the absence of the K pockets. For PDW, we therefore conclude from the same reasoning that no instability from repulsion can occur without the Γ pocket. With the Γ pocket, the singlet instability is promoted by the Umklapp process h_4, while the interpocket exchange h_3 (which is also effectively a backscattering process) promotes the triplet instability.

2.2.3 RG Flow for Vertices and the Order Parameters

As discussed in the general presentation of the RG analysis, an instability in the interaction channels indicates a formation of bound states, in this case the SC or PDW condensate. A differnet approach to testing symmetry breaking phases in RG is to add vertices of the form

$$H_\Delta = \frac{1}{2}\sum_{\mathbf{p}\alpha\beta\eta\zeta}\left[\Delta_{\eta\zeta}(\mathbf{p})\right]_{\alpha\beta}\bar{d}_{\mathbf{p}\eta\alpha}\bar{d}_{-\mathbf{p}\zeta\beta} + h.c. \tag{2.130}$$

The same kind of anti-commutation analysis we did for interactions shows that after anti-symmetrizing, the gap functions satisfy

$$\Delta_{\eta\zeta}(\mathbf{p}) = -\Delta^T_{\zeta\eta}(-\mathbf{p}) \tag{2.131}$$

with the transpose in the spin indices. This is referred to as the particle hole symmetry (PHS) that encodes the redundancy due to the anti-commutation relations. We found in Eq. (2.103) that

$$\Delta_{\eta\zeta}(\mathbf{p}) = \sum_{\ell\mu} \Delta^{(\ell\mu)}_{\eta\zeta}(\mathbf{p}) = \sum_{\ell\mu} \Sigma^{(\ell\mu)}_{\eta\zeta}(\theta) D^{(\ell\mu)}_{\eta\zeta} \tag{2.132}$$

where $D^{(\ell\mu)}_{\eta\zeta}$ are complex numbers that flow under RG according to Eq. (2.104):

$$\dot{\tilde{D}}^{(\ell\mu)}_{\eta\zeta} = -\tanh\left[\frac{\beta\Lambda}{2}\right] \tilde{g}^{(\ell\mu)}_{\eta\zeta;\eta'\zeta'} \tilde{D}^{(\ell\mu)}_{\eta'\zeta'} \tag{2.133}$$

The basis functions $\Sigma^{(\ell\mu)}_{\eta\zeta}(\theta)$ determine the form of the gap function in the corresponding channel. The $\mu = 0$ terms are the singlet gap function components, while $\mu = j = x, y, z$ terms are the triplet components. The leading basis functions corresponding to momentum independent interactions and therefore momentum independent gap functions are given in Table 2.1. For completeness, Table 2.3 lists the leading form of the gap functions point in all irreps of D_{3h}. Note that PHS implies that $D^{(\ell\mu)}_{\eta\zeta} = D^{(\ell\mu)}_{\zeta\eta}$.

$\ell(D_{3h})$	$\Sigma^{(\ell 0)}_{\eta\eta} = \Theta^{(\ell 0)}_{\eta\eta}(\theta) i\sigma^y$	$\Sigma^{(\ell j)}_{\eta\eta} = \Theta^{(\ell j)}_{\eta\eta}(\theta)\sigma^j i\sigma^y$
$A_1^{'}$	$i\sigma^y$	$\cos 3\theta\ \sigma^z i\sigma^y$
$A_2^{'}$	$\sin 6\theta\ i\sigma^y$	$\sin 3\theta\ \sigma^z i\sigma^y$
$A_1^{''}$	$p_z \cos 3\theta\ i\sigma^y$	$p_z\sigma^z i\sigma^y$, $(\cos\theta\ \sigma^x + \sin\theta\ \sigma^y)\, i\sigma^y$
$A_2^{''}$	$p_z \sin 3\theta\ i\sigma^y$	$(\sin\theta\ \sigma^x - \cos\theta\ \sigma^y)\, i\sigma^y$
$E^{'}$	$\cos 2\theta i\sigma^y$, $\cos\theta\cos 3\theta\ i\sigma^y$ $\sin 2\theta i\sigma^y$, $\sin\theta\cos 3\theta\ i\sigma^y$	$\cos\theta\sigma^z i\sigma^y$ $\sin\theta\sigma^z i\sigma^y$
$E^{''}$	$p_z \cos\theta i\sigma^y$ $p_z \sin\theta i\sigma^y$	$\cos 3\theta\sigma^x i\sigma^y$, $(\cos\theta\sigma^x - \sin\theta\sigma^y)\, i\sigma^y$ $\cos 3\theta\sigma^y i\sigma^y$, $(\sin\theta\sigma^x + \cos\theta\sigma^y)\, i\sigma^y$

Table 2.3: Basis functions $\Sigma^{(\ell\mu)}_{\eta\eta}$ transforming according to listed irreps of D_{3h}. The basis functions $\Sigma^{(\ell\mu)}_{\eta\zeta}$ with $\eta \neq \zeta$ are the same except $\cos 3\theta \to \epsilon_{\eta\zeta}$, $\sin 6\theta = 2\sin 3\theta\epsilon_{\eta\zeta}$, etc., where $\epsilon_{\eta\zeta}$ is the Levi-Civita anti-symmetric symbol.

The gap functions are often themselves referred to as order parameters. Note that $\zeta = -\eta$ corresponds to pairs with zero total momentum, i.e. the SC state, while $\pm K + \zeta = \pm K - \eta$

corresponds to pairs with a total momentum $\pm 2K = \mp K$, i.e. the PDW state. We therefore define

$$\Delta_{\eta}^{(\ell\mu;\zeta)}(\mathbf{p}) = \Delta_{\eta,-\eta+2\zeta}^{(\ell\mu)}(\mathbf{p}) \tag{2.134}$$

with $(\ell\mu;\zeta)$ indicating pairing with total momentum $2\zeta K$, i.e. SC for $\zeta = 0$ and PDW for $\zeta = \pm 1$. Correspondingly, we define the $D_{\eta}^{(\ell\mu;\zeta)}$ order parameters. Due to momentum conservation, the $(\ell\mu;\zeta)$ channels decouple in the vertex flow equation for different ζ, as they did in the interaction flow. We can then express the flow equation as a matrix equation for the vector order parameter $\mathbf{D}^{(\ell\mu;\zeta)} = (D_K^{(\ell\mu;\zeta)}, D_\Gamma^{(\ell\mu;\zeta)}, D_{-K}^{(\ell\mu;\zeta)})^T$. For the SC channel,

$$\dot{\tilde{\mathbf{D}}}^{(\ell\mu;0)} = \frac{d}{dt}\begin{pmatrix} \tilde{D}_K^{(\ell\mu;0)} \\ \tilde{D}_\Gamma^{(\ell\mu;0)} \\ \tilde{D}_{-K}^{(\ell\mu;0)} \end{pmatrix} = -\tanh\left[\frac{\beta\Lambda}{2}\right]\begin{pmatrix} \tilde{g}_{23}^{(\ell\mu)} & \tilde{g}_4^{(\ell\mu)} & \tilde{g}_{23}^{(\ell\mu)} \\ \tilde{g}_4^{(\ell\mu)} & \tilde{g}_1^{(\ell\mu)} & \tilde{g}_4^{(\ell\mu)} \\ \tilde{g}_{23}^{(\ell\mu)} & \tilde{g}_4^{(\ell\mu)} & \tilde{g}_{23}^{(\ell\mu)} \end{pmatrix}\begin{pmatrix} \tilde{D}_K^{(\ell\mu;0)} \\ \tilde{D}_\Gamma^{(\ell\mu;0)} \\ \tilde{D}_{-K}^{(\ell\mu;0)} \end{pmatrix} \tag{2.135}$$

To find the RG channels in the vertex flow calculation we thus need to diagonalize the matrix in (2.135). One advantage over the interaction flow calculation is that matrix diagonalization is a linear problem and it is easier than solving a non-linear differential equation. In this case it is particularly simple because the matrix is clearly singular since the top and bottom rows are the same (as are left and right columns). We can easily see that this corresponds to a zero eigenvalue with eigenvector $(1, 0, -1)$, i.e. $D_\Gamma^{(\ell\mu;0)} = 0$ and $D_K^{(\ell\mu;0)} = -D_{-K}^{(\ell\mu;0)}$. But this is precisely ruled out by the PHS condition, i.e. this 'marginal' channel is just a result of a redundancy due to anti-commutation relations. This is precisely the marginal θ channel in (2.120), which we can now conclude must be marginal to all loops.

We can thus restrict our attention to $D_K^{(\ell\mu;0)} = D_{-K}^{(\ell\mu;0)}$, which reduces the RG flow to a system of two equations:

$$\frac{d}{dt}\begin{pmatrix} \tilde{D}_\Gamma^{(\ell\mu;0)} \\ \tilde{D}_K^{(\ell\mu;0)} \end{pmatrix} = -\tanh\left[\frac{\beta\Lambda}{2}\right]\begin{pmatrix} \tilde{g}_1^{(\ell\mu)} & 2\tilde{g}_4^{(\ell\mu)} \\ \tilde{g}_4^{(\ell\mu)} & 2\tilde{g}_{23}^{(\ell\mu)} \end{pmatrix}\begin{pmatrix} \tilde{D}_\Gamma^{(\ell\mu;0)} \\ \tilde{D}_K^{(\ell\mu;0)} \end{pmatrix} \tag{2.136}$$

The eigenvalues are

$$\gamma^{(\ell\mu\pm)} = -\frac{\tanh\frac{\beta\Lambda}{2}}{2}\left(\tilde{g}_1^{(\ell\mu)} + 2\tilde{g}_{23}^{(\ell\mu)} \mp \sqrt{\left(\tilde{g}_1^{(\ell\mu)} - 2\tilde{g}_{23}^{(\ell\mu)}\right)^2 + 8\left(\tilde{g}_4^{(\ell\mu)}\right)^2}\right) \tag{2.137}$$

i.e. precisely the other two SC channels (2.125), of which $\gamma^{(\ell\mu+)}$ is the largest. Similarly, we find

the PDW order parameter flows by taking $g \to h$ and $\Gamma \to K$:

$$\frac{d}{dt}\begin{pmatrix} \tilde{D}_K^{(\ell\mu;\pm 1)} \\ \tilde{D}_\Gamma^{(\ell\mu;\pm 1)} \end{pmatrix} = -\tanh\left[\frac{\beta\Lambda}{2}\right]\begin{pmatrix} \tilde{h}_1^{(\ell\mu)} & 2\tilde{h}_4^{(\ell\mu)} \\ \tilde{h}_4^{(\ell\mu)} & 2\tilde{h}_{23}^{(\ell\mu)} \end{pmatrix}\begin{pmatrix} \tilde{D}_K^{(\ell\mu;\pm 1)} \\ \tilde{D}_\Gamma^{(\ell\mu;\pm 1)} \end{pmatrix} \tag{2.138}$$

with eigenvalues

$$\kappa^{(\ell\mu\pm)} = -\frac{\tanh\frac{\beta\Lambda}{2}}{2}\left(\tilde{h}_1^{(\ell\mu)} + 2\tilde{h}_{23}^{(\ell\mu)} \mp \sqrt{\left(\tilde{h}_1^{(\ell\mu)} - 2\tilde{h}_{23}^{(\ell\mu)}\right)^2 + 8\left(\tilde{h}_4^{(\ell\mu)}\right)^2}\right), \tag{2.139}$$

again precisely the PDW channels (2.126). As before, we keep only the dominant solution and drop the $\pm$ index (so $\gamma^{(\ell\mu)}$ is understood to be $\gamma^{(\ell\mu+)}$).

The chief advantage of looking at the vertex flow is that we also get the form of the gap function and the order parameters. In particular, we also have the eigenvectors (removing the DOS rescaling)

$$\begin{pmatrix} D_\Gamma^{(\ell\mu;0)} \\ D_K^{(\ell\mu;0)} \end{pmatrix} \propto \begin{pmatrix} \gamma^{(\ell\mu)} + 2\tilde{g}_{23}^{(\ell\mu)} \\ -\tilde{g}_4^{(\ell\mu)}\sqrt{\frac{N_\Gamma}{N_K}} \end{pmatrix} = \begin{pmatrix} \gamma^{(\ell\mu)} + 2N_K g_{23}^{(\ell\mu)} \\ -N_\Gamma g_4^{(\ell\mu)} \end{pmatrix} \tag{2.140}$$

For example, we learn immediately how the singlet instability can occur from repulsive interactions when all coupling constants are positive: in that case the order parameter changes sign between $D_\Gamma^{(\ell\mu;0)}$ and $D_K^{(\ell\mu;0)}$. This confirms that the singlet state realized by momentum independent interactions is essentially the $s^\pm$ state [171, 65]. Similarly, for the PDW channels we have

$$\begin{pmatrix} D_K^{(\ell\mu;\pm 1)} \\ D_\Gamma^{(\ell\mu;\pm 1)} \end{pmatrix} \propto \begin{pmatrix} \kappa^{(\ell\mu)} + 2\tilde{h}_{23}^{(\ell\mu)} \\ -\tilde{h}_4^{(\ell\mu)}\sqrt{\frac{N_\Gamma + N_K}{2N_\Gamma}} \end{pmatrix} \tag{2.141}$$

and we can make similar conclusions. Note that at this level of analysis, the two PDW are degenerate, i.e. both instabilities happen simultaneously. In general this will not be the case if we include subleading (non-logarithmic) corrections, which leads to possible further symmetry breaking. We analyze this in more detail in Chapter 5.

The actual form of the gap functions is determined by the basis functions $\Sigma_{\eta\zeta}^{(\ell\mu)}(\theta)$, and in particular we find that the momentum-independent pairing interactions lead to either the usual momentum-independent s-wave singlet type of superconductivity or an A_1' or E'' f-wave triplets. For the latter, we can gain some insight into why it is possible by considering the form of the leading order parameter in the SC case (the PDW case is similar). In particular, consulting with Table 2.1,

the gap function is

$$\Delta_{\eta,-\eta} = \epsilon_{\eta,-\eta}\sigma^j i\sigma^y \tag{2.142}$$

where ϵ is the Levi-Civita symbol. The gap is thus non-vanishing only for $\eta = \pm K$. Note that it is important that there are *two* gaps forming the order parameter: $\Delta_{K,-K}$ and $\Delta_{-K,K}$. The triplet is possible because they can have a relative sign between them. Although this is different from the $s^{\pm}$ phase, the principle is similar: to make the wave function anti-symmetric, a sign needs to change somewhere, and here we have an extra degree of freedom to anti-symmetrize in the 'valley' index η. Recently it was suggested that spin fluctuation may be strong in 1H-$NbSe_2$ and that they can promote triplet pairing [184].

If we try to expand the gap function at the K pockets in the triplet phase to the whole Brillouin zone,

$$[\Delta_{\eta,-\eta}(\mathbf{p})]_{\alpha\beta}\, \bar{d}_{\mathbf{p}\eta\alpha}\bar{d}_{-\mathbf{p}-\eta\beta} \to \Delta_{\alpha\beta}(\mathbf{P})\bar{d}_{\mathbf{P}\alpha}\bar{d}_{-\mathbf{P}\beta} \tag{2.143}$$

with $\mathbf{P} = \mathbf{p} + \eta\mathbf{K}$, we would conclude that $\Delta_{\alpha\beta}(\mathbf{P}) \propto \cos 3\theta$ with θ measured from the Γ point. The corresponding subleading gap function in the triplet phase is thus f-wave, at least for the A_1'; for E'', p-wave components are also possible. Note that since orbital angular momentum is not conserved, different (same) l's can belong to the same (different) irreps of D_{6h} (or D_{3h}). In particular, both p- and f-wave E'' gaps belong to the E_{2u} irrep of D_{6h}.

This concludes our (parquet) RG analysis of 1H-TMDs. We could of course go on to include SOC in the analysis, which induces mixing between singlet and triplet gaps that do not belong to the same irreps, but as mentioned above we will use a mean-field approach to study such mixing in Chapter 4. The fact that singlet and triplet states can mix and that we found in the RG analysis that the triplet gap components can be large means that the resulting superconducting state can be robust against strong in-plane magnetic fields due to the absence of Pauli limiting in that case. It then becomes interesting to study the superconducting phase in the presence of the magnetic field. Finally, the fact that the E'' irrep can be relevant in RG means there is a possibility of additional symmetry breaking, as we will see.

Chapter 3

Symmetry Protected Topological Phases

In this chapter we will consider several examples of topological phases and their topological invariants that will be relevant to the uniform and non-uniform superconducting (SC) phases we will find in 1H-TMDs. We will only consider single body Hamiltonians for which topological invariants are easy to compute and have been classified in various situation (see [30] for a good review).[1] The fundamental object of our study will therefore be the two-level spin-1/2 single-body ('second-quantized') Hamiltonian (in momentum space, with periodic boundary conditions assumed most of the time):

$$H = \mathcal{H}_{\alpha\beta}(\mathbf{p})\bar{d}_{\mathbf{p}\alpha}d_{\mathbf{p}\beta} \equiv \psi^\dagger_{\mathbf{p}}\mathcal{H}(\mathbf{p})\psi_{\mathbf{p}} \tag{3.1}$$

with $\alpha, \beta = \pm 1$ for spin up and down respectively and with spinor $\psi_{\mathbf{p}} = (d_{\mathbf{p}\uparrow}, d_{\mathbf{p}\downarrow})^T$. We will also refer to the 2×2 matrix $\mathcal{H}$ as the Hamiltonian, or the (first-quantized) Hamiltonian matrix when the distinction is important. It can be written very generally as

$$\mathcal{H}(\mathbf{p}) = \beta_\mu(\mathbf{p})\sigma^\mu = \beta_0 + \boldsymbol{\beta}\cdot\boldsymbol{\sigma} \tag{3.2}$$

(to conform with the notation in the rest of the thesis). It turns out that topological invariants for systems with more than two bands (labeled $\alpha = 1, 2, 3, \ldots$) can be computed by considering pairs of bands at a time, so the results we obtain for the two-level system generalize straightforwardly.

[1] Note that the two-point Green's function contains the same information as the single body Hamiltonian, and there are formulas for the invariants in terms of Green's functions that we do not present here. In principle higher-order correlation functions can also have non-trivial topology, and more generally topological invariants can be defined using the many-body wave-function directly, which requires a new classification [159].

As both a warm-up and a way to introduce the notion of topology of a wave-function, we will first consider a 1D two-level system with mirror symmetry in Section 3.1. The key concept will turn out to be the Berry connection that encodes the topology of the eigenstates of the Hamiltonian in a given energy band and which we can use to compute all topological invariants as integrals of the Berry connection over loops (the Berry phases) and surfaces (the Berry curvature flux). In 2D, the former yield winding numbers that characterize nodal phases that we discuss in Section 3.2, while the latter yield Chern numbers that characterize fully gapped phases, discussed in Section 3.3. The latter is the topological invariant that leads to the quantum hall effect (QHE), which is the only topological phase that is defined in 2D in the absence of symmetry.

The presence of symmetry can both trivialize topological invariants and lead to new ones. This is exemplified by the quantum spin hall effect and topological insulators, where the symmetries are spin rotation (about the out-of-plane axis) and time reversal (TRS), respectively. Both of these symmetry imply that the total Chern number vanishes (as we will confirm for TRS below). However, they also partition the Hilbert space into two parts (in spin or momentum respectively), that allow us to compute an invariant for that subset, resulting in a $\mathbb{Z}_2$ valued index. In Section 3.4 we present a derivation of this index that elucidates its meaning extending a derivation of the Chern number due to Simon [161]. Though the final formula is well-known, I include this derivation as I am not aware of it appearing elsewhere.

The $\mathbb{Z}_2$ index is an example of a topological invariant that is quantized due to a symmetry, and phases characterized by such invariants are known as symmetry protected topological phases (SPTs). The best known class of such phases are those protected by combinations of TRS T, particle-hole symmetry (PHS) C, and their product, the chiral symmetry $S = TC$ (sometimes also called sub-lattice symmetry or SLS). The QHE can be considered as a special case when none of T, C, or S symmetries hold. The first two symmetries are anti-unitary, e.g. $TiT^{-1} = -i$, so the chiral symmetry is unitary, and all act on the (second-quantized) Hamiltonian H by conjugation, e.g. THT^{-1}, as they do on all operators including creation and annihilation operators.

For the creation/annihilation operators, it is more convenient (and conventional) to write the action of the symmetries on the spinors as (mimicking the action of the symmetries on the state vectors)

$$\begin{aligned} T\psi_{\mathbf{p}}T^{-1} &= \mathcal{T}\psi_{-\mathbf{p}} \\ C\psi_{\mathbf{p}}C^{-1} &= \mathcal{C}\psi_{-\mathbf{p}} \\ S\psi_{\mathbf{p}}S^{-1} &= \mathcal{S}\psi_{\mathbf{p}} \end{aligned} \tag{3.3}$$

where $\mathcal{T}, \mathcal{C}, \mathcal{S}$ are matrices in the spinor indices; note that they do not include momentum reversal. When the symmetries are satisfied by the total second-quantized Hamiltonian, the first-quantized Hamiltonian matrix then satisfies

$$\begin{aligned} \mathcal{T}\mathcal{H}(\mathbf{p})\mathcal{T}^{-1} &= \mathcal{H}(-\mathbf{p}) \\ \mathcal{C}\mathcal{H}(\mathbf{p})\mathcal{C}^{-1} &= -\mathcal{H}(-\mathbf{p}) \\ \mathcal{S}\mathcal{H}(\mathbf{p})\mathcal{S}^{-1} &= -\mathcal{H}(\mathbf{p}) \end{aligned} \tag{3.4}$$

Typically for spin 1/2, $\mathcal{T} = i\sigma^y\mathcal{K}$ where $\mathcal{K}$ is complex conjugation. More generally, any symmetry under which the Hamiltonian satisfies the first or second of these relations is called TR-like or PH-like respectively. From these relations it follows that in general $T^2 = \pm 1$ and $C^2 = \pm 1$ while $S^2 = 1$ (when the symmetries hold), which results in ten possible cases (nine for all possible combinations of TRS and PHS cases, plus one case when chiral symmetry alone holds). The topological invariants for fully gapped phases in all ten cases in any dimension have been classified under the so-called 10-fold way classification [10, 132, 99]. In addition, gapless (including nodal) phases can be classified under the same framework, as done in [105, 197].

There are of course other symmetries that a system may have, such as crystalline symmetries like mirror symmetries and rotations. The classification has recently been extended to include some of these for both fully gapped [29, 38] and gapless phases [28, 158, 167]. The resulting phases are called *crystalline* SPTs, to distinguish them from non-crystalline phases. As we will see in Chapter 4 and Chapter 5, some of the topological phases of 1H-TMDs are protected by mirror symmetries, which is thus of main interest to us. Here we will take the mirror plane to be in the xy plane, and denote the symmetry as M_z (acting in 2D and 1D by restricting dimensions; in 1D it acts in the same way as inversion, i.e. $p \to -p$). This acts on the spinors as

$$M_z \psi_{\mathbf{p}} M_z^{-1} = \mathcal{M}_z \psi_{\bar{\mathbf{p}}} \tag{3.5}$$

where $\bar{\mathbf{p}} = (p_x, p_y, -p_z)$ is the reflection of $\mathbf{p} = (p_x, p_y, p_z)$. For spin, we have $\mathcal{M}_z = i\sigma^z$ (the factor of i is conventional): in general the spin components perpendicular to the mirror plane remain fixed while the parallel components are inverted under reflection (see Figure 3.1). If mirror symmetry holds, then the first-quantized Hamiltonian satisfies

$$\mathcal{M}_z \mathcal{H}(\mathbf{p}) \mathcal{M}_z^{-1} = \mathcal{H}(\bar{\mathbf{p}}) \tag{3.6}$$

We will now consider the consequences of this symmetry (as well as the anti-unitary ones) on the topology of a two-state system, and see how some of the topological invariants come about.

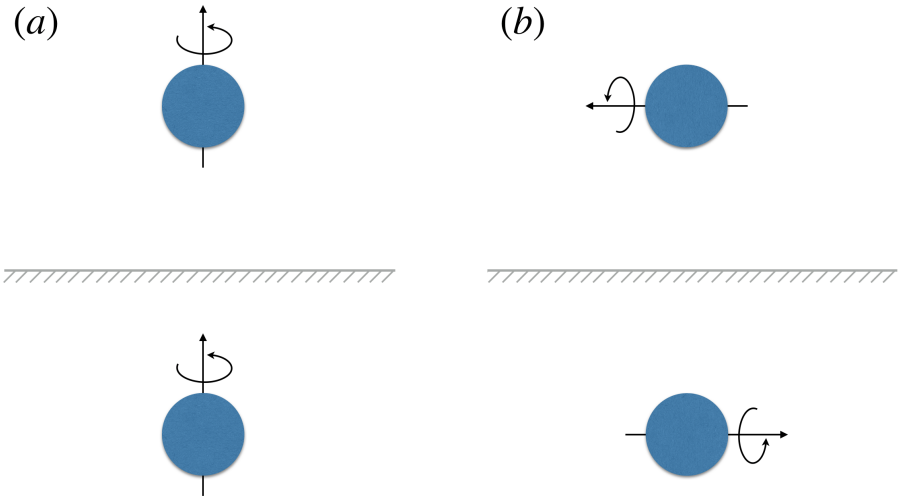

Figure 3.1: Action of mirror symmetry on spin (illustrated as rotating spheres) oriented perpendicular (a) and parallel (b) to the reflection plane, shown in gray.

3.1 1D System with Mirror/Inversion Symmetry

Topological properties of the Hamiltonian (3.2) are perhaps most clearly seen in 1D for a system with mirror symmetry taking $p \to -p$. This case is mathematically equivalent to inversion, with spin up/down corresponding to states even and odd under inversion respectively (we will take $\mathcal{M}_z = i\sigma^z$ when acting on spin), which was studied in detail in [89, 12] and as a special case in [69]. In particular, Eq. (3.6) becomes simply

$$\mathcal{M}_z \mathcal{H}(-p) \mathcal{M}_z^{-1} = \mathcal{H}(p) = \beta_0(p) + \boldsymbol{\beta}(p) \cdot \boldsymbol{\sigma} \tag{3.7}$$

which means that $\beta_{x/y}(p)$ are odd functions and $\beta_{0/z}(p)$ are even functions in (3.2). Importantly, (3.7) means that the mirror symmetry commutes with $\mathcal{H}(p)$ when $p = -p$, i.e. if $p = 0$ or $\pi = -\pi$ (for periodic boundary conditions). This means that we can simultaneously diagonalize $\mathcal{H}$ and $\mathcal{M}_z$ at those points and characterize the eigenstates of the Hamiltonian as either mirror even or mirror odd, i.e. with $\mathcal{M}_z$ acting as $\pm i$ on the state (again, only at those points). This means the spins point up or down at these momenta. This allows us to define integers $n_0^{\pm}$ and $n_\pi^{\pm}$ which count the number of occupied mirror even/odd states (spins up/down) at $p = 0$ and π respectively, respectively. The

topological invariant in this case is then defined as $N_{M\mathbb{Z}} = |n_0^+ - n_\pi^+| = |n_0^- - n_\pi^-|$ (equal since we assume the total number of occupied states is equal at all momenta), i.e. the difference between the number of mirror even and mirror odd states between $p = 0$ and $p = \pi$.

We want to verify both claims, i.e. that this is an invariant, and that it is topological. The invariance follows from the fact that we cannot continuously change the number of occupied mirror even/odd states without closing the gap: in order to change the parity under reflection of a state at $p = 0$, for example, we need to flip the spin from down to up or vice-versa; but since the spin at $p = 0$ is fixed by the mirror symmetry, the only way to do that continuously is to bring down another state with the opposite spin, make the two states degenerate, and 'exchange' the spins between the two states (see Figure 3.2). A topological phase transition thus occurs when the two states become degenerate.

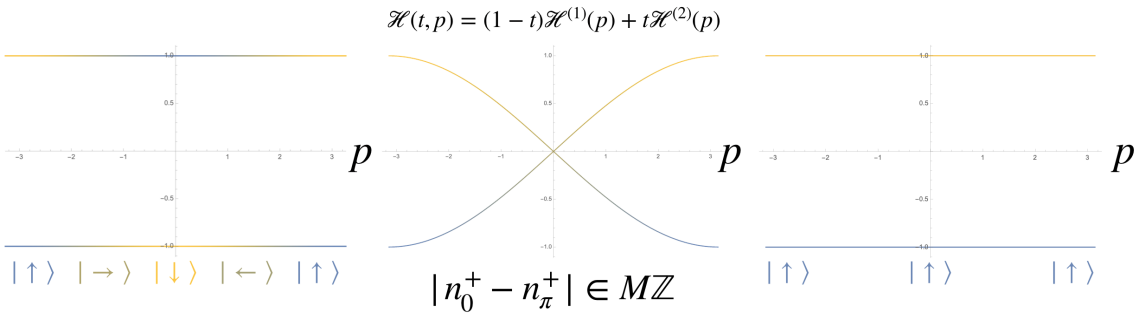

Figure 3.2: Spectrum of two topologically distinct mirror symmetric two-state Hamiltonians $\mathcal{H}_1$ (left) and $\mathcal{H}_2$ (right) with identical spectrum, and a homotopy between them at the critical point corresponding to a topological phase transition at which the bands cross. Spin texture of the eigenstate is indicated in color (blue for up and yellow for down). Note that the spins at $p = 0$ and $\pi = -\pi$ have to point up or down due to the mirror symmetry.

To see why the phase transition is topological, let us consider two concrete examples of $\mathcal{H}$,

$$\mathcal{H}_1(p) = \sigma^z \cos p + \sigma^x \sin p = \begin{pmatrix} \cos p & \sin p \\ \sin p & -\cos p \end{pmatrix} \tag{3.8}$$

and

$$\mathcal{H}_2(p) = -\sigma^z \tag{3.9}$$

(note that $\mathcal{H}_1$ happens to correspond to the Kitaev chain in momentum space [81], which is because it also satisfies PHS with $\mathcal{C} = \sigma^x\mathcal{K}$). Note that the two Hamiltonians have the same spectra, ± 1,

but the eigenspinors are different. In particular, $\mathcal{H}_2$ has eigenspinors $|u^2_\pm\rangle = (1,0)^T$ and $(0,1)^T$, while the eigenspinors for $\mathcal{H}_1$ are

$$|u^1_+\rangle = \begin{pmatrix} \cos\frac{p}{2} \\ \sin\frac{p}{2} \end{pmatrix} \qquad |u^1_-\rangle = \begin{pmatrix} \sin\frac{p}{2} \\ -\cos\frac{p}{2} \end{pmatrix} \tag{3.10}$$

The spectra and the corresponding spin texture indicated in colors are shown in Figure 3.2. The main thing to notice about $|u^1_\pm\rangle$ is that they are discontinuous at the edge of the Brillouin zone $p = \pm\pi$: going along p, the spin rotates by 2π and therefore picks up a phase of -1. To see this more clearly we can plot $|u^1_-\rangle$ and $|u^2_-\rangle$ in the spinor Hilbert spaces $\{|\uparrow\rangle, |\downarrow\rangle\}$ as a function of p (we can do this here since the eigenvectors are real), as shown in Figure 3.3. Note that the horizontal and vertical axes correspond to spin up and down states respectively, and the arrows represent the spinor orientation in Hilbert space and not the spin orientation in real space. From Figure 3.3, we see that $|u^1_-\rangle$ thus parametrizes a Möbius strip in the Hilbert space, whose defining property is precisely that a vector pointing from 'one' edge to the 'other' flips when parallel transported around the middle circle. The fact that $\mathcal{H}_1$ and $\mathcal{H}_2$ cannot be continuously mapped into each other is a consequence of the fact that $|u^1_-\rangle$ is twisted, and for the same reason a Möbius strip cannot be continuously mapped to a cylinder without being cut. Note the role of symmetry: if it were not there, we could 'untwist' the Möbius strip by rotating the spin at $p = \pi$, but we are forbidden to do so when it is present.

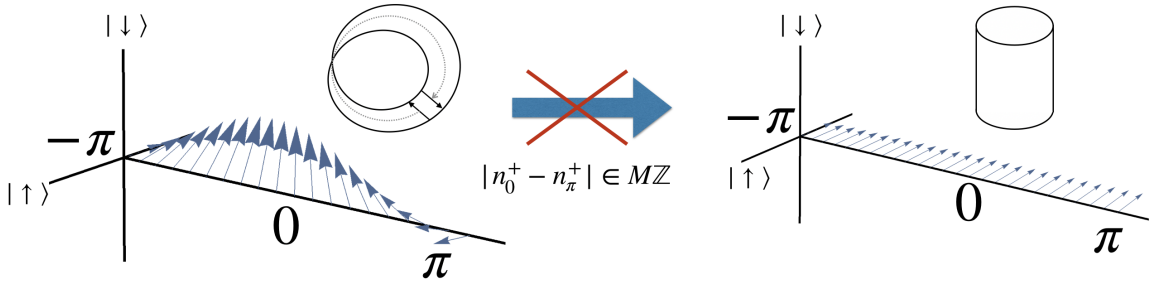

Figure 3.3: Lowest energy eigenstates $|u^1_-\rangle$ (left) and $|u^2_-\rangle$ (right) shown in spinor Hilbert spaces. $|u^1_-\rangle$ can be seen to parametrize a Möbius strip, which is characterized by vectors changing sign when parallel transported around the strip once (i.e. the strip is non-orientable). $|u^2_-\rangle$, on the other hand, parametrizes a cylinder. Note again that the arrows have to align with the axes at $p = 0, \pm\pi$ due to the mirror symmetry.

The topology is thus encoded in the fact that for the twisted eigenstate $\langle u_-(-\pi)|u_-(\pi)\rangle = -1$, where $|u_-(\pi)\rangle$ is the parallel transport of $|u_-(-\pi)\rangle$ (i.e. this is the Wilson loop around the 1D Brillouin zone). We can in fact always make the eigenstates of $\mathcal{H}_1$ continuous by performing a

(momentum-independent) unitary transformation:

$$|\tilde{u}^1_\pm\rangle = U|u^1_\pm\rangle = \frac{1}{\sqrt{2}}\begin{pmatrix} 1 & i \\ 1 & -i \end{pmatrix}|u^1_\pm\rangle \to \frac{1}{\sqrt{2}}\begin{pmatrix} e^{\pm ip} \\ \pm 1 \end{pmatrix} \tag{3.11}$$

The fact that the eigenstate is twisted is now encoded in the phase winding of the relative phase between the spin up and down components. This winding can be computed as a Berry phase, i.e. an integral of the Berry 'connection' [14]:

$$A^{(\pm)}(p) = i\,\langle\tilde{u}_\pm(p)|\,\nabla_p\,|\tilde{u}_\pm(p)\rangle \tag{3.12}$$

where note that the factor of i makes it real, since we are assuming normalized eigenstates.[2] We then have

$$\int_{-\pi}^{\pi} A^{(-)}(p)dp = -i\log\langle\tilde{u}_-(-\pi)|\tilde{u}_-(\pi)\rangle \tag{3.13}$$

For $|\tilde{u}^1_-\rangle$, we have $A^{(-)}(p) = \frac{1}{2}$, so the integral is simply π, and under the parallel transport we have $\langle\tilde{u}_-(-\pi)|\tilde{u}_-(\pi)\rangle = e^{i\pi} = -1$. Note that the Berry phase for $|\tilde{u}^1_+\rangle$ is opposite, reflecting the fact that the sum of Berry phases over all bands always vanishes, so a two-level system can only be topological at half-filling. In a system with more than two bands the topological invariant is similarly defined as a sum of the Berry phases over all occupied bands. Note that the continuity of the eigenstate is necessary when using (3.13).

We mentioned above that the only way to map continuously from $\mathcal{H}_1$ to $\mathcal{H}_2$ is to close the gap at some point. The simplest such map is

$$\mathcal{H}(z,p) = (1-z)\mathcal{H}_1(p) + z\mathcal{H}_2(p) \tag{3.14}$$

with some arbitrary parameter $z \in [0,1]$, which we show in Figure 3.4. As shown in the middle panel in Figure 3.2, the gap closes at $z = 1/2$, at which point the Berry phases changes discontinuously. In general, two Hamiltonians are topologically equivalent only if they can be adiabatically transformed into each other, i.e. if the map (3.14) has a continuous Berry connection for each band (the technical mathematical term for such a map is a homotopy, and it defines an equivalence between functions, in this case functions of p). Note that we have to make sure that $\mathcal{H}(z,p)$ respects the mirror symmetry

[2] More generally in any dimension, $\nabla\langle\tilde{u}_\pm(\mathbf{p})|\tilde{u}_\pm(\mathbf{p})\rangle = \nabla(1) = 0 = \langle\nabla\tilde{u}_\pm(\mathbf{p})|\tilde{u}_\pm(\mathbf{p})\rangle + \langle\tilde{u}_\pm(\mathbf{p})|\nabla\tilde{u}_\pm(\mathbf{p})\rangle = \langle\tilde{u}_\pm(\mathbf{p})|\nabla\tilde{u}_\pm(\mathbf{p})\rangle^* + \langle\tilde{u}_\pm(\mathbf{p})|\nabla\tilde{u}_\pm(\mathbf{p})\rangle = 2\,\mathrm{Re}[\langle\tilde{u}_\pm(\mathbf{p})|\nabla|\tilde{u}_\pm(\mathbf{p})\rangle] = -2\,\mathrm{Im}[\mathbf{A}^{(\pm)}]$.

for any fixed value of z: otherwise the Berry phase is not quantized since we can then rotate the spin at $p = 0$ or $\pm\pi$ off of the z axis.

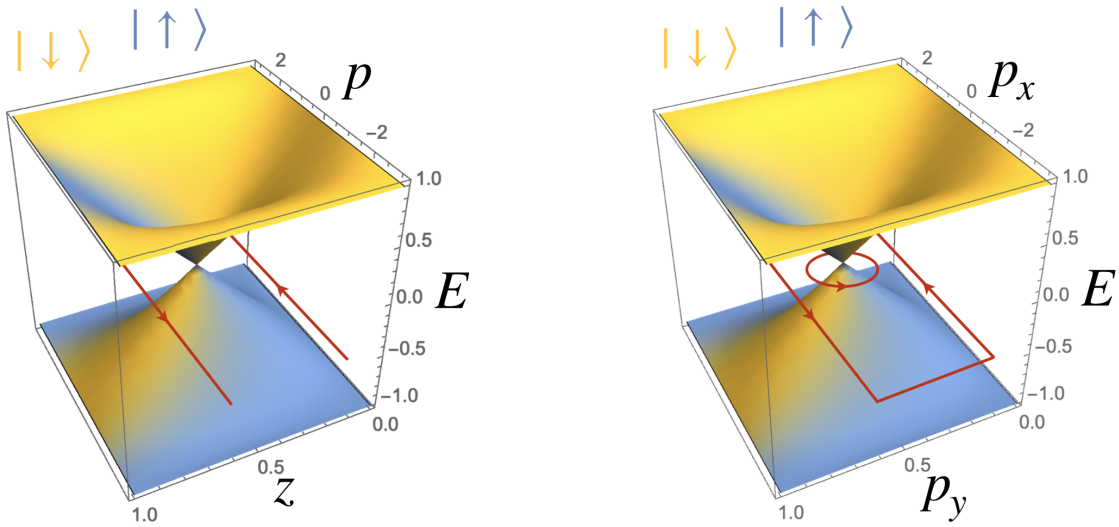

$\mathcal{H}(z,p) = (1-z)\mathcal{H}^{(1)}(p) + z\mathcal{H}^{(2)}(p)$ $\quad$ $\mathcal{H}(p_x,p_y) = (1-p_y)\mathcal{H}^{(1)}(p_x) + p_y\mathcal{H}^{(2)}(p_x)$

Figure 3.4: Energy spectrum of the homotopy $\mathcal{H}(z,p)$ for all values of z with spin texture shown in color (blue for up, yellow for down), which can be thought of as a Hamiltonian of a nodal topological phase in 2D (shown on right). Red lines indicate contours along which the Berry phases are computed: on the left, the left contour has a Berry phase of π, while the right contour has a trivial Berry phase. The two contours can be connected as shown in the right figure since the additional contours have canceling phases, and then deformed into a small loop around the node that therefore carries a Berry phase of π.

Importantly, from a mathematical point of view it does not matter what the parameter z is physically. Typically it is an external parameter like pressure or temperature. Intuitively, one can also consider z as parametrizing a family of Hamiltonians that change in space, describgin a system with an edge between two topologically distinct phases, with an 'end mode' at $z = 1/2$ at which the system becomes gapless. Since p and z are not commuting variable in quantum mechanics,[3] this is only a loose analogy, but the conclusion happens to be correct quite generally: topological systems are generally characterized by end modes, which is known as the bulk-boundary correspondence.

Note that $\mathcal{H}_1$ also happens to be an example of a Kitaev chain Hamiltonian, as we noted above. As shown in [81], the Kitaev chain explicitly harbors Majorana zero modes at its end-points, protected by PHS. We therefore know that $\mathcal{H}_1$ exhibits the same kind of end modes. Unlike in the Kitaev

[3]Here this is a problem because momentum is not conserved due to the edge breaking translational invariance. If the Hamiltonian varies slowly, however, it is approximately conserved over short distances, and the quasiclassical (aka the Wentzel-Kramers-Brillouin) approximation can be used.

chain case, however, mirror symmetry (unlike PHS) allows a constant term in the Hamiltonian, which means that the energy can always be shifted by any value. The mirror protected topological phase thus does not have zero energy modes in general, though it does have end modes. These modes are therefore fragile in the sense that they can be moved out of the gap and into the bulk spectrum, but as noted in [69] it will leave a signature in the entanglement spectrum.

3.2 2D (Crystalline) Nodal Topological Phases

We can use $\mathcal{H}(z,p)$ in (3.14) to now make the jump from 1D to 2D: mathematically, the arbitrary parameter z can also be a second momentum perpendicular to p. We can then relabel $p \to p_x$ and $z \to p_y$. The topological phase transition then corresponds to a node in the spectrum of the 2D Hamiltonian $\mathcal{H}(z,p) \to \mathcal{H}(p_x,p_y)$. See Figure 3.4; note that the Berry phases evaluated along the two lines in the left panel differ by π, but the sum of the phases is equal to the Berry phase evaluated along the square loop in the right subfigures since the phases along additional paths cancel due to periodic boundary conditions. That loop can then be deformed to the smaller one encircling the loop with the Berry phase being unchanged (because the Berry phase vanishes for any loop not encircling the node). This is a characteristic of 2D nodal phases: the Berry phase going around a node is quantized, with the node acting as a source of the phase. This translates to the statement that the node cannot be gapped out by any symmetry allowed terms. The reverse is also true: if a node is symmetry protected, the Berry phase is quantized. One possible approach to proving that a given nodal phase is topological is therefore to prove that no symmetry allowed terms can gap out a node, which is the approach we adopt in Section 4.4.2. This is also the approach used to classify gapless phases, as done for example in [28] for crystalline phases. A more formal approach that can be shown to give equivalent results is to use K theory, as done for example in [158].

Doing the inverse Fourier transform for p_x, we obtain a family of 1D systems $\mathcal{H}_{p_y}(x)$, which as we saw are topologically distinct for $p_y < 1/2$ and $p_y > 1/2$. This means that $\mathcal{H}_{p_y}(x)$ will have end modes are is boundaries for $p_y < 1/2$. The union of these end modes taken together thus forms an edge mode of the 2D system, terminating at the node at $p_y = 1/2$. This can also be seen by a direct computation in an effective $\mathbf{k}\cdot\mathbf{p}$ model in the continuum limit [185, 60]. For the anti-unitary symmetries, the resulting modes are moreover flat since the 1D edge modes are zero energy modes, and the edge modes are referred to as flat bands [151, 145, 19, 152, 150]; for a crystalline symmetry, as we saw, the energy is not pinned to zero, so the edge modes are not flat in general (as seen in 3D 'drumhead' surface states [23, 15], and in some 2D examples in [28]). The nodes themselves are

moreover not fixed to zero energy, and as a result can be 'inflated' into Fermi surfaces: importantly, it is only the minimal dimension of the gapless manifold (i.e. the co-dimension of the manifold that cuts it out of the Brillouin zone) that enters the classification in [28, 158].

3.3 Fully Gapped 2D Topological Phases

When the spectrum in 2D is fully gapped, we can introduce another quantity using the Berry connection, namely the Chern number. The Berry vector potential extends to higher dimensions (and for an arbitrary number of bands labeled with $\alpha = 1, 2, \ldots$) as

$$\mathbf{A}^{(\alpha)}(\mathbf{p}) = i\langle u_\alpha(\mathbf{p})|\nabla|u_\alpha(\mathbf{p})\rangle \tag{3.15}$$

where differentiation is with respect to momentum (for which we can pick a basis $\{\mathbf{e}_j\}$, denoting the corresponding directional derivative ∇_j). In two and higher dimensions we can then define the Berry curvature as

$$F^{(\alpha)}_{jk}(\mathbf{p}) = \nabla_j A^{(\alpha)}_k - \nabla_k A^{(\alpha)}_j \tag{3.16}$$

which can be arranged into a curvature vector:

$$\mathbf{F}^{(\alpha)}(\mathbf{p}) = \nabla \times \mathbf{A}^{(\alpha)}(\mathbf{p}) \tag{3.17}$$

in analogy with the magnetic field. Note that when restricted to 2D, this only has a z component, which we call $F^{(\alpha)}$ (not to be confused with the magnitude of the vector). The Chern number for band α is then defined as the flux of the corresponding Berry curvature through the entire BZ which is topologically a torus (see Figure 3.5):

$$Ch^{(\alpha)} = \frac{1}{2\pi}\int_{BZ} F^{(\alpha)} d^2p \tag{3.18}$$

We will show in the next section that the Chern number is an integer in the absence of any symmetry (unlike the Berry phase in the 1D case that is only quantized in presence of a symmetry), and that the sum of Chern numbers over all bands α always vanishes. To obtain a non-trivial topological invariant, we need to restrict the number of bands under consideration, which is usually done by restricting the sum to occupied bands only. In that case it is also known as the TKNN

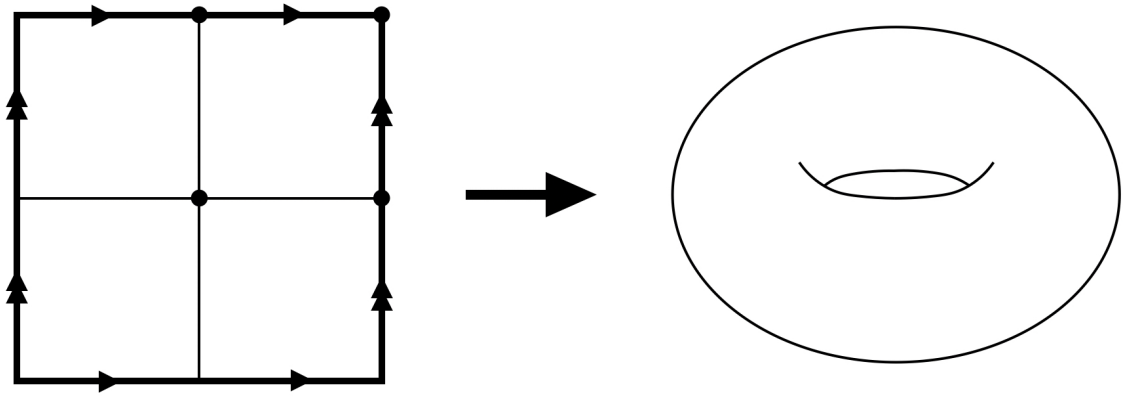

Figure 3.5: The Brillouin zone (BZ) is topologically a torus. The arrows indicate periodic boundary conditions, which tell us how to glue the edges of the square together; the dots are time reversal invariant momenta (TRIM), which will be relevant in the following section.

invariant [170].

Anti-unitary symmetries can have two effects on the Chern number. Such a symmetry in general either splits bands into pairs, or splits each band into two parts related by the symmetry. In either case, the Berry curvature may be either even or odd under the symmetry, so the Chern numbers either cancel or double (between bands or for each band respectively). In the latter case (which in the tenfold way only happens for Cartan class C in which $C^2 = -1$ and there is no TRS) the topological invariant becomes $2\mathbb{Z}$, i.e. it is an even integer. In the latter case, the topology may simply be trivial, but sometimes the Chern number either on half the bands or computed on half the BZ may be an integer. Only the parity of this integer turns out to be invariant (as we show in detail Section 3.4 for class AII with $T^2 = -1$, to which 2D topological insulator in particular belong), so the topological invariant is a $\mathbb{Z}_2 = \{1, -1\}$ index.

Topological Invariants for Superconductors

All the classifications mentioned above include topological (fermionic) superconductors that we are mostly interested in, for which PHS acts as $C^2 = 1$. In this case the Berry curvature is neither even nor odd under PHS, and the topological invariants are computed in the same way as in the absence of PHS. In particular, in the absence of TRS (class D) the invariant is just the Chern number, while with TRS $T^2 = -1$ (class DIII) the invariant is the $\mathbb{Z}_2$ index from class AII. The only caveat is that

the invariants are computed for BdG Hamiltonians:

$$\mathcal{H}^{(BdG)}(\mathbf{p}) = \begin{pmatrix} \mathcal{H}(\mathbf{p}) & \Delta(\mathbf{p}) \\ \Delta^\dagger(\mathbf{p}) & -\mathcal{H}^T(-\mathbf{p}) \end{pmatrix} \tag{3.19}$$

on which PHS acts as $\varsigma^x\mathcal{K}$ (ς^μ being Pauli matrices in the Nambu particle/hole indices) due to the requirement that $\Delta(\mathbf{p}) = -\Delta^T(-\mathbf{p})$. The only technical difficulty is that usually the gap function is only determined close to the Fermi surface and not known in the whole BZ, so a natural question is whether the topology of the SC phase is determined solely by the gap function in the vicinity of the Fermi surface. The answer is yes in the weak coupling limit: in order to change the topology of the phase, the gap in the spectrum must close; if the BdG Hamiltonian is symmetric under momentum reversal $\mathbf{p} \to -\mathbf{p}$ (which can be due to inversion or TRS symmetry), the gap can close only when the superconducting gap function vanishes somewhere *along* the Fermi surface, where a band crossing occurs at zero energy. Therefore the topology of the SC phase is determined only by the form of the gap function on the Fermi surface.

More generally, if there is no momentum-reversal symmetry (as is the case for non-centrosymmetric systems in a magnetic field), the band crossing may occur away from the Fermi surface and not at zero energy. More precisely, if $\xi_\alpha(\mathbf{p})$ are the eigenvalues of $\mathcal{H}(\mathbf{p})$, the band crossing can occur at momenta defined by $\xi_\alpha(\mathbf{p}) = -\xi_\alpha(-\mathbf{p})$ instead. We will be interested in cases when $\xi_\alpha(-\mathbf{p}) \neq \xi_\alpha(\mathbf{p})$, so we prove the following simple theorem with those cases included.

Theorem 3.1

Suppose the gap function $\Delta(\mathbf{p})$ is specified in the vicinity of the surface defined by $\xi_{S\alpha}(\mathbf{p}) = \frac{\xi_\alpha(\mathbf{p})+\xi_\alpha(-\mathbf{p})}{2} = 0$, and we have two extension $\tilde{\Delta}_1(\mathbf{p})$ and $\tilde{\Delta}_2(\mathbf{p})$ defined on the whole BZ such that $|\tilde{\Delta}_1(\mathbf{p}) + \tilde{\Delta}_2(\mathbf{p})| \ll |\xi_\alpha(\mathbf{p}) - \xi_\beta(\mathbf{p})|$ for all bands α and $\beta \neq \alpha$ and $\tilde{\Delta}_1(\mathbf{p}) = \tilde{\Delta}_2(\mathbf{p}) = \Delta(\mathbf{p})$ where $\Delta(\mathbf{p})$ is defined. Then BdG Hamiltonians $\mathcal{H}_1^{(BdG)}(\mathbf{p})$ with gap function $\tilde{\Delta}_1(\mathbf{p})$ and $\mathcal{H}_2^{(BdG)}(\mathbf{p})$ with gap function $\tilde{\Delta}_2(\mathbf{p})$ are topologically equivalent. □

Proof 3.1

Take $\tilde{\Delta}(\mathbf{p}, t) = (1-t)\tilde{\Delta}_1(\mathbf{p}) + t\tilde{\Delta}_2(\mathbf{p})$ as the gap in $\mathcal{H}^{(BdG)}(\mathbf{p}, t)$, which gives a family of Hamiltonians that smoothly extrapolate between $\mathcal{H}_1^{(BdG)}(\mathbf{p})$ and $\mathcal{H}_2^{(BdG)}(\mathbf{p})$. By assumption, no gap closing occurs in the vicinity of the surface defined $\xi_{S\alpha}(\mathbf{p}) = 0$, while away from it no gap closing occurs because the difference and sum of the two gap extensions are assumed to be smaller than the band splitting. Therefore the two BdG Hamiltonians can be adiabatically connected without the gap closing and

so are topologically equivalent.

We can therefore always compute topological invariants by taking the gap function to vanish fast but smoothly away from the $\xi_{S\alpha}(\mathbf{p}) = 0$ surfaces. In the vicinity of the surfaces, we then have

$$\mathcal{H}_{\alpha}^{(BdG)}(\mathbf{p}) = \begin{pmatrix} \xi_{\alpha}(\mathbf{p}) & \Delta_{\alpha}(\mathbf{p}) \\ \Delta_{\alpha}^{*}(\mathbf{p}) & -\xi_{\alpha}(-\mathbf{p}) \end{pmatrix} \tag{3.20}$$

which has Nambu eigenspinors

$$|\Upsilon_{\alpha}\rangle = \begin{pmatrix} u_{\alpha}(\mathbf{p}) \\ v_{\alpha}(\mathbf{p}) \end{pmatrix} = \frac{1}{\sqrt{(\xi_{\alpha}(\mathbf{p}) - E_{\alpha}(\mathbf{p}))^2 + |\Delta_{\alpha}(\mathbf{p})|^2}} \begin{pmatrix} \xi_{\alpha}(\mathbf{p}) - E_{\alpha}(\mathbf{p}) \\ \Delta_{\alpha}^{*}(\mathbf{p}) \end{pmatrix} \tag{3.21}$$

with the BdG spectrum

$$E_{\alpha}(\mathbf{p}) = \xi_{A\alpha}(\mathbf{p}) + \sqrt{\xi_{S\alpha}^2(\mathbf{p}) + |\Delta_{\alpha}(\mathbf{p})|^2} \tag{3.22}$$

where $\xi_{A\alpha}(\mathbf{p}) = \frac{\xi_{\alpha}(\mathbf{p}) - \xi_{\alpha}(-\mathbf{p})}{2}$ (the second branch is given by $-E_{\alpha}(-\mathbf{p})$ by PHS). Taking $\Delta_{\alpha} = |\Delta_{\alpha}|e^{i\Phi_{\alpha}}$, a simple calculation then shows that the Berry connection is

$$A^{(\alpha)}(\mathbf{p}) = i\langle\Upsilon_{\alpha}|\nabla|\Upsilon_{\alpha}\rangle = -|v_{\alpha}(\mathbf{p})|^2\nabla\Phi_{\alpha}(\mathbf{p}) \tag{3.23}$$

To get the Chern number for the α band we extend the gap function as mentioned above, and get

$$\begin{aligned} Ch_{\alpha} &= \frac{1}{2\pi}\int \left(F^{(\alpha)}(\mathbf{p})\right)_{p\theta} dp\, d\theta = \frac{1}{2\pi}\int \partial_p \left(A^{(\alpha)}(\mathbf{p})\right)_{\theta} dp\, d\theta \\ &= \frac{1}{2\pi}\left[\int \left(A_{\eta\tau}(\mathbf{p})\right)_{\theta} d\theta\right]_{p=0}^{p=\infty} = -\frac{1}{2\pi}\left[\Phi_{\eta\tau}(\mathbf{p})\right]_0^{2\pi} \end{aligned} \tag{3.24}$$

where we used the fact that $|v_{\alpha}(\mathbf{p})|^2$ goes between 0 and 1 as $\Delta_{\alpha} \to 0$ for $\xi_{S\alpha} > 0$ and $\xi_{S\alpha} < 0$ respectively, which is true independently of the details of the extension. In other words, the Chern number is simply the phase winding of the gap function around the Fermi surface. This is the case for example for a fully gapped superconductor with a single spin-polarized band (therefore necessarily triplet). Since the gap function must be odd in momentum, a phase winding is necessary for the spectrum to be fully gapped, resulting in the chiral SC phase, as shown in [130]. A similar topological invariant can be defined when TRS is present, resulting in a helical SC [128]. This is a $\mathbb{Z}_2$ invariant which is computed in the same way as for a system without PHS and which we derive

in the following section.

When considering crystalline symmetries in superconductors, another technical difficulty we will encounter is that in the BdG formalism there is inherently an ambiguity in their definition, because the action of the symmetry on the particle and hole sectors may differ by a $U(1)$ phase factor (as discussed in, e.g., [79, 126]). Given a unitary symmetry $\mathcal{U}(\mathbf{p})$ (possibly a function of momentum) acting on the normal state Hamiltonian $\mathcal{H}$, the action on the BdG Hamiltonian is given by

$$\tilde{U} = \begin{pmatrix} U(\mathbf{p}) & 0 \\ 0 & e^{i\phi_U} U^*(-\mathbf{p}) \end{pmatrix} \tag{3.25}$$

where in principle $e^{i\phi_U}$ can be any phase. This is the case for, e.g., TRS, where the phase $e^{i\phi_T}$ corresponds to the phase of the gap function which is arbitrary. The correct view is that a symmetry holds for the BdG Hamiltonian as long as there is *a* choice of the phase for which the symmetry holds. In particular, this is always the case if the gap transforms according to a 1D irreducible representation (irrep) of the relevant point group (higher dimensional irreps can lead to spontaneous symmetry breaking). For gaps that are even or odd under reflection symmetries, for example, $e^{i\phi_U} = \pm 1$ respectively. See also [143], which includes a more general review of topological SC, as well as topological invariants in general. The topological invariants for fully gapped *crystalline* topological SC phases are given in [29].

3.4 Chern Number and $\mathbb{Z}_2$ Topological Invariant from Gauss' Law

The purpose of this section is to introduce the 2D topological invariants for fully gapped systems in a more didactic manner. As we will see, we will in particular derive the Kane-Mele (or Fu-Kane) $\mathbb{Z}_2$ index in a novel way (I am not aware of this exact derivation appearing elsewhere). The main idea is to note the analogy between the Berry vector potential $\mathbf{A}^{(\alpha)}(\mathbf{p}) = i\langle u_\alpha(\mathbf{p})|\nabla|u_\alpha(\mathbf{p})\rangle$ (defined in any dimension) and the usual magnetic vector potential, and to use Stokes' theorem, with the Berry curvature field $\mathbf{F}^{(\alpha)}(\mathbf{p}) = \nabla \times \mathbf{A}^{(\alpha)}(\mathbf{p})$ being analogous to the magnetic field.

To begin, we return to the mirror-symmetric 2D nodal system $\mathcal{H}(p_x, p_y)$ discussed in Section 3.2 as defined in (3.14) and shown in Figure 3.4. We expand it around the node as

$$\mathcal{H}(p_x, p_y) = p_x \sigma^x + p_y \sigma^z \tag{3.26}$$

In the same way we extended from 1D to 2D, we can now extend to 3D, which allows a new term to appear:

$$\mathcal{H}(p_x, p_y, p_z) = p_x\sigma^x + p_y\sigma^z + p_z\sigma^y \tag{3.27}$$

such that at $p_z = \pm m \neq 0$, the spectrum is fully gapped. $\mathcal{H}(p_x, p_y, p_z)$ can now be thought of as an adiabatic transformation between $\mathcal{H}(p_x, p_y, m)$ and $\mathcal{H}(p_x, p_y, -m)$, with a phase transition (gap closing) occurring at $p_z = 0$. We will see momentarily that the topological invariant that changes across the transition is the Chern number.[4]

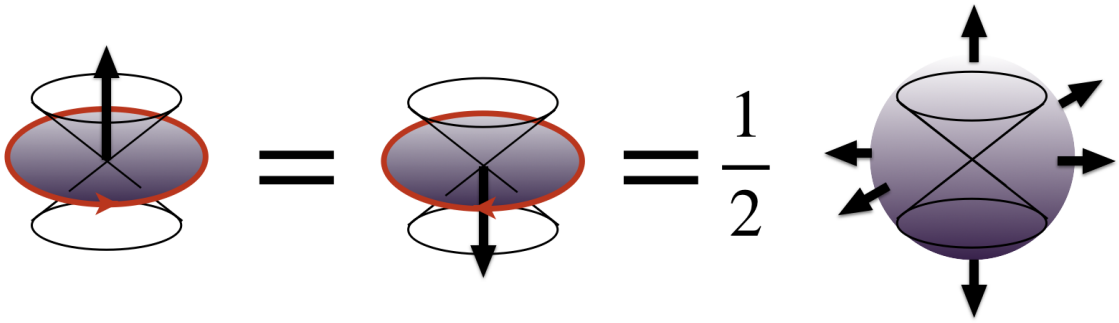

Figure 3.6: Applying Stoke's theorem to relate the Berry phase evaluated around a loop encircling a node to the Berry curvature flux through surfaces bounded by the loop; the flux through the sphere on the right is therefore twice the Berry phase along its equator.

To see this, we apply Stoke's theorem which says that the Berry phase calculated around the loop in Figure 3.4 and in Figure 3.6 is equal to the flux of the Berry curvature vector through an oriented surface whose boundary is the loop, two of which are shown in Figure 3.6. Gluing the two such surfaces together, we conclude that the Berry flux through a sphere enclosing the node is equal to twice the Berry phase of the loop, i.e. $\pm 2\pi$. Note that we need to pick which band we compute the flux for, and they are opposite for the two bands intersecting at the node. We conclude that nodes act as sources of Berry flux. This will be the key observation. Next, we use the same trick as we did with the Berry phase: deform the sphere into two surfaces at fixed $p_z = m$ and $-m$, with the surfaces along the BZ boundary vanishing due to periodic boundary conditions. We conclude that the Chern numbers for $\mathcal{H}(p_x, p_y, m)$ and $\mathcal{H}(p_x, p_y, -m)$ differ by one.

Consider now an arbitrary fully gapped 2D Hamiltonian $\mathcal{H}(\mathbf{p})$ with $\mathbf{p} = (p_x, p_y)$ and periodic boundary conditions, i.e. defined on $BZ \cong \mathbb{T}^2$, where $\mathbb{T}^2$ is the 2D torus, Figure 3.5. We will first

[4]Note that we can extend the logic chain 1D (gapped)→2D (nodal)→3D (nodal)→2D (gapped) to 3D (nodal)→4D (nodal) → 3D (gapped), which is related to the Bott periodicity used to construct classification tables [30].

ignore any symmetries it may have (i.e. consider it to be in class A). To test if it is topologically equivalent to a trivial insulator (meaning one adiabatically connected to a product state of atomic limit wave functions), we can define $\mathcal{H}(\mathbf{p}, p_z)$ as an arbitrary extension of $\mathcal{H}(\mathbf{p}) = \mathcal{H}(\mathbf{p}, 1)$ to the trivial Hamiltonian $\mathcal{H}(\mathbf{p}, 1/2)$, which is defined on the solid torus that I will denote $\mathbf{T}$ whose surface is the BZ (see Figure 3.7; we can 'fill-in' the torus by taking the Hamiltonian to be constant on the inner solid torus shown in Figure 3.8). From the observation above, we expect that if $\mathcal{H}(\mathbf{p})$ is topologically non-trivial, $\mathcal{H}(\mathbf{p}, p_z)$ will have band crossings acting as sources of Berry curvature flux. This is essentially the idea behind the proof of quantization and invariance of the Chern number due to [161].

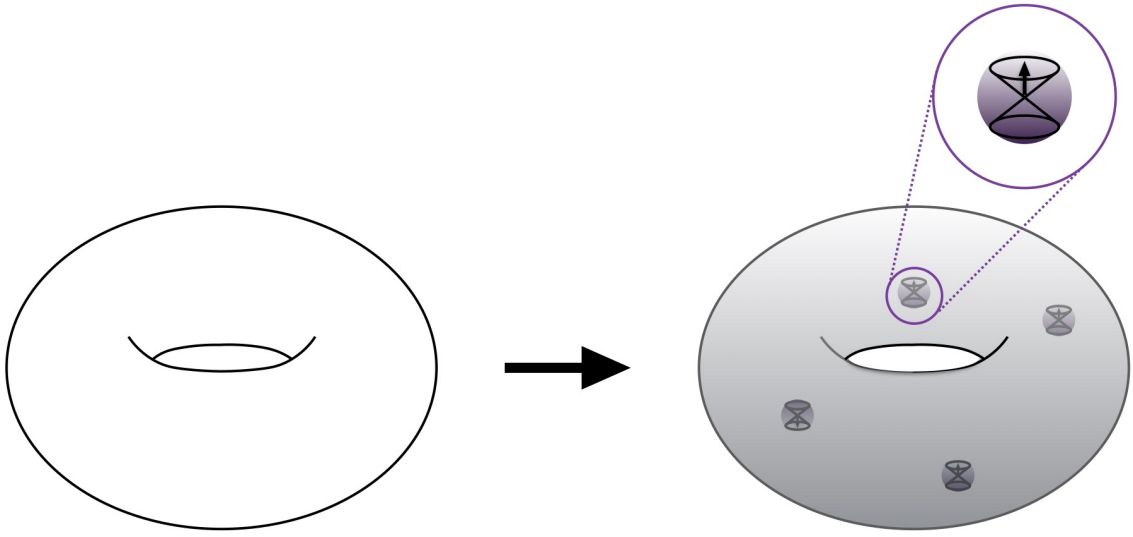

Figure 3.7: Visual representation of the extension Hamiltonian $\tilde{H}(\mathbf{p})$. The BZ torus is filled in, making a solid torus $\mathbf{T}$. A given band may intersect at several isolated points. We remove little solid spheres $\mathbf{S}_j$ around these points. As indicated in the figure, the extended Hamiltonian $\tilde{H}(\mathbf{p})$ may be approximated as a Weyl cone on those spheres (the arrow indicates whether the band under consideration crosses from above or from below, giving a sense of chirality).

For a general fully gapped Hamiltonian, the existence of such an extension is not completely trivial, but in fact by the Wigner-von Neumann avoided crossing theorem we can make an even stronger assumption about $\mathcal{H}(\mathbf{p}, p_z)$, namely that it is degenerate only at isolated points $\{\mathbf{p_j}\} \subset \mathbf{T}$, and that the degeneracy only involved pairs of bands (intuitively it is clear that any higher degeneracies can be 'moved apart' by making smooth deformations). To compute the Berry flux through the original BZ, we can thus take the Berry curvature in 3D, which is defined everywhere except the degeneracy points. We then consider the solid torus with little solid spheres $\mathbf{S}_j$ removed

around the degenerate points. The Wigner-von Neumann theorem additionally tells us that in sufficiently small solid spheres, we can take the effective Hamiltonian to be $\mathcal{H}_k(\mathbf{k}) = \pm\boldsymbol{\sigma}\cdot\mathbf{k}$ (i.e. we can ignore all bands but two). We now again use Stoke's theorem but in the Gauss' law form: since we want the integral of $F^{(\alpha)}$ on the surface of the solid torus, we should integrate the divergence $\nabla\cdot\mathbf{F}^{(\alpha)}$ over the bulk of the solid torus with the bad points removed. But $\nabla\cdot\nabla\times = 0$, so Gauss's law gives:

$$0 = \int_{\mathbf{T}} \nabla\cdot\mathbf{F}^{(\alpha)} d^3p = \int_{\mathbb{T}^2=BZ} \mathbf{F}^{(\alpha)}\cdot d^2\mathbf{p} + \sum_j \int_{\mathbb{S}^2_j} \mathbf{F}^{(\alpha)}\cdot d^2\mathbf{p} \tag{3.28}$$

where in the sum the integrals are over the surfaces of spheres removed. We conclude, since $\mathbf{F}^{(\alpha)}$ is perpendicular to the surfaces, that

$$\int_{BZ} \mathbf{F}^{(\alpha)}\cdot d^2\mathbf{p} = \int_{BZ} F^{(\alpha)} d^2p = -\sum_j \int_{\mathbb{S}^2_j} F^{(\alpha)} d^2p \tag{3.29}$$

As we saw above (or as can easily be computed directly), we have

$$\int_{\mathbb{S}^2_j} F^{(\alpha)} d^2p = \pm 2\pi \tag{3.30}$$

The plus minus depends on whether the α band crosses with the $\alpha+1$ band from below or with the $\alpha-1$ band from above, reflected in the sign in $\mathcal{H}_k(\mathbf{p}) = \pm\boldsymbol{\sigma}\cdot\mathbf{p}$. The conclusion is that the Berry curvature flux through the BZ is quantized:

$$\int_{BZ} F^{(\alpha)} d^2p = 2\pi\ Ch^{(\alpha)} \tag{3.31}$$

where $Ch^{(\alpha)}$ is the Chern number of the α band, which we now know is an integer. Since each band crossing contributes +1 to one Chern number and -1 to another, we have the further conclusion that the sum of Chern numbers over all bands is always zero. Thus to get a topologically non-trivial system, the sum has to be restricted to a subset of (filled) bands.

3.4.1 Time Reversal Symmetry and the Kane-Mele $\mathbb{Z}_2$ Index

We can use Simon's construction to also derive the topological $\mathbb{Z}_2$ index characterizing the QSHE discussed by Kane and Mele [76, 77] and topological insulators (TIs). Both cases involve additional symmetries (spin rotation symmetry and TRS respectively) that render the total Chern number zero.

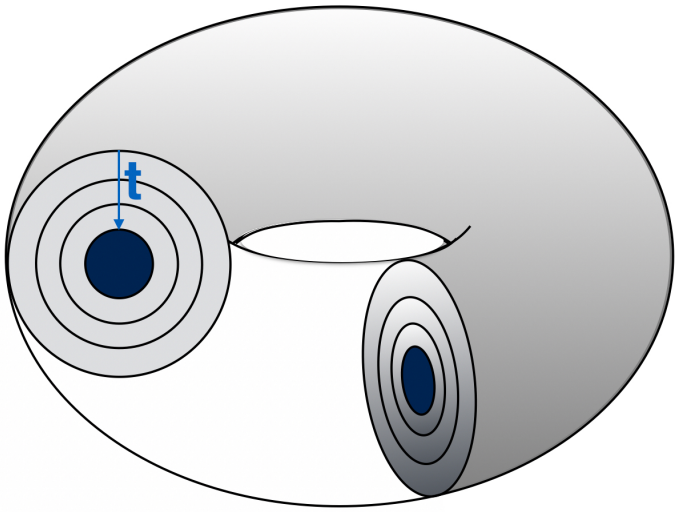

Figure 3.8: Hamiltonian on the solid torus as a family of Hamiltonians on 2D tori transforming into the vacuum Hamiltonian as a parameter t is varied, possibly undergoing a topological phase transition. The blue region in the middle of the solid torus represents the trivial extension of the vacuum Hamiltonian to a solid torus.

Here I will consider TRS, but the idea is similar for both: as in the case with mirror symmetry, we need to consider families of Hamiltonians $\mathcal{H}(\mathbf{p}, p_z)$ with the restriction that they satisfy the symmetry at each value of p_z.

The Chern numbers vanish for each band α in presence of TRS because the Berry curvature then satisfies $F^{(\alpha)}(\mathbf{p}) = -F^{(\alpha)}(-\mathbf{p})$, and the integral over the whole BZ vanishes. The idea is that since TRS identifies states with $\mathbf{p}$ and $-\mathbf{p}$, the real invariant would correspond to the Berry curvature integrated over half the Brillouin zone with only unidentified momenta (therefore mapped to the other half by TRS), which we call the effective BZ or EBZ and which we can take to be a cylinder. Note that the boundary of the EBZ necessarily contains the time reversal invariant momenta $\mathbf{p} = -\mathbf{p}$, or TRIM (see Figure 3.5). This is almost correct. The problem is that when the momenta $\mathbf{p}$ and $-\mathbf{p}$ are identified, the BZ is mapped to a sphere (see Figure 3.9; this is a well-known so-called doubled cover of the sphere by a torus). However, if the eigenstates are continuous on the torus, they may not be on the sphere. As we saw, such discontinuities indicate non-trivial topology.

The discontinuity is due to the existence of Kramers pairs, which follows from the fact that TRS is antiunitary and $\mathcal{T}^2 = -1$. The former means that $\langle \mathcal{T} u_\alpha(\mathbf{p}) | \mathcal{T} u_\beta(\mathbf{p}) \rangle = \langle u_\beta(\mathbf{p}) | u_\alpha(\mathbf{p}) \rangle$. But then the latter implies $\langle \mathcal{T}^2 u_\alpha(\mathbf{p}) | \mathcal{T} u_\alpha(\mathbf{p}) \rangle = -\langle u_\alpha(\mathbf{p}) | \mathcal{T} u_\alpha(\mathbf{p}) \rangle = \langle u_\alpha(\mathbf{p}) | \mathcal{T} u_\alpha(\mathbf{p}) \rangle = 0$, so the eigenstates $|u_\alpha(\mathbf{p})\rangle$ and $\mathcal{T}|u_\alpha(\mathbf{p})\rangle$ are orthogonal. In particular, at TRIM points $\mathbf{p} = -\mathbf{p}$ the states are doubly

degenerate since $\mathcal{T}$ commutes with the first-quantized Hamiltonian and so $\mathcal{T}|u_\alpha(\mathbf{p})\rangle$ is an eigenstate of $\mathcal{T}H(\mathbf{p})\mathcal{T}^{-1} = H(-\mathbf{p})$, in addition to $|u_\alpha(-\mathbf{p})\rangle = |u_\alpha(\mathbf{p})\rangle$. The obstruction to passing to the sphere is that $\mathcal{T}|u_\alpha(\mathbf{p})\rangle \neq |u_\alpha(\mathbf{p})\rangle$ in general, which results in discontinuous eigenstates when the two are identified on the sphere.

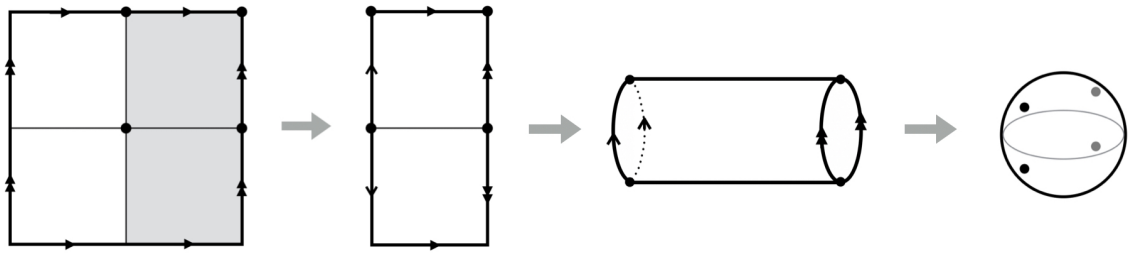

Figure 3.9: The map taking a the BZ torus to a sphere by identifying TR pairs. The grey region amounts to a choice of between TR pairs. For this choice, we first fold the BZ in half, then identify top and bottom edges to obtain the EBZ. The remaining arrows indicate the identification made by TR symmetry on the EBZ, and gluing them together produces a sphere.

The reason for this obstruction can be seen more clearly using the same extension construction to the solid torus $\mathbf{T}$ we used above for proof of Chern number quantization, with the additional restriction that $\mathcal{H}(\mathbf{p}, p_z)$ respects TRS for each fixed p_z. This means that any band crossing at $\mathbf{p}_j$ is necessarily accompanied by an anti-crossing (because $\mathcal{T}H(\mathbf{p})\mathcal{T}^{-1} = H(-\mathbf{p})$) at $-\mathbf{p}_j$. This proves the total Chern number is zero. We can alse see why the Berry flux through the EBZ is not an invariant: if we cut the solid torus into a solid cylinder with the surface being the EBZ, there is flux escaping through the 'caps' of the solid cylinder that are not part of the EBZ itself (see Figure 3.10). Moving 'charges' inside the solid torus around will change the flux through the EBZ, which is therefore not well-defined.

The invariant, which we call the half Chern number $Ch^{(\alpha)}_{1/2}$, is rather the flux through the surfaces of the half of the solid torus including the caps, which we can see is quantized as before. Note that again by Stokes' theorem, the Berry curvature flux through the caps can be computed as a Berry phase along the loops forming their boundaries that connect TRIM points in the original BZ. The half Chern number expressed in terms of the Berry vector potential on the EBZ only is thus

$$2\pi\ Ch^{(\alpha)}_{1/2} = \int_{EBZ} F^{(\alpha)} d^2p + \oint_{\partial EBZ} \mathbf{A}^{(\alpha)} \cdot d\mathbf{p} = -\sum_j \int_{\mathbb{S}^2_j \subset \mathbf{T}/\mathcal{T}} F^{(\alpha)} d^2p \tag{3.32}$$

which is the formula obtained by different means in [113, 52].

The advantage of the extension construction is that there are now multiple ways to see why the

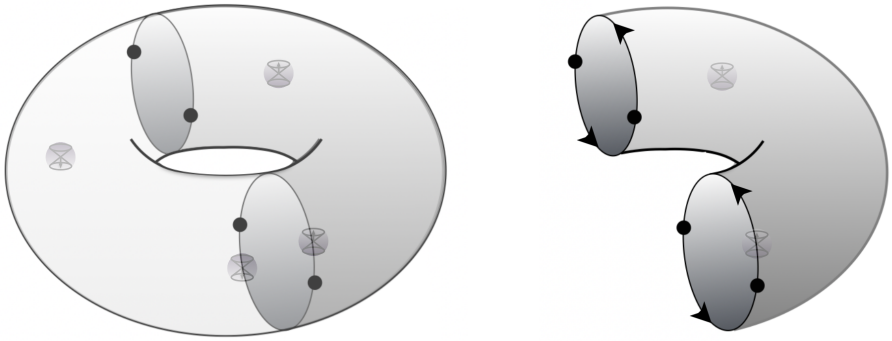

Figure 3.10: The extended EBZ. Note that on the full torus, crossings/anti-crossings appear in pairs, so the total Chern number is zero, but the half Chern number may not be. To compute $Ch^{(\alpha)}_{1/2}$, we only count the spheres in the indicated half. Note that part of the Berry flux goes through the 'caps' that are not part of the original Hamiltonian, but their contribution can be computed as the Berry phase around the bounding loops using the Berry connection on the original EBZ only.

half Chern number is only well-define mod 2, so that the $\mathbb{Z}_2$ topological invariant is its parity. First of all, there is an ambiguity in the smooth extension. It is possible to move the band crossings around, provided we move the corresponding anti-crossings so as to preserve TR symmetry. In particular, one can remove a band crossing from the half solid torus, at the cost of moving in an anti-crossing (see Figure Figure 3.11). In that process, the half Chern number changes precisely by 2, so it is always possible to make it 0 or 1 by moving around some of the crossings (we can think of this as moving charges around, and note that the total charge is conserved since the flux through the BZ is fixed).

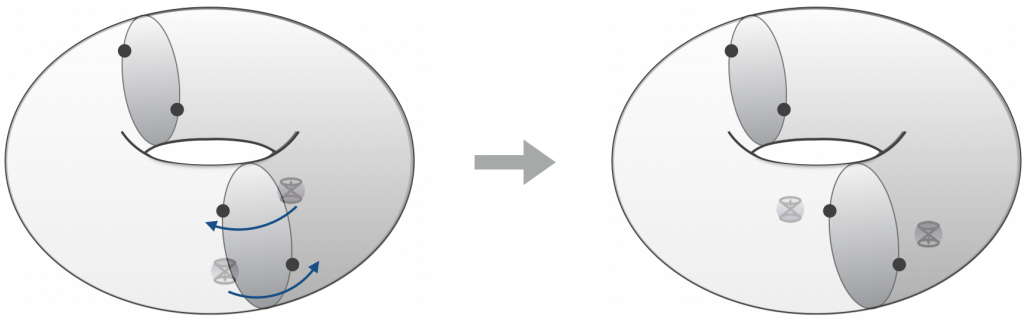

Figure 3.11: Moving a band crossing from one half of the torus to the other half. In this process, we have to move the corresponding anti-crossing in the opposite direction, so the Chern number changes by two.

Alternatively, it is possible to annihilate a crossing with an anti-crossing (if this is done at $\mathbf{p}$,

one simultaneously annihilates an anti-crossing with a crossing at $-\mathbf{p}$). Doing this in reverse, we can create a crossing/anti-crossing pair at $\mathbf{p}$, while simultaneously creating an anti-crossing/crossing pair at $-\mathbf{p}$ (see Figure 3.12). Moving the band crossings around as in the previous case, we again can change the half Chern number by two, which shows that all half Chern numbers of the same parity can be obtained. Thus Hamiltonians with the same parity $(-1)^{Ch_{1/2}^{(\alpha)}}$ are topologically equivalent, but not if they have opposite parity.

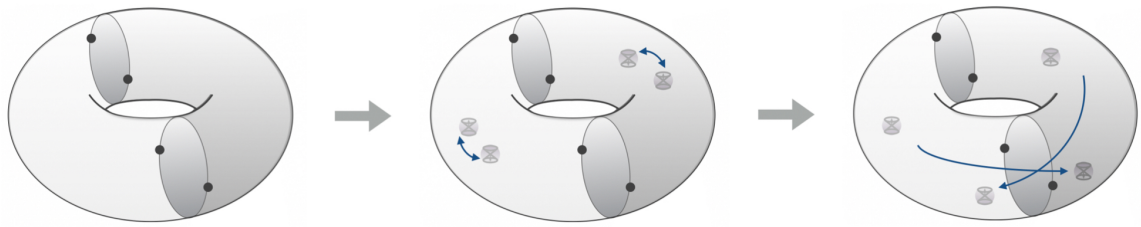

Figure 3.12: Creating a crossing/anti-crossing pair (which requires simultaneously creating an anti-crossing/crossing pair in the opposite half), and the moving the crossing to the other half as in the previous process. This again changes the Chern number by two.

A third way to see this is to note that there are multiple ways to form an EBZ, either cutting along different lines, or even cutting in multiple places in which case the EBZ may have several disconnected pieces. For example, one can take two disconnected quarters instead of a halves, as shown in the Figure 3.13. This effectively changes crossings to anti-crossings in the exchanged quarter. Instead of quarters, any fraction of the half torus can be exchanged for its time reversal partner, which again changes the half Chern number by ± 2.

Finally, a fourth way is to pick different partitions on each of the 2D tori making up the solid torus (the choice has to be smooth as a function of the minor radius of the tori). Visually, this amounts to deforming the 'caps' of the solid half-torus, which has to be done such that TR symmetry is respected. As one cap moves past a band crossing, the opposite cap thus has to move past an anti-crossing in the opposite sense, again changing the half Chern number by two. This is effectively the way the $\mathbb{Z}_2$ invariant was originally derived (without an explicit solid extension) in [113]. Note that other invariants from other classes can similarly be derived using the Berry connection.

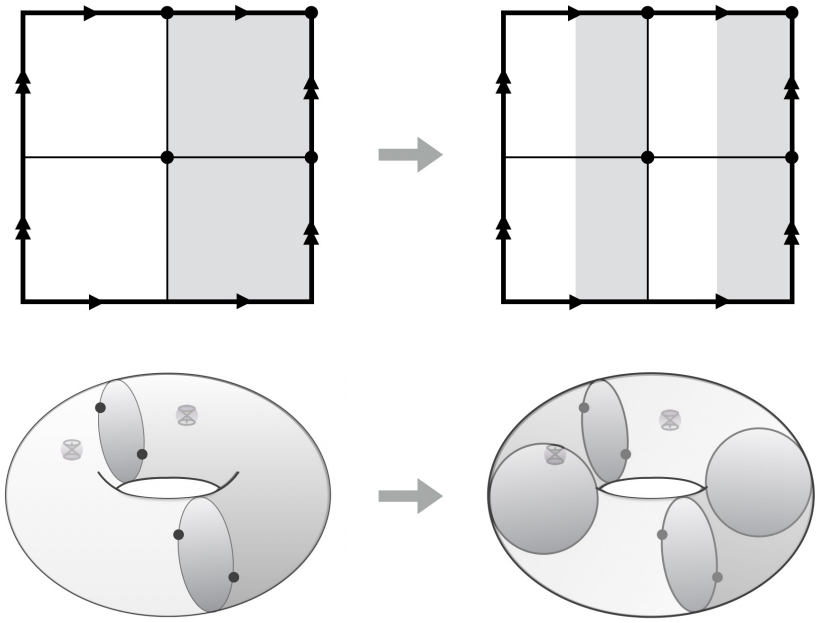

Figure 3.13: Choosing a different partition of the BZ can change the half Chern number. There is a crossing/anti-crossing pair in the solid torus, we can pick a partition that includes either one or the other (and never both).

Chapter 4

Superconductivity in 1H-TMDs

Material in this chapter first appeared in [153].

In this chapter we carry out a self-consistent mean field analysis of superconductivity in 1H transition metal dichalcogenides (TMDs) and other similar systems that we studied in Section 2.2 using RG, but now including spin-orbit coupling (SOC). Recall that in the absence of SOC we found uniform SC and PDW channels. Here we will consider only the uniform SC channel and look at the PDW channel in Chapter 5. The 1H-TMDs have a strong Ising-type SOC at the K pockets and possibly also at the Γ pocket. We will therefore consider the limit of strong SOC in which we only keep the pairing within inner and outer Fermi surfaces split by the SOC in Section 4.2, and study spontaneous time-reversal symmetry breaking in Section 4.3. We discuss the topology of the non-trivial phases we find in Section 4.4. For reference, we summarize the $\mathbf{k}\cdot\mathbf{p}$ model from Section 1.2 in Section 4.1 that we will be using in this chapter.

4.1 Single-Body Model of 1H-TMDs with SOC

Recall that the normal state of 1H-TMDs is described by the Hamiltonian that we discussed in Section 1.2:

$$H = \sum_{\mathbf{p}\eta\alpha\beta} \bar{d}_{\mathbf{p}\eta\alpha} \left[\mathcal{H}_\eta(\mathbf{p})\right]_{\alpha\beta} d_{\mathbf{p}\eta\beta} \tag{4.1}$$

with

$$\mathcal{H}_\eta(\mathbf{p}) = \epsilon_\eta(\mathbf{p}) + \boldsymbol{\beta}_\eta(\mathbf{p})\cdot\boldsymbol{\sigma} \tag{4.2}$$

with valley index $\eta = 0, \pm 1$ corresponding to ηK pockets (we also interchangeably use $\eta = \Gamma, \pm K$ when it is more clear), in the hexagonal Brillouin zone with $\mathbf{p}$ measured from the pocket centers,

$$\epsilon_\eta(\mathbf{p}) = -\frac{p^2}{2m_\eta} - \mu_\eta \tag{4.3}$$

with

$$\boldsymbol{\beta}_\eta = \beta_{\eta z}(\mathbf{p})\hat{\mathbf{z}} + \alpha_R\left(p_y\hat{\mathbf{x}} - p_x\hat{\mathbf{y}}\right) + \mathbf{b} \tag{4.4}$$

where $\beta_{\eta j}$ are $j = x, y, z$ components of $\boldsymbol{\beta}_\eta$ which include $\beta_{\eta z}$being the Ising SOC, α_R terms are the Rashba SOC, and the magnetic field $\mathbf{b} = \frac{1}{2}g_L\mu_B\mathbf{B}$ is in units of the Bohr magneton μ_B with Landé g-factor g_L. We pick $\mathbf{K}$ to lie along the $\hat{\mathbf{x}}$ direction, from which we measure all angles.

The Hamiltonian is diagonalized by operators

$$c_{\mathbf{p}\eta\tau} = U^\alpha_{\eta\tau}(\mathbf{p})d_{\mathbf{p}\eta\tau} \tag{4.5}$$

where

$$U^\alpha_{\eta\tau}(\mathbf{p}) = \frac{1}{\sqrt{2}}\sqrt{1 + \frac{\tau\alpha\beta_{\eta z}(\mathbf{p})}{\beta_\eta(\mathbf{p})}}\left(\tau e^{-i\phi_\eta}\right)^{\frac{1+\alpha}{2}} \tag{4.6}$$

with

$$e^{i\phi_\eta(\mathbf{p})} = \frac{\beta_{\eta x} + i\beta_{\eta y}}{|\beta_{\eta x} + i\beta_{\eta y}|} = \frac{\alpha_R p_y + b_x + i(-\alpha_R p_x + b_y)}{\sqrt{(\alpha_R p_y + b_x)^2 + (\alpha_R p_x - b_y)^2}}, \tag{4.7}$$

and where $\beta_\eta = |\boldsymbol{\beta}_\eta(\mathbf{p})|$. This is the SOC (also band or helical) basis. The normal state dispersions are

$$\xi_{\eta\tau}(\mathbf{p}) = \epsilon_\eta(\mathbf{p}) + \tau\left|\boldsymbol{\beta}_\eta(\mathbf{p})\right| \equiv \epsilon_\eta(\mathbf{p}) + \tau\beta_\eta(\mathbf{p}) \tag{4.8}$$

which determines the Fermi surfaces that are shown in Figure 4.1 with and without Rashba SOC/in-plane magnetic field.

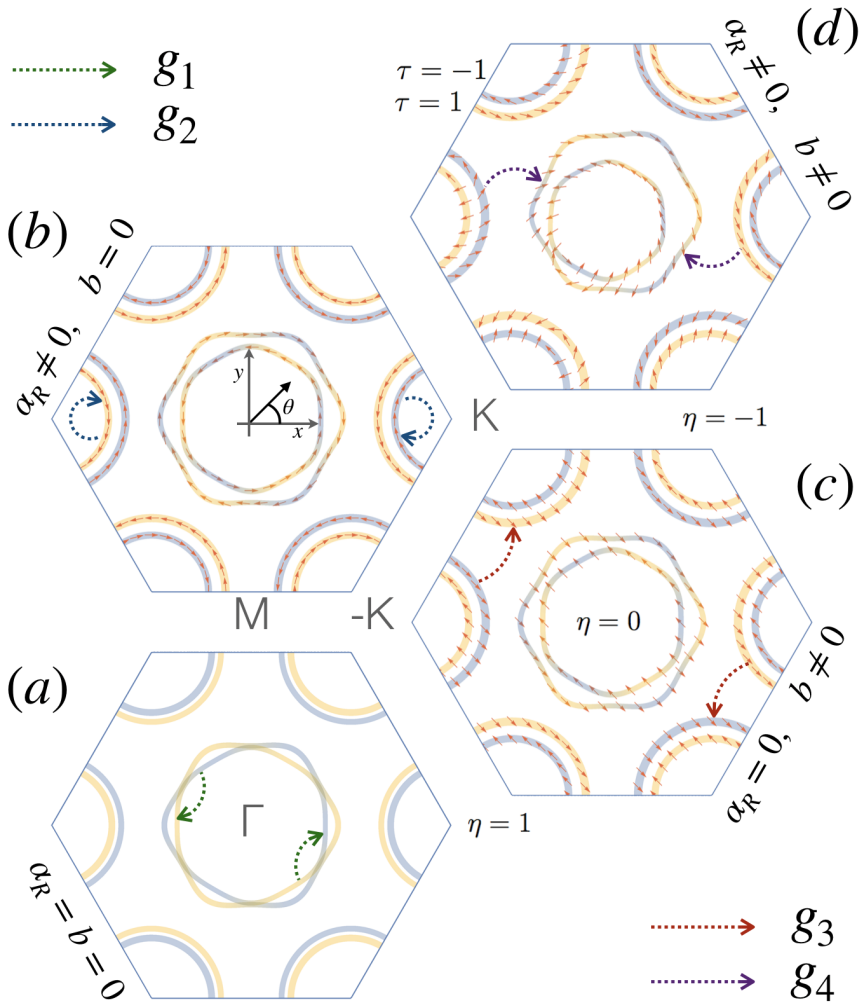

Figure 4.1: Fermi surfaces for Hamiltonian (4.2) with Ising SOC and (a) no Rashba SOC or magnetic field; (b) Rashba SOC and no magnetic field; (c) in-plane magnetic field and no Rashba (note that Fermi surfaces remain symmetric under momentum reversal even though TRS is broken); and (d) with both Rashba SOC and in-plane magnetic field. Note that in the latter case the Fermi surfaces are shifted. Yellow/blue colors indicate spin up/down polarization respectively, while red arrow indicate the in-plane spin components. The pairing interactions $g_{1,\ldots,4}$ relevant to the SC instability are also shown.

4.1.1 Interactions Near the Fermi Surfaces

Symmetry constrains the possible spin-conserving, momentum-direction-independent electronic interactions between the low-energy fermionic operators to eight. Of these, the four interactions that contribute to superconductivity are (see Figure 4.1): intra-pocket density-density interactions involving the Γ (g_1) and the $\pm K$ (g_2) pockets; and inter-pocket pair-hopping interactions between K and $-K$ (g_3) and between Γ and $\pm K$ (g_4). Thus we consider the following interacting Hamiltonian:

$$\begin{aligned} H_{\text{Int}} =& V^{\alpha'\beta';\alpha\beta}_{\Gamma;\Gamma}(\mathbf{p};\mathbf{k})\ d^\dagger_{\Gamma,\mathbf{p}\alpha} d^\dagger_{\Gamma,-\mathbf{p}\beta'} d_{\Gamma,\mathbf{k}\alpha'} d_{\Gamma,-\mathbf{k}\beta'} + \\ & V^{\alpha'\beta';\alpha\beta}_{\pm K;\pm K}(\mathbf{p};\mathbf{k})\ d^\dagger_{\pm K,\mathbf{p}\alpha} d^\dagger_{\mp K,-\mathbf{p}\beta} d_{\pm K,\mathbf{k}\alpha'} d_{\mp K,-\mathbf{k}\beta'} + \\ & V^{\alpha'\beta';\alpha\beta}_{\pm K;\mp K}(\mathbf{p};\mathbf{k})\ d^\dagger_{\pm K,\mathbf{p}\alpha} d^\dagger_{\mp K,-\mathbf{p}\beta} d_{\mp K,\mathbf{k}\alpha'} d_{\pm K,-\mathbf{k}\beta'} + \\ & V^{\alpha'\beta';\alpha\beta}_{\Gamma;\pm K}(\mathbf{p};\mathbf{k})\ d^\dagger_{\pm K,\mathbf{p}\alpha} d^\dagger_{\mp K,-\mathbf{p}\beta} d_{\Gamma,\mathbf{k}\alpha'} d_{\Gamma,-\mathbf{k}\beta'} + \text{h.c.} \end{aligned} \tag{4.9}$$

Accounting for the anti-symmetric nature of the fermion operators (and including all Hermitian conjugates), the uniform part of the interactions can be separated into singlet and triplet interaction channels, as follows:

$$\begin{aligned} [V^s]^{\alpha'\beta';\alpha\beta}_{\Gamma;\Gamma} &= \frac{g_1}{2}(i\sigma^y)^{\alpha\beta}(i\sigma^y)^{\alpha'\beta'} \\ [V^s]^{\alpha'\beta';\alpha\beta}_{\Gamma;\pm K} &= \pm\frac{g_4}{2}(i\sigma^y)^{\alpha\beta}(i\sigma^y)^{\alpha'\beta'} \\ [V^s]^{\alpha'\beta';\alpha\beta}_{\pm K;\pm K} &= \frac{1}{4}(g_2+g_3)(i\sigma^y)^{\alpha\beta}(i\sigma^y)^{\alpha'\beta'} \\ \left[V^t\right]^{\alpha'\beta';\alpha\beta}_{\pm K;\pm K} &= \frac{1}{4}(g_2-g_3)\sum_{j=x,y,z}(\sigma^j i\sigma^y)^*_{\alpha\beta}(\sigma^j i\sigma^y)^{\alpha'\beta'} \end{aligned} \tag{4.10}$$

Since $V_{K,K}$ and $V_{K,-K}$ are related by interchanging the spin indices α', β', combined with an overall minus sign for interchanging two fermion operators, in this representation we have

$$\begin{aligned} [V^s]^{\alpha'\beta';\alpha\beta}_{\pm K;\mp K} &= [V^s]^{\alpha'\beta';\alpha\beta}_{\pm K;\pm K} \\ \left[V^t\right]^{\alpha'\beta';\alpha\beta}_{\pm K;\mp K} &= -\left[V^t\right]^{\alpha'\beta';\alpha\beta}_{\pm K;\pm K} \end{aligned} \tag{4.11}$$

From Eq. (4.10), we see that $V_{\pm K,\pm K}$ (and thus $V_{\pm K,\mp K}$) have contributions in both the singlet channel (labeled s) and the triplet channel (labeled t), while for momentum-direction-independent interactions, $V_{\Gamma,\Gamma}$ and $V_{\Gamma,K}$ have contributions only in the singlet channel. In addition to these interactions, in order to ensure that the gap on the Γ pocket does not artificially vanish in the triplet

regime, we also include weak (but symmetry-allowed) momentum-direction dependent interactions:

$$\begin{aligned}\left[V^t(\mathbf{p};\mathbf{k})\right]^{\alpha'\beta';\alpha\beta}_{\Gamma;\Gamma} &= \frac{g_1^t}{2}\cos 3\theta_{\mathbf{k}}\cos 3\theta_{\mathbf{p}}(\boldsymbol{\sigma} i\sigma^y)^*_{\alpha\beta}\cdot(\boldsymbol{\sigma} i\sigma^y)^{\alpha'\beta'}\\ \left[V^t(\mathbf{p};\mathbf{k})\right]^{\alpha'\beta';\alpha\beta}_{\Gamma;\pm K} &= \pm\frac{g_4^t}{\sqrt{2}}\cos 3\theta_{\mathbf{k}}(\boldsymbol{\sigma} i\sigma^y)^*_{\alpha\beta}\cdot(\boldsymbol{\sigma} i\sigma^y)^{\alpha'\beta'}\end{aligned} \tag{4.12}$$

where $\theta_{\mathbf{k}}$ refers to the angle of the momentum on the Γ pocket. Note that all higher harmonics can be included in a similar fashion, but they do not qualitatively affect our conclusions. We take $|g_i^t| \ll |g_i|$, so these interactions have a negligible effect on whether the system enters the singlet or triplet regime.

Note that there are four other possible interactions, which we do not include in our analysis here,

$$\begin{aligned}H_{\text{Int}} = &\frac{g_5}{2}d^\dagger_{K\alpha}d^\dagger_{K\beta}d_{K\beta}d_{K\alpha} + \frac{g_6}{2}d^\dagger_{-K\alpha}d^\dagger_{\Gamma\beta}d_{\Gamma\beta}d_{-K\alpha} +\\ &+\frac{g_7}{2}d^\dagger_{-K\alpha}d^\dagger_{\Gamma\beta}d_{-K\beta}d_{\Gamma\alpha} + \frac{g_8}{2}d^\dagger_{-K\alpha}d^\dagger_{\Gamma\beta}d_{K\beta}d_{K\alpha} + \text{h.c.}\end{aligned} \tag{4.13}$$

where we omitted momentum indices and symmetry related terms for simplicity. These interactions decouple from $g_1, ...g_4$, and hence need not be included when analyzing the possible superconducting instabilities. They can in principle give rise to a pair density wave (PDW) which may compete with superconductivity, depending on the microscopic values of $g_5, ...g_8$. We defer analysis to the next chapter.

4.2 Superconductivity in the presence of SOC and magnetic field

The parquet RG treatment of Chapter 2 shows that superconductivity is the only instability generated by the interactions in Eq. (4.9) within weak-coupling. If the superconducting transition temperature was larger than the Fermi energy, then the superconducting problem would have been essentially solved. However, since $T_c \ll E_F$ in $NbSe_2$, one needs to proceed to energy scales below the Fermi energy, where Ising and Rashba SOC and the magnetic field become relevant. Since superconductivity is the leading instability and decouples from other channels below the Fermi energy, it is sufficient to consider a simpler mean-field approach to include the additional terms in the Hamiltonian that were neglected in analysis above.

4.2.1 Mean-Field Gap Equation in the Presence of SOC and Magnetic Field

In order to determine the appropriate BCS gap equation, we first project the interactions onto the spin-split Fermi surfaces, by using the transformation (4.6) between eigenstates of spin and eigenstates of the non-interacting Hamiltonian and restricting the gap functions to involve pairs on the same Fermi surface only. Throughout the phase diagrams shown in Figure 4.2, the Fermi surfaces are qualitatively similar to those shown in Figure 4.1, with the important caveat that in the presence of both Rashba SOC and magnetic field inversion symmetry is broken, as we discuss in more detail below. Our analysis assumes that the minimum splitting between Fermi surfaces (with an associated energy scale on the order of the magnetic field b and/or Rashba SOC $\alpha_R p_F$) is large compared to the superconducting pairing strength, whose energy scale is on the order of the superconducting gap function. In particular, close to the phase transition at which the gap function vanishes this is valid almost everywhere in our phase diagram. Note, however, that for $\alpha_R = b = 0$, or for $\alpha_R = b$ with $\mathbf{B}$ along a $\Gamma - K$ line, the inner and outer Fermi surfaces at the Γ pocket touch along the $\Gamma - M$ lines, and our approach is insufficient to resolve the gap in the immediate vicinity of these loci even very close to T_c.

After the projection, the interactions generally acquire a dependence on the momentum direction. Explicitly, this gives:

$$\begin{aligned} H_{\text{Int}} =& \tilde{V}^{\tau,\tau'}_{\Gamma,\Gamma} c^\dagger_{\Gamma\tau} c^\dagger_{\Gamma\tau} c_{\Gamma\tau'} c_{\Gamma\tau'} + \\ & \tilde{V}^{\tau,\tau'}_{\pm K,\pm K} c^\dagger_{\pm K\tau} c^\dagger_{\mp K\tau} c_{\pm K\tau'} c_{\mp K\tau'} + \\ & \tilde{V}^{\tau,\tau'}_{\pm K,\mp K} c^\dagger_{\pm K\tau} c^\dagger_{\mp K\tau} c_{\mp K\tau'} c_{\pm K\tau'} + \\ & \tilde{V}^{\tau,\tau'}_{\Gamma\pm K} c^\dagger_{\pm K\tau} c^\dagger_{\mp K\tau} c_{\Gamma\tau'} c_{\Gamma\tau'} \end{aligned} \tag{4.14}$$

with

$$\tilde{V}^{\tau,\tau'}_{\eta,\eta'}(\mathbf{p},\mathbf{k}) = \frac{1}{2} \sum_{\mu=0,x,y,z} g^{(\mu)}_{\eta,\eta'} Q^{(\mu)}_{\eta\tau}(\mathbf{p}) Q^{(\mu)*}_{\eta'\tau'}(\mathbf{k}) \tag{4.15}$$

$(\eta, \eta' = \Gamma, \pm K)$. Here terms on the right-hand side with $\mu = 0$ are projections of singlet interactions in (4.10), while those with $\mu = j \equiv x, y, z$ are projections of the three triplet interactions respectively, into the relevant Fermi surface. Since spin is not conserved in the presence of SOC and/or magnetic

field, these three spin polarizations are no longer equivalent. Explicitly,

$$\begin{aligned} Q^{(0)}_{\eta\tau}(\mathbf{p}) &= \sum_{\alpha\beta}(i\sigma^y)_{\alpha\beta}U^{\alpha}_{\eta\tau}(\mathbf{p})U^{\beta}_{-\eta\tau}(-\mathbf{p}) \\ Q^{(j)}_{\pm K\tau}(\mathbf{p}) &= \pm\sum_{\alpha\beta}(i\sigma^j i\sigma^y)_{\alpha\beta}U^{\alpha}_{K\tau}(\mathbf{p})U^{\beta}_{-K\tau}(-\mathbf{p}) \\ Q^{(j)}_{\Gamma\tau}(\mathbf{p}) &= \sqrt{2}\cos(3\theta_{\mathbf{p}})\sum_{\alpha\beta}(i\sigma^j i\sigma^y)_{\alpha\beta}U^{\alpha}_{\Gamma\tau}(\mathbf{p})U^{\beta}_{\Gamma\tau}(-\mathbf{p})\ . \end{aligned} \tag{4.16}$$

There is a phase ambiguity in the definitions of $Q^{(\mu)}_{\eta\tau}(\mathbf{p})$; the additional factors of i in the last two expressions are chosen to simplify the gap equation below. Here $g^{(\mu)}_{\eta,\eta'}$ are constants independent of $\mathbf{p}$ and $\mathbf{k}$ (with $j = x, y, z$):

$$\begin{aligned} g^{(0)}_{\Gamma,\Gamma} &= g_1 \qquad g^{(j)}_{\Gamma,\Gamma} = g_1^t \\ g^{(0)}_{\Gamma,\pm K} &= g^{(0)}_{\pm K,\Gamma} = g_4 \\ g^{(j)}_{\Gamma,\pm K} &= g^{(j)}_{\pm K,\Gamma} = g_4^t \\ g^{(0)}_{\pm K,\pm K} &= g^{(0)}_{\pm K,\mp K} = \frac{g_2+g_3}{2} \\ g^{(j)}_{\pm K,\pm K} &= g^{(j)}_{\pm K,\mp K} = \frac{g_2-g_3}{2} \end{aligned} \tag{4.17}$$

where $g_1, ...g_4$ are the values of the couplings at the end of the RG procedure described above.

For uniform SC (i.e. with zero center-of-mass momentum), the paired electrons are either both from inner pockets or both from outer pockets, with corresponding gap functions

$$\begin{aligned} \Delta_{\Gamma\tau}(\mathbf{p}) &\propto \langle c_{\Gamma,\mathbf{p}\tau}c_{\Gamma,-\mathbf{p}\tau}\rangle \\ \Delta_{\pm K\tau}(\mathbf{p}) &\propto \langle c_{\pm K,\mathbf{p}\tau}c_{\mp K,-\mathbf{p}\tau}\rangle \end{aligned} \tag{4.18}$$

where the momentum $\mathbf{p}$ is measured with respect to the center of the relevant Fermi pocket. The gaps are diagonal in the index τ, as we assume there is no pairing between inner and outer Fermi surfaces. Note that particle-hole symmetry imposes $\Delta_{-K\tau}(\mathbf{p}) = -\Delta_{K\tau}(-\mathbf{p})$, so these are not two separate order parameters. The new self-consistent gap equation is (see Section 4.3):

$$\Delta_{\eta\tau}(\mathbf{p}) = \sum_{\eta',\tau'}\oint \Pi_{\eta'\tau'}(\theta_{\eta',\mathbf{k}})\tilde{V}^{\tau,\tau'}_{\eta,\eta'}(\mathbf{p};\mathbf{k})\Delta_{\eta'\tau'}(\mathbf{k})\frac{d\theta_{\eta',\mathbf{k}}}{2\pi} \tag{4.19}$$

After integrating over momenta, the (angle resolved) particle-particle pairing susceptibility $\Pi_{\eta\tau}(\theta_{\eta,\mathbf{p}})$

becomes:

$$\Pi_{\eta\tau}(\theta_{\eta,\mathbf{p}}) = -\sum_p \frac{\tanh\left(\frac{\beta\xi_{\eta\tau}(\mathbf{p})}{2}\right) + \tanh\left(\frac{\beta\xi_{-\eta\tau}(-\mathbf{p})}{2}\right)}{\xi_{\eta\tau}(\mathbf{p}) + \xi_{-\eta\tau}(-\mathbf{p})} \tag{4.20}$$

where $\theta_{\eta,\mathbf{p}}$ is the angle along the τ Fermi surface relative to the center of the pocket η (below we simply use θ when this is clear from context). Assuming that the Fermi surface is inversion symmetric, we find

$$\Pi_{\eta\tau}(\theta_{\eta,\mathbf{p}}) = -N_{\eta\tau} \ln \frac{1.13\Lambda}{T_c} \tag{4.21}$$

with $N_{\eta\tau}$ the density of states at the inner or outer Fermi surface at the η pocket and Λ is the cut-off energy. Although the Fermi surface is only inversion symmetric when $\alpha_R = 0$ or $b = 0$, the expression (4.21) is approximately correct when either is sufficiently small; this issue will be discussed in more detail in Sec. Section 4.2.3.

Plugging Eq. (4.15) into Eq. (4.19), we find

$$\Delta_{\eta\tau}(\mathbf{k}) = \sum_\mu D^{(\mu)}_{\eta\tau} Q^{(\mu)}_{\eta\tau}(\mathbf{p}) \tag{4.22}$$

where $\mathbf{D}_{\eta\tau} = (D^{(0)}_{\eta\tau}, D^{(x)}_{\eta\tau}, D^{(y)}_{\eta\tau}, D^{(z)}_{\eta\tau})$ are momentum independent gap coefficients. The structure of Eq. (4.19) implies that we can take $D^{(\mu)}_{\eta\tau} = D^{(\mu)}_{\eta-\tau} \equiv D^{(\mu)}_{\eta}$, and we thus drop the τ index on D hereafter. Moreover, particle-hole symmetry enforces $D^{(\mu)}_K = D^{(\mu)}_{-K}$, consistent with the fact that $\Delta_{-K\tau}(\mathbf{p}) = -\Delta_{K\tau}(-\mathbf{p})$. Plugging the form (4.22) back into the gap equation (4.19) yields the reduced gap equations

$$\begin{aligned}
D^{(0)}_\Gamma &= \sum_\mu \left(g_1 f^{(0)\Gamma}_{(\mu)} D^{(\mu)}_\Gamma + 2g_4 f^{(0)K}_{(\mu)} D^{(\mu)}_K\right) \\
D^{(0)}_K &= \sum_\mu \left(g_4 f^{(0)\Gamma}_{(\mu)} D^{(\mu)}_\Gamma + (g_2+g_3) f^{(0)K}_{(\mu)} D^{(\mu)}_K\right) \\
D^{(j)}_\Gamma &= \sum_\mu \left(g^t_1 f^{(j)\Gamma}_{(\mu)} D^{(\mu)}_\Gamma + 2g^t_4 f^{(j)K}_{(\mu)} D^{(\mu)}_K\right) \\
D^{(j)}_K &= \sum_\mu \left(g^t_4 f^{(j)\Gamma}_{(\mu)} D^{(\mu)}_\Gamma + (g_2-g_3) f^{(j)K}_{(\mu)} D^{(\mu)}_K\right)
\end{aligned} \tag{4.23}$$

where $j = x, y, z$ and the form factors $f^{(\mu')\eta}_{(\mu)}$ are given by

$$f^{(\mu')\eta}_{(\mu)} = \frac{1}{2}\oint \sum_\tau \Pi_{\eta\tau} Q^{(\mu)*}_{\eta\tau} Q^{(\mu')}_{\eta\tau} \frac{d\theta_{\eta,\mathbf{k}}}{2\pi} \tag{4.24}$$

In the presence of SOC and magnetic field none of the channels ($\mu = 0, x, y, z$) decouple in general. Eqs. (4.23) thus can be viewed as an 8×8 matrix equation, leading to 8 possible superconducting solutions, of which we choose the one with the highest T_c. The choice of phases in Eq. (4.16) was made to make the form factors $f_{(\mu)}^{(\mu')\eta}$ real when the densities of state on inner and outer Fermi surfaces are equal in which case the coefficients $D_\eta^{(\mu)}$ can also be taken to be real.

4.2.2 Phase Diagrams

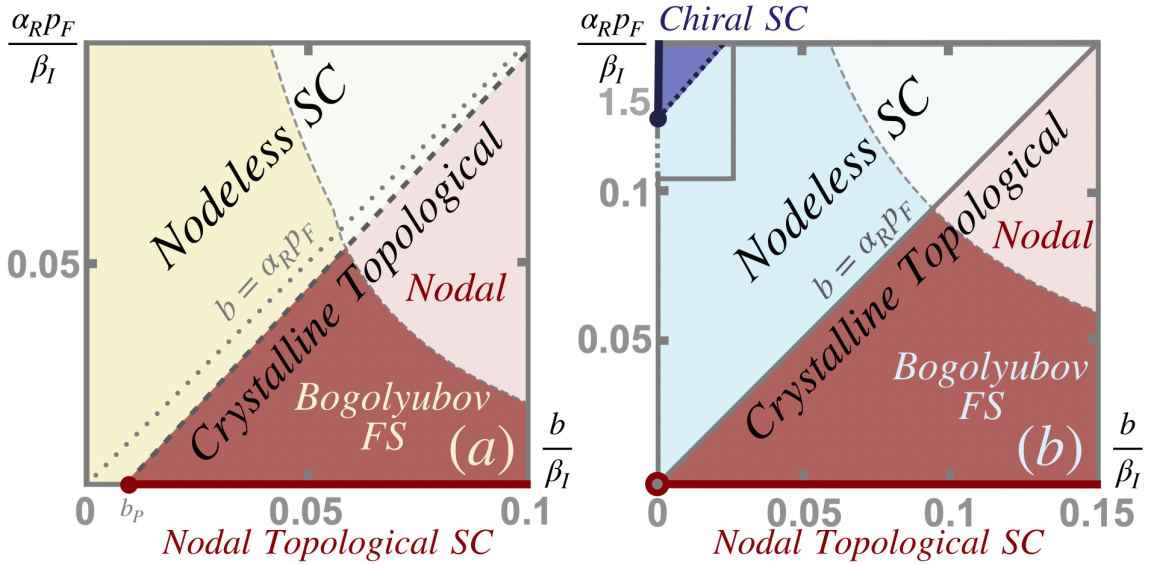

Figure 4.2: Phase diagram for $NbSe_2$ as a function of the Rashba SOC (α_R) and in-plane magnetic field $\mathbf{B}$ oriented along the Γ-K direction, in units of the Ising SOC β_I. The leading SC instability at $\alpha_R = B = 0$ is a singlet extended s-wave state or triplet f-wave state in panel (a) and (b) respectively. Solid (dashed) lines indicate exact (approximate) phase boundaries. Uniform SC becomes unstable in the light-shaded regions, but finite-momentum pairing remains possible. We discuss the phases in more detail in Section 4.2.2. For parameter values we used $m = 1.5\frac{p_F^2}{\beta_I}, \mu = -5\beta_I, \lambda = 0.5\beta_I$ and values listed in (4.26).

To study the possible superconducting phases, it is useful to define singlet and triplet instability regimes by considering the limit of no SOC and magnetic field. We define a dominant singlet (dominant triplet) instability to occur when the largest eigenvalue of the gap equation is for the spin singlet (spin triplet) gap with SOC and magnetic field set to 0. The transition temperature for each channel (when the corresponding eigenvalue of the gap equation equals 1) is determined by the

couplings $g_1, ...g_4$ via

$$T_c^{(a)} = 1.13\Lambda e^{-1/\gamma^{(a+)}} \ , \tag{4.25}$$

where Λ is the upper energy cutoff, and $\gamma^{(a+)}$ are identical to the couplings obtained in the RG analysis in Eq. (2.125) ($a = s, t$ for singlet and triplet respectively). Figure 4.2 shows the phase diagrams corresponding to singlet (a) and triplet (b) instability regimes as a function of Rashba SOC and in-plane magnetic field. We emphasize that the resulting SC states themselves are always a mixture of singlet and triplet Cooper pairs.

With equal DOS in all bands, for repulsive interactions the singlet instability dominates for large g_4, while the triplet instability dominates for large g_3. For concreteness, in this section we take

$$g_2 = 1.2g_1, \quad g_4 = 2g_1, \quad g_1^t = 0.2g_1, \quad g_4^t = 0.1g_1 \tag{4.26}$$

with $g_3 = 1.05g_1$ ($4.2g_1$) to produce a singlet (triplet) instability.

To describe the phase diagrams in Figure 4.2, it is useful to classify the solutions to the gap equations (4.22) by the irreducible representations (irreps) of the relevant point group. In the absence of Rashba SOC and magnetic field, the point group of 1H-$NbSe_2$ is D_{3h} [1]. We find that the $\mu = 0, z$ terms on the right-hand side of Eq. (4.22) both belong to the A_1' irrep of D_{3h}, indicating that the singlet and z-polarized spin-triplet gaps are mixed in the presence of Ising SOC. In our model, this mixing is proportional to the difference between the densities of states $N_{\eta\tau}$ on the inner ($\tau = -1$) and outer ($\tau = 1$) Fermi surfaces. Since these densities of states are not expected to differ significantly in two dimensions, this mixing is weak in our model. The remaining components $\mu = x, y$ of the triplet gap transform as the two dimensional E'' irrep of D_{3h}. We find that, in the absence of both Rashba SOC and magnetic field, the highest T_c corresponds to the A_1' irrep in our model.

Rashba SOC transforms as the A_2'' irrep of D_{3h}. This lowers the point group to C_{3v}, but does not mix the A_1' and E'' gaps. In contrast, the in-plane magnetic field $\mathbf{b}$ transforms according to the E'' irrep of D_{3h}. As a result, it mixes the E'' gap with the A_1' one [109]. Thus, in the presence of an in-plane magnetic field, all μ terms in Eq. (4.22) are mixed.

The electronic spectrum in the superconducting phase is obtained by diagonalizing the Bogolyubov-

[1] The relevant functional forms for the gap in each irrep can be found in the spin basis in Ref. [109]; these are related to our gaps by the basis transformation (4.6).

de Gennes (BdG) Hamiltonian:

$$H = \frac{1}{2}\sum_{\mathbf{p}\eta\tau} \Psi^{\dagger}_{\mathbf{p}\eta\tau}\mathcal{H}_{\eta\tau}(\mathbf{p})\Psi_{\mathbf{p}\eta\tau} \tag{4.27}$$

where $\Psi_{\eta\tau}(\mathbf{p}) = (c_{\eta,\mathbf{p}\tau}, c^{\dagger}_{-\eta,-\mathbf{p}\tau})^T$ and

$$\mathcal{H}_{\eta\tau}(\mathbf{p}) = \begin{pmatrix} \xi_{\eta\tau}(\mathbf{p}) & \Delta_{\eta\tau}(\mathbf{p}) \\ \Delta^{*}_{\eta\tau}(\mathbf{p}) & -\xi_{-\eta\tau}(-\mathbf{p}) \end{pmatrix} \tag{4.28}$$

with $\xi_{\eta\tau}(\mathbf{p})$ given in Eq. (4.8). Note that when time reversal symmetry (TRS) is broken, $\xi_{-\eta\tau}(-\mathbf{p}) \neq \xi_{\eta\tau}(\mathbf{p})$ in general. The BdG spectra are given by $E_{\eta\tau}(\mathbf{p}), -E_{-\eta\tau}(-\mathbf{p})$, with:

$$E_{\eta\tau}(\mathbf{p}) = \xi_{A\eta\tau}(\mathbf{p}) + \sqrt{\xi_{S\eta\tau}(\mathbf{p})^2 + |\Delta_{\eta\tau}(\mathbf{p})|^2} \tag{4.29}$$

where

$$\xi_{S\eta\tau}(\mathbf{p}) = \frac{\xi_{\eta\tau}(\mathbf{p}) + \xi_{-\eta\tau}(-\mathbf{p})}{2} \tag{4.30}$$

$$\xi_{A\eta\tau}(\mathbf{p}) = \frac{\xi_{\eta\tau}(\mathbf{p}) - \xi_{-\eta\tau}(-\mathbf{p})}{2} \tag{4.31}$$

Clearly, nodes only occur if both $\xi_{S\eta\tau}$ and $\Delta_{\eta\tau}$ vanish simultaneously. Note that, in our case, the Fermi surface is symmetric under momentum inversion, $\mathbf{p} \to -\mathbf{p}$, only when either α_R or b vanish. In this case, $\xi_{A\eta\tau} = 0$ and $\xi_{S\eta\tau} = \xi_{\eta\tau}$.

We are now in position to describe the SC phase diagrams of Figure 4.2, obtained for a fixed value of the Ising SOC and varying the magnitude of the magnetic field b and Rashba SOC α_R. In all cases, the gap at the $\pm K$ pockets is nearly isotropic, so we focus on the Γ pocket. We first analyze the phase diagram of Figure 4.2(a), where the dominant g_4 interaction gives the singlet extended s-wave state in the limit of vanishing SOC and magnetic field. Along the $b = 0$ axis, the main effect of increasing the Rashba SOC α_R is to change the anisotropy of $\Delta_{\Gamma\tau}(\mathbf{p})$, due to the small admixture with the $\mu = z$ nodal triplet gap. Importantly, no phase transition happens along this axis, as the dominant instability is always in the A_1' irrep of the original D_{3h} point group. In contrast, along the $\alpha_R = 0$ axis, a phase transition takes place to a nodal topological SC state for $b = b_P$, where $b_P \approx \Delta_{\Gamma 1}$ corresponds roughly to the Pauli-limiting field [24, 36]. Because our assumption of well-separated Fermi surfaces is not valid for fields smaller than b_P, our analysis is not sufficient to determine the phase boundary quantitatively, but we show it qualitatively in

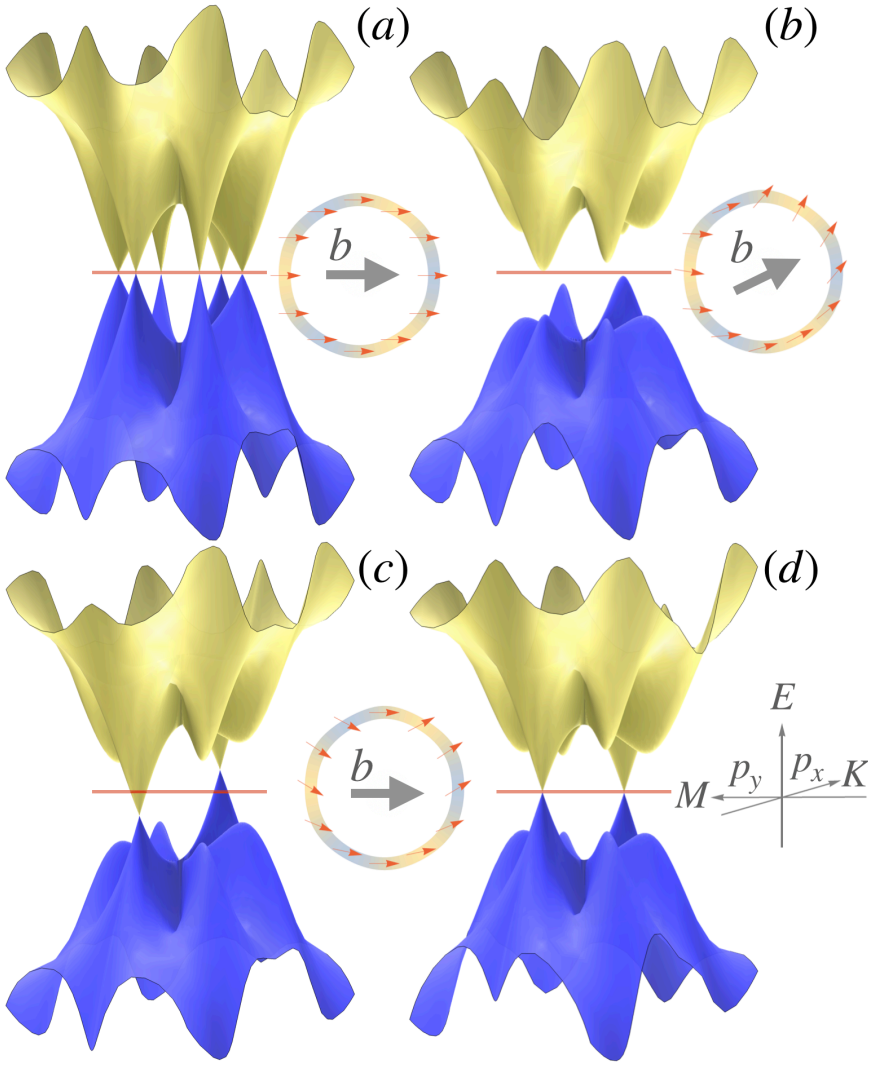

Figure 4.3: Superconducting excitation spectrum, Eq. (4.29), for the inner Fermi surface at Γ in the presence of an in-plane magnetic field and without (panel a) or with (panels b, c, d) Rashba SOC. In panel b (panels c and d), **B** is aligned along $\vartheta = \pi/7$ ($\vartheta = 0$) from the Γ-K lines; panel a is the same for any field direction. In panel c (panel d), the Cooper pair has zero (non-zero) center-of-mass momentum. Insets show the resulting spin textures along the normal-state Fermi surfaces for the corresponding field directions, with colors as in Figure 4.1 and arrows indicating in-plane spin components. We used the normal state dispersion from Eq. (4.2) with the same parameter values given in Figure 4.2, and took $b = 5\beta_I$, as well as $\alpha_R = 2\beta_I$ in panels b-d. We set $D^{(0)}_{\Gamma,-1} = 20\beta_I$ and $D^{(z)}_{\Gamma,-1} = 20\beta_I$ in Eq. (4.22), and $p_{\text{shift}} = -0.3p_F$ in panel d.

Figure 4.2(a). This phase transition, and the topological character of the resulting nodal SC state, were previously predicted in Ref. [62] and can be understood as a consequence of the vanishing of the Ising SOC along the six Γ-M directions, where the SC gap vanishes and 12 nodes (6 for each Γ Fermi surface) appear due to spins aligning with the magnetic field. This gap structure is shown in the BdG spectrum of the inner Γ Fermi surface, displayed in Figure 4.3(a) together with the spin texture of the normal-state Fermi surface.

Turning on the Rashba SOC introduces a second spin-orbit energy scale that does not vanish along the Γ-M directions. As a result, generally even an infinitesimal Rashba SOC lifts the nodes and destroys the topological character of this state, as shown by the fully gapped BdG spectrum in Figure 4.3(b). The only exception is when $\mathbf{b}$ is aligned along one of the Γ-K directions: in this case, as we discuss in detail in Section 4.4.2, the system has a mirror symmetry. For $\alpha_R p_F < b$, this symmetry forces spins along the Γ-M line perpendicular to $\mathbf{b}$ to align (anti-align) with the magnetic field on the inner (outer) Γ pocket, as shown in the inset of Figure 4.3(c). As a consequence, the gap vanishes along the line perpendicular to $\mathbf{b}$, as displayed by the BdG spectrum of Figure 4.3(c). Therefore, two pairs of nodes originally present on this line are protected, whereas the remaining eight nodes are gapped, resulting in a *crystalline* gapless topological SC state. Because the Fermi surfaces are no longer symmetric under momentum inversion (i.e. $\xi_{A\eta\tau} \neq 0$), these protected nodes are generally shifted away from the Fermi level, resulting in the Bogolyubov Fermi surfaces shown in Figure 4.3(c). As we discuss in the next section, however, the nodes can move back to the Fermi level if the Cooper pair acquires a finite center-of-mass momentum, which is expected to happen for large enough b and α_R (Figure 4.3(d)). For $\alpha_R p_F > b$, however, the pair of nodes on the inner and outer Fermi surfaces merge and the superconducting state becomes fully gapped. While we could not precisely locate this phase boundary, it is expected to interpolate between $b = \alpha_R p_F$ for large values of α_R to $b = b_P$ for $\alpha_R = 0$, as shown by the dashed line in Figure 4.2(a). The evolution of the gap at the outer Γ Fermi surface across this transition is shown in Figure 4.4(a) and (b). In panel (a), the magnetic field is applied along a direction that does not coincide with the $\Gamma - K$ direction. As a result, the nodal superconducting state only exists for $\alpha_R = 0$ (red curve). In contrast, when the magnetic field is applied along the $\Gamma - K$ direction (panel (b)), two nodes persist even when $\alpha_R \neq 0$ (dark orange curve).

We now turn to the case of dominant triplet instability shown in Figure 4.2(b), obtained for a dominant g_3 interaction. As in the singlet regime, we observe a nodal topological superconductor for $\alpha_R = 0$. In the triplet regime, however, the superconducting gap on the Γ pocket is nodal along the entire $\alpha_R = 0$ line (except for very small magnetic fields, where the small difference in density of

states on the inner and outer Fermi surfaces can open a gap); hence the nodal topological SC state occurs for all values of b, as there is no Pauli limit in this case [24, 36]. Similarly, the transition into the crystalline nodal topological phase happens close to the $\alpha_R p_F = b$ line.

Along the $b = 0$ line, the nodes on the Γ pocket in the $\mu = z$ triplet state are lifted due to the admixture with the sub-leading s-wave $\mu = 0$ state generated by Ising SOC, resulting in an anisotropic gap. This is shown in Figure 4.4(c), which presents the evolution of $\Delta_{\Gamma 1}(\mathbf{p})$ along the $b = 0$ axis for increasing α_R. Note that to generate singlet-triplet mixing, we must include a small difference between the inner and outer DOS in the plots of Figure 4.4; the magnitude of this mixing increases with α_R. Thus, although the superconducting gap on Γ in the triplet regime remains strongly modulated as a function of angle for modest α_R (see Figure 4.4(c)), the superconducting phase in this region is nonetheless fully gapped.

For large values of α_R (of the order of the Ising SOC), the dominant instability shifts from being in the A_1 irrep of C_{3v} (previously the A_1' irrep of the original D_{3h} group) to the 2-dimensional E irrep (previously the E'' irrep of the original D_{3h} group). As a result, a new chiral $p \pm ip$ superconducting state emerges in the triplet regime at $b = 0$. The chiral phase, shown in Figure 4.4(d), occurs because in this 2-dimensional irrep the free energy is minimized by a spontaneous breaking of time reversal symmetry, as we discuss in Section 4.3.1. This is in agreement with the general result in [137, 148]. As we show in Section 4.3.1, this results in a gapped chiral topological SC with gapless chiral edge modes resulting in a thermal Hall conductance $\kappa_{xy} = \pm 6\left(\pi^2 k_B^2/3h\right) T$ [130]. This topological SC phase survives for sufficiently small in-plane magnetic fields, but our approach is insufficient to quantitatively obtain the phase boundary (see blue dashed line in Figure 4.2(b)).

4.2.3 Broken Momentum Inversion Symmetry: Bogolyubov Fermi Surfaces and Finite-Momentum Pairing

In the presence of both α_R and b, the Fermi surfaces are no longer inversion-symmetric under $\mathbf{p} \to -\mathbf{p}$. The key quantity that measures the degree of symmetry breaking is

$$\xi_{A\eta\tau}(\mathbf{p}) = \frac{\xi_{\eta\tau}(\mathbf{p}) - \xi_{-\eta\tau}(-\mathbf{p})}{2} \tag{4.32}$$

previously defined in Eq. (4.31). Here we discuss two important consequences of this inversion symmetry breaking for the crystalline topological SC state. First, within the crystalline topological SC state, breaking inversion symmetry moves the two nodes on the same Fermi surface at Γ in opposite directions away from the Fermi level. This follows directly from Eq. (4.29) as the nodes

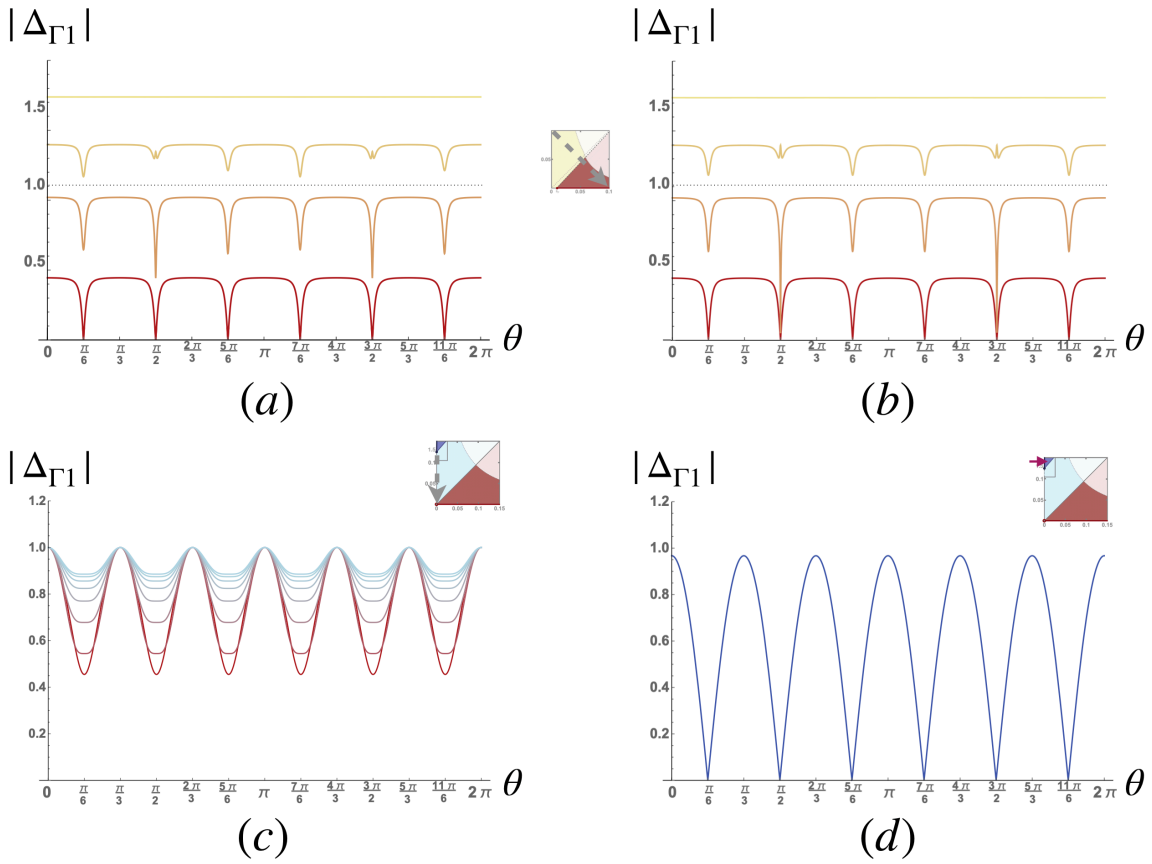

Figure 4.4: Superconducting gap $\Delta_{\Gamma 1}$ in Eq. (4.22) at the outer Γ pocket, as a function of the angle θ along the Fermi surface with respect to the Γ-K direction, in various regions of the phase diagrams of Figure 4.2. Panels (a) and (b) correspond to the cuts across the phase diagram of Figure 4.2(a) shown in the insets, with a magnetic field away from the Γ-K direction by an angle $\vartheta = 2\pi/25$ (panel (a)) and along the Γ-K direction (panel (b)). Panels (c) and (d) correspond to cuts along the $b = 0$ axis of the phase diagram of Figure 4.2(b), outside and inside the chiral SC phase, respectively (see insets). Note that the gap amplitudes have been rescaled for clarity, since they are not fixed by the linearized gap equations. We used coupling constants given in Eq. (4.26) and parameters for the non-interacting Hamiltonian as in Figure 4.2. We also took the inner and outer densities of states to differ by ten percent to ensure that the symmetry allowed mixings between the singlet and triplet channels are present in our solutions.

move by an energy $\xi_{A\Gamma\tau}(\mathbf{p}_{node})$. As we showed in Figure 4.3(c), this results in the nodes 'inflating' into Bogolyubov Fermi surfaces (*cf.* [7, 20, 194, 167]). These Fermi surfaces are protected by mirror symmetry, due to the topological stability of the band crossings in the BdG spectrum, as we show in the next section.

Second, breaking momentum inversion symmetry cuts off the Cooper logarithm in the particle-particle bubble in Eq. (4.21). As a result, the pairing interaction must be larger than a certain threshold, proportional to how much inversion symmetry is broken, for a uniform SC state to onset. To show this explicitly, we evaluate the particle-particle bubble in Eq. (4.20) in the absence of inversion symmetry. Assuming that $\xi_{A\eta\tau}$ is a function only of the direction θ around the Fermi surface, in the limit of $\Lambda \gg \xi_{A\eta\tau}$ we find

$$\frac{\Pi_{\eta\tau}(\theta)}{N_{\eta\tau}} = -\ln\frac{1.13\Lambda}{T_c} + \mathrm{Re}\left[\psi\left(\frac{1}{2} + \frac{i\xi_{A\eta\tau}(\theta)}{2\pi T_c}\right) - \psi\left(\frac{1}{2}\right)\right] \tag{4.33}$$

where ψ is the digamma function. As a result, at zero temperature

$$\Pi_{\eta\tau}(\theta) = -N_{\eta\tau}\ln\frac{\Lambda}{|\xi_{A\eta\tau}(\theta)|} \tag{4.34}$$

i.e. the infrared logarithmic divergence originally present is cutoff by $|\xi_{A\eta\tau}(\theta)|$. This means that there is a critical value of the parameter $\xi^c_{A\eta\tau}$ beyond which uniform SC is no longer stable. The resulting critical lines are shown in Figure 4.2 and for a larger range in Figure 4.5 for both singlet and triplet instabilities. Note that because this is a multi-band superconductor, the critical line has a (weak) dependence on the cutoff Λ.

The general shape of the critical lines can be understood from a simple approximation, noting that

$$\xi_{A\eta\tau}(\mathbf{p}) = \frac{\tau}{2}\left(\beta_\eta(\mathbf{p}) - \beta_{-\eta}(-\mathbf{p})\right), \tag{4.35}$$

where β_η are functions of $\alpha_R p_F$ and b as given in (4.4). For $\alpha_R p_F, b \ll \beta_I$,

$$\xi_{A\eta\tau}(\mathbf{p}) \approx \tau\frac{\alpha_R p_F b}{\beta_I}\sin(\theta - \vartheta) \tag{4.36}$$

where β_I is the Ising SOC on the relevant pocket and ϑ is the direction of the magnetic field. From (4.34), we can estimate that the characteristic scale of $\xi^c_{A\eta\tau}$, properly averaged, is of the order $T_{c0}/1.13$, where T_{c0} is the solution of the gap equation when $\xi^c_{a\eta\tau} = 0$, see Eq. (4.21). The critical

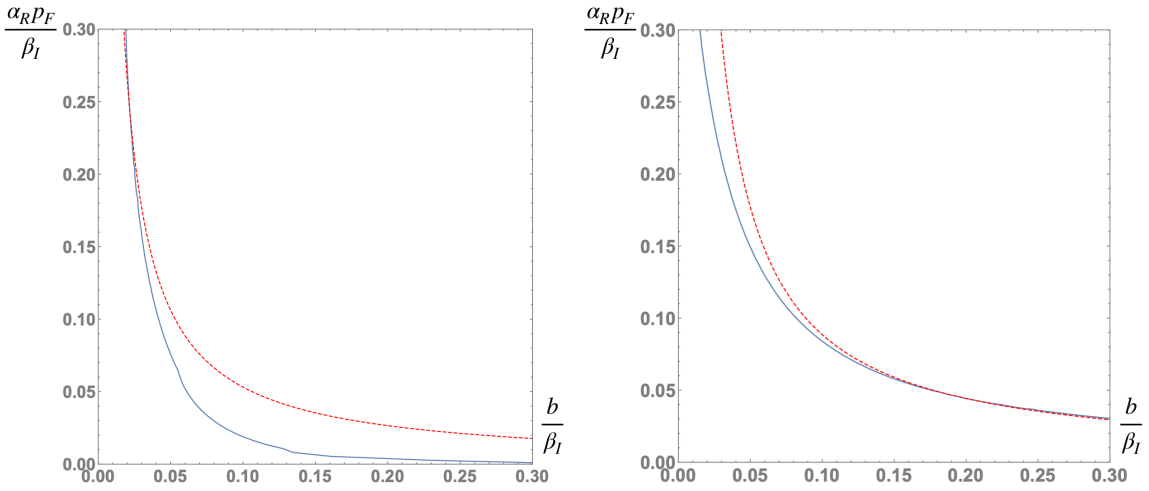

Figure 4.5: Critical lines above which uniform SC becomes unstable for the singlet (left) and triplet (right) phase diagrams shown in Figure 4.2. Blue line is the numerical solution from the full gap equation, while the red dashed line is given by the approximation $\alpha_R p_F b = \frac{\beta_I T_{c0}}{1.13}$. In addition to the parameters used in Figure 4.4, we took $T_c = 0.01\beta_I$ and $\Lambda = 25\beta_I$, roughly corresponding to the observed values [187, 40, 110].

curve is thus roughly given by

$$\alpha_R p_F b \sim \frac{\beta_I T_{c0}}{1.13} \tag{4.37}$$

As shown in Figure 4.5, this approximation reasonably captures the exact result for the critical line.

For inversion symmetry breaking exceeding the critical value, where the uniform SC state is no longer stable, superconductivity with finite center-of-mass momentum $\mathbf{p}_{\text{shift}} \neq 0$, i.e. a so-called FFLO phase [3, 85, 94], is still possible. Note that the momentum shift is not necessarily equal for each Fermi surface, so more generally there are four parameters $\mathbf{p}_{\text{shift},\eta\tau}$. Depending on whether $\mathbf{p}_{\text{shift},\eta\tau} = \mathbf{p}_{\text{shift},\eta-\tau}$ or $\mathbf{p}_{\text{shift},\eta\tau} = -\mathbf{p}_{\text{shift},\eta-\tau}$, the FFLO phase is classified as helical and stripe, respectively, and may even compete with the uniform SC phase below the threshold curve in the $(\alpha_R p_F, b)$ plane [3]. Ultimately, the four parameters $\mathbf{p}_{\text{shift},\eta\tau}$ must be obtained by minimization of the free energy, which is a computationally involved task beyond the scope of our work. It is interesting to note, however, that by matching $\mathbf{p}_{\text{shift}}$ with the geometric shift of the center of the corresponding Fermi surface, the nodes of the superconducting ground state move back to the Fermi level since the shift compensates for the finite $\xi_{A\eta\tau}$, as shown in Figure 4.3(d). Because this configuration maximizes the gap around the Fermi surface, it is expected to maximize the condensation energy. In any case, as we show in the next section, the finite momentum pairing does not affect the topological

properties of the SC phase.

4.3 Ginzburg-Landau Free Energy and Time-Reversal Symmetry Breaking

Here we write down the Ginzburg-Landau free energy in the presence of SOC and magnetic field to analyze spontaneous TRS breaking. We start with the Bogolyubov-Gor'kov Hamiltonian obtained after doing a Hubbard-Stratonovich transformation:

$$H = \frac{1}{2}\sum_{\mathbf{p}\eta\tau} \Psi^{\dagger}_{\mathbf{p}\eta\tau}\mathcal{H}_{\eta\tau}(\mathbf{p})\Psi_{\mathbf{p}\eta\tau} + \frac{1}{2}\sum_{\mathbf{p}\eta\tau}\xi_{\eta\tau}(\mathbf{p}) + \mathcal{H}_0\left(\Delta^2\right) \tag{4.38}$$

where

$$\mathcal{H}_0\left(\Delta^2\right) = -\frac{1}{4}\sum_{\substack{\mathbf{p}\eta\tau \\ \mathbf{k}\eta'\tau'}} \Delta^{*}_{\eta\tau}(\mathbf{p})\left(\tilde{V}^{-1}(\mathbf{p};\mathbf{k})\right)^{\eta'\tau'}_{\eta\tau}\Delta_{\eta'\tau'}(\mathbf{k}) \tag{4.39}$$

and where we use the Nambu-Gor'kov representation $\Psi_{\eta\tau}(\mathbf{p}) = (c_{\eta,\mathbf{p}\tau}, c^{\dagger}_{-\eta,-\mathbf{p}\tau})^T$ and the BdG Hamiltonian Eq. (4.28). Recall that the BdG spectrum has two branches, $E_{\eta\tau}(\mathbf{p})$ and, by particle-hole symmetry, $-E_{-\eta\tau}(-\mathbf{p})$. Using the fact that

$$\det\left[-i\omega + \mathcal{H}_{\eta\tau}(\mathbf{p})\right] = \left(-i\omega + E_{\eta\tau}(\mathbf{p})\right)\left(-i\omega - E_{-\eta\tau}(-\mathbf{p})\right) \tag{4.40}$$

we obtain the Ginzburg-Landau free energy:

$$\mathcal{F} = -\frac{T}{2}\sum_{\mathbf{p}\eta\tau}\ln\left[2\cosh\left(\frac{\beta E_{\eta\tau}(\mathbf{p})}{2}\right)\right] - \frac{T}{2}\sum_{\mathbf{p}\eta\tau}\ln\left[2\cosh\left(\frac{\beta E_{-\eta\tau}(-\mathbf{p})}{2}\right)\right] + \mathcal{H}_0\left(\Delta^2\right) \tag{4.41}$$

To obtain the linearized gap equation we expand $\mathcal{F}$ to first order in $|\Delta_{\eta\tau}|^2$, which yields

$$\mathcal{F}^{(2)} = -\sum_{\mathbf{p}\eta\tau}\frac{\tanh\left(\frac{\beta\xi_{\eta\tau}(\mathbf{p})}{2}\right) + \tanh\left(\frac{\beta\xi_{-\eta\tau}(-\mathbf{p})}{2}\right)}{4\xi_{S\eta\tau}(\mathbf{p})}|\Delta_{\eta\tau}(\mathbf{p})|^2 + \mathcal{H}_0\left(\Delta^2\right) \tag{4.42}$$

Minimizing the free energy Eq. (4.42) with respect to $\Delta^{*}_{\eta\tau}(\mathbf{p})$, we obtain the gap equation (4.19).

4.3.1 Spontaneous Time-Reversal Symmetry Breaking

As we discussed above, at zero magnetic field and in the dominant triplet instability regime, at large $\alpha_R p_F$ the leading superconducting instability is in the two-dimensional E irrep of the point group C_{3v}. Here we show that this state spontaneously breaks time-reversal symmetry (TRS) and compute its Chern number to show that it is a chiral topological state.

We begin by observing that for $b = 0$, and assuming equal densities of states on inner and outer Fermi surfaces, the reduced gap equation (4.23) can be solved analytically, giving:

$$\begin{aligned}
\Delta^{(0)}_{\Gamma\tau}(\mathbf{p}) &= \tau i e^{-i\theta} D^{(0)}_{\Gamma} \\
\Delta^{(0)}_{\pm K\tau}(\mathbf{p}) &= \tau i e^{-i\theta} D^{(0)}_{K} \\
\Delta^{(z)}_{\Gamma\tau}(\mathbf{p}) &= \sqrt{2} i e^{-i\theta} \cos^2 3\theta \frac{\lambda p_F^3}{\beta_\eta(\mathbf{p})} D^{(z)}_{\Gamma} \\
\Delta^{(z)}_{\pm K\tau}(\mathbf{p}) &= \pm i e^{-i\theta} \frac{\beta_I}{\beta_\eta(\mathbf{p})} D^{(z)}_{K} \\
\Delta^{(x)}_{\Gamma\tau}(\mathbf{p}) &= \sqrt{2} i e^{-i\theta} \sin\theta \ \cos 3\theta \frac{\alpha_R p_F}{\beta_\eta(\mathbf{p})} D^{(x)}_{\Gamma} \\
\Delta^{(x)}_{\pm K\tau}(\mathbf{p}) &= \pm i e^{-i\theta} \sin\theta \ \frac{\alpha_R p_F}{\beta_\eta(\mathbf{p})} D^{(x)}_{K} \\
\Delta^{(y)}_{\Gamma\tau}(\mathbf{p}) &= \sqrt{2} i e^{-i\theta} \cos\theta \ \cos 3\theta \frac{\alpha_R p_F}{\beta_\eta(\mathbf{p})} D^{(y)}_{\Gamma} \\
\Delta^{(y)}_{\pm K\tau}(\mathbf{p}) &= \pm i e^{-i\theta} \cos\theta \ \frac{\alpha_R p_F}{\beta_\eta(\mathbf{p})} D^{(y)}_{K}
\end{aligned} \tag{4.43}$$

At large α_R, there is a transition from a mixed $D^{(0)}, D^{(z)}$ solution to a solution with $D^{(0)} = D^{(z)} = 0$, $D^{(x,y)} \neq 0$. This solution belongs to the 2D E irrep of C_{3v}, the relevant point group in this regime. In other words, the (x) and (y) solutions are degenerate, i.e. have the same T_c.

This degeneracy opens the possibility of spontaneous time-reversal symmetry breaking at $b = 0$. In the SOC basis (4.6), TRS acts as

$$\begin{aligned}
c_{\eta,\mathbf{p}\tau} &\xrightarrow{\mathcal{T}} i\tau e^{i\theta} c_{-\eta,-\mathbf{p}\tau} \\
\Delta_{\eta\tau}(\mathbf{p}) c^\dagger_{\eta,\mathbf{p}\tau} c^\dagger_{-\eta,-\mathbf{p}\tau} &\xrightarrow{\mathcal{T}} -e^{-2i\theta} \Delta^*_{\eta\tau}(\mathbf{p}) c^\dagger_{\eta,\mathbf{p}\tau} c^\dagger_{-\eta,-\mathbf{p}\tau}.
\end{aligned} \tag{4.44}$$

Taking $\Delta_{\eta\tau}(\mathbf{p}) = e^{i\Phi_{\eta\tau}(\mathbf{p})} |\Delta_{\eta\tau}(\mathbf{p})|$, TRS is therefore satisfied when $e^{i\Phi_{\eta\tau}(\mathbf{p})} = \pm i e^{-i\theta}$.

In the linearized gap equation (4.19), since the $\mu = x$ and $\mu = y$ channels are degenerate (i.e. they have equal critical temperatures), in principle the relative amplitudes and phases of $D^{(x)}_\eta$ and $D^{(y)}_\eta$ are not fixed (i.e. any linear combination of the two solutions is allowed). This is no longer the

case if we consider the non-linear gap equations. Alternatively, in terms of the Ginzburg-Landau free energy (4.41), the relative amplitudes and phases are fixed by the quartic terms in the gap functions. Since $b = 0$, $\xi_{\eta\tau}(-\mathbf{p}) = \xi_{\eta\tau}(\mathbf{p})$, the free energy simplifies to

$$\mathcal{F} = -T\sum_{\mathbf{p}\eta\tau} \ln\left[2\cosh\left(\frac{\beta E_{\eta\tau}(\mathbf{p})}{2}\right)\right] + \mathcal{H}_0\left(\Delta^2\right) \tag{4.45}$$

Expanding in powers of the gap function, we obtain the fourth order correction (in addition to (4.42)):

$$\mathcal{F}^{(4)} = \frac{7\zeta(3)}{64\pi^2 T^2}\sum_{\eta\tau}\int N_{\eta\tau}\left|\Delta_{\eta\tau}(\mathbf{p})\right|^4 \frac{d\theta_{\mathbf{p}}}{2\pi} \tag{4.46}$$

where $\zeta(x)$ is the Riemann zeta function. Substituting the general form of the gap function in the (x),(y) channel:

$$\begin{aligned}
\Delta_{\Gamma\tau}(\mathbf{p}) &= \sqrt{2}ie^{-i\theta}\cos 3\theta\frac{\alpha_R p_F}{\delta_\eta(\mathbf{p})}\left(D_\Gamma^{(x)}\cos\theta + D_\Gamma^{(y)}\sin\theta\right)\\
\Delta_{\pm K\tau}(\mathbf{p}) &= \pm ie^{-i\theta}\frac{\alpha_R p_F}{\delta_\eta(\mathbf{p})}\left(D_K^{(x)}\cos\theta + D_K^{(y)}\sin\theta\right)
\end{aligned}$$

and approximating $\frac{\alpha_R p_F}{\delta_\eta(\mathbf{p})} \approx 1$ (which is valid as long as $\alpha_R p_F \gg \lambda p_F^3$), we obtain:

$$\begin{aligned}
\mathcal{F}^{(4)} = \frac{7\zeta(3)}{2048\pi^2 T^2}\sum_{\eta\tau} N_{\eta\tau}\Bigg[&3\left(\left|D_\eta^{(x)}\right|^2 + \left|D_\eta^{(y)}\right|^2\right)^2\\
&-4\left|D_\eta^{(x)}\right|^2\left|D_\eta^{(y)}\right|^2\sin^2\phi_{xy}\Bigg]
\end{aligned} \tag{4.47}$$

where ϕ_{xy} is the relative phase between $D_\eta^{(x)}$ and $D_\eta^{(y)}$. Minimization gives $\phi_{xy} = \pm\frac{\pi}{2}$, which implies that the superconducting gap has the form

$$\begin{aligned}
\Delta_{\Gamma\tau}(\mathbf{p}) &\propto \sqrt{2}i\cos 3\theta\frac{\alpha_R p_F}{\delta_\eta(\mathbf{p})}e^{-i(\theta\mp\theta)}\\
\Delta_{\pm K\tau}(\mathbf{p}) &\propto \pm i\frac{\alpha_R p_F}{\delta_\eta(\mathbf{p})}e^{-i(\theta\mp\theta)}
\end{aligned} \tag{4.48}$$

which is not invariant under the time-reversal symmetry transformation (4.44). We thus find that time reversal is spontaneously broken, in agreement with the general result in [137, 148] (a similar TRS-breaking from higher order terms in the free energy has also been found in [101, 64]). Note

that while $\Delta_{\Gamma\tau}(\mathbf{p})$ obtained from our calculation is nodal, there is an additional symmetry allowed term $\Delta^{(3)} = e^{3i\theta}$ that belongs to the same E irreducible representation. Adding this term lifts the nodes and results in a fully gapped, time-reversal symmetry broken phase.

4.4 Topology of the Phases

Above we found three kinds of topological phases: a chiral SC phase in presence of Rashba SOC, a nodal topological phase protected by a time-reversal like symmetry $\tilde{\mathcal{T}}$ in presence of an in-plane magnetic field, and a crystalline nodal topological phase protected by a vertical mirror symmetry $\mathcal{M}_x$ in presence of both.We now discuss their topological properties using some of what we learned in Chapter 3.

4.4.1 Chiral SC

Above we found that at large Rashba SOC and with dominant triplet interactions the SC phase breaks TRS. To show that it is a topological chiral phase, we need to compute its Chern number, which as we saw in Section 3.4 relates to the winding of its phase around the Fermi surface. Recall that the Chern number is given by

$$Ch = \frac{1}{2\pi} \sum_{\eta\tau} \int_{BZ} \mathbf{F}_{\eta\tau}(\mathbf{p}) \cdot d^2\mathbf{p} \tag{4.49}$$

where the Berry curvature vector is given by

$$\mathbf{F}_{\eta\tau}(\mathbf{p}) = \boldsymbol{\nabla} \times \mathbf{A}_{\eta\tau}(\mathbf{p}) \tag{4.50}$$

with $\mathbf{A}_{\eta\tau}(\mathbf{p})$ the Berry vector potential or connection associated with the occupied (i.e. particle) band only. For a superconductor, the Berry connection is defined in terms of the normalized eigenvectors of the BdG Hamiltonian (4.28): $\Upsilon_{\eta\tau}(\mathbf{p}) = u_{\eta\tau}(\mathbf{p}) c_{\eta,\mathbf{p}\tau} + v_{\eta\tau}(\mathbf{p}) c^{\dagger}_{-\eta,-\mathbf{p}\tau}$, via

$$A_{\eta\tau}(\mathbf{p}) = i\langle \Upsilon_{\eta\tau}(\mathbf{p}) | \nabla_{\mathbf{p}} | \Upsilon_{\eta\tau}(\mathbf{p}) \rangle. \tag{4.51}$$

It is important to note that in our case the $c_{\eta,\mathbf{p}\tau}$ operators themselves carry a nontrivial Berry phase due to the momentum-dependent change of basis (this is analogous to using a non-inertial frame of reference). One should therefore consider $|\Upsilon_{\eta\tau}(\mathbf{p})\rangle$ as a four component eigenvector in a basis of Nambu-Gor'kov 4-spinors $\Psi^{(4)}_{\eta\tau}(\mathbf{p}) = (d_{\eta,\mathbf{p}\uparrow}, d_{\eta,\mathbf{p}\downarrow}, d^{\dagger}_{-\eta,-\mathbf{p}\uparrow}, d^{\dagger}_{-\eta,-\mathbf{p}\downarrow})^T$. Using the change of basis

(4.6), we find

$$|\Upsilon_{\eta\tau}\rangle = \begin{pmatrix} U^1_{\eta\tau}(\mathbf{p})u_{\eta\tau}(\mathbf{p}) \\ U^{-1}_{\eta\tau}(\mathbf{p})u_{\eta\tau}(\mathbf{p}) \\ U^{1*}_{-\eta\tau}(-\mathbf{p})v_{\eta\tau}(\mathbf{p}) \\ U^{-1*}_{-\eta\tau}(-\mathbf{p})v_{\eta\tau}(\mathbf{p}) \end{pmatrix}. \tag{4.52}$$

where $u_{\eta\tau}$ and $v_{\eta\tau}$ are found to be

$$u_{\eta\tau}(\mathbf{p}) = \frac{\xi_{\eta\tau} - E_{\eta\tau}(\mathbf{p})}{\sqrt{\left(\xi_{\eta\tau} - E_{\eta\tau}(\mathbf{p})\right)^2 + |\Delta_{\eta\tau}(\mathbf{p})|^2}} \tag{4.53}$$

$$v_{\eta\tau}(\mathbf{p}) = \frac{\Delta_{\eta\tau}(\mathbf{p})}{\sqrt{\left(\xi_{\eta\tau} - E_{\eta\tau}(\mathbf{p})\right)^2 + |\Delta_{\eta\tau}(\mathbf{p})|^2}} \tag{4.54}$$

where we use the notation of Eq. (4.31). Defining $\Delta_{\eta\tau}(\mathbf{p}) = |\Delta_{\eta\tau}(\mathbf{p})|\, e^{i\Phi_{\eta\tau}(\mathbf{p})}$ and noting that $U^1_{\eta\tau}(\mathbf{p}) = \left|U^1_{\eta\tau}(\mathbf{p})\right| e^{-i\phi_\eta(\mathbf{p})}$, the Berry connection turns out to be

$$A_{\eta\tau}(\mathbf{p}) = \left|U^1_{\eta\tau}(\mathbf{p})\right|^2 u^2_{\eta\tau}(\mathbf{p})\nabla\phi_\eta(\mathbf{p}) - \left|U^1_{-\eta\tau}(-\mathbf{p})\right|^2 |v_{\eta\tau}(\mathbf{p})|^2 \nabla\left(\phi_\eta(-\mathbf{p})\right) - |v_{\eta\tau}(\mathbf{p})|^2 \nabla\Phi_{\eta\tau}(\mathbf{p}) \tag{4.55}$$

Below we calculate the Chern number for $b = 0$ and non-zero α_R only, in which case $U^1_{\eta\tau}(\mathbf{p}) = -i\left|U^1_{\eta\tau}(\mathbf{p})\right| e^{-i\theta}$ where θ is the angle of the momentum $\mathbf{p}$ measured relative to the center of the Fermi pocket. The Berry vector potential simplifies to

$$A_{\eta\tau}(\mathbf{p}) = \left|U^1_{\eta\tau}(\mathbf{p})\right|^2 \nabla\theta - |v_{\eta\tau}(\mathbf{p})|^2 \left(\nabla\Phi_{\eta\tau}(\mathbf{p}) + \nabla\theta\right) \tag{4.56}$$

Note that for the two TRS-breaking solutions belonging to the E irrep we have $\Phi_{\eta\tau} = 0$ or $\Phi_{\eta\tau} = -2\theta$. Following the same steps as in Section 3.4, we thus find

$$Ch_\eta = \frac{1}{2\pi}\int \left(F_{\eta\tau}(\mathbf{p})\right)_{p\theta}\, dp\; d\theta = \frac{1}{2\pi}\int \partial_p \left(A_{\eta\tau}(\mathbf{p})\right)_\theta\, dp\; d\theta \tag{4.57}$$

$$= \frac{1}{2\pi}\left[\int \left(A_{\eta\tau}(\mathbf{p})\right)_\theta d\theta\right]_{p=0}^{p=\infty} = -\frac{1}{2\pi}\left[\Phi_{\eta\tau}(\mathbf{p}) + \theta_{\eta,\mathbf{p}}\right]_0^{2\pi} \tag{4.58}$$

where the integrals over θ and p are understood to be over the tangential and normal directions in a disk including the Fermi surface of the η pocket. This gives a net Chern number of ± 6, with a total

contribution of ± 4 from the $\pm K$ pockets, and of ± 2 from the Γ pocket. As noted in Section 3.4, this result is independent of the choice of $\Delta_{\eta\tau}$ away from the Fermi surface.

4.4.2 Crystalline Nodal Topological SC

We now discuss the nodal and crystalline nodal phases that we found and show that they are indeed symmetry protected by the TR-like symmetry $\tilde{\mathcal{T}} = i\sigma^x\mathcal{K}$ and mirror symmetry $\mathcal{M}_x$ respectively. The former has been proposed and discussed before in [62], so we mostly focus on the latter.

As we discussed in Chapter 3, symmetry protected topological phases with anti-unitary symmetries can be classified according to the ten-fold way that can be extended to include nodal phase as well as crystalline phases [144, 151, 145, 105, 28, 158, 30]. Here, $\tilde{\mathcal{T}}^2 = 1$, and since the system has PHS $\mathcal{C} = \varsigma^x\mathcal{K}$ being a superconductor (ς^μ acting on the Nambu spinor indices), this puts the system with an in-plane magnetic field but no Rashba into topological (Cartan or AZ for Altland-Zirnbauer [10, 132, 99]) class BDI. Consulting the classification table [105], we see that it can indeed host nodes that are topologically protected by a $\mathbb{Z}$ topological invariant, which means in particular that once there are nodes (as we have) they are topologically protected. The invariant is the Wilson loop going around individual nodes and summed over the nodes. As we saw in Chapter 3 it can be evaluated as the Berry phase once the wave-function is made continuous; note that the Berry phase is only quantized in the presence of the symmetry. Nodal phases are weak topological phases in the sense that nodes can be removed by pair-wise annihilation.

When Rashba SOC is introduced, the TR-like symmetry is broken and the system is in class D, which also has a topological invariant ($\mathbb{Z}_2$) but that can only protect nodes at high symmetry points [28, 30], which the nodes in our case are not. As we saw the nodes are lifted in that case. When the magnetic field is applied along a Γ-K direction, however, the system has an additional mirror symmetry. In that case the topological invariant depends on whether the mirror symmetry commutes or anti-commutes (or more precisely can be made so by a unitary transformation) with the anti-unitary symmetries, with all cases classified in [28]. For superconductors, whether the mirror symmetry commutes or anti-commutes with PHS depends on the form of the gap, in particular whether it is even or odd under reflection (as discussed in [143]). Consulting the classification table in [28], we find that if the mirror symmetry anti-commutes with PHS, which we will see corresponds to a gap function that is odd under reflection, there is an integer valued topological invariant $M\mathbb{Z}$ that can again protect the nodes, with the invariant again being given by the Wilson loop (when the mirror symmetry commutes with PHS, only nodes at high symmetry points are protected). The nodes we found for $b > \alpha_R p_F$ are therefore topologically protected by the mirror

symmetry. Importantly, the classification only determines the minimal dimension of the protected 'Fermi surface' [158, 30], and in particular the nodes can be 'inflated' into small Bogolyubov Fermi surfaces as we saw (when present, the invariant can be computed as the Berry phase accumulated going around the Bogolyubov Fermi surface). Importantly, although the two pairs of nodes coincide with the nodes in the absence of Rashba SOC, the classification is different and this is a distinct *crystalline* nodal topological phase.

To show that the nodes are indeed protected in the crystalline nodal phase, we will follow the approach of [28] and write down the general effective low energy Hamiltonian for the nodes and consider all possible symmetry allowed mass terms that can gap them out (this approach can be shown to be equivalent to the more rigorous K theory approach of [158]). For this purpose we will need to establish the action of the symmetries. Recall that $\mathcal{M}_x$ acts on the non-interacting Hamiltonian as

$$\mathcal{M}_x H(\mathbf{p}) \mathcal{M}_x^{-1} = H(\bar{\mathbf{p}}) \tag{4.59}$$

where $\bar{\mathbf{p}} = (-p_x, p_y)$. Since this reflection also reverses the y and z components of the spin, in the spin basis $\mathcal{M}_x$ acts as $i\sigma^x$, but in the SOC basis (4.6) it is momentum dependent, $\mathcal{M}_x(\mathbf{p}) = U^{\alpha}_{\eta\tau}(\mathbf{p}) i\sigma^x_{\alpha\beta} U^{\beta *}_{\eta\tau'}(\bar{\mathbf{p}}) = i\tau e^{-i\phi(\mathbf{p})}\delta_{\tau\tau'}$ (note the $\bar{\mathbf{p}}$).[2] To get the last expression we make use of the fact that in the presence of the mirror symmetry,

$$\begin{aligned} \beta_{-\eta z}(\bar{\mathbf{p}}) &= -\beta_{\eta z}(\mathbf{p}) \\ \beta_{-\eta}(\bar{\mathbf{p}}) &= \beta_{\eta}(\mathbf{p}) \\ e^{i\phi(\bar{\mathbf{p}})} &= e^{-i\phi(\mathbf{p})} \end{aligned} \tag{4.60}$$

the last of which follows from the fact that in this case

$$e^{i\phi(\mathbf{p})} = \frac{\alpha_R p_y + b_x - i\alpha_R p_x}{\sqrt{(\alpha_R p_y + b_x)^2 + (\alpha_R p_x)^2}} \tag{4.61}$$

[2]Note that in the absence of Rashba SOC, $\tilde{\mathcal{T}}$ has almost the same form as $\mathcal{M}_x$ in the spin basis except for the complex conjugation. As a result, when it holds, in the SOC basis the TR-like symmetry becomes $\tilde{\mathcal{T}} = \tau e^{i\vartheta}\delta_{\tau\tau'}$ where ϑ is the angle of the magnetic field.

The action of mirror symmetry needs to be extended to the BdG spinors as

$$\begin{aligned}\tilde{\mathcal{M}}_x(\mathbf{p}) &= \begin{pmatrix} \mathcal{M}_x(\mathbf{p}) & 0 \\ 0 & \pm\mathcal{M}_x^\dagger(-\mathbf{p}) \end{pmatrix} \\ &= \begin{pmatrix} e^{i\phi(\mathbf{p})} & 0 \\ 0 & \pm e^{-i\phi(-\mathbf{p})} \end{pmatrix}\end{aligned} \tag{4.62}$$

where the $\pm$ depends on whether the gap function is odd or even under $\mathbf{p} \to \bar{\mathbf{p}}$ (see Section 3.4). The leading solution for $b > \alpha_R p_F$ is odd (which can be shown using (4.60)), and the correct choice is $-$. This ensures that the mirror symmetry thus acts on the BdG Hamiltonian Eq. (4.28) as

$$\tilde{\mathcal{M}}_x \mathcal{H}_{\eta\tau}(\mathbf{p}) \tilde{\mathcal{M}}_x^{-1} = \mathcal{H}_{\eta\tau}(\bar{\mathbf{p}}) \ . \tag{4.63}$$

Note that the classification in [28] assumes that $\tilde{\mathcal{M}}_x$ either commutes of anti-commutes with PHS $\mathcal{C} = \varsigma^x \mathcal{K}$, which is not the case for (4.62). It can be made to commute or anti-commute with PHS by a unitary transformation, in this case $c_{\mathbf{p}\eta\tau} \to \mathcal{U}_\eta(\mathbf{p}) c_{\mathbf{p}\eta\tau} = e^{i\phi_\eta(\mathbf{p})/2} c_{\mathbf{p}\eta\tau}$, under which $\tilde{\mathcal{M}}_x \to \varsigma^z$ or ς^0 depending on which sign of the square root we choose. The ambiguity is due to the branch cut of the square root, but the correct sign is fixed by ensuring the continuity of the wave function (meaning the branch cut needs to be avoided). This reveals that there is an obstruction determined by the phase winding $\Delta\phi_\eta$ of $e^{i\phi_\eta(\mathbf{p})}$ around the Fermi surface, which can be easily evaluated using (4.61) to be $\Delta\phi_\eta = \pi\,(1 + \mathrm{sgn}[\alpha_R p_F - b])$: we thus find that $\tilde{\mathcal{M}}_x \to \varsigma^0$ for $b < \alpha_R p_F$ and $\tilde{\mathcal{M}}_x \to \varsigma^z$ for $b > \alpha_R p_F$. According to the classification, the nodes are therefore only topologically protected for $b > \alpha_R p_F$.

There is, however, a simpler way to determine which choice correct by noting that $\tilde{\mathcal{M}}_x$ does commute or anti-commute with PHS on the mirror plane $p_x = 0$, on which it is given by

$$\mathcal{M}_x(\mathbf{p}) = \begin{pmatrix} \mathrm{sgn}[\alpha_R p_y + b] & 0 \\ 0 & \mathrm{sgn}[\alpha_R p_y - b] \end{pmatrix} \tag{4.64}$$

so in the mirror plane $\tilde{\mathcal{M}}_x = \mathrm{sgn}\, p_y \varsigma^0$ for $b < \alpha_R p_F$ and $\tilde{\mathcal{M}}_x = \varsigma^z$ for $b > \alpha_R p_F$. This gives a simpler criterion for the classification [28], namely whether the mirror symmetry commutes or anti-commutes with PHS (and/or TRS) in the mirror plane.

Having established the action of the mirror symmetry, we can now see what happens to the nodes in the mirror plane. As they are related by PHS, we have to consider a pair of nodes that

we label L and R. τ^μ to Pauli matrices acting on the L, R indices. In this basis the particle-hole symmetry, which interchanges the two nodes, acts via $\mathcal{C} = \varsigma^x \otimes \tau^x \mathcal{K}$. The mirror symmetry acts *within* the mirror plane differently depending on whether $b > \alpha_R p_F$ or not: in the former case it acts as $\tilde{\mathcal{M}}_x = \varsigma^z \otimes \tau^0$, while for $b < \alpha_R p_y$ one gets $\tilde{\mathcal{M}}_x = \varsigma^0 \otimes \tau^z$ (note the factor of $\operatorname{sgn} p_y$).

We now consider all leading terms of the generic form $h(\delta p_y, p_x)\varsigma^\mu \otimes \tau^\nu$ allowed by symmetry, with $\delta p_y = p_y - p_y^{(\text{node})}$. Terms that couple the two nodes break translational symmetry, which is assumed in the topological classification. We thus require $\nu = 0$ or z. With these coordinates, the symmetries act as

$$\begin{aligned} \mathcal{C}^{-1}\mathcal{H}(\delta p_y, p_x)\mathcal{C} &= -\mathcal{H}(-\delta p_y, -p_x) \\ \tilde{\mathcal{M}}_x^{-1}\mathcal{H}(\delta p_y, p_x)\tilde{\mathcal{M}}_x &= \mathcal{H}(\delta p_y, -p_x) \quad . \end{aligned} \tag{4.65}$$

Thus $h(-\delta p_y, -p_x) = \pm h(\delta p_y, p_x)$ when $\mathcal{C}^{-1}\varsigma^\mu \otimes \tau^\nu \mathcal{C} = \mp \varsigma^\mu \otimes \tau^\nu$. Similarly $h(\delta p_y, -p_x) = \pm h(\delta p_y, p_x)$ when $\tilde{\mathcal{M}}_x^{-1}\varsigma^\mu \otimes \tau^\nu \tilde{\mathcal{M}}_x = \pm \varsigma^\mu \otimes \tau^\nu$. To gap out the nodes we must have $h(0,0) \neq 0$, and so we only need to consider plus signs in both cases. Hence $\varsigma^\mu \otimes \tau^\nu$ anti-commutes with $\varsigma^x \otimes \tau^x \mathcal{K}$ and commutes with $\tilde{\mathcal{M}}_x$. If $b < \alpha_R p_F$, $m\varsigma^y \otimes \tau^z$ with constant m is the only symmetry allowed mass term and one can check that this indeed gaps out the nodes, in agreement with the classification according to which they are not protected in this case.

We are thus more interested in the case $b > \alpha_R p_F$, for which the linearized Hamiltonian is to leading order

$$\mathcal{H} = \delta p_y \varsigma^z \otimes \tau^z + p_x \varsigma^x \otimes \tau^0 + m\varsigma^z \otimes \tau^0 + \xi_A \varsigma^0 \otimes \tau^z \tag{4.66}$$

where m and ξ_A are constants (for simplicity, we take the Fermi velocity to be 1, so all parameters have the same units). The m term, which plays the role of a chemical potential shift at each node, does not lift the nodes; rather it shifts them in opposite directions along the p_y axis, from $p_y = \pm p_F$ to $p_y = \pm(p_F + m)$.

The $\xi_A \varsigma^0 \otimes \tau^z$ term, on the other hand, shifts the nodes in opposite directions in energy by an amount ξ_A, inflating the nodes into small Bogolyubov Fermi surfaces (see also [7, 20, 194, 167]). Comparing with the BdG spectrum Eq. (4.29), we find that ξ_A is precisely the value of $\xi_{A\Gamma\tau}$ when $\xi_{S\Gamma\tau}(\mathbf{p}) = 0$ in Eq. (4.30). Since a constant shift in energy cannot change the Berry connection, the winding numbers are unaffected in the presence of Bogolyubov Fermi and remain non-trivial [30, 158], as can be verified by direct computation. The Bogolyubov Fermi surfaces are therefore topologically

protected only in a fragile sense [38], as they can be removed by mixing with additional bands, similar to what has been observed theoretically in 1D crystalline topological insulators [69, 89]. As in those systems, we expect some experimental signatures to remain even when the Bogolyubov Fermi surfaces are removed.[3]

Boundary modes

By the bulk-boundary correspondence [28, 158], there are edge bands terminating at the nodes. However, unlike other nodal topological superconductors with Majorana flat band edge modes [62, 151, 145, 82], the edge modes in the crystalline topological phase under consideration are not in general flat and not necessarily at zero energy. The edge bands can be studied following the methods of [185, 60]; we find that for open boundary conditions in x and p_y close to the node, the edge mode has energy ξ_A. When ξ_A vanishes at the node (e.g. if a stripe FFLO phase is realized in the bulk) this means that the boundary modes cross zero energy– but they are not flat in general as ξ_A does not have to vanish for all p_y. Similar edge states have been studied in 3D crystalline topological insulators, where they are referred to as drumhead states [15, 23, 156].

An alternative way to understand the edge modes is to view them as topological boundary modes of the family of 1D Hamiltonians $\mathcal{H}_{p_y}(p_x) = \mathcal{H}(p_x, p_y)$ at fixed p_y (see discussion in Section 3.2), which are in topological class A and respect mirror symmetry. Since mirror symmetry is equivalent to inversion in 1D, these are the same systems as studied in [69, 89] and that we analyzed in Section 3.1. As p_y crosses the node, $\mathcal{H}_{p_y}(p_x)$ undergoes a topological phase transition from trivial to non-trivial. The 1D topological invariant is the mirror index $N_{M\mathbb{Z}} = |n_+^{(0)} - n_+^{(\pi)}|$ that we defined in Section 3.1 (see [69, 29]). There are then $2N_{M\mathbb{Z}}$ edge states, with each state even under reflection being degenerate with an edge state that is odd under reflection. Taken together these edge states form the band of edge modes of the 2D system. At a node (which is at $p_x = 0$), $\mathcal{H}^+_{p_y}(0)$ crosses with a state in $\mathcal{H}^-_{p_y}(0)$, which changes the $n_+^{(0)}$ invariant by one and the number of edge states by two. The edge mode thus splits into two bulk modes which cross at the node.

To study the boundary modes of our model in the uniform superconducting state, in Appendix A we describe a tight-binding model that captures the key features of our gapless topological superconducting phase. The result is shown in Fig. Figure 4.6, which shows the Bogolyubov-de Gennes spectrum on a $150 \times \infty$ unit cell strip with open zig-zag edges parallel to the $\hat{y}$ direction (with $\mathbf{B} = B\hat{x}$) in the uniform superconducting state. Each state $\psi(p_y)$ is colored according to the inverse

[3] The proof of topological protection of nodes for the non-crystalline phase is almost identical, but with $\tilde{\mathcal{T}} \to \varsigma^z \otimes \tau^x$, which rules out the ξ_A term.

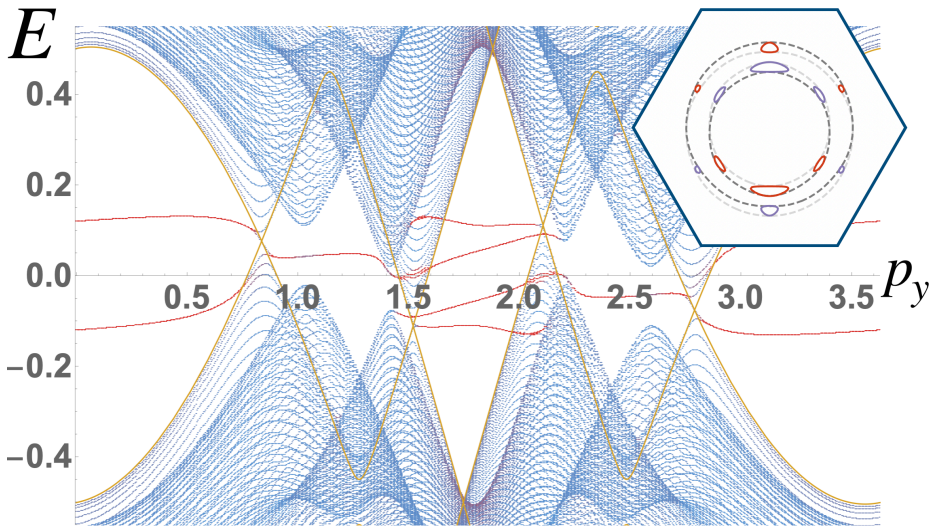

Figure 4.6: Excitation spectrum in the topological crystalline SC phase on a $150 \times \infty$ unit cell strip with $\mathbf{B} = B\hat{\mathbf{x}}$. Blue indicates delocalized bulk eigenstates, red indicates eigenstates concentrated near the boundaries, and yellow shows a cut of the bulk BdG spectrum at $p_x = 0$. The inset illustrates the Bogolyubov Fermi surfaces and the original Fermi surfaces (dashed black lines) and its inverse image under $\mathbf{p} \to -\mathbf{p}$ (dashed gray lines). For detailed parameter values, see Appendix A.

participation ratio $\sum_x |\psi(p_y, x)|^4$ with the boundary modes in red and bulk modes in blue. A cut containing the nodes along $p_x = 0$ of the bulk BdG spectrum is shown in yellow.

Chapter 5

Pair Density Wave in 1H-TMDs

In the RG analysis in Section 2.2 we found that there are two possible pairing channels in 1H-$NbSe_2$ (and similar 1H-TMDs): a uniform superconducting (SC) channel and two pair-density wave (PDW) channels that we will refer to as $\text{PDW}_\pm$ with pairing momentum $\pm 2K = \mp K$ ($3K$ is an Umklapp momentum). In this chapter we consider the PDW channels in more detail, mostly neglecting SOC and only comment on its effect in Section 5.3. Note that for repulsive interactions we saw that the PDW instability is only possible in the presence of the Γ pocket mediated either by an Umklapp process (an A_1' singlet instability) or exchange interactions between Γ and K (A_1' or E'' triplet instabilities). In systems without a Γ pocket like MoS_2, some attraction is therefore necessary to produce the PDW instability, which is an unlikely scenario but to which our analysis applies as well. As always, we will use pocket indices $\eta, \zeta = 0, \pm 1$ interchangeably with Γ, $\pm K$ (i.e. ηK with $0K = \Gamma$).

The relevant order parameters enter the Hamiltonian in momentum space as

$$H = \frac{T}{2} \sum_{\mathbf{p}\eta\zeta\alpha\beta} \bar{\Psi}_{\mathbf{p}\eta\alpha} \left[\mathcal{H}^{(BdG)}_{\eta\zeta}(\mathbf{p}) \right]_{\alpha\beta} \Psi_{\mathbf{p}\zeta\beta} \tag{5.1}$$

where we defined the Nambu spinors $\Psi_{\mathbf{p}\eta\alpha} = (d_{\mathbf{p}\eta\alpha}, \bar{d}_{-\mathbf{p}\eta\alpha})^T$ and the Bogolyubov-de Gennes (BdG) Hamiltonian

$$\mathcal{H}^{(BdG)}_{\eta\zeta}(\mathbf{p}) = \begin{pmatrix} \epsilon_\eta(\mathbf{p})\delta_{\eta\zeta} & \Delta_{\eta\zeta}(\mathbf{p}) \\ \Delta^\dagger_{\zeta\eta}(\mathbf{p}) & -\epsilon_\zeta(\mathbf{p})\delta_{\eta\zeta} \end{pmatrix} \tag{5.2}$$

with $\left[\Delta^{\dagger}_{\zeta\eta}\right]_{\alpha\beta} = \left[\bar{\Delta}_{\zeta\eta}\right]_{\beta\alpha}$, and where

$$\epsilon_{\eta}(\mathbf{p}) = -\frac{p^2}{2m_{\eta}} - \mu_{\eta} \tag{5.3}$$

is the normal state dispersion without SOC. Due to anti-commutation relations, the gaps satisfy particle-hole symmetry (PHS)

$$\Delta_{\eta\zeta}(\mathbf{p}) = -\Delta^{T}_{\zeta\eta}(-\mathbf{p}) \tag{5.4}$$

This implies in particular that $\Delta_{\eta\zeta}$ and $\Delta_{\zeta\eta}$ are not independent and should be considered as two components of a single field. A non-vanishing $\Delta_{\eta\zeta}$ indicates a formation of a condensate of a pair with total momentum $(\eta+\zeta)K$. In particular $\Delta_{\Gamma\Gamma}$, $\Delta_{K,-K}$ and $\Delta_{-K,K}$ are uniform SC gaps, while $\Delta_{\pm K,\pm K}$, $\Delta_{\Gamma,\mp K}$ and $\Delta_{\mp K,\Gamma}$ are PDW gaps with pair momentum $\pm 2K = \mp K$ respectively. See Table 5.1 and Figure 5.1.

SC	$\Delta_{\Gamma\Gamma}$	$\Delta_{K,-K}, \Delta_{-KK}$
PDW_+	Δ_{-K-K}	$\Delta_{\Gamma K}, \Delta_{K\Gamma}$
PDW_-	Δ_{KK}	$\Delta_{\Gamma,-K}, \Delta_{-K\Gamma}$

Table 5.1: SC and PDW gap functions

Symmetry-wise, either of the $\text{PDW}_{\pm}$ phases is similar to the FFLO [87, 53] phase as both are inhomogeneous superconducting phases with a real space order parameter $\Delta \sim e^{i\mathbf{r}\cdot\mathbf{Q}}$, with $\mathbf{Q} = \mp\mathbf{K}$ being the total momentum of the Cooper pairs. Unlike FFLO, however, PDW emerges spontaneously in a material with no external fields breaking time reversal symmetry (TRS). Note that if only one of $\text{PDW}_{\pm}$ is present, it spontaneously breaks TRS as well as translation symmetry (and can also break point group symmetries), in which case it can also induce a loop current order. This has been, for example, invoked to explain possible TRS breaking in the pseudogap regime in cuprates [90].[1] If both PDW's are present, TRS is not broken.

The TRS breaking and preserving cases are referred to as FF- and LO-type PDW's respectively, since [53] considered an order parameter of the form $\Delta \sim e^{i\mathbf{r}\cdot\mathbf{Q}}$ and [87] instead proposed $\Delta \sim \cos\mathbf{r}\cdot\mathbf{Q}$ that by itself does not break TRS. In order to see which case happens in 1H-TMDs, in Section 5.1 we consider a phenomenological Ginzburg-Landau (GL) description of the PDW phases.

[1] In that case it has also been suggested that the loop current order may be vestigial, with the PDW order itself destroyed due to fluctuations [6]. Other orders induced by PDW may similarly remain in the absence of PDW order itself, and can be viewed as vestigial or driven by PDW fluctuations, which in themselves may be interesting [4].

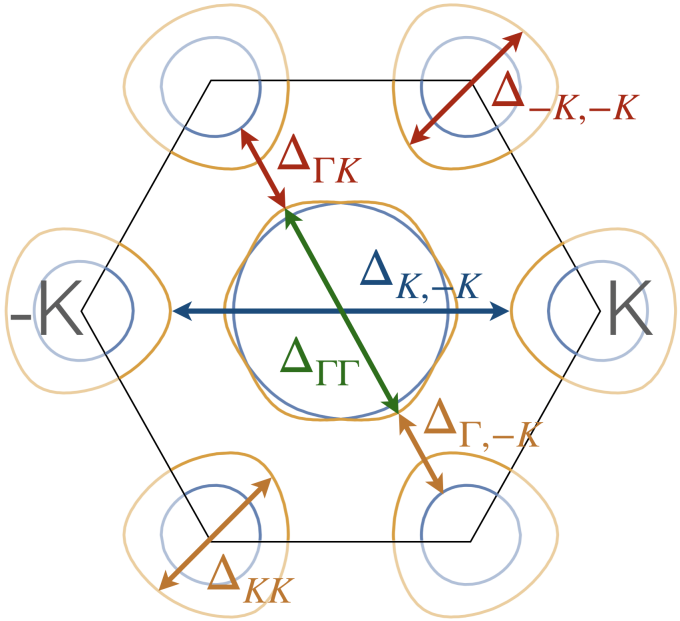

Figure 5.1: SC and PDW order parameters shown in the Brillouin zone (green and blue are uniform SC, red is PDW_-, orange is PDW_+). The Fermi surfaces were obtained from the tight-binding model summarized in Appendix A. Note the trigonal warping at K points.

We also consider which orders can be induced in the same framework. The GL free energy can be derived from a microscopic theory, which for simplicity we do only for a system without a Γ pocket, in which case the PDW turns out to always be LO-type.

Only uniform SC has been seen in experiment, which is why we had focused on the SC channel in Chapter 4. The PDW is likely suppressed relative to SC in 1H-$NbSe_2$ due to trigonal warping at the K pockets and Fermi momentum mismatch between the Γ and K pockets. Under different conditions (gating, applying magnetic fields, etc.) or in other materials with similar Fermi surfaces but where these effects are smaller a PDW instability may, however, be possible. We quantify this statement in Section 5.2 using a mean field analysis. Finally, we will discuss effects of Ising SOC in Section 5.3.

5.1 Ginzburg-Landau Theory of PDW

To gain a better understanding of the PDW states, below we consider a general Ginzburg-Landau (GL) free energy for $\text{PDW}_\pm$ order parameters $\Delta_{\pm K} \sim e^{\pm i\mathbf{K}\cdot\mathbf{r}}$ on a triangular lattice with a D_{3h} point group. This is somewhat similar to the analysis of PDW on a hexagonal lattice [5], the main

difference is that here we have an Umklapp momentum $3K$ and the three values of $\mathbf{K}$ are equivalent.

The order parameters $\Delta_{\pm K}$ are the order parameters in real space, and are related to the gap functions $\Delta_{\Gamma,\pm K}$ and $\Delta_{\mp K,\mp K}$ defined above by a Fourier transform. In principle there can be different order parameters $\Delta_{\pm K} \sim \sigma^\mu i\sigma^y$ corresponding to spin-singlet for $\mu = 0$ and spin-triplet paring for $\mu = x, y, z$. The spin spin-singlet (onsite) PDW$_-$ enters the Hamiltonian in real space on a lattice as (that can be obtained by Fourier transforming (5.1)):

$$H_{PDW_-} = \sum_{j\alpha\beta} e^{-i\mathbf{K}\cdot\mathbf{R}_j} \Delta^{(0)}_{-K} i\sigma^y_{\alpha\beta} d^\dagger_{\mathbf{R}_j\alpha} d^\dagger_{\mathbf{R}_j\beta} + h.c. \tag{5.5}$$

The spin-triplet PDW$_-$, to leading order in lattice harmonics, enters as

$$H_{PDW_-} = \sum_{\langle ij\rangle\alpha\beta} e^{-i\mathbf{K}\cdot\mathbf{R}_j} \nu_{ij} \Delta^{(\mu)}_{-K} (\sigma^\mu i\sigma^y)_{\alpha\beta} d^\dagger_{\mathbf{R}_i\alpha} d^\dagger_{\mathbf{R}_j\beta} + h.c. \tag{5.6}$$

The triplet order involves nearest neighbor terms with $\nu_{ij} = \pm 1$ if $\mathbf{R}_j - \mathbf{R}_i$ points along $\pm K$ (see Figure 5.2). We will assume that the order parameter is some linear combination of singlet and triplet parameters (that can mix if we add SOC), and drop the (μ) superscript below. Note that for nearest neighbors, $e^{-i\mathbf{K}\cdot(\mathbf{R}_j-\mathbf{R}_i)} = e^{\pm 2\pi i/3}$ for $\mathbf{R}_j - \mathbf{R}_i$ pointing along $\pm K$, for any choice of the three equivalent $\mathbf{K}$. The three-fold rotational symmetry therefore remains unbroken. Note that comparing phases of the order parameter going around a triangular loop, a total phase of $\pm 2\pi$ is accumulated, which indicates a loop supercurrent (see Figure 5.3). Equivalently, we can think of three currents propagating along the three equivalent $-\mathbf{K}$ directions, as one would expect since the Cooper pairs have a total momentum of $-\mathbf{K}$. If PDW$_+$ is also present, the currents cancel by superposition.

Before writing down the GL free energy, we discuss the relevant symmetries. In addition to breaking TRS and translational symmetry, a single PDW (+ or -) also breaks the out-of-plane mirror symmetries σ_h of the D_{3h} point group that takes K to $-K$, and so the PDW states are classified according to irreps of C_{3h}, all of which are 1D (note that no rotational symmetry is broken). When both PDW$_\pm$ are present with equal magnitudes (LO-type PDW), all the symmetries except for translational symmetry are restored. Both LO- and FF-type PDW's break translational symmetry, expanding the unit cell by a factor of three in real space (since $3K = 0$). Note that under TRS $T = e^{i\phi} i\sigma^y \mathcal{K}$ (where $\mathcal{K}$ is complex conjugation and we include an arbitrary constant phase ϕ) we

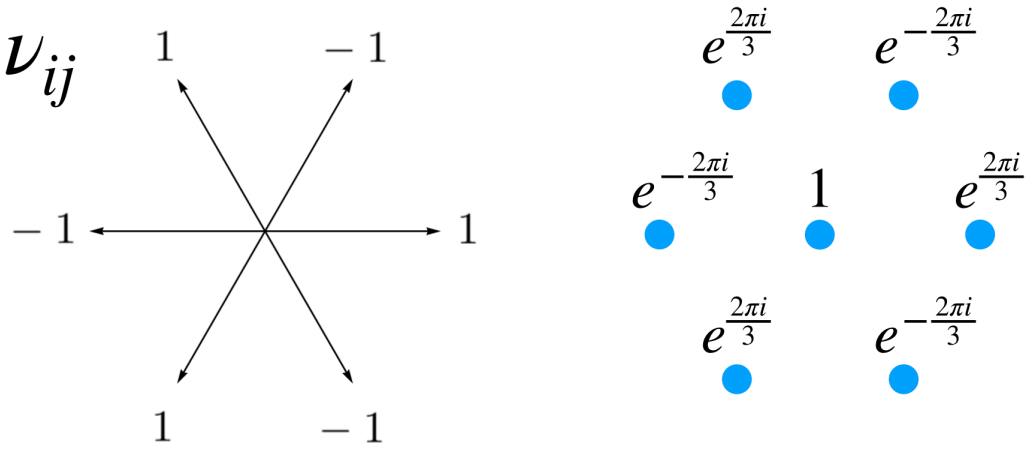

Figure 5.2: ν_{ij} and relative phases of nearest neighbors in FF PDW$_+$ with total momentum K in real space (opposite phases for PDW$_-$).

have in momentum space

$$\Delta_{\eta\zeta}(\mathbf{p}) \to e^{2i\phi}\sigma^y \Delta^*_{-\eta-\zeta}(-\mathbf{p})\sigma^y \tag{5.7}$$

where $\eta, \zeta = 0, \pm 1$ being pocket indices corresponding to $\Gamma, \pm K$ (the formula applies to uniform SC as well). TRS thus associates a PDW with pair momentum $(\eta + \zeta)K = \pm K$ with a PDW with opposite pair momentum $\mp K$. The phase ϕ is included in order to make the $U(1)$ symmetries explicit. If we fix $\phi = 0$, Δ_K and Δ_{-K} must be equal and real for TRS to hold, but for arbitrary ϕ TRS holds as long as $|\Delta_K| = |\Delta_{-K}|$. The correct statement is that TRS holds as long as there is *a* value of ϕ for which (5.7) holds. There are therefore two $U(1)$ symmetries broken in the LO PDW: one by the global phase, and one by the relative phase between Δ_K and Δ_{-K}.

The leading PDW instabilities we found in RG are either in A' or in E'' irreps of C_{3h}, with both singlet and triplet orders in A' but only triplet in E''. In the LO-type PDW these are lifted to A'_1 and E'' irreps, but note that the E'' irrep is actually two 1D irreps in C_{3h} with complex-valued characters. A 2D irrep has two degenerate solutions at second order in the free energy. As we saw, the degeneracy is typically lifted at fourth order and can spontaneously break TRS. Because E'' is 1D in C_{3h}, however, there is no degeneracy already at second order in general, and it does not break TRS in the LO-type PDW. We will also include the uniform SC order Δ_0, which as we saw in Chapter 2 can belong to a 1D or a 2D irrep of D_{3h}; in the latter case, the phase between the components of the 2D irrep is generally fixed at the fourth order of the free energy (as we saw in

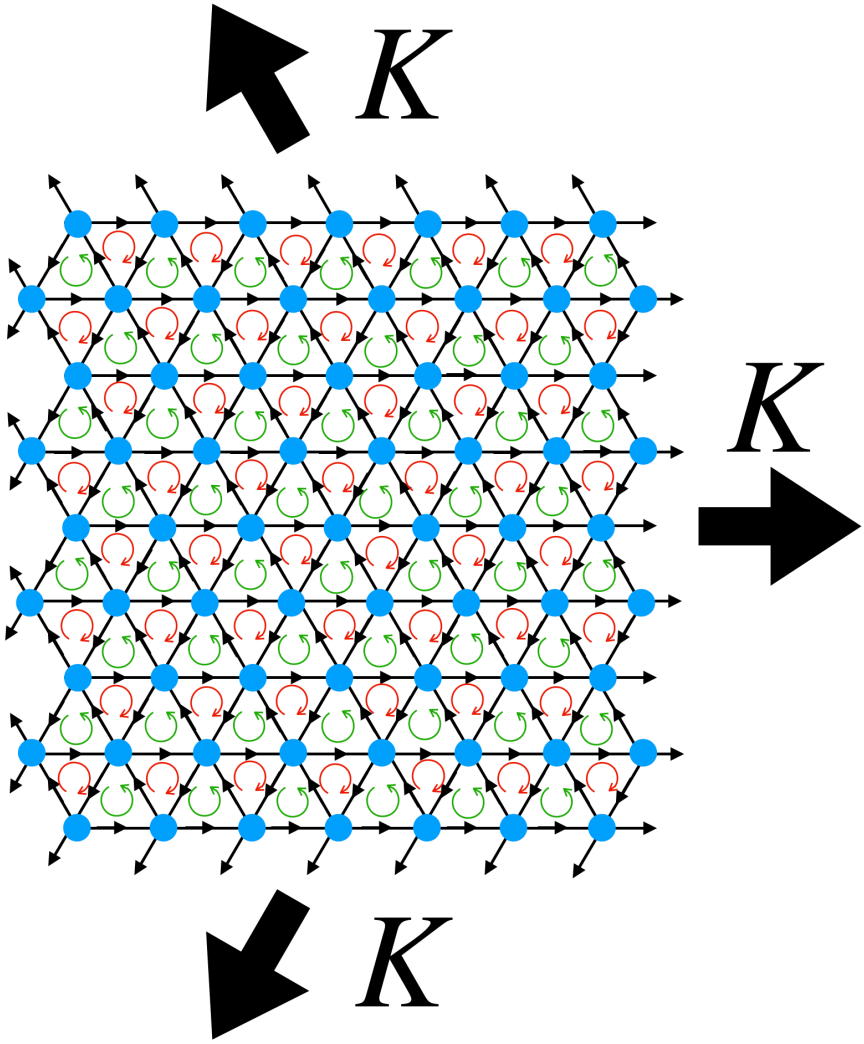

Figure 5.3: Cartoon picture of PDW_+ with total momentum K illustrated in real space where each arrow represents a jump in the complex phase of the order parameter by $2\pi/3$. Loosely we can think of the arrows as induced currents along the three equivalent directions, equivalent to loop currents shown in red and green that break both translation and mirror symmetries. All arrows are reversed for PDW_-.

Section 4.4), after which it can be characterized by a single order parameter (after breaking a $\mathbb{Z}_n$ symmetry that we will not be interested in here). With that in mind, we drop the irrep indices in the free energy.

We now write down the GL free energy for the real space order parameters and see if any of the symmetries are broken. We assume that the order parameters belong to a single irrep, and as discussed above the GL free energy to fourth order has the same form regardless of the choice (i.e., we neglect mixing between different irreps and components of the same irrep):

$$\mathcal{F} = a_0|\Delta_0|^2 + a_K\left(|\Delta_K|^2 + |\Delta_{-K}|^2\right) + \mathcal{F}^{(4)} + \dots \tag{5.8}$$

where

$$\begin{aligned}\mathcal{F}^{(4)} &= \beta_0|\Delta_0|^4 + \beta_1\left(|\Delta_K|^4 + |\Delta_{-K}|^4\right) + \beta_2|\Delta_0|^2\left(|\Delta_K|^2 + |\Delta_{-K}|^2\right) + \beta_3|\Delta_K|^2|\Delta_{-K}|^2 + \\ &+ \beta_4\left(\Delta_0^2\Delta_K^*\Delta_{-K}^* + c.c.\right) + \beta_5\left(\Delta_K^2\Delta_0^*\Delta_{-K}^* + \Delta_{-K}^2\Delta_0^*\Delta_K^* + c.c.\right)\end{aligned} \tag{5.9}$$

For PDW only, this becomes

$$\mathcal{F}^{(4)}_{PDW} = \beta_1\left(|\Delta_K|^4 + |\Delta_{-K}|^4\right) + \beta_3|\Delta_K|^2|\Delta_{-K}|^2 \tag{5.10}$$

There are two cases: if $\beta_3 > 2\beta_1$, the ground state is an FF-type PDW ($\Delta_{-K} = 0$ or $\Delta_K = 0$); for $\beta_3 < 2\beta_1$, the ground state is an LO-type PDW ($|\Delta_{-K}| = |\Delta_K|$). The relative phase is not fixed in the latter case, so the ground state degeneracy is $U(1)\times U(1)$. This degeneracy is lifted at the sixth order in the free energy:

$$\mathcal{F}^{(6)}_{PDW} = \Gamma_1\left(|\Delta_K|^6 + |\Delta_{-K}|^6\right) + \Gamma_2\left(|\Delta_K|^4|\Delta_{-K}|^2 + |\Delta_K|^2|\Delta_{-K}|^4\right) + \Gamma_3\left(\Delta_K^3(\Delta_{-K}^*)^3 + c.c.\right) \tag{5.11}$$

where the Γ_3 term is minimized when the relative phase satisfies $\cos 3(\phi_K - \phi_{-K}) = 1$ (-1) if $\Gamma_3 < 0$ (> 0), corresponding to $\phi_K - \phi_{-K} = \frac{n\pi}{3}$ for even (odd) integers n; the $U(1)$ symmetry corresponding to the relative phase is thus broken down to $\mathbb{Z}_3$. We summarize the results in Table 5.2.

Type	(Δ_K, Δ_{-K})	Induced Orders	Degeneracy
FF	$(e^{i\phi_K}, 0)$	ℓ, Δ_{6e}	$U(1)$
FF	$(0, e^{i\phi_{-K}})$	$-\ell, \Delta_{6e}$	$U(1)$
LO	$(e^{i\phi_K}, e^{i\phi_{-K}})$	$\rho_{\pm K}, \Delta_{4e}, \Delta_{6e}$	$U(1)\times\mathbb{Z}_3$

Table 5.2: PDW ground states analogous to Table 1 in [8].

5.1.1 Induced Orders

As we mentioned, PDW has often been associated with other observed orders that it can in principle induce [8]. We list the possible induced orders corresponding to the FF- and LO-PDW in Table 5.2. We already mentioned when discussing the order parameter on a lattice in (5.5) that the relative phases between neighboring sites in the FF-PDW indicate supercurrent in the system (since the Cooper pairs carry a total momentum). This results in a loop current order $\ell \propto |\Delta_K|^2 - |\Delta_{-K}|^2$ that *preserves* translational symmetry unlike the FF-PDW itself [90, 6]. Physically, it corresponds to a non-zero expectation value of the current operator along loops connecting nearest neighbor cites (see Figure 5.3), which in this case is equivalent to a superposition of three currents along the three equivalent K directions.

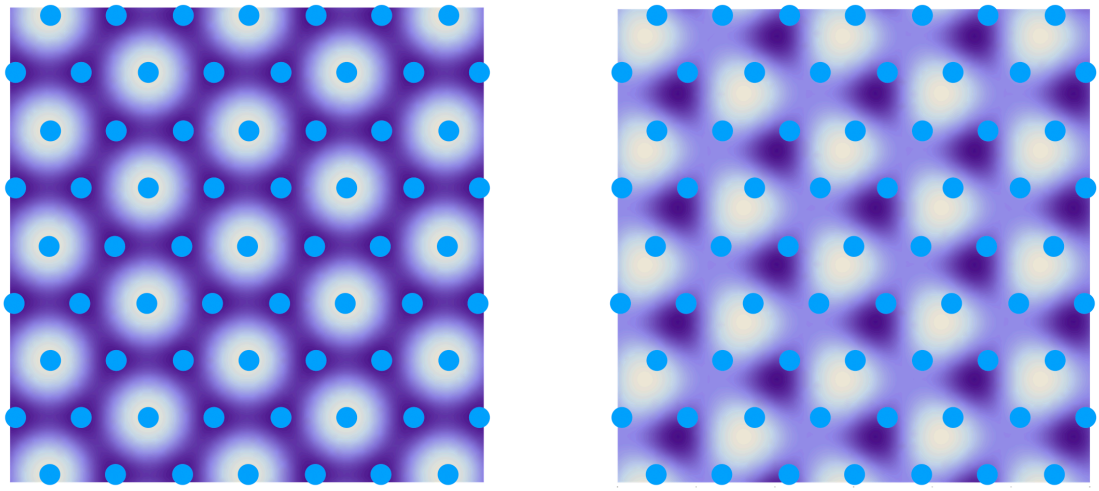

Figure 5.4: CDW induced by LO-type PDW in real space for $\phi_K - \phi_{-K} = 0$ and $\pi/3$ respectively. Note that only the value at the metallic sites shown in blue are physical in the lattice model.

In the LO-PDW phase, a mixing term with CDW is allowed of the form

$$\mathcal{F}_1^{(3)} = \Lambda_1 \rho_K \Delta_{-K} \Delta_K^* + c.c. \tag{5.12}$$

note that by hermiticity, $\rho_K = \rho_{-K}^*$, so ρ_{-K} is part of the same order parameter. If uniform SC is present, mixing terms like

$$\mathcal{F}_2^{(3)} = \Lambda_2 \rho_K \Delta_K \Delta_0^* + c.c. \tag{5.13}$$

are also allowed. Adding quadratic terms $\mathcal{F}_\rho \propto \rho_K \rho_{-K}^*$ and minimizing with respect to ρ_{-K}^*, we find

that $\rho_K \propto \Delta_K \Delta^*_{-K}$ is induced at the minimum of the free energy for the LO PDW term (similarly for the second term with uniform SC). The relative phases of the two PDW's thus enter into the CDW order parameter (and thus can be measured). See Figure 5.4 for an illustration.

Finally, higher order uniform superconductivity involving bound states of four or six fermions can be induced in LO-type PDW as $\Delta_{4e} \propto \Delta_K \Delta_{-K}$ and $\Delta_{6e} \propto \Delta_K^3 + \Delta_{-K}^3$; the latter arises due to Umklapp since $3K = 0$. In FF-type PDW, only $\Delta_{6e} \propto \Delta_K^3$ can arise. Note that non-uniform charge $4e$ and $6e$ (as well as bound states with even more fermions) are in principle possible. We will not consider these higher order SC orders in detail.

5.1.2 Microscopic Derivation of GL Free Energy without a Γ Pocket

The GL free energy can be derived microscopically, with the result (assuming that all Fermi surfaces are circular and of the same radius)

$$\mathcal{F}^{(4)} = \Gamma^{(0)} \int \mathrm{Tr}\left[\Delta^\dagger \Delta \Delta^\dagger \Delta\right] \frac{d\theta}{2\pi} \tag{5.14}$$

where

$$\Gamma^{(0)} = \frac{7\zeta(3)N}{32\pi^2 T^2} \tag{5.15}$$

with $\zeta(3) \approx 1.202$ is the Riemann zeta function. The trace is over both spin and pocket indices, with Δ considered as a matrix in both with elements $[\Delta_{\eta\zeta}]_{\alpha\beta}$.

The general expression is somewhat involved due to the number of order parameters (even ignoring spin degrees of freedom), so here we just consider the case with no Γ pocket, applicable to, e.g., doped MoS_2 (or if $\Delta_{\Gamma \pm K} \approx 0$, e.g. due to Fermi momentum mismatch). The microscopic free energy is then

$$\begin{aligned} \mathcal{F}^{(4)} &= \Gamma^{(0)} \left(2|\Delta_0|^4 + |\Delta_K|^4 + |\Delta_{-K}|^4\right) + \\ &+ 4\Gamma^{(0)} \left(|\Delta_0|^2|\Delta_K|^2 + |\Delta_0|^2|\Delta_{-K}|^2\right) \pm \\ &\pm 4\Gamma^{(0)}|\Delta_0|^2|\Delta_K||\Delta_{-K}|\cos\phi \end{aligned} \tag{5.16}$$

where $\phi = 2\phi_0 - \phi_K - \phi_{-K}$ with ϕ_η being the phase of SC and $\mathrm{PDW}_\pm$ order parameters for $\eta = 0$ and $\pm K$ respectively. Note that some terms are zero due to the absence of the Γ pocket, in particular $|\Delta_{-K}|^2|\Delta_K|^2$ and $|\Delta_{\pm K}|^2|\Delta_0||\Delta_{\mp K}|$ terms are not allowed in the microscopic theory though they

are present in (5.9). The only mixing between the PDWs is therefore via uniform SC. The mixing is never energetically favored (except at the degeneracy point of SC and PDW), however, which means that the two PDWs decouple in the free energy. This in turn means that both appear with equal magnitudes (as both satisfy the same saddle point equations), and the ground state is an LO-type PDW. The relative phases are then fixed at the sixth order as we saw.

Although there is no direct coupling between the two PDWs at fourth order, we note that such a coupling can be mediated by SC fluctuations assuming we are above the superconducting T_c. We then have the partition function

$$\mathcal{Z}_{PDW} = \int e^{-\beta \mathcal{F}} \mathcal{D}[\Delta_0] \tag{5.17}$$

with

$$\begin{aligned} \mathcal{F} &= -a_0|\Delta_0|^2 - a_1|\Delta_1|^2 - a_1|\Delta_{-K}|^2 + \Gamma^{(0)}\left(|\Delta_K|^4 + |\Delta_{-K}|^4\right) + \\ &+ 4\Gamma^{(0)}|\Delta_0|^2\left(|\Delta_1|^2 + |\Delta_{-K}|^2 \pm |\Delta_K||\Delta_{-K}|\cos\phi_\Gamma\right) \end{aligned} \tag{5.18}$$

We can re-write this in term of real and imaginary parts $\Delta_0 = \Delta_0' + i\Delta_0''$:

$$\mathcal{F} = -a_1|\Delta_K|^2 - a_1|\Delta_{-K}|^2 + \Gamma^{(0)}\left(|\Delta_K|^4 + |\Delta_{-K}|^4\right) + \begin{pmatrix} \Delta_0' \\ \Delta_0'' \end{pmatrix} \cdot A \begin{pmatrix} \Delta_0' \\ \Delta_0'' \end{pmatrix} \tag{5.19}$$

where

$$A = (-a_0 + 4\Gamma^{(0)}\left(|\Delta_K|^2 + |\Delta_{-K}|^2\right))\sigma^0 \pm 4\Gamma^{(0)}\mathrm{Re}[\Delta_K\Delta_{-K}]\sigma^z \pm 4\Gamma^{(0)}\mathrm{Im}[\Delta_K\Delta_{-K}]\sigma^x \tag{5.20}$$

is a real symmetric matrix with determinant

$$\det[A] = (-a_0 + 4\Gamma^{(0)}\left(|\Delta_K|^2 + |\Delta_{-K}|^2\right))^2 - (4\Gamma^{(0)})^2|\Delta_K\Delta_{-K}|^2 \tag{5.21}$$

We then perform the Gaussian integral to get

$$\mathcal{Z}_{PDW} = e^{-\beta\tilde{\mathcal{F}}} \tag{5.22}$$

working to quadratic order in Δ_0 and quartic in $\Delta_{\pm K}$. Explicitly, we have

$$\int \exp\left[-\beta \begin{pmatrix} \Delta_0' \\ \Delta_0'' \end{pmatrix} \cdot A \begin{pmatrix} \Delta_0' \\ \Delta_0'' \end{pmatrix}\right] d\Delta_0' d\Delta_0'' = \sqrt{\frac{\pi^2}{\beta^2 \det[A]}} = \pi e^{-\frac{1}{2}\ln\beta^2 \det[A]} \tag{5.23}$$

Expanding to fourth order in $\Delta_{\pm K}$, we have (dropping irrelevant overall constant factors)

$$\begin{aligned} \tilde{\mathcal{F}} &= -\left(a_1 + \frac{4\Gamma^{(0)}}{\beta a_0}\right)\left(|\Delta_K|^2 + |\Delta_{-K}|^2\right) + \left(\Gamma^{(0)} - \frac{1}{2\beta}\left(\frac{4\Gamma^{(0)}}{a_0}\right)^2\right)\left(|\Delta_K|^4 + |\Delta_{-K}|^4\right) - \\ &- \frac{3}{2\beta}\left(\frac{4\Gamma^{(0)}}{a_0}\right)^2 |\Delta_1|^2 |\Delta_{-1}|^2 \end{aligned} \tag{5.24}$$

Note the last term now couples the two PDWs, corresponding to the β_3 term in (5.9). The free energy is easily minimized, but the conclusion remains the same as before: both PDWs coexist with equal magnitudes and LO-type PDW is established in the ground state.

5.2 Mean Field PDW without SOC: Imperfect Nesting

As alluded to earlier, PDW is generally suppressed due to the fact that in general symmetry allows for $\epsilon_K(\mathbf{p}) \neq \epsilon_K(-\mathbf{p}) \neq \epsilon_\Gamma(\mathbf{p})$. We refer to the conditions $\epsilon_K(\mathbf{p}) = \epsilon_K(-\mathbf{p})$ and $\epsilon_K(\mathbf{p}) = \epsilon_\Gamma(-\mathbf{p})$ as (perfect) nesting conditions, and say that there is imperfect nesting if they hold approximately. In particular, the nesting is not perfect because the Fermi surfaces are not perfectly circular at K points due to trigonal warping and Fermi surfaces do not necessarily have the same radius (or shape) at Γ and K points. In order to study when the PDW phase is nevertheless viable, we perform a mean field analysis using the linearized gap equation:

$$\begin{aligned} \left[\Delta_{\eta\zeta}(\mathbf{p})\right]_{\alpha\beta} &= -T \sum_{\substack{\omega \mathbf{k} \eta'\zeta' \\ \alpha'\beta'}} V^{\eta'\zeta';\alpha'\beta'}_{\eta\zeta;\alpha\beta}(\mathbf{p};\mathbf{k}) \left[G^{(0)}_{\eta'}(i\omega,\mathbf{k})\Delta_{\eta'\zeta'}(\mathbf{k})G^{(0)T}_{-\zeta'}(-i\omega,-\mathbf{k})\right]_{\alpha'\beta'} = \\ &= -T \sum_{\substack{\mathbf{k} \eta'\zeta' \\ \alpha'\beta'}} V^{\eta'\zeta';\alpha'\beta'}_{\eta\zeta;\alpha\beta}(\mathbf{p};\mathbf{k}) \left[\Pi_{\eta'\zeta'}(\mathbf{k})\Delta_{\eta'\zeta'}(\mathbf{k})\right]_{\alpha'\beta'} \end{aligned} \tag{5.25}$$

where $V^{\eta'\zeta';\alpha'\beta'}_{\eta\zeta;\alpha\beta}$ are the same interactions as in Section 2.2 in Eq. (2.112):

$$V^{\eta'\zeta';\alpha'\beta'}_{\eta\zeta;\alpha\beta}(\mathbf{p},\mathbf{k}) = V^{\eta'\zeta';\alpha'\beta'}_{\eta\zeta;\alpha\beta}(\theta,\theta') = \sum_{\ell\mu\nu} g^{(\ell\mu)}_{\eta'\zeta';\eta\zeta} \left[\Sigma^{(\ell\mu)}_{\eta\zeta}(\theta)\right]_{\alpha\beta} \left[\Sigma^{(\ell\mu)*}_{\eta'\zeta'}(\theta')\right]_{\alpha'\beta'} \tag{5.26}$$

where

$$\Sigma^{(\ell\mu)}_{\eta\zeta}(\theta) = \Theta^{(\ell\mu)}_{\eta\zeta}(\theta)\sigma^{\mu} i\sigma^{y} \tag{5.27}$$

are basis function with $\Theta^{(\ell\mu)}_{\eta\zeta}(\theta)$ being $\pm 1, \sqrt{2}\cos n\theta, \sqrt{2}\sin n\theta$, listed in Table 5.3. By momentum conservation, the interactions vanish unless $\eta + \eta' = \zeta + \zeta'$ mod three; this means in particular that the uniform SC and each of the $\pm K$ PDW's decouple in the gap equation. As usual the momenta $\mathbf{p}$, $\mathbf{k}$ are measured from the center of the Fermi pocket, and we assume that the gaps and interactions are independent of the radial component of the momentum $\mathbf{k}$, and drop sharply to zero at the cutoff Λ. In Eq. (5.25) we also used the fact that the Green's functions are proportional to the identity in spin indices in the absence of SOC to get the angle resolved particle-particle susceptibility

$$\begin{aligned} \Pi_{\eta\zeta}(\theta) &= -\frac{1}{8\pi^2}\int_{\Lambda} \frac{\tanh\left(\frac{\varepsilon_{\eta}(\mathbf{Q})}{2T}\right) + \tanh\left(\frac{\varepsilon_{\zeta}(-\mathbf{Q})}{2T}\right)}{\varepsilon_{\eta}(\mathbf{Q}) + \varepsilon_{\zeta}(-\mathbf{Q})} QdQ \approx \\ &\approx \frac{N_{\eta}N_{\zeta}}{N_{\eta}+N_{\zeta}} \varpi\left(\epsilon_{\eta}(\mathbf{k}) - \epsilon_{\zeta}(-\mathbf{k})\right) \end{aligned} \tag{5.28}$$

where

$$\varpi(x) = -\log\frac{1.13\Lambda}{T} + \mathrm{Re}\left[\psi\left(\frac{1}{2} + \frac{ix}{4\pi T}\right) - \psi\left(\frac{1}{2}\right)\right] \tag{5.29}$$

and ψ is the digamma function. At perfect nesting, $\varpi(0) = -\log\frac{1.13\Lambda}{T}$.

Before we proceed to solve the gap equation, we make several important comments about the interactions. From a microscopic point of view, an effective attraction in the SC channel is known to arise from onsite interactions via electron-phonon coupling (as in the BCS or Eliashberg theory), or as we saw in Section 2.2 from purely repulsive *multi-band* interactions. However, we do not know of any situation in which onsite interactions can give rise to a PDW instability. For repulsive interactions, we saw that a Γ pocket is necessary to produce an effective attraction in the PDW channel in one loop RG. We also generally expect that only interactions that are mostly independent of momentum can drive any instability, with possibly small admixtures of higher order harmonics.

Keeping only such terms as well as the leading f-wave triplet terms (to avoid Δ_{KK} vanishing in the triplet channels) gives what we will call the minimal model (first given in Table 2.1). We mark these terms with (*) in Table 5.3 and label the corresponding coupling constants are $g_1^{(\ell\mu)}, g_{23}^{(\ell\mu)}, g_4^{(\ell\mu)}$ in the uniform SC channels and $h_1^{(\ell\mu)}, h_{23}^{(\ell\mu)}, h_4^{(\ell\mu)}$ in the PDW channel, as given in Table 2.2. As we saw in Section 2.2, these arise from eight momentum-conserving processes: intrapocket g_1 at Γ,

$\ell(D_{3h})$	$\Sigma^{(\ell 0)}_{KK} = \Theta^{(\ell 0)}_{KK}(\theta) i\sigma^y$	$\Sigma^{(\ell j)}_{KK} = \Theta^{(\ell j)}_{KK}(\theta)\sigma^j i\sigma^y$	$\Theta^{(\ell\mu)}_{KK}(\theta) W^{(0)}_{KK;\tau}$
$A_1^{'}$	$i\sigma^y$ (*)	$\cos 3\theta\ \sigma^z i\sigma^y$ (*)	0
$A_2^{'}$	$\sin 6\theta\ i\sigma^y$	$\sin 3\theta\ \sigma^z i\sigma^y$	0
$A_1^{''}$	$p_z \cos 3\theta\ i\sigma^y$	$p_z\sigma^z i\sigma^y$, $(\cos\theta\ \sigma^x + \sin\theta\ \sigma^y)\, i\sigma^y$	$i\tau e^{-i\tau\theta}$
$A_2^{''}$	$p_z \sin 3\theta\ i\sigma^y$	$(\sin\theta\ \sigma^x - \cos\theta\ \sigma^y)\, i\sigma^y$	$e^{-i\tau\theta}$
$E^{'}$	$\cos 2\theta i\sigma^y$, $\cos\theta\cos 3\theta\ i\sigma^y$ $\sin 2\theta i\sigma^y$, $\sin\theta\cos 3\theta\ i\sigma^y$	$\cos\theta\sigma^z i\sigma^y$ $\sin\theta\sigma^z i\sigma^y$	0
$E^{''}$	$p_z\cos\theta i\sigma^y$ $p_z\sin\theta i\sigma^y$	$\cos 3\theta\sigma^x i\sigma^y$ (*), $(\cos\theta\sigma^x - \sin\theta\sigma^y)\, i\sigma^y$ (†) $\cos 3\theta\sigma^y i\sigma^y$ (*), $(\sin\theta\sigma^x + \cos\theta\sigma^y)\, i\sigma^y$ (†)	$i\tau\cos 3\theta$, $i\tau e^{i\tau\theta}$ $-\cos 3\theta$, $e^{i\tau\theta}$

Table 5.3: Lattice harmonics/basis functions for the PDW$_-$ gap functions in the spin basis for intrapocket pairing within the K pocket. Terms in the minimal model are marked (*) and includes s-wave singlet and f-wave triplet terms. (†) marks the p-wave E'' term for later reference. For pairing between Γ and $-K$, take $\cos 3\theta \to \varepsilon_{\eta\zeta}$ wherever it appears (including $\sin 6\theta$), with $\epsilon_{\eta\zeta}$ being the Levi-Civita symbol. Note that the f-wave terms then become momentum independent. PDW$_+$ expressions are related to these by TRS, obtained by taking $K \to -K$ and complex conjugating. C_{3h} irreps are obtained by dropping the $1, 2$ subscripts on the 1D D_{3h} irreps. Rightmost column shows the gap projections into the SOC basis in the limit of strong Ising SOC that we will use in Section 5.3.

interpocket g_2 at $\pm K$, exchange g_3 between $\pm K$, pair-hopping g_4 between Γ and $\pm K$ relevant to the SC channel; and intrapocket h_1 at $\pm K$, interpocket h_2 between Γ and $\pm K$, exchange h_3 between Γ and $\pm K$, h_4 scattering a pair at Γ and $\pm K$ to a pair at $\mp K$ relevant for the PDW channel. As we are mostly interested in the latter, we show the PDW interaction processes in Figure 5.5.

More exotic source of effective attraction are in principle possible, of course, which would be necessary to stabilize a PDW in systems like doped MoS_2 that lack a Γ pocket. One possible source of attraction in that case may be the Kohn-Luttinger mechanism, as pointed out in [67] who considered a system with very strong Ising SOC and a single spin-polarized Fermi surface at each K point. As they showed and as we also discuss in Section 5.3, in that case the PDW is necessarily between equal spins and belongs to the E'' irrep, which has no momentum-independent terms. The Kohn-Luttinger mechanism favors the p-wave terms (marked with (†) in Table 5.3). Though this is not our main goal here, the mean field analysis in the absence of detuning we present below is sufficiently general to include the more exotic interactions as well, including the case without a K pocket. We will, however, restrict the detuning analysis below to the minimal model.

Returning to the gap equation, we find that as before ((2.103))

$$\Delta_{\eta\zeta}(\mathbf{p}) = \sum_{\ell\mu} \Delta^{(\ell\mu)}_{\eta\zeta}(\mathbf{p}) = \sum_{\ell\mu} \Sigma^{(\ell\mu)}_{\eta\zeta}(\theta) D^{(\ell\mu)}_{\eta\zeta} \tag{5.30}$$

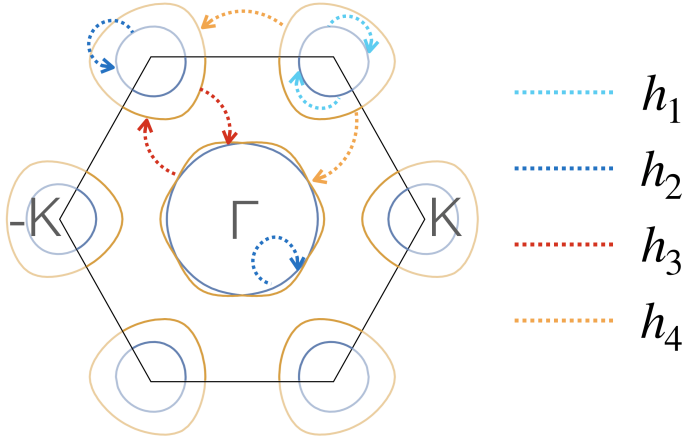

Figure 5.5: PDW$_+$ interactions in the Brillouin zone, with $h_1^{(A_1'0)} = h_1$, $h_{23}^{(A_1'0)} = \frac{h_2+h_3}{2}$, $h_4^{(A_1'0)} = h_4$, and $h_{23}^{(\ell j)} = \frac{h_2-h_3}{2}$ for $(\ell\mu) = (A_1'z)$, $(E''x)$ and $(E''y)$. Note that h_2 and h_3 contribute to both spin-singlet and spin-triplet channels, and therefore mix. For PDW$_-$, exchange K with $-K$.

solves the gap equation when the momentum-independent coefficients $D_{\eta\zeta}^{(\ell\mu)}$ satisfy

$$D_{\eta\zeta}^{(\ell\mu)} = \sum_{\eta'\zeta'} g_{\eta'\zeta';\eta\zeta}^{(\ell\mu)} \bar{\Pi}_{\eta'\zeta'}^{(\ell\mu)} D_{\eta',-\zeta'}^{(\ell\mu)} \tag{5.31}$$

where

$$\bar{\Pi}_{\eta\zeta}^{(\ell\mu)} = \int \Pi_{\eta\zeta}(\theta) \mathrm{Tr}\left[\Sigma_{\eta\zeta}^{(\ell\mu)}(\theta)\Sigma_{\eta\zeta}^{(\ell\mu)*}(\theta)\right] \frac{d\theta}{2\pi} \tag{5.32}$$

are Fermi surface averages of $\Pi_{\eta\eta'}(\theta)$ in Eq. (5.28) weighted by traces of the irrep basis functions.

Here it is convenient to absorb the particle-particle susceptibility into the coupling constants and define

$$\begin{aligned} \hat{g}_1^{(\ell\mu)} &= \bar{\Pi}_{\Gamma\Gamma}^{(\ell\mu)} g_1^{(\ell\mu)}, \quad \hat{g}_{4\eta}^{(\ell\mu)} = \bar{\Pi}_{\eta,-\eta}^{(\ell\mu)} g_4^{(\ell\mu)}, \quad \hat{g}_{23}^{(\ell\mu)} = \bar{\Pi}_{K,-K}^{(\ell\mu)} g_{23}^{(\ell\mu)} \\ \hat{h}_1^{(\ell\mu)} &= \bar{\Pi}_{KK}^{(\ell\mu)} h_1^{(\ell\mu)}, \quad \hat{h}_{4\eta}^{(\ell\mu)} = \bar{\Pi}_{1+\eta,1-\eta}^{(\ell\mu)} h_4^{(\ell\mu)}, \quad \hat{h}_{23}^{(\ell\mu)} = \bar{\Pi}_{\Gamma,-K}^{(\ell\mu)} h_{23}^{(\ell\mu)} \end{aligned} \tag{5.33}$$

The reduced gap equations then simply read

$$\begin{pmatrix} D_{\pm K\pm K}^{(\ell\mu)} \\ D_{\Gamma,\mp K}^{(\ell\mu)} \end{pmatrix} = \begin{pmatrix} \hat{h}_4^{(\ell\mu)} & 2\hat{h}_{4K}^{(\ell\mu)} \\ \hat{h}_{4\Gamma}^{(\ell\mu)} & 2\hat{h}_{67}^{(\ell\mu)} \end{pmatrix} \begin{pmatrix} D_{\pm K\pm K}^{(\ell\mu)} \\ D_{\Gamma,\mp K}^{(\ell\mu)} \end{pmatrix} \tag{5.34}$$

in the PDW channels. For completeness (since we have not written down the mean field SC equations without SOC above), we also have

$$\begin{pmatrix} D_{\Gamma\Gamma}^{(\ell\mu)} \\ D_{K,-K}^{(\ell\mu)} \end{pmatrix} = \begin{pmatrix} \hat{g}_1^{(\ell\mu)} & 2\hat{g}_{4K}^{(\ell\mu)} \\ \hat{g}_{4\Gamma}^{(\ell\mu)} & 2\hat{g}_{23}^{(\ell\mu)} \end{pmatrix} \begin{pmatrix} D_{\Gamma\Gamma}^{(\ell\mu)} \\ \Delta_{K,-K}^{(\ell\mu)} \end{pmatrix} \tag{5.35}$$

in the uniform SC channels. Note that all $(\ell\mu)$ channels decouple and the triplet channels and the two PDW channels are degenerate.

As the matrices are 2×2, the eigenvalues are easily found to be

$$\kappa^{(\ell\mu\pm)} = \frac{1}{2}\left(\hat{h}_1^{(\ell\mu)} + 2\hat{h}_{23}^{(\ell\mu)} \pm \sqrt{(\hat{h}_1^{(\ell\mu)} - 2\hat{h}_{23}^{(\ell\mu)})^2 + 8\hat{h}_{h\Gamma}^{(\ell\mu)}\hat{h}_{4K}^{(\ell\mu)}}\right) \tag{5.36}$$

in the PDW channel and

$$\gamma^{(\ell\mu\pm)} = \frac{1}{2}\left(\hat{g}_1^{(\ell\mu)} + 2\hat{g}_{23}^{(\ell\mu)} \pm \sqrt{(\hat{g}_1^{(\ell\mu)} - 2\hat{g}_{23}^{(\ell\mu)})^2 + 8\hat{g}_{4\Gamma}^{(\ell\mu)}\hat{g}_{4K}^{(\ell\mu)}}\right) \tag{5.37}$$

in the SC channel. The eigenvectors are

$$\begin{pmatrix} D_{\pm K,\pm K}^{(\ell\mu+)} \\ D_{\Gamma,\mp K}^{(\ell\mu+)} \end{pmatrix} \propto \begin{pmatrix} \kappa^{(\ell\mu+)} - 2\hat{h}_{23}^{(\ell\mu)} \\ \hat{h}_{4\Gamma}^{(\mu)} \end{pmatrix} \tag{5.38}$$

for PDW and (again for completeness)

$$\begin{pmatrix} D_{\Gamma\Gamma}^{(\ell\mu+)} \\ D_{K-K}^{(\ell\mu+)} \end{pmatrix} \propto \begin{pmatrix} \gamma_+^{(\ell\mu)} - 2\hat{g}_{23}^{(\ell\mu)} \\ \hat{g}_{4\Gamma}^{(\ell\mu)} \end{pmatrix} \tag{5.39}$$

for SC. Note that these correspond precisely to the RG channels in Eqs. (2.125) and (2.126) for perfect nesting (since mean field is then equivalent to the RG analysis). As in that case, the $\kappa^{(\ell\mu-)}$ solutions always yield lower T_c's than $\kappa^{(\ell\mu+)}$ and so can be ignored. Whether PDW occurs depends on whether one of $\kappa^{(\ell\mu+)}$ exceeds all of $\gamma^{(\ell\mu+)}$, which is in principle possible depending on the values of the bare coupling constants g_j and h_j.

However, unlike the SC channel, there is no symmetry that guarantees the logarithmic instability in the PDW channel. As alluded to above, there are two sources of detuning from perfect nesting in PDW that disfavor it relative to uniform SC. First, the pockets at Γ and K are not identical. Second, the pockets centered at $\pm K$ are not perfectly circular, but instead have trigonal warping

[84], such that the dispersion at the $\pm K$ pockets is instead

$$\varepsilon_{\pm K}(\mathbf{p}) = -\frac{p^2}{2m_K} + \mu_K \pm w\cos 3\theta \tag{5.40}$$

where w parametrizes the magnitude of the warping. This affects both nesting between $\pm K$ and Γ pockets, and nesting of PDW pairs within K and within $-K$ pockets (see Figure 5.1). Note that this decreases the susceptibility to PDW but not to uniform SC pairing.

If the deviation from perfect nesting is large, it can eliminate the instability to a PDW phase entirely, since without nesting the PDW couplings will no longer grow logarithmically in the RG flow. In this case, the only possible low-temperature perturbative instability is to uniform BCS superconductivity. Although in general any deviation from perfect nesting disfavors PDW pairing relative to uniform superconductivity when all coupling constant are of comparable magnitude, if the shape of the Fermi surfaces deviates only slightly from perfect nesting, the PDW phase remains viable.

Detuning by Trigonal Warping in the Absence of a Γ Pocket

Although as we argued no PDW channel arises from *repulsive* interactions without a Γ pocket, it is nevertheless instructive to first consider the MoS_2 scenario with only the K pocket present and trigonal warping is the only relevant detuning parameter, and later include the Γ pocket. In either case, attractive interactions are included in the model, including within K pockets (which amounts to taking $h_1 < 0$).

Without a Γ pocket the only PDW gap functions are Δ_{KK} and Δ_{-K-K} (and two SC gap functions Δ_{K-K} and Δ_{-KK}, corresponding to a single order parameter by PHS). In this case the reduced gap equations Eqs. (5.35) and (5.34) become simply

$$2\hat{g}_{23}^{(\ell\mu)} = -2(g_2 \pm g_3)N_K \log\frac{1.13\Lambda}{T_c^{(\ell\mu)}} = 1 \tag{5.41}$$

for uniform SC and

$$\hat{h}_1^{(\ell\mu)} = \bar{\Pi}_{KK}^{(\ell\mu)} h_1^{(\ell\mu)} = 1 \tag{5.42}$$

for PDW. Note that in the PDW triplet channels $\mu \neq 0$, there are no uniform gap functions independent of the small momentum, so we would expect those channels to be subleading with $h_1^{(\ell\mu)} \approx 0$.

Assuming the trigonal warping is much smaller than the cutoff Λ we have

$$\Pi_{KK}(\theta) = -N_K \log \frac{1.13\Lambda}{T_{c,PDW}^{(\ell\mu)}} + N_K \mathrm{Re}\left[\psi\left(\frac{1}{2} + \frac{iw\cos 3\theta}{2\pi T_{c,PDW}^{(\ell\mu)}}\right) - \psi\left(\frac{1}{2}\right)\right] \tag{5.43}$$

where $T_{c,PDW}^{(\ell\mu)}$ is the PDW critical temperature in the $(\ell\mu)$ channel. Taking $T_{c0,PDW}^{(\ell\mu)}$ to be the critical temperature for PDW at perfect nesting $w = 0$, we thus have

$$\begin{aligned} \log \frac{T_{c,PDW}^{(\ell\mu)}}{T_{c0,PDW}^{(\ell\mu)}} &= -\frac{1}{2}\int \left(\frac{\Pi_{KK}(\theta)}{N_K} - \log \frac{1.13\Lambda}{T_{c,PDW}^{(\ell\mu)}}\right) \mathrm{Tr}\left[\Sigma_{KK}^{(\ell\mu)}(\theta)\Sigma_{KK}^{(\ell\mu)*}(\theta)\right] \frac{d\theta}{2\pi} = \\ &= -\frac{1}{2}\int \mathrm{Re}\left[\psi\left(\frac{1}{2} + \frac{iw\cos 3\theta}{2\pi T_{c,PDW}^{(\ell\mu)}}\right) - \psi\left(\frac{1}{2}\right)\right] \mathrm{Tr}\left[\Sigma_{KK}^{(\ell\mu)}(\theta)\Sigma_{KK}^{(\ell\mu)*}(\theta)\right] \frac{d\theta}{2\pi} \end{aligned} \tag{5.44}$$

Thus $T_{c,PDW}^{(\ell\mu)}$ follows a universal curve independent of g_5, N_K and Λ once $T_{c0,PDW}^{(\ell\mu)}$ is set. These are shown in Figure 5.6. At zero temperature

$$\Pi_{KK}(\theta) = -N_K \log \frac{\Lambda}{2|w\cos 3\theta|} \tag{5.45}$$

The integrals can be done analytically for the leading channels and we find

$$\bar{\Pi}_{KK}^{(A_1'0)} = -N_K \log \frac{\Lambda}{|w|} \tag{5.46}$$

and

$$\bar{\Pi}_{KK}^{(\ell j)} = -N_K \log \frac{\Lambda}{e^{1/2}|w|} \tag{5.47}$$

for $\ell = A_1', E''$ and $j = x, y, z$, so the curves approach upper critical values $w_c^{(\ell\mu)}$ as $T \to 0$ that differ by a factor of $e^{1/2} \approx 1.64$:

$$w_c^{(A_1'0)} = \frac{\pi}{2e^{\gamma}} T_{c0,PDW}^{(A_1'0)} \approx 0.88\ T_{c0,PDW}^{(A_1'0)} \tag{5.48}$$

while for f-wave triplet PDW it is

$$w_c^{(\ell j)} = \frac{\pi}{2e^{\gamma+1/2}} T_{c0,PDW}^{(\ell j)} \approx 0.54\ T_{c0,PDW}^{(\ell j)} \tag{5.49}$$

for $\ell = A_1', E''$ and $j = x, y, z$. Unlike in the Pauli limit, the phase transition remains second

order down to zero temperature in the singlet channel, which is thus in a sense more stable against trigonal warping than triplet PDW. We note however that the particular factor is specific to the model in which we took the irrep basis functions for triplet interactions to all be f-wave (proportional to $\cos 3\theta$). There are however also p-wave triplet basis functions (proportional to $\cos\theta$ and $\sin\theta$) belonging to the E'' irrep as shown in Table 5.3, and for those we get $w_c^{(\ell j)} = w_c^{(A_1' 0)}$ for $j = x, y$, i.e. the same susceptibility as in the singlet channel. In particular, this means trigonal warping may favor p-wave over f-wave triplet pairing (depending on the corresponding interaction strengths).

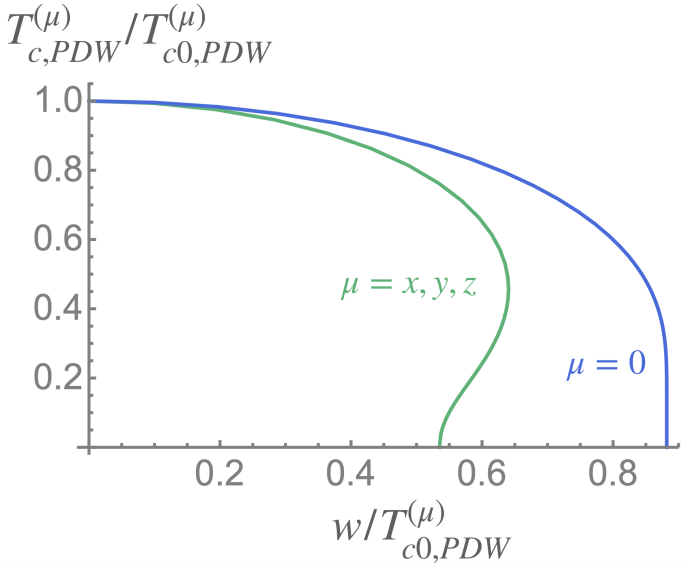

Figure 5.6: Critical temperature $T^{(\ell\mu)}_{c,PDW}$ for PDW as a function of trigonal warping w, both in units of $T^{(\ell\mu)}_{c0,PDW}$, for s-wave singlet ($\ell = A_1'$, $\mu = 0$ in blue) and f-wave triplet ($\ell = A_1', E''$, $\mu = x, y, z$ in green) channels, determined by Eq. (5.44). The p-wave triplet curve coincides with the singlet curve.

PDW Detuning in Presence of the Γ Pocket

In the presence of the Γ pocket, in addition to $\Delta_{\pm K,\pm K}$ there are also interpocket PDW gap functions $\Delta_{\Gamma,\mp K}$ with additional susceptibility $\Pi_{\Gamma K}$ that has two sources of detuning: it is also affected by the trigonal warping, but there is an additional detuning due to the mismatch of Fermi momentum at Γ and K pockets. For a parabolic dispersion, the Fermi momentum mismatch can be due to a difference in masses m_η or chemical potentials μ_η. Assuming $\sqrt{m_\Gamma/m_K}$ and $\sqrt{m_K/m_\Gamma}$ are both

small compared to Λ/T_c and

$$\hat{\mu} = \frac{|m_\Gamma \mu_\Gamma - m_K \mu_K|}{m_\Gamma + m_K} \ll \Lambda \tag{5.50}$$

where $\hat{\mu}$ is roughly the energy difference between the two parabolic dispersions at equal small momenta, we find

$$\Pi_{\Gamma K}(\theta) = -\frac{2N_\Gamma N_K}{N_\Gamma + N_K} \log \frac{1.13\Lambda}{T_{c,PDW}^{(\ell\mu)}} + \frac{2N_\Gamma N_K}{N_\Gamma + N_K} \mathrm{Re}\left[\psi\left(\frac{1}{2} + \frac{i(\hat{\mu} + w\cos 3\theta)}{4\pi T_{c,PDW}^{(\ell\mu)}}\right) - \psi\left(\frac{1}{2}\right)\right] \tag{5.51}$$

Note that the trigonal warping w also enters into this expression.

At zero temperature, the Fermi surface averaging can be done analytically:

$$\bar{\Pi}_{\Gamma K}^{(\ell\mu)} = -\frac{2N_\Gamma N_K}{N_\Gamma + N_K} \log \frac{2\Lambda}{\left|\hat{\mu} + \sqrt{\hat{\mu}^2 - \frac{w^2}{4}}\right|} \tag{5.52}$$

Note that this happens to be constant as a function of $\hat{\mu}$ for $\hat{\mu} < w/2$, i.e. when the at least some Fermi momenta (relative to the pocket centers) are equal. This is a somewhat particular feature of our simplified model, but similar non-analyticities are generically present in $\bar{\Pi}_{\Gamma K}^{(\ell\mu)}$ for other interaction and detuning parameterizations.

Plugging the expressions (5.43), (5.52) into Eq. (5.34), we obtain T_c as a function of the detuning parameters w and $\hat{\mu}$. The results are shown in Figure 5.7 and Figure 5.8 for a singlet ($\mu = 0$) and triplet ($\mu = x, y, z$) cases respectively. The plots on top right show the phase diagram in the $(T, w, \hat{\mu})$ space, with PDW being stable inside the surface. T_c as a function of w ($\hat{\mu}$) for various fixed $\hat{\mu}$ (w) is shown on top (bottom) left. Finally, the critical values of the detuning parameters at various fixed temperatures are shown on bottom right; the values at $T = 0$ are obtained analytically. Note that since this is now a multiband calculation, the curves are no longer universal and depend (weakly) on the cutoff Λ.

Several observations can be made. For the singlet case, PDW is fairly stable against $\hat{\mu}$ at small w, and $T_{c,PDW}^{(0)}$ only goes to zero for $\hat{\mu} \sim \Lambda$ (as can be shown analytically).This is because increasing $\hat{\mu}$ only directly affects $\Delta_{\Gamma K}$, but condensation at the K pocket remains energetically favorable (note that the effective attraction within the K pocket in this case still arises from pair hopping, and all interactions here are repulsive). On the other hand, both singlet and triplet PDW's are unstable with respect to trigonal warping, as it reduces the paring susceptibilities for both $\Delta_{\Gamma K}$ and Δ_{KK}. Because $\bar{\Pi}_{\Gamma K}$ is constant for $\hat{\mu} < w/2$ at zero temperature, the critical value of w is constant for

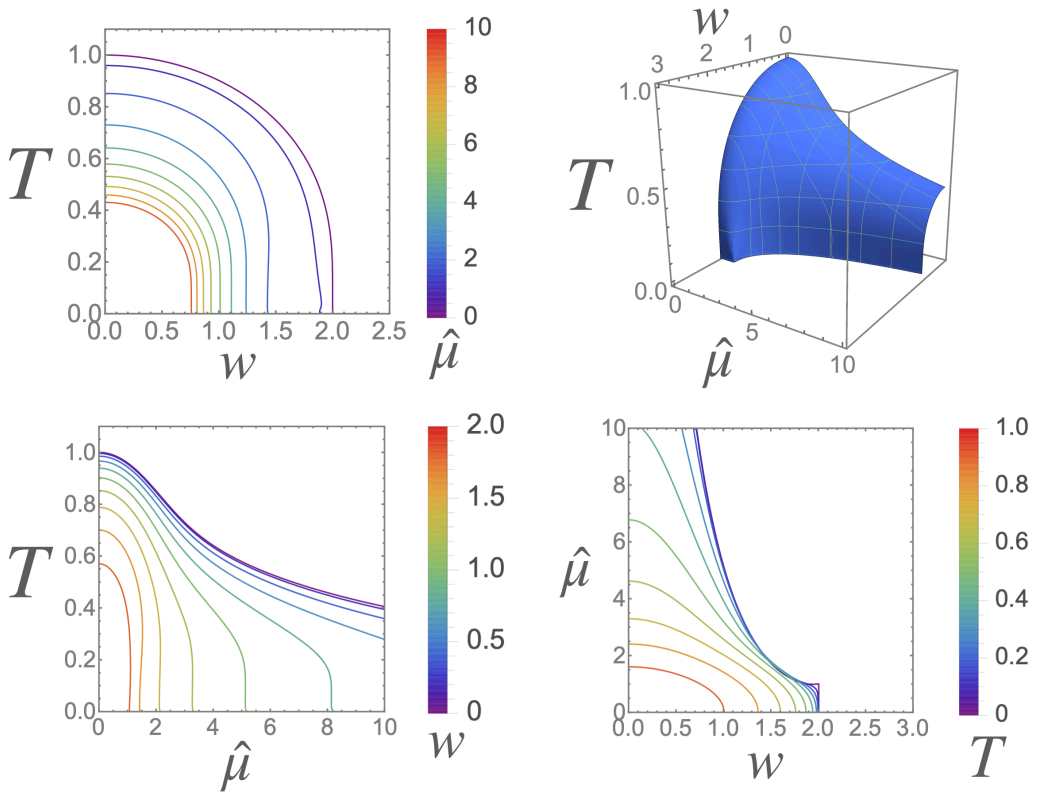

Figure 5.7: Critical surface for an instability of the singlet ($A_1'0$) PDW channel (PDW$_\pm$ are degenerate) determined by (5.34) in the phase space of temperature T, trigonal warping w, and Fermi surface mismatch between Γ and K pockets $\hat{\mu}$, top right. Cuts are shown at constant $\hat{\mu}$ (top left), constant w (bottom left), and constant T (bottom right) in units of T_{c0} (T_c at zero detuning). Parameters used are the same as in Figure 4.2.

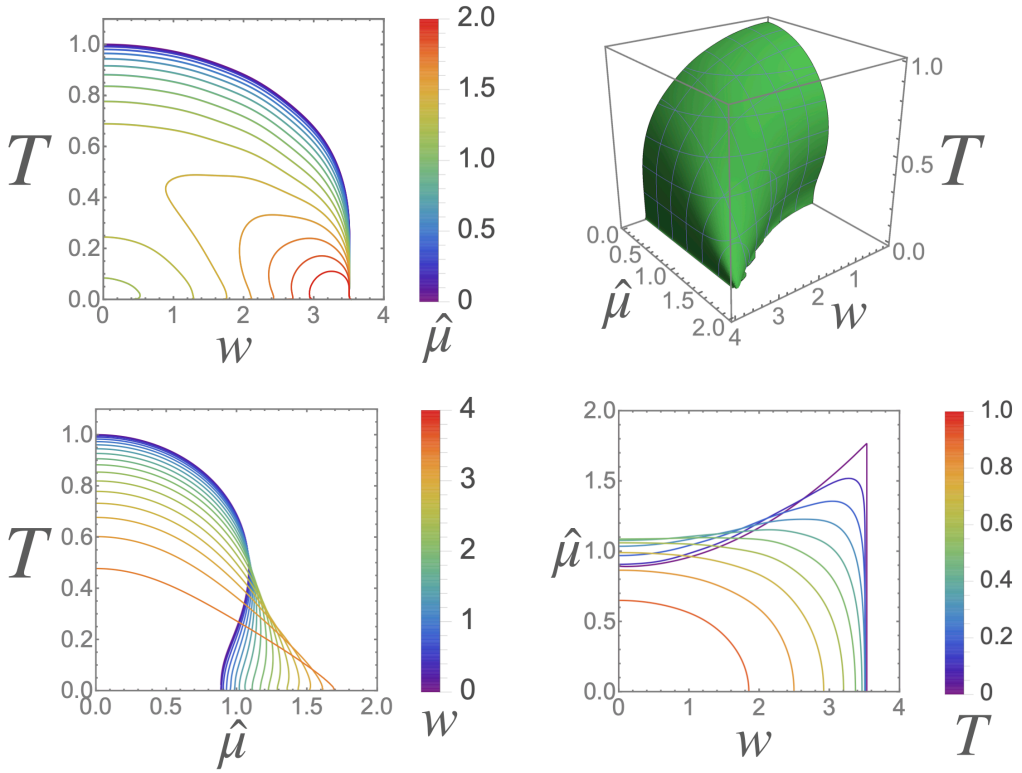

Figure 5.8: Same as Figure 5.7, but for the triplet PDW instabilities $(A_1' z)$, $(E'' x)$ and $(E'' y)$ that are degenerate in the absence of SOC. All parameters are in units of T_{c0}. The reentrant behavior in the T_c vs w plot (top left) is in part due to the non-single-valuedness of T_c as a function of $\hat{\mu}$ that can be seen in the T_c vs $\hat{\mu}$ plot (bottom left), which indicates that a first order rather than a second order phase transition likely takes place for sufficiently large $\hat{\mu}$. See also discussion in the text.

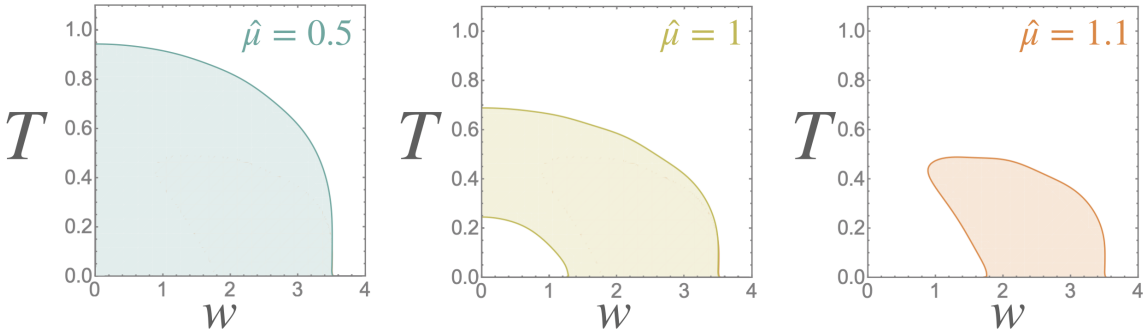

Figure 5.9: Three types of behavior of stability regions in temperature T/trigonal warping w phase space for the triplet PDW instabilities at fixed values of $\hat{\mu}$. For larger $\hat{\mu}$, the instability may vanish at $T = w = 0$, but due to the spinodal curve having two branched in the T vs $\hat{mu}$ phase space (bottom left panel in Figure 5.8), increasing the temperature can stabilize the phase. Similarly, increasing w can also stabilize the phase, resulting in behavior in the middle panel. Ateven larger $\hat{mu}$ stability of PDW is completely lost at $w = 0$, but not at $T = 0$, resulting in behavior in the right panel.

$\hat{\mu} < w/2$, resulting in straight lines in the corresponding plots in Figure 5.7 and Figure 5.8. This is a particular feature of our model, as mentioned above, but in general there is an upper critical value of w beyond which PDW is unstable for any $\hat{\mu}$ because it enters both $\bar{\Pi}_{\Gamma K}$ and $\bar{\Pi}_{KK}$, while $\hat{\mu}$ does not. As a result there may not be an upper critical value of $\bar{\mu}$ at $w = 0$, as in the case of singlet PDW channel.

In the triplet case, we only include small subleading f-wave terms in the interactions, and $\Delta^{(j)}_{KK}$ is therefore small for $j = x, y, z$, and the PDW is mostly stabilized by paring between Γ and K fermions, i.e. by $\Delta_{\Gamma K}$. Consequently, the triplet channel is much more sensitive to the Fermi surface mismatch due to $\hat{\mu}$, and $T^{(j)}_{c,PDW}$ drops off sharply as $\hat{\mu}$ increases and there is now a critical value of $\hat{\mu}$ at zero temperature, as shown in bottom left of Figure 5.8. Note that this critical value actually increases with increasing trigonal warping, suggesting that trigonal warping actually stabilizes PDW agains Fermi surface mismatch. As a result, there can be a reentrant phase transition into PDW as either T or w increase. For the latter, this happens because $\bar{\Pi}_{\Gamma K}$ actually increases with w when $\hat{\mu} > w/2$, which is when the Fermi surfaces at Γ and K (shifted to a common center) no longer overlap. As w increases, some points on the Fermi surfaces come closer, which increases $\bar{\Pi}_{\Gamma K}$.

As a result, three types of stability regions in the T/w plane are possible, as shown in Figure 5.9: PDW may be stable in a region under a single curve including the origin (left panel), between two curves excluding the origin (middle panel), or under a single curve but excluding the origin (right panel). In the latter case, PDW is not possible at $w = 0$ for any T, but it remains possible for $T = 0$ for sufficiently large w.

This reentrant behavior is a result of the fact that at $w = 0$, $T^{(j)}_{c,PDW}$ is not a single-valued function of $\hat{\mu}$ (purple curve in bottom right corner of Figure 5.8), indicative of a the phase transition becoming first order beyond some value of $\hat{\mu}$. Obtaining the first order phase transition line requires a further calculation beyond the scope of this thesis, but it has been shown in [178] that for a mathematically similar problem for an SDW instability, instead of a first order phase transition a different phase emerges with a shifted pairing momentum (similar to FFLO, in this case a PDW with pairing momentum slightly different from $\pm K$, i.e. slightly incommensurate), and the phase transition remains second order at least up to an even larger detuning.

5.3 Effects of SOC on PDW

As pointed out by [67] for systems with no Γ pocket and Fermi surfaces at K points completely polarized by Ising SOC, the PDW pairing is necessarily between equal spins. The same conclusion

holds when the K Fermi surfaces are split by the Ising SOC but are not polarized (i.e. there is both an inner and an outer Fermi surface). Since spins at the K points in both cases point in or out of the plane due to Ising SOC, pairing within the Fermi surface with equal spins is favored, which correspond to channels with $\mu = x, y$, and the leading terms we find in RG correspond to the E'' irrep in agreement with [67].

We can see this directly by projecting the PDW gap functions $\Delta_{\pm K,\pm K}$ from the spin basis onto the split Fermi surfaces, as we did for uniform SC in Chapter 4. The Pauli matrix projections in the strong SOC limit analogous to (4.22) are

$$\Delta_{\pm K,\pm K;\tau}(\mathbf{p}) = \sum_{\ell\mu} \Theta^{(\ell\mu)}_{\pm K,\pm K}(\mathbf{p}) W^{(\mu)}_{\pm K,\pm K;\tau}(\mathbf{p}) D^{(\ell\mu)}_{\pm K,\pm K} \tag{5.53}$$

where

$$\begin{aligned} W^{(0)}_{\pm K,\pm K;\tau}(\mathbf{p}) &= U^{\alpha}_{\pm K\tau}(\mathbf{p}) U^{\beta}_{\pm K\tau}(-\mathbf{p}) \left[i\sigma^y\right]_{\alpha\beta} \\ W^{(j)}_{\pm K,\pm K;\tau}(\mathbf{p}) &= U^{\alpha}_{\pm K\tau}(\mathbf{p}) U^{\beta}_{\pm K\tau}(-\mathbf{p}) \left[i\sigma^j i\sigma^y\right]_{\alpha\beta} \end{aligned} \tag{5.54}$$

with $j = x, y, z$ and the unitary transformation given in (4.6). A simple calculation then shows that

$$\begin{aligned} W^{(0)}_{\pm K,\pm K;\tau}(\mathbf{p}) &= 0 \\ W^{(x)}_{\pm K,\pm K;\tau}(\mathbf{p}) &= \pm i\tau \\ W^{(y)}_{\pm K,\pm K;\tau}(\mathbf{p}) &= -1 \\ W^{(z)}_{\pm K,\pm K;\tau}(\mathbf{p}) &= 0 \end{aligned} \tag{5.55}$$

Note that as expected, the $\mu = 0, z$ Pauli matrices corresponding to opposite spin pairing are thus projected out. With $\Theta^{(E''x/y)}_{\pm K,\pm K} = \sqrt{2}\cos 3\theta$, this means that the inner/outer gaps are

$$\Delta_{\pm K,\pm K;\tau} = \sqrt{2}\left(-D^{(E''y)}_{\pm K,\pm K} \pm i\tau D^{(E''x)}_{\pm K,\pm K}\right)\cos 3\theta \tag{5.56}$$

Although this is nodal, since the E'' irrep also contains p-wave terms listed in Table 5.3, there can be additional terms of the form

$$\Delta_{\pm K,\pm K;\tau} = \sqrt{2}\left(D^{(E''y)}_{\pm K,\pm K} \pm i\tau D^{(E''x)}_{\pm K,\pm K}\right) e^{\pm i\tau\theta} \tag{5.57}$$

that lift the nodes and moreover add phase windings $e^{\pm i\tau\theta}$ that are opposite on inner and outer

Fermi surfaces, and also opposite on a given inner or outer band on opposite pockets (the nodal gap is thus at a critical point of a topological phase transition). As mentioned in [67], if the inner Fermi surfaces at each K point are removed, this leads to chiral or helical PDW in the FF- and LO-type PDW respectively. With both inner and outer Fermi surfaces, the corresponding Chern numbers and $\mathbb{Z}_2$ invariants vanish because the windings are opposite, but crystalline topological invariants may remain non-trivial (a question we leave for future research).

The situation with the Γ pocket, which as we saw is necessary to produce a PDW from repulsive interactions, is more complicated. Because the Ising SOC is momentum dependent on the Γ pocket, in the projection of $\Delta_{\Gamma K}$ neither singlet nor triplet components vanish, and which one is favored depends on the model parameters. Though we do not solve the gap equation here, we can gain a bit of insight by looking at the pairing susceptibility in the SOC basis, which for pairing between inner and outer Fermi surfaces (labeled with $\tau, \upsilon = \pm 1$) at Γ and $\pm K$ pockets reads (cf. (5.28)-(5.29)):

$$\Pi_{\Gamma\tau;\pm K\upsilon}(\theta) = \frac{N_{\Gamma\tau}N_{K\upsilon}}{N_{\Gamma\tau}+N_{K\upsilon}}\varpi\left(\xi_{\Gamma\tau}(\mathbf{k}) - \xi_{\pm K\upsilon}(-\mathbf{k})\right) \tag{5.58}$$

where the detuning parameter is

$$\xi_{\Gamma\tau}(\mathbf{k}) - \xi_{\pm K\upsilon}(-\mathbf{k}) = \hat{\mu} \mp \upsilon\beta_I + (\tau\lambda_I p_F^3 \pm w)\cos 3\theta \tag{5.59}$$

(the parameters $\xi_{\eta\tau}, \beta_I, \lambda_I$ are summarized in Section 4.1). In particular the best nesting may be between inner Γ and outer K (or vice versa) which can favor opposite spin pairing including singlet pairing, and the nesting can improve with non-zero $\hat{\mu}, w$.

For pairing within K points, the susceptibility is

$$\Pi_{\pm K\tau;\pm K\upsilon}(\theta) = \frac{N_{K\tau}N_{K\upsilon}}{N_{K\tau}+N_{K\upsilon}}\varpi\left((\tau-\upsilon)\beta_I \pm 2w\cos 3\theta\right) \tag{5.60}$$

so for $w < \beta_I$, pairing within inner or outer Fermi surfaces is clearly preferred (note that this susceptibility has the same functional form as (5.52), so for $w > 2\beta_I$ it is largely independent of β_I, i.e. nesting is equally bad for interband and intraband pairing). On the other hand, even if the E'' PDW instability is favored for Ising SOC much larger than w, the singlet PDW instability may start to compete with it if $\beta_I \lesssim w$. Solving the gap equation numerically is necessary to identify the correct phase, which is a problem we leave for a future study.

Chapter 6

Comparison with Experiment: Unexpected 2-fold Anisotropic Response

In the previous chapters we have identified several interesting superconducting phases that may theoretically be realized in 1H-TMDs, including chiral SC, possibly topologically nontrivial FF- and LO-type PDWs, and nodal topological SC phases. The real systems are of course much more complicated than the simple model that was presented, and experiments are necessary to establish if any one of those phases is in fact realized. Since 1H-$NbSe_2$ is known to remain a (uniform) 2D superconductor in large in-plane magnetic fields, the most likely phase to look for seems to be one of the nodal topological SC phases driven by such fields that we discussed in Chapter 4. The crystalline nodal phase in particular appears in a large portion of the phase diagram and is largely independent of the details of the microscopic interactions. All that is required is a magnetic field exceeding the Rashba SOC (expected to be small, especially in encapsulated samples) applied along a particular direction that is relatively easy to tune in experiment. Since this phase depends sensitively on the direction of the applied field, a natural experiment is to look for any anisotropy in the SC response of 1H-$NbSe_2$. Since the system appears identical for fields directed along any one of the Γ-K directions, we would expect a six-fold symmetric response in for example H_c measurements (we discuss this in more detail below).

Precisely this kind of experiment has been carried out by [58] and independently by [186]. Both performed transport experiments, and a tunneling experiment was also carried out by [58]. Surprisingly, a two-fold anisotropy in the applied field direction is seen in both experiments, inconsistent with the crystal symmetry (see Figure 6.1). In this chapter we discuss possible explanations for these results. We will use a phenomenological approach following [160] and that appeared originally

in [58].

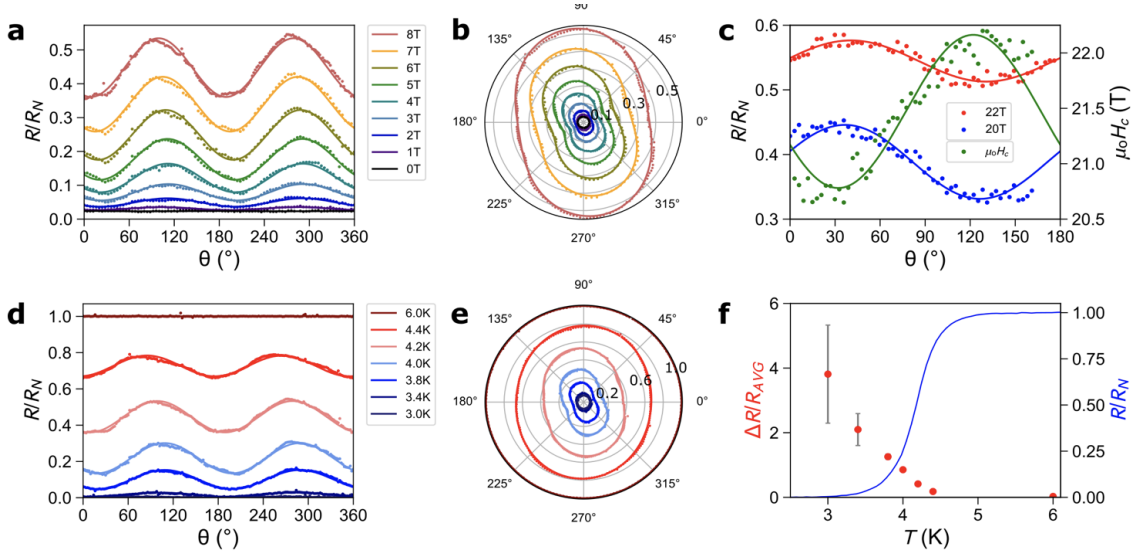

Figure 6.1: Two-fold anisotropy observed in transport experiment, figure adapted with permision from [58]. Plots show resistance R of the samples normalized by the resistance in the normal state R_N. Panels a-e show the resistance as a function of the direction of the magnetic field at various magnetic field strengths (a-c) and various temperature (d-e), with the rest of the parameters being fixed. c shows data obtained at high magnetic fields, with the green curve showing the extracted H_c. Panel f shows the resistance as a function of temperature, with T_c around 4 K, as well as the relative amplitude of the oscillations (red dots).

6.1 Necessary Conditions for Anisotropy

An unfortunate fact of life is that most things that are easy to measure experimentally are hard to calculate theoretically, and vice-versa. What is more or less both calculable and measurable, on the other hand, carries somewhat limited information about the phase and the order parameter. In this case, the quantities that are both relatively easy (i.e. practical) to measure and calculate are T_c, the superconducting critical temperature, and H_c, the critical magnetic field. Note that both do not explicitly depend on the details of the form of the gap function. On the experimental side, the difficulty is that while these are thermodynamic quantities, the easiest experiments are transport experiments that generally require the system to be out of equilibrium. Disorder and quantum fluctuations can also significantly affect the experiments, and the theoretical calculations including those effects are quite involved and require a more detailed model of the band structure and order parameters than we presented. This makes it more difficult to make a quantitive comparison with

the data.

On the qualitative side, however, at a minimum we expect that the response of the system to a symmetry breaking field like the magnetic field will have the same symmetry as the system. for example, if the system has trigonal symmetry, we expect the conductivity (a response to a current that breaks rotational symmetry as well as time reversal symmetry) to have at a minimum a three-fold symmetry as a function of the direction of the applied current (actually six-fold by TRS; it may even be isotropic). A constant magnetic field breaks two symmetries: TRS and mirror symmetries with respect to reflection planes containing the magnetic field. Note that the latter includes spin-rotation symmetry: the horizontal mirror symmetry acts on spin as $\mathcal{M}_z = i\sigma^z$, while the spin rotation by ϕ about the z axis acts as $R_z(\phi) = e^{i\phi\sigma^z/2}$. The orbital effects, i.e. vortices, break the same mirror symmetry (spin and vortex currents are loosely analogous in classical physics, and in particular have the same symmetry properties). Note that we do not expect the orbital effect to be significant in very thin samples a few monolayers thick (we discuss this point below). An anisotropic response to an in-plane magnetic field is therefore strongly suggestive of a broken spin rotation symmetry. We can prove this explicitly as a theorem for all thermodynamic quantities, assuming no orbital effect.

Theorem 6.1

The spectrum cannot depend on the direction of the in-plane magnetic field in a superconductor with horizontal mirror symmetry (i.e. with the magnetic field in the mirror plane). □

Proof 6.1

Consider a single band superconductor (the multiband case is identical but with additional indices). Very generally, in the spin basis we can take the gap function to be

$$\Delta = (D^{(0)} + D^{(x)}\sigma^x + D^{(y)}\sigma^y + D^{(z)}\sigma^z)i\sigma^y \tag{6.1}$$

(with $D^{(\mu)}$ possibly functions of momentum and magnetic field). The BdG Hamiltonian for a system with horizontal mirror symmetry (which forces any SOC to be of 'Ising' type) in an in-plane magnetic

field then reads

$$\mathcal{H}_{BdG}(\mathbf{p},\mathbf{b}) = \begin{pmatrix} \varepsilon(\mathbf{p})+\beta_I(\mathbf{p}) & be^{i\vartheta} & -D^{(x)}+iD^{(y)} & D^{(0)}+D^{(z)} \\ be^{-i\vartheta} & \varepsilon(\mathbf{p})-\beta_I(\mathbf{p}) & -D^{(0)}+D^{(z)} & D^{(x)}+iD^{(y)} \\ -D^{(x)*}-iD^{(y)*} & -D^{(0)*}+D^{(z)*} & -\epsilon(\mathbf{p})+\beta_I(\mathbf{p}) & -be^{-i\vartheta} \\ D^{(0)*}+D^{(z)*} & D^{(x)*}+iD^{(y)*} & -be^{i\vartheta} & -\varepsilon(\mathbf{p})-\beta_I(\mathbf{p}) \end{pmatrix} \tag{6.2}$$

where ε is the usual dispersion in the absence of the magnetic field or SOC (and momentum even), and ϑ is the direction of the magnetic field. Now, the BdG spectrum is unchanged under a unitary transformation. In particular, take

$$\mathcal{U} = \begin{pmatrix} e^{-i\vartheta'} & 0 & 0 & 0 \\ 0 & 1 & 0 & 0 \\ 0 & 0 & 1 & 0 \\ 0 & 0 & 0 & e^{-i\vartheta'} \end{pmatrix} \tag{6.3}$$

(essentially just redefining the x, y spin quantization directions). Then

$$\mathcal{U}\mathcal{H}_{BdG}(\mathbf{p},\mathbf{b})\mathcal{U}^\dagger = \begin{pmatrix} \epsilon(\mathbf{p})+\beta_I(\mathbf{p}) & be^{i(\vartheta-\vartheta')} & (-D^{(x)}+iD^{(y)})e^{-i\vartheta'} & D^{(0)}+D^{(z)} \\ be^{-i(\vartheta-\vartheta')} & \epsilon(\mathbf{p})-\beta_I(\mathbf{p}) & -D^{(0)}+D^{(z)} & (D^{(x)}+iD^{(y)})e^{i\vartheta'} \\ -(D^{(x)*}+iD^{(y)*})e^{i\vartheta'} & -D^{(0)*}+D^{(z)*} & -\epsilon(\mathbf{p})+\beta_I(\mathbf{p}) & -be^{-i(\vartheta-\vartheta')} \\ D^{(0)*}+D^{(z)*} & (D^{(x)*}+iD^{(y)*})e^{-i\vartheta} & -be^{i(\vartheta-\vartheta')} & -\epsilon(\mathbf{p})-\beta_I(\mathbf{p}) \end{pmatrix} \tag{6.4}$$

i.e. the BdG Hamiltonian but for a magnetic field direction shifted from ϑ to $\vartheta-\vartheta'$. It follows that if Δ minimizes the free energy at angle ϑ, it also minimizes the free energy at $\vartheta-\vartheta'$ provided we take

$$D^{(x)}+iD^{(y)} \propto e^{-i\vartheta} \tag{6.5}$$

□

i.e. the vector $\mathbf{D} = (D_x, D_y)$ is perpendicular to the magnetic field. Note that at zero magnetic field we must have $\mathbf{D} = 0$, as this term by itself breaks mirror symmetry. This fixes the dependence of the gap function on the direction of the magnetic field.

But note that this means that the BdG Hamiltonian for $\vartheta-\vartheta'$ can be obtained from the BdG Hamiltonian for ϑ by a unitary transformation. Therefore, the spectrum of the BdG Hamiltonian is independent of the direction of the magnetic field. Since many thermodynamic quantities are only functions of the BdG spectrum, they are similarly independent of the direction of the magnetic field.

For the orbital effects (which again we do not expect to be significant), the proof of the same statement follows from the fact that with the canonical (Peierls, minimal coupling) substitution, $\mathbf{p} \to \mathbf{p} - e\mathbf{A}$, for an in-plane magnetic field directed along ϑ we can take $\mathbf{A} = A_z\hat{\mathbf{z}} = (x\sin\vartheta - y\cos\vartheta)\hat{\mathbf{z}}$, which does not enter the BdG Hamiltonian and only couples to $\mathbf{D}$ for a 2D system; again with $\mathbf{D} \perp \mathbf{B}$ this implies the free energy (or action) are invariant under rotations of the magnetic field up to a unitary transformation. The orbital effect in particular has been studied in detail in [175], who reach the same conclusion for trigonal systems using a Ginzburg-Landau free energy (specifically for the D_{3d} point group, which has additional terms in the free energy compared to D_{3h}).

The 'exception' to both the orbital and paramagnetic instances of the theorem is if the mirror/spin-rotation symmetry is broken spontaneously by the system, in which case the vector $\mathbf{D}$ selects a direction not necessarily related to the magnetic field. Breaking a discrete symmetry requires the gap to transform according to a two (or higher) dimensional irreducible representation (irrep).[1] We saw an example of this in Section 4.3.1, and this is also found by [175] for the orbital effects. Of course, the mirror symmetry may be explicitly broken by a substrate. In this case, as we saw, this generally correspond to the presence of Rashba SOC, as and as we noted several times it is generally expected to be present in the system.

The discussion above addresses the question of when an anisotropic response to an in-plane magnetic field is at all possible. We see that it generally requires either Rashba SOC or a presence of a 2D irrep, in this case the E'' irrep (note that E' is symmetric under $\mathcal{M}_z$ and so cannot break the spin-rotation symmetry). In fact we would expect that the layers in a bilayer (as well as samples with more layers) have strong Rashba SOC because of locally broken inversion symmetry if the layers are not too strongly coupled [112, 47, 193, 183, 116], even in h-BN encapsulated samples.

A second question, however, is why the anisotropy is two-fold symmetric. This again can be a result of either a spontaneous symmetry breaking by E'' or E' (i.e. condensation of an order parameter that itself breaks the C_3 rotation symmetry), or symmetry breaking by an external field which in this case would most naturally be provided by strain, which itself transforms according to the E' irrep. Regardless of the microscopic mechanism, therefore, the experiment shows that (i) the horizontal mirror symmetry is broken; and (ii) rotational symmetry is broken. Both may or may not be broken spontaneously, but the latter symmetry always requires a 2D irrep of D_{3h} to be present in the gap function.

[1] A subtle note: for 1D irreps, the gap function may transform non-trivially under point group symmetries if it's not in the trivial irrep, but the BdG Hamiltonian nevertheless does not break the point group symmetries which note have to be extended to the particle-hole space of the BdG Hamiltonian, as we saw in Section 3.3.

6.2 Ginzburg-Landau Free Energy

We now demonstrate how the symmetry breaking may occur using a phenomenological Ginzburg-Landau free energy: since we do not know the microscopic origin of the two-fold symmetry, here we simply consider all symmetry allowed terms (essentially generalizing [160]). Since we expect the behavior of few-layer $NbSe_2$ to be representative of the monolayer compound, we consider the point group of the latter, which is D_{3h}. This point group is non-centrosymmetric, reflecting the fact that it incorporates the effects of the Ising spin-orbit coupling (SOC). When mirror symmetry is broken e.g. by Rashba SOC, the point group symmetry is reduced to to C_{3v}.

For simplicity, we only consider the SC gap function on the Γ pocket. The possible superconducting gaps, which we denote $\Delta^{(\ell\mu m)}$, can be classified based on the irreducible representation ℓ of D_{3h} or C_{3v} under which they transform, as well as whether they correspond to spin-singlet $\mu = 0$ or one of three spin-triplet $\mu = x, y, z$ Cooper pairs. When ℓ is not 1-dimensional, we use the index m to distinguish different components of the corresponding multiplet. Recall that since D_{3h} is noncentrosymmetric, a given irrep contains both singlet and triplet gap components.

$\ell(D_{3h})$	$\ell(C_{3v})$	$\Sigma_\Gamma^{(\ell 0)} = \Theta_\Gamma^{(\ell 0)}(\theta) i\sigma^y$	$\Sigma_\Gamma^{(\ell j)} = \Theta_\Gamma^{(\ell j)}(\theta)\sigma^j i\sigma^y$	Field
$A_1^{'}$	A_1	$i\sigma^y$	$\cos 3\theta\ \sigma^z i\sigma^y$	NA
$A_2^{'}$	A_2	$\sin 6\theta\ i\sigma^y$	$\sin 3\theta\ \sigma^z i\sigma^y$	B_z
$A_1^{''}$	A_2	$p_z \cos 3\theta\ i\sigma^y$	$p_z\sigma^z i\sigma^y$, $(\cos\theta\ \sigma^x + \sin\theta\ \sigma^y)\, i\sigma^y$	$B_z \times E_z$
$A_2^{''}$	A_1	$p_z \sin 3\theta\ i\sigma^y$	$(\sin\theta\ \sigma^x - \cos\theta\ \sigma^y)\, i\sigma^y$	E_z
$E^{'}$	E	$\cos 2\theta i\sigma^y$, $\cos\theta\cos 3\theta\ i\sigma^y$ $\sin 2\theta i\sigma^y$, $\sin\theta\cos 3\theta\ i\sigma^y$	$\cos\theta\sigma^z i\sigma^y$ $\sin\theta\sigma^z i\sigma^y$	$\mathcal{E}_x$ $\mathcal{E}_y$
$E^{''}$	E	$p_z \cos\theta i\sigma^y$ $p_z \sin\theta i\sigma^y$	$\cos 3\theta\sigma^x i\sigma^y$, $(\cos\theta\sigma^x - \sin\theta\sigma^y)\, i\sigma^y$ $\cos 3\theta\sigma^y i\sigma^y$, $(\sin\theta\sigma^x + \cos\theta\sigma^y)\, i\sigma^y$	B_y $-B_x$

Table 6.1: Lattice harmonics/basis functions for the gap function in the spin basis expanded around the Γ pocket belonging to various irreps of D_{3h} and C_{3v}. For the $\pm K$ pockets, take $\cos 3\theta \to \pm 1$ wherever it appears (including $\sin 6\theta$). Note that in 2D, $p_z = 0$. We also list the external perturbing fields transforming according to each irrep. $\mathbf{B} = (B_x, B_y, B_z)$ is the magnetic field, $\boldsymbol{\mathcal{E}} = (\mathcal{E}_x, \mathcal{E}_y)$ is the shear strain field (electric field $\mathbf{E}$ transforms in the same way). Note that E_z induces Rashba SOC as discussed in Section 1.2, which is therefore in the same irrep.

The total SC gap $\Delta(\mathbf{p})$ is in general

$$\Delta(\mathbf{p}) = \sum_{\ell\mu m} \Sigma^{(\ell\mu m)}(\mathbf{p}) D^{(\ell\mu m)} \tag{6.6}$$

where $D^{(\ell\mu m)}$ are complex scalars that are the order parameters of the corresponding irrep. We

take $\Sigma^{(\ell\mu m)}(\mathbf{p})$ to be functions of only the angle θ with respect to the Γ-K direction. Recall that by particle hole symmetry, $\Delta(\mathbf{p}) = -\Delta^T(-\mathbf{p})$, which implies that $\Sigma^{(\ell 0m)}(\mathbf{p})$ ($\Sigma^{(\ell jm)}(\mathbf{p})$ with $j = x, y, z$) is an even (odd) function of $\mathbf{p}$. All the irreps relevant to our analysis here are shown in Table 6.1. As we saw in Chapter 2, the leading instabilities in the microscopic theory are in the A_1' and E'' irreps, which we will therefore focus on. Since we are also including strain as a possible explanation of the two-fold anisotropy, we will also consider the E' irrep.

Note that in the phenomenological approach, the functional form of the gap is not determined, only the relative weights of each irrep. In particular, if an irrep has a non-zero weight, all terms (including singlet and triplet terms) belonging to that irrep are in general present in the solution. In practice, one of the terms within a given irrep in Table 6.1 is usually dominant, and the rest can be dropped. We can therefore drop the superscript on the coefficients in front of the gap function within a given irrep and label them as $D_{A_1'}$, $\mathbf{D}_{E'}$, and $\mathbf{D}_{E''}$, where the latter are 2-component vectors representing the doublet that as we will see give rise to the two-fold anisotropy.

We assume that the dominant superconducting instability in the absence of perturbing field is in the A_1' irrep (recall that the E'' is projected out by Ising SOC in the absence of Rashba SOC/magnetic field). Near the superconducting transition temperature (in the absence of a magnetic field or strain), the free energy has the form

$$\mathcal{F}_0 = \mathcal{F}_0\left[D_{A_1'}\right] + \frac{1}{2}\left(\chi_{E'}^{-1}(T)|\mathbf{D}_{E'}|^2 + \chi_{E''}^{-1}(T)|\mathbf{D}_{E''}|^2\right) \ . \tag{6.7}$$

Here $\chi_\ell(T) \propto 1/(T - T_c^{(\ell)})$ is the susceptibility associated with superconducting fluctuations in the ℓ irrep with transition temperature $T_c^{(\ell)}$. Our main assumption is that the leading superconducting instability takes place at a temperature $T_c^{(A_1')}$ that is larger than $T_c^{(E')}$ and $T_c^{(E'')}$.

Perturbations like strain and magnetic field that transform according to non-trivial irrep of D_{3h} (and therefore break it down to a smaller point group) introduce couplings between gaps in the corresponding irrep and in the A_1' irrep, since we can construct a scalar from the product of the field and the two gaps (one gap being conjugated to make it a real scalar) that is therefore allowed in the free energy.

First, since the in-plane magnetic field $\mathbf{b}$ (in units of the Bohr magneton times the Landé g-factor, $\mathbf{b} = \frac{1}{2} g_L \mu_B \mathbf{B}$) transforms according to the E'' irrep and the Ising spin-orbit coupling vector $\lambda p_F^3 \cos 3\theta \hat{\mathbf{z}}$ transforms according to A_1', a singlet A_1'-triplet E'' mixing term of the form $\lambda p_F^3 D_{A_1'} \mathbf{b} \cdot (\hat{z} \times \mathbf{D}_{E''})$ is allowed, corresponding to the $s + if$ mixing we saw in Section 4.2 and as noted in [109].

The resulting term in the free energy is

$$\mathcal{F}[D_{A_1'}, \mathbf{D}_{E''}] = \lambda_1 \mathrm{Re}\left[D^*_{A_1'}\left(b_y D_{E'',1} - b_x D_{E'',2}\right)\right]. \tag{6.8}$$

where λ_1 is some coupling constant proportional to λ. Minimizing the resulting free energy with respect to $D_{E'',m}$, we find that

$$(D_{E'',1}, D_{E'',2}) = -\lambda_1 \chi_{E''} D_{A_1'}(b_y, -b_x) \tag{6.9}$$

and the total superconducting gap is

$$\Delta(\mathbf{p}) = D_{A_1'}\left[\Sigma^{(A_1')}(\mathbf{p}) - \lambda_1 \chi_{E''} \mathbf{\Sigma}^{(E'')}(\mathbf{p}) \cdot (\hat{z} \times \mathbf{b})\right] \tag{6.10}$$

which is a mixture of the s-wave singlet A_1' gap and the p- or f-wave triplet E'' gap. Note that since the magnetic field components break the D_{3h} symmetry, they also lift the degeneracy of the E'' solution and fix the direction of the E'' order parameter (in particular, the magnetic field sets the direction of the vector $\mathbf{D}^{(E'')}$ to be perpendicular to the field). The magnitude of $D_{E''}$ (relative to that of $D_{A_1'}$) is set by the coefficient $\lambda_1 \chi_{E''} |\mathbf{b}|$. Since the magnetic field $\mathbf{b}$ is a small perturbation, generically we expect this coefficient to be small, and the corresponding mixing to be weak. However, if $T_c^{(E'')}$ is comparable to $T_c^{(A_1')}$ (which in the model presented in Chapter 4 may be the case when the instability is predominantly triplet and Rashba SOC is large), then in the vicinity of $T_c^{(A_1')}$ the susceptibility $\chi_{E''}(T) \sim 1/(T_c^{(A_1')} - T_c^{(E'')})$ is very large.

We can similarly consider the shear strain $\boldsymbol{\mathcal{E}} = (\varepsilon_{xx} - \varepsilon_{yy}, 2\varepsilon_{xy})$, which transforms according to the E' irreducible representation, where $\varepsilon_{ij} \equiv \frac{1}{2}(\partial_i u_j + \partial_j u_i)$ is the strain tensor and $\mathbf{u}$ is the displacement vector. This leads to a coupling between A_1' and E' gaps of the form:

$$\mathcal{F}[D_{A_1'}, \mathbf{D}_{E'}] = \lambda_2 \left[(\varepsilon_{xx} - \varepsilon_{yy})\mathrm{Re}\left(D^*_{A_1'} D_{E',1}\right) + 2\varepsilon_{xy}\mathrm{Re}\left(D^*_{A_1'} D_{E',2}\right)\right] . \tag{6.11}$$

where λ_2 is some coupling constant. Minimizing the free energy leads to a mixed s-wave and d-wave superconducting gap

$$\Delta(\mathbf{p}) = \Delta_{A_1'}\left[\Sigma^{(A_1')}(\mathbf{p}) - \lambda_2 \chi_{E'} \mathbf{\Sigma}^{(E')} \cdot \boldsymbol{\mathcal{E}}\right] \tag{6.12}$$

Again, small strains will only lead to a significant E' component in the superconducting gap if the A_1' and E' superconducting instabilities have similar transition temperatures. In addition to the second

order terms above that correspond to explicit symmetry breaking, there are fourth order terms linear in the A_1' gap function and cubic in either the E' and E'' gap functions that couples them directly, leading to spontaneous symmetry breaking for $T < T_c$. This has been pointed out in [186] and earlier for twisted bilayer graphene in [26]. This term has the same form as Eq. (6.12) but with a strain field being induced by the E' or E'' order parameters as $\boldsymbol{\mathcal{E}} \propto (|\Delta_{E1}|^2 - |\Delta_{E2}|^2, \Delta_{E1}^* \Delta_{E2} + \Delta_{E2}^* \Delta_{E1})$ (with $E = E'$ or E''). We do not speculate here on whether the symmetry breaking is explicit or spontaneous; there is some evidence for spontaneous symmetry breaking in some samples as the measured anisotropy seems to be directed along a crystal symmetry axis, but it alone is unlikely to explain the data since the effect would only be relevant far below T_c.

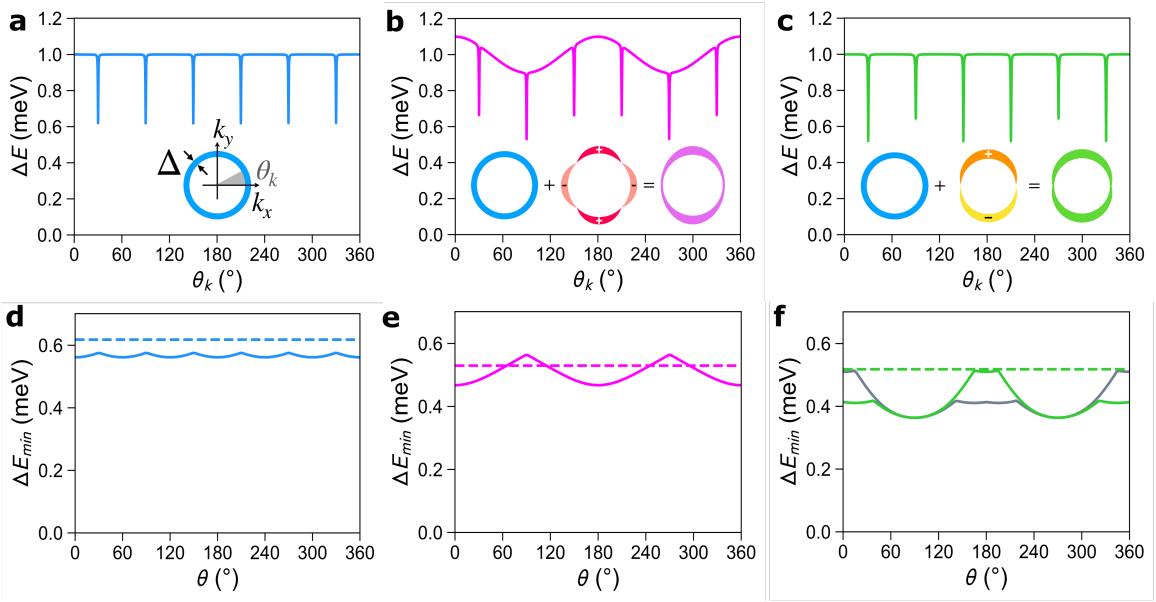

Figure 6.2: (a-c): the energy gap in the BdG spectrum ΔE as a function of momentum angle θ_k along the Fermi surface obtained with parameters listed under (6.16) for (a) pure s-wave singlet A_1' gap, (b) A_1' mixed with E' gap, and (c) A_1' mixed with E'' gap. Note that the inner and outer gaps are essentially identical in this case. The sharp minima are due to Ising SOC, which for higher magnetic fields become nodes. Insets show schematic forms of the gap around the Fermi surface. (d-f): the energy gap minimum (in meV) as a function of *field angle* $\theta \equiv \vartheta$ in the presence of Rashba SOC for the same cases as in (a-c). Note that with triplet E'' mixed in, the inner and outer gaps now differ (shown in green and gray), and only the global minimum is two-fold symmetric. Figure adapted with permission from [58].

Note that the d-wave E' terms and p-wave E'' term lead to a 2-fold anisotropy of the superconducting gap around the Γ pocket *in momentum space*. We show this in Figure 6.2(a-c). We obtained

the plots using a simple model of the single-body Hamiltonian in momentum space:

$$H(\mathbf{p}) = \sum_{\mathbf{p}\alpha} \varepsilon(\mathbf{p}) d^\dagger_{\mathbf{p}\alpha} d_{\mathbf{p}\alpha} + \sum_{\mathbf{p}\alpha\beta} d^\dagger_{\mathbf{p}\alpha} \left[\lambda p_F^3 \cos 3\theta \sigma^z + \mathbf{b}\cdot\boldsymbol{\sigma}\right]_{\alpha\beta} d_{\mathbf{p}\beta} = \sum_{\mathbf{p}\alpha\beta} d^\dagger_{\mathbf{p}\alpha} \left[\mathcal{H}_0\right]_{\alpha\beta} d_{\mathbf{p}\beta} \tag{6.13}$$

where α and β are spin indices,

$$\varepsilon(\mathbf{p}) = -\frac{p^2}{2m} - \mu, \tag{6.14}$$

and θ, as above, is the angle measured from the center of the Γ pocket with $\theta = 0$ corresponding to the direction towards the K point. We use $\lambda p_F^3 = 40$ meV, which is the Ising SOC value reported in the literature once averaged over all Fermi surfaces [40]. We also set $\mu = -0.4$ eV, which gives $m = p_F^2/2\mu \approx 2m_0$ when the wavenumber corresponding to the Fermi momentum is $p_F/\hbar = 0.45$ Å^{-1} [18]. Here, m_0 is the electron rest mass. All these parameters were chosen so that the Fermi surface of the toy-model parabolic dispersion is similar to that obtained from first principle calculations [62, 110, 40, 184]. These values should thus not be understood as actual parameters that a first-principle calculation would yield. The key point is that our conclusions do not rely on this set of parameter values, as they are used to illustrate the two-fold gap anisotropy that must follow from mixing an A_1' gap with either E' or E'' gaps. Finally, for the magnetic field, we use $b = 0.5$ meV, which is about 8.3 T.

The superconducting excitation spectrum is then given by the eigenvalues of the Bogolyubov-de Gennes (BdG) Hamiltonian:

$$H_{BdG} = \frac{1}{2}\sum_{\mathbf{p}} \Psi^\dagger_{\mathbf{p}} \mathcal{H}(\mathbf{p}) \Psi_{\mathbf{p}} \tag{6.15}$$

where we use the Nambu-Gor'kov representation $\Psi_{\mathbf{p}} = (d_{\mathbf{p}\uparrow}, d_{\mathbf{p}\downarrow}, d^\dagger_{-\mathbf{p}\uparrow}, d^\dagger_{-\mathbf{p}\downarrow})^T$ and

$$\mathcal{H}(\mathbf{p}) = \begin{pmatrix} \mathcal{H}_0(\mathbf{p}) & \Delta(\mathbf{p}) \\ \Delta^\dagger(\mathbf{p}) & -\mathcal{H}_0^T(-\mathbf{p}) \end{pmatrix}. \tag{6.16}$$

We took $\Delta(\mathbf{p})$ as in Eqs. (6.10) and (6.12) with the singlet d-wave term for E' and the triplet p-wave term for E'' from Table 6.1. For all plots, we took $\Delta_{A_1'} = 1$ meV (on the order of T_c). For the mixed A_1'/E' gaps, we took $|\boldsymbol{\Delta}_{E'}| = 0.1$ meV and a uniaxial strain along the x axis, $\boldsymbol{\mathcal{E}} \propto (1, 0)$. For the mixed A_1'/E'' gap, the mixing is relatively weak unless the mixed gaps are close in magnitude; for this reason, we used $|\boldsymbol{\Delta}_{E''}| = 0.5$ meV in the plot. Note that we plot the energy gap in the spectrum

of H_{BdG} (i.e. difference between bottom positive energy band and top negative energy band) along both the inner and outer Fermi surfaces. The resulting gaps on the inner and outer surfaces are identical within the resolution of the figure.

Note that since we did not include Rashba SOC, the spectra are independent of the direction of the applied in-plane field, which was set to $\theta = 0$. This is a consequence of the horizontal mirror symmetry (equivalent to spin-rotation about the z axis) discussed above. It must be broken in order to explain the experimental data, which we account for by adding Rashba SOC:

$$\mathcal{H}_R = \alpha_R \left(p_y \sigma^x - p_x \sigma^y\right) \tag{6.17}$$

Rashba SOC belongs to the A_2'' irrep and reduces D_{3h} to C_{3v}; although in principle this introduces additional gap functions $\Delta_{A_2''}$, these are three-fold symmetric and so we do not include them in our analysis. With Rashba SOC included, however, the BdG spectrum does depend on the direction of the applied magnetic field. A quantity that illustrates this (and may possibly be relevant to experiment) is the minimum of the energy gap, which we plot if Figure 6.2(d-f) for the three cases considered above with $\alpha_R p_F = 0.2$ meV (for comparison, $\alpha_R p_F$ was estimated to be about 0.8 meV in gated MoS_2 in [98]). As we saw in Section 4.2, in the absence of Rashba SOC the minima become nodes when the magnetic field exceeds the Pauli limit. Recall that Rashba SOC lifts the nodes unless the magnetic field points along one of the K directions, in which case two pairs of the original 12 nodes remain. Below the Pauli limit (as we consider here) the nodes become sharp minima. In the pure A_1' case, this results in a six-fold symmetric signal, with sharp peaks when the magnetic field points along Γ-M due to the minimum moving from Γ-M direction to the next. When E' or E'' terms are included, the minima of the gap function for magnetic field pointing along different Γ-M lines are no longer equal, and the signal becomes two-fold symmetric.

6.3 Other Scenarios

For completeness, we consider some scenarios beyond one involving nearby E' or E'' instabilities that we presented above, and discuss why they are unlikely to explain the data by themselves. Nevertheless, some of them may still play a complementary role. The fact that a 2D irrep along with horizontal mirror symmetry breaking must be present is of course true for all the scenarios.

The most trivial explanation would be that the magnetic field was not perfectly aligned with the sample plane as it was rotated in the field, which would result in a small out-of-plane component

of the magnetic field with a magnitude that varies as $|\sin\vartheta|$ as the sample rotates in the magnetic field. This has been considered in more detail in [58]. The main argument against this is that this would lead to cusps in the signal due to the absolute value, which is not seen.

6.3.1 Microscopic Calculation with Strain Without Closely Competing Irreps

As noted above, the mixing between the A_1' irrep and E' or E'' irreps requires the channels to have comparable T_c's. In the presence of Rashba SOC, in-plane magnetic field and strain there is another term, however, that in principle can lead to a two-fold anisotropy and that does not require channel mixing. Rather the anisotropy in that case arises from the Fermi surface/band structure. Here we show that this effect requires unrealistically large strain in order to explain the observed data.

Microscopically, the additional twofold anisotropic term arises in the pairing susceptibility/particle-particle bubble in Eq. (4.33) (now including K pockets and taking the strong SOC limit):

$$\Pi_{\eta\tau}(\theta') = \frac{N_{\eta\tau}}{2}\varpi\left(\frac{2\xi_{A\eta\tau}(\theta)}{T}\right) \tag{6.18}$$

with $N_{\eta\tau}$ the density of states on the η pocket on the τ Fermi surface and

$$\varpi\left(x\right) = -\log\frac{1.13\Lambda}{T} + \mathrm{Re}\left[\psi\left(\frac{1}{2}+\frac{ix}{4\pi}\right) - \psi\left(\frac{1}{2}\right)\right] \tag{6.19}$$

where ψ is the digamma function. Recall that

$$\xi_{A\eta\tau}(\mathbf{p}) = \frac{\xi_{\eta\tau}(\mathbf{p}) - \xi_{-\eta\tau}(-\mathbf{p})}{2} \tag{6.20}$$

where

$$\xi_{\eta\tau}(\mathbf{p}) = \epsilon_\eta(\mathbf{p}) + \tau\left|\boldsymbol{\beta}_\eta(\mathbf{p})\right| \equiv \epsilon_\eta(\mathbf{p}) + \tau\beta_\eta(\mathbf{p}) \tag{6.21}$$

is the normal state dispersion including the SOC and magnetic field:

$$\boldsymbol{\beta}_\eta = \beta_{\eta z}(\mathbf{p})\hat{\mathbf{z}} + \alpha_R\left(p_y\hat{\mathbf{x}} - p_x\hat{\mathbf{y}}\right) + \mathbf{b} \tag{6.22}$$

In addition, we include strain by taking

$$\epsilon_\eta(\mathbf{p}) = \frac{p_0^2}{2m_\eta}\left((1+\varepsilon)^2\cos^2\theta + (1+\varepsilon)^{-2}\sin^2\theta\right) \tag{6.23}$$

which effectively stretches the Fermi surfaces along which $p_x = (1+\varepsilon)p_0\cos\theta$ and $p_y = (1+\varepsilon)^{-1}p_0\cos\theta$ (note that the areas enclosed by the Fermi surfaces remains the same for all ε; this is also equivalent to taking unequal effective masses for different directions). Recall (as we saw in Section 4.2.3) that for large Ising SOC,

$$\xi_{A\eta\tau}(\mathbf{p}) \approx \tau\frac{\alpha_R(p_y b_x - p_x b_y)}{\beta_I} \approx \tau\frac{\alpha_R p_0 b}{\beta_I}\left[\sin(\theta-\vartheta) - \varepsilon\sin(\theta+\vartheta)\right] \tag{6.24}$$

and the last term gives rise to the aforementioned twofold anisotropic term.[2] Although the term is small, because it enters the detuning parameter, T_c (and hence B_c) are relatively sensitive to it. Including the strain in the linearized gap equation (4.19) by taking $p_x = (1+\varepsilon)p_0\cos\theta$ and $p_y = (1+\varepsilon)^{-1}p_0\cos\theta$ and solving it numerically, we find that B_c varies by about 4-10% as a function of field angle for $\alpha_R p_0 b\varepsilon \approx 0.001\beta_I^2$, with $\varepsilon = 0.2$. See Figure 6.3. Realistically, we expect ε on the order of 10^{-4}, so this cannot explain the data.

Although the input gap function is in this case pure A_1', the energy gap has E' and E'' components due to the projection onto the Fermi surface. This result is therefore consistent with the general requirement that gap components belonging to a 2D irrep must be present in order to break the rotational symmetry.

6.3.2 Superconducting Fluctuations and Non-equilibrium

Another 'trivial' explanation could be that the symmetry is broken by the experimental apparatus in some way. The most obvious symmetry-breaking part of the 'apparatus' is the applied current direction, and related to it the contact geometry. Unfortunately a detailed theoretical treatment of the system including the supercurrent is somewhat involved, as the system is not in equilibrium. Heuristically, we can argue that in the normal state a static current amounts to a shift of the entire band structure (including the Fermi surface) by an amount $\mathbf{q}_{drift}$. For a sufficiently large supercurrent, this can eventually drive an FFLO state that we mentioned in Section 4.2.3 (the particle branch shifts by $\mathbf{q}_{drift}$ while the hole branch shifts by $-\mathbf{q}_{drift}$ by PHS).[3] More intuitively,

[2] Recall that $\varpi(x) - \varpi(0) \approx \frac{7\zeta(3)x^2}{16\pi^2}$ for small x, and expanding $\xi^2_{A\eta\tau}$ gives a correction proportional to $\alpha_R p_0 b\varepsilon$.

[3] Non-equilibrium properties of FFLO states in systems with applied currents has apparently not been studied in detail until recently [139].

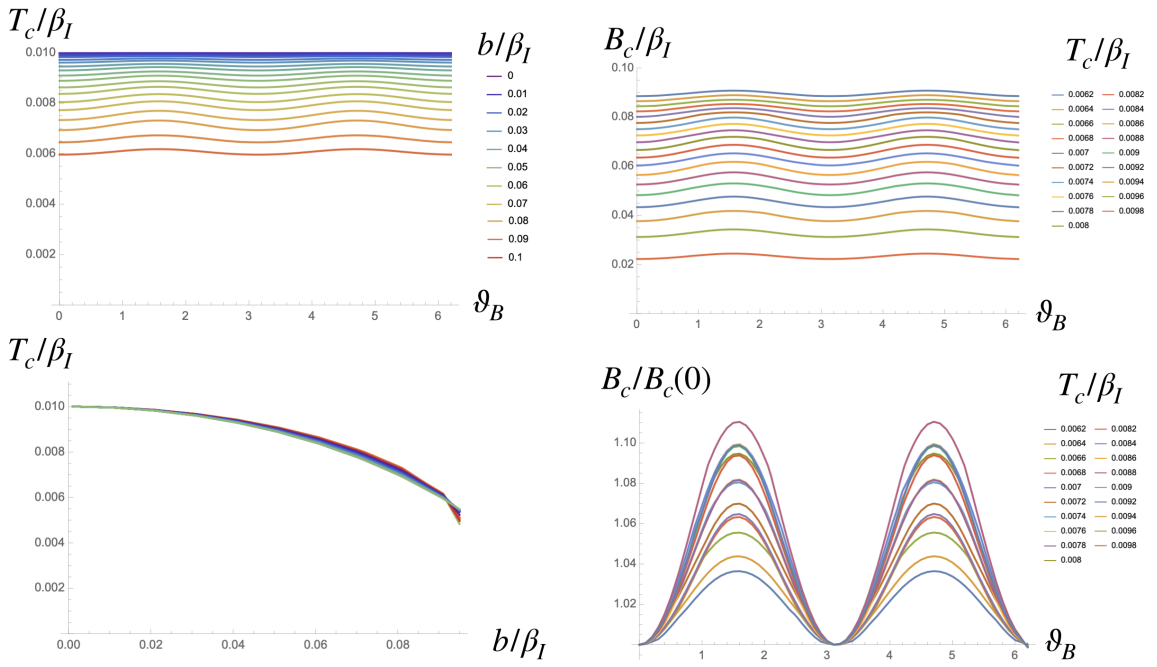

Figure 6.3: Numerical solutions of the gap equation (4.19) including strain demonstrating the two-fold anisotropy. Top left plot shows T_c as a function of magnetic field angle at various magnetic field strength, bottom left shows T_c as a function of magnetic field strength for various field angles. Top (bottom) right shows the critical magnetic field B_c (normalized by $B_c(\vartheta = 0)$) as a function of field direction at various temperatures. All parameters are in units of Ising SOC β_I. Model parameters used were $g_1 = -1.7$, $g_2 + g_3 = -0.6$, $g_4 = 0.2$ (other coupling constants set to zero), $\lambda p_0^3 = \beta_I$, $\alpha_R p_0 = 0.05\beta_I$, and $\varepsilon = 0.2$.

one can imagine that the gap is sampled by the current with a momentum bias $\mathbf{q}_{drift}$, so that if the gap function itself has both a momentum dependence and a magnetic field dependence (as it does in presence of Rashba SOC, e.g. see Figure 4.3) it could potentially translate to a two-fold signal (note that spin rotation symmetry breaking is still required for this explanation). One would expect the maximum signal to be then correlated with the direction of the applied current. This appears to not be the case in experiment, however, where the maximum is not correlated with the current direction or contact geometry.

A more likely effect could be due to SC fluctuations in the vicinity of the phase transition which are well-known to affect conductivity, in this regime called paraconductivity [88] (note that this is precisely the regime in which the transport experiments are performed). Since the samples are 2D, fluctuations are moreover expected to be large and likely explain why the transition into the SC phase as temperature is lowered appears to be smooth and not as sharp as in conventional BCS theory. Unfortunately, the computation of paraconductivity is somewhat involved (computation of Maki-Tompson and Aslamazov-Larkin corrections to conductivity are required [88]). We can, however, again take a phenomenological approach to look at SC fluctuations that arise from gradient terms in the free energy that we have so far neglected (which in this case do not cause vortices as they normally would). For the one-component A_1' irrep, the only allowed gradient term is of the form $\mathcal{F}_{\nabla}^{(A_1')} = K_0|\nabla D^{(0)}|^2$, which is clearly rotationally invariant. For the two dimensions E' and E'' representations the terms in $\mathcal{F}$ involving gradients of the gap functions are more interesting [160]:

$$\mathcal{F}_{\nabla}^{(\ell)} = K_1|\nabla \cdot \mathbf{\Delta}_\ell|^2 + K_2|\nabla \times \mathbf{\Delta}_\ell|^2 + K_3\left(|\partial_x\Delta_{\ell 1} - \partial_y\Delta_{\ell 2}|^2 + |\partial_x\Delta_{\ell 2} + \partial_y\Delta_{\ell 1}|^2\right) \tag{6.25}$$

where $\ell = E', E''$. These terms can be understood as corresponding to the scalar, (axial) vector, and tensor components of the total derivative $\nabla\mathbf{\Delta}$, assuming no z dependance (respectively the trace, anti-symmetric part, and traceless symmetric part analogous to the expansion, rotation, and shear parts of the deformation/strain tensor). Fourier transforming this expression it follows that, in the presence of an external symmetry-breaking field such as strain, the total gradient term is twofold anisotropic. We therefore expect the paraconductivity corrections to also exhibit twofold anisotropy. Note that this particular explanation does not require mirror symmetry to be broken by the system, as the magnetic field that breaks the symmetry itself contributes to the conductivity. The main issue with this explanation, however, is that it does not seem to account for the tunneling data that probed a system deep inside the ordered phase where the fluctuations are strongly suppressed. This therefore cannot alone explain the data.

Chapter 7

Conclusions

7.1 What We Did

To summarize, in this dissertation we have performed an analysis of 1H-$NbSe_2$ and similar 1H-TMD systems. We first used a parquet RG approach in Chapter 2 to identify possible instabilities of the system: uniform superconductivity (SC) and pair density wave (PDW) channels. Within each channel, we find that interactions uniform of the Fermi pockets can give rise to both s-wave singlet and f-wave triplet instabilities, even if the bare interactions are repulsive. For SC, the singlet interaction can be driven by repulsive pair hopping processes between pairs at Γ and at $\pm K$, while the triplet phase is stabilized by repulsive exchange interactions between the pairs at K pockets (a process equivalent to backscattering under which $K \leftrightarrow -K$). The key for the latter is that the pairing is between disconnected Fermi surfaces. Bare attraction of course can always lead to either singlet or triplet instabilities even without K points, but repulsive interactions can only drive either SC instability in the presence of the K pockets (neglecting the Kohn-Luttinger effect and similar mechanisms).

We then included Ising spin-orbit coupling (SOC) in a self-consistent mean-field analysis in Chapter 4, including also known symmetry breaking perturbations, namely Rashba SOC, due to substrate effects, and an in-plane magnetic field, since we know that SC is stable in large in-plane magnetic fields (above the Pauli limit) due to the strong SOC. Both symmetry breaking terms are known to produce unconventional SC phases, as previously found for 1H-$NbSe_2$ in large in-plane magnetic fields in [62]. In particular, they find a nodal topological SC phase above the Pauli limit. This phase protected by a time-reversal-like symmetry that is product of the time-reversal symmetry (TRS) and the horizontal mirror symmetry. Both TRS and the mirror symmetry are broken by the magnetic field, but their product is not. This moreover ensures the symmetry of the Fermi surfaces

under momentum reversal $\mathbf{p} \to -\mathbf{p}$ that is necessary to guarantee the SC instability.

While in our work [153] we confirm the existence of the nodal topological phase, we also find that it is unstable against even small Rashba SOC that breaks the TR-like symmetry and generally lifts all of the nodes. The main finding, however, is that a different, *crystalline*, nodal topological phase can be realized instead in presence of both Rashba SOC and in-plane magnetic fields, provided the field points along one of the Γ-K directions. The reason is that a single vertical mirror symmetry (with the reflection plane containing the Γ-M line perpendicular to the magnetic field) remains in that case and protects two pairs out of the original six pairs that lie in the mirror plane. Because this phase is protected by a crystalline symmetry rather than an anti-unitary one, it falls outside of the more familiar tenfold classification of topological phases.We discussed some of the topological invariants that characterize topological phases in Chapter 3 and showed how they can be computed using the Berry connection including some in the tenfold classification, as well as an example of a crystalline phase in 1D and a crystalline nodal phase in 2D, which happens to be precisely in the same class as the phase that we found in 1H-$NbSe_2$.

Because the combination of Rashba SOC and the in-plane magnetic field breaks the momentum-reversal symmetry and shifts the Fermi surfaces, the SC phase in that case becomes unstable once the symmetry breaking is too large. We confirmed, however, that the SC phase is stabilized in a large region of the phase diagram thanks to Ising SOC. When SC becomes unstable, FFLO phases with pairing relative the shifted centers of the Fermi surfaces (i.e. with Cooper pairs with equal energies) are moreover expected to be realized, and we showed that the crystalline nodal topological phase remains protected in the FFLO case as well. In the uniform SC phase, the symmetry breaking moreover shifts the nodes away from zero energy, resulting in small Bogolyubov Fermi surfaces.

In the absence of the magnetic field but in the limit of strong Rashba SOC (compared to Ising SOC), we also find that in the limit of strong triplet interactions a chiral SC emerges (which we also discussed in Chapter 3), consistent with earlier results in the absence of Ising SOC. Although it is not likely to be realized in 1H-$NbSe_2$ due to the Ising SOC being too strong, it may be relevant in other similar systems. As we mentioned above, the origin of the triplet instability lies in the fact that pairing is between disconnected Fermi surfaces at K points, and importantly Rashba SOC favors a gap function belonging to a 2D irreducible representation (irrep) of D_{3h} (E''), which is known to spontaneously break time reversal symmetry, as we confirmed along with its chiral nature. The recipe for such a phase is therefore a combination of pairing between K pockets giving rise to the triplet instability and strong Rashba SOC giving rise to a 2D irrep.

Next, in Chapter 5 we turned to a closer study of the PDW channel we also found in the RG

analysis. While in principle attractive interactions could result in a PDW instability, no mechanism is know by which they can favor a PDW phase over an SC phase. In the case of repulsive interactions, however, we find that a singlet PDW instability can be driven by an Umklapp process taking a pair within a K pocket to a pair on Γ and $-K$ (allowed since $3K$ is an Umklapp momentums), and a triplet PDW can be driven by an exchange process between Γ and $-K$ pockets. As the K pocket was necessary to produce instabilities from repulsion in the SC channel, repulsion in the PDW channel can only drive an instability if a Γ pocket is present. This is consistent with the results of [67], who considered a system without a Γ pocket and found that the Kohn-Luttinger mechanism (in a two-loop RG calculation) was needed to produce a PDW in that case. Although we do not find a microscopic mechanism for a PDW instability arising in the absence of a Γ pocket, our phenomenological and mean-field analyses naturally include such a possibility, which we consider to compare our results with previous literature.

There are in fact two degenerate PDW channels in RG: one with pairing momentum K, and one with $-K$ (with order parameters $\Delta_{\pm K}$ respectively). Using a phenomenological Ginzburg-Landau free energy, we find that higher order terms lift this degeneracy, producing either an FF-type PDW with only one order parameter present (i.e. $\Delta_K = 0$ or $\Delta_{-K} = 0$, but not both), or an LO-type PDW with both orders present with equal magnitudes ($|\Delta_K| = |\Delta_{-K}|$). Both types of PDW break translational symmetry, but the FF-type PDW additionally breaks TRS. We discuss additional orders that may be induced by either type of PDW which may be more directly measurable in experiment. We also consider the microscopic free energy for our model without a Γ pocket, in which case we find that the LO-type PDW is favored, even when uniform SC fluctuations are integrated out.

Since, unlike the SC instability, the PDW instability is not guaranteed by symmetry, we perform a stability analysis using a self-consistent mean-field calculation, both with and without a Γ pocket (though we emphasize that we do not find a microscopic mechanism for the latter). The two symmetry breaking effects are trigonal warping at the K points, and mismatch between the band structures at Γ and K pockets. As expected, we find that a PDW instability remains possible as long as those effects are small compared to T_{c0} the PDW critical temperature in the absence of those effects.

Though we do not perform a full self-consistent calculation of PDW with Ising SOC included, we comment on the effects of Ising SOC on the PDW phase. From the same argument as in [67], we find that at K points Ising SOC results in triplet pairing between equal spins, with the corresponding LO-type PDW belonging to a 2D irrep. As also found in [67], we see that the gap function in

general exhibit phase winding, which results in non-zero Chern numbers (as we saw in Chapter 3). We comment that the PDW pairing between Γ and K pockets is not as simple, and neither a triplet nor singlet PDWs are obviously favored. We leave the precise calculation of the self-consistent gap functions and their topology to a future study.

Finally, in Chapter 6, we discussed a recent experiment [58] performed on few-layer superconducting 1H-$NbSe_2$. Contrary to our expectations based on the mean-field calculation in Chapter 4, a twofold anisotropy with respect to the direction of the in-plane magnetic field is observed. From a symmetry point of view, we argue that this necessarily implies the breaking of the horizontal mirror symmetry already in the absence of the magnetic field, and an additional order belonging to a 2D irrep (in this case the E irrep of C_{3v}). The best-known sources of such symmetry breaking are Rashba SOC and strain respectively. Moreover, using a phenomenological Ginzburg-Landau free energy we argue that a mixing between nearby instabilities belonging to the A_1' and either of E' or E'' irreps of D_{3h} is necessary. We also consider some complementary effects that may also result in a twofold anisotropy, but rule them out as its sole sources.

7.2 What We Did Not Do

Having summarized what we did, to conclude let us mention some of the things that we did not do, some of which have been done by others, while some may provide avenues for future research. We have for example completely neglected CDW which is known to exist in these systems, a question that has been considered in [91, 117, 198]. Another thing that we haven't included in our analysis is disorder, which has been considered in 1H-TMDs in the absence of Rashba SOC in particular to study its effects on the upper critical magnetic field [70, 110, 111, 115, 166]. Note that TMDs are known to be very disordered, and the mean field theory predicts critical magnetic fields much higher than actually observed. Part of this may be explained by Rashba SOC (which as we saw destabilizes the SC phase), though in our calculations we find that it has to be very strong to match the experiment. Likely a combination of both Rashba SOC and disorder (and strain) may be necessary to provide a full explanation. Strain has also not been considered in these systems, but may be interesting in light of the recent experimental results in [58, 186].

Another obvious calculation relevant to experiment would be a calculation of the paraconductivity [88], as we discussed briefly in Chapter 6. This is a somewhat involved calculation and to the best of our knowledge has not been done for 2D non-centrosymmetric systems to study anisotropy with respect to in-plane magnetic fields. Similarly, a calculation of the tunneling rates relevant to some

of the experiments may be of interest. These generally fall into the category of non-equilibrium effects, which also include the possibility of systems driven by external fields. Driven TMD systems have been considered in [165, 59, 31]. Another transport phenomenon that has been considered in TMDs is the (reverse) Edelstein magnetoelectric effect [43], which causes a magnetization to appear perpendicular to an applied supercurrent, considered in systems with SOC in [61], and more generally is known to occur in some non-centrosymmetric systems [13, 108].

Another experimental limitation is that most samples produced are few-layer systems rather than true monolayers, which can result in interesting effects of their own. Heterostructures of 2D materials in general have received a lot of interest, and bilayer and trilayer superconducting TMD systems have been considered in [183, 116, 94, 25].[1] The orbital effect, which is absent for monolayers, has been found in particular to lead to interesting vortex-like phases, including some similar to Josephson vortices known in thin films [16], or two counter-propagating FFLO phases in each layer similar to the one we discussed in Chapter 4.

Superconductivity has also more recently been observed in a related family of monolayer TMDs, like the 1T'-TMDs like WTe_2 [44, 134]. Unlike the 1H family, these are centrosymmetric, but have a different property symmetry interesting property of being nonsymmorphic, meaning systems with symmetries involving a point group symmetry like rotation or reflection combined with a translation (that are not symmetries on their own). Nonsymmorphic materials are known to potentially host interesting topological phases including crystalline, superconducting and higher-order phases [95, 180, 93], as well as the better-known and recently reported quantum spin Hall effect [129, 125]. 1T'-TMDs like WTe_2 has been reported to host the QSHE and more recently to become superconducting when gated in [44, 134]. The possibility of interesting topological SC phases has already been considered [68] but is an area of active research.

Interesting questions remain about the superconducting phase 1H-TMDs like $NbSe_2$, especially in light of recent experimental evidence of competing instabilities [58, 186] that we discussed, as well as some recent theoretical evidence that spin fluctuations may be strong in these systems [184, 75]. These may lead to some of the phases that we have considered in this thesis. Possibly, and perhaps more likely, even more novel phases may be realized.

[1] Bilayers with Rashba SOC have also been predicted to host a helical topological SC phase [118].

Appendix A

Tight Binding Model of TMDs

Here we present a simple tight-binging model that we used to study the edge modes and produce the plots in Figure 1.2, Figure 4.6 and Figure 5.1. The tight binding model is defined on the triangular lattice with sites we label with indices i and j, which stand for $\mathbf{R}_i = n_i\mathbf{a}_1 + m_i\mathbf{a}_2$, where $\mathbf{a}_1 = (a, 0)$ and $\mathbf{a}_2 = \frac{a}{2}(1, \sqrt{3})$ are the lattice basis vectors. We take $a = 1$ for convenience below, and also define $\mathbf{a}_3 = \mathbf{a}_2 - \mathbf{a}_1 = \frac{a}{2}(-1, \sqrt{3})$. Each site then has six nearest neighbors at $\pm\mathbf{a}_1$, $\pm\mathbf{a}_2$ and $\pm\mathbf{a}_3$.

The Hamiltonian has the general form

$$H = H_0 + H_Z + H_{SC} \tag{A.1}$$

The first term describes the normal state band structure in the presence of SOC; the second-term is the Zeeman coupling due to in-plane magnetic field; and the last term represents the superconducting pairing gap. For simplicity we use a tight-binding model that only includes the $\eta = \Gamma$ pocket Fermi surface, since the $\pm K$ pockets are unimportant for the crystalline nodal topological superconductor.

We describe our model in terms of the creation operators $d^\dagger_{i,\alpha}$, where $\alpha = \uparrow, \downarrow$ is a spin index, and i is a site index. We have

$$\begin{aligned} H_0 &= \sum_{i\alpha} \mu\, d^\dagger_{i\alpha} d_{i\alpha} + \sum_{\langle ij\rangle\alpha} t\, d^\dagger_{i\alpha} d_{j\alpha} \\ &\quad + \sum_{\langle ij\rangle\alpha\beta} \left[4i\lambda\nu_{ij}\sigma^z_{\alpha\beta} + \frac{i\alpha_R}{3}\hat{\mathbf{z}}\cdot(\boldsymbol{\sigma}\times\mathbf{a}_{ij})_{\alpha\beta} \right] d^\dagger_{i\alpha} d_{j\beta} \\ H_Z &= \sum_{i\alpha\beta} (\mathbf{b}\cdot\boldsymbol{\sigma})_{\alpha\beta}\, d^\dagger_{i\alpha} d_{i\beta} \\ H_{SC} &= \frac{1}{2}\sum_{ij\alpha\beta} [\Delta]^{ij}_{\alpha\beta}\, d^\dagger_{i\alpha} d^\dagger_{j\beta} + \text{h.c.} \end{aligned} \tag{A.2}$$

where $\nu_{ij} = 1$ (-1) if the vector is $\mathbf{a}_1$, $-\mathbf{a}_2$, $\mathbf{a}_3$ ($-\mathbf{a}_1$, $\mathbf{a}_2$, $-\mathbf{a}_3$). For Figure 4.6 we considered the singlet-instability regime in the crystalline nodal topological phase with $b \gg \alpha_R$. In this region the self-consistent solutions of the gap equation obtained in a $\mathbf{k}\cdot\mathbf{p}$ model are well-approximated by

$$\Delta^{ij} = \Delta_t \nu_{ij} \left(\sigma^x \cos\vartheta + \sigma^y \sin\vartheta\right) i\sigma^y + \Delta_s i\sigma^y \tag{A.3}$$

where ϑ is the direction of the magnetic field, assuming $\Delta_s \ll \Delta_t$ (higher lattice harmonics are in general needed to match the $\mathbf{k}\cdot\mathbf{p}$ model exactly). The numerical coefficients are chosen to match the $\mathbf{k}\cdot\mathbf{p}$ Hamiltonian (including the value of p_F).

Appendix A. Tight Binding Model of TMDs

The cylinder is created by taking periodic boundary conditions in the vertical y direction, and open zig-zag boundary conditions along the x direction. To produce the plot, we Fourier transform in the y direction:

$$d_{\mathbf{R_i}\alpha} = \frac{1}{\sqrt{N}} \sum_{p_y} d_{R_{ix} p_y \alpha} e^{-i p_y R_{iy}} \equiv \frac{1}{\sqrt{N}} \sum_{p_y} d_{i p_y \alpha} e^{-i p_y R_{iy}} \tag{A.4}$$

where $\mathbf{R}_i = (R_{ix}, R_{iy})$. Note that i labels the x coordinates of the sites which go in increments of $a/2$, while the period along the y axis is actually doubled since identical sites are now separated by $2\mathbf{a}_2$, resulting in the folding of the 1D Brillouin zone (which has a period of $\frac{2\pi}{\sqrt{3}a}$).

The resulting BdG Hamiltonian on the cylinder can be expressed

$$H_{BdG} = \frac{1}{2} \sum_{ij, p_y} \Psi^\dagger_{i,p_y} \mathcal{H}^{ij}(p_y) \Psi_{j,-p_y} \tag{A.5}$$

where $\Psi_{i,p_y} = \left(d_{i,p_y\uparrow}, d_{i,p_y\downarrow}, d^\dagger_{i,-p_y\uparrow}, d^\dagger_{i,-p_y\downarrow} \right)$ and

$$\mathcal{H}^{ij}(p_y) = \begin{pmatrix} \mathcal{H}^{ij}_{kin}(p_y) & \Delta^{ij}(p_y) \\ -\left(\Delta^{ij}(-p_y)\right)^* & -\left(\mathcal{H}^T_{kin}(-p_y)\right)^{ji} \end{pmatrix} \tag{A.6}$$

where we have defined

$$H_0 + H_Z = \sum_{ij\alpha\beta} \left(\mathcal{H}_{kin}(p_y)\right)^{ij}_{\alpha\beta} d^\dagger_{i p_y \alpha} d_{j p_y \beta} \tag{A.7}$$

In Figure 4.6 we plot the spectrum of (A.6) with the number of sites along the non-periodic x direction $N = 300$ (which corresponds to 150 unit cells due to period doubling) and took $t = 1$, $\mu = 0$, $\lambda = 0.2$, $b = 1$, $\alpha_R = 0.1$, $\Delta_t = 1$ and $\Delta_s = 0.1$. The magnetic field was again aligned along one of the Γ-K directions, $\vartheta = 0$.

Note that we have only included the Γ pocket above. The K pockets originate from next nearest-neighbor hopping terms:

$$H_{nnn} = \sum_{\langle\langle ij \rangle\rangle \alpha} t_{nnn}\, d^\dagger_{i\alpha} d_{j\alpha} \tag{A.8}$$

where the next nearest neighbors are at $\mathbf{a}_1 + \mathbf{a}_2$, $2\mathbf{a}_2 - \mathbf{a}_2$, $\mathbf{a}_2 - 2\mathbf{a}_1$, and their opposites. To make Figure 5.1 we took $t = 1$, $\lambda = 0.4$, $\alpha_R = b = 0$ and $t_{nnn} = 2.5$.

References

[1] *Renormalization Group and Effective Field Theory Approaches to Many-Body Systems*. Springer, Berlin, 2012. doi:https://doi.org/10.1007/978-3-642-27320-9.

[2] A. A. Abrikosov, L. P. Gorkov, and I. E. Dzyaloshinski. *Methods of Quantum Field Theory in Statistical Physics*. Dover, 2012.

[3] D. F. Agterberg and R. P. Kaur. Magnetic-field-induced helical and stripe phases in rashba superconductors. *Phys. Rev. B*, 75:064511, Feb 2007. doi:10.1103/PhysRevB.75.064511. URL `https://link.aps.org/doi/10.1103/PhysRevB.75.064511`.

[4] D. F. Agterberg and H. Tsunetsugu. Dislocations and vortices in pair-density-wave superconductors. *Nature Physics*, 4(8):639–642, 2008. doi:10.1038/nphys999. URL `https://doi.org/10.1038/nphys999`.

[5] D. F. Agterberg, M. Geracie, and H. Tsunetsugu. Conventional and charge-six superfluids from melting hexagonal Fulde-Ferrell-Larkin-Ovchinnikov phases in two dimensions. *Phys. Rev. B*, 84:014513, Jul 2011. doi:10.1103/PhysRevB.84.014513. URL `https://link.aps.org/doi/10.1103/PhysRevB.84.014513`.

[6] D. F. Agterberg, D. S. Melchert, and M. K. Kashyap. Emergent loop current order from pair density wave superconductivity. *Phys. Rev. B*, 91:054502, Feb 2015. doi:10.1103/PhysRevB.91.054502. URL `https://link.aps.org/doi/10.1103/PhysRevB.91.054502`.

[7] D. F. Agterberg, P. M. R. Brydon, and C. Timm. Bogoliubov Fermi surfaces in superconductors with broken time-reversal symmetry. *Phys. Rev. Lett.*, 118:127001, Mar 2017. doi:10.1103/PhysRevLett.118.127001. URL `https://link.aps.org/doi/10.1103/PhysRevLett.118.127001`.

[8] D. F. Agterberg, J. S. Davis, S. D. Edkins, E. Fradkin, D. J. Van Harlingen, S. A. Kivelson, P. A. Lee, L. Radzihovsky, J. M. Tranquada, and Y. Wang. The physics of pair-density waves: Cuprate superconductors and beyond. *Annual Review of Condensed Matter Physics*, 11(1): 231–270, 2020. doi:10.1146/annurev-conmatphys-031119-050711. URL `https://doi.org/10.1146/annurev-conmatphys-031119-050711`.

[9] A. Altland and B. D. Simons. *Condensed Matter Field Theory*. Cambridge University Press, 2 edition, 2010. doi:10.1017/CBO9780511789984.

[10] A. Altland and M. R. Zirnbauer. Nonstandard symmetry classes in mesoscopic normal-superconducting hybrid structures. *Phys. Rev. B*, 55:1142–1161, Jan 1997. doi:10.1103/PhysRevB.55.1142. URL `https://link.aps.org/doi/10.1103/PhysRevB.55.1142`.

[11] C. J. Arguello, S. P. Chockalingam, E. P. Rosenthal, L. Zhao, C. Gutiérrez, J. H. Kang, W. C. Chung, R. M. Fernandes, S. Jia, A. J. Millis, R. J. Cava, and A. N. Pasupathy. Visualizing the charge density wave transition in 2H-$NbSe_2$ in real space. *Phys. Rev. B*, 89:235115, Jun 2014. doi:10.1103/PhysRevB.89.235115. URL https://link.aps.org/doi/10.1103/PhysRevB.89.235115.

[12] M. Bahari and M. V. Hosseini. One-dimensional topological metal. *Phys. Rev. B*, 99:155128, Apr 2019. doi:10.1103/PhysRevB.99.155128. URL https://link.aps.org/doi/10.1103/PhysRevB.99.155128.

[13] E. Bauer and M. Sigrist. *Non-Centrosymmetric Superconductors: Introduction and Overview*, volume 847. Springer Science & Business Media, 2012.

[14] M. V. Berry. Quantal phase factors accompanying adiabatic changes. *Proceedings of the Royal Society of London. A. Mathematical and Physical Sciences*, 392(1802):45–57, 1984. doi:10.1098/rspa.1984.0023. URL https://royalsocietypublishing.org/doi/abs/10.1098/rspa.1984.0023.

[15] G. Bian, T.-R. Chang, H. Zheng, S. Velury, S.-Y. Xu, T. Neupert, C.-K. Chiu, S.-M. Huang, D. S. Sanchez, I. Belopolski, N. Alidoust, P.-J. Chen, G. Chang, A. Bansil, H.-T. Jeng, H. Lin, and M. Z. Hasan. Drumhead surface states and topological nodal-line fermions in $TlTaSe_2$. *Phys. Rev. B*, 93:121113, Mar 2016. doi:10.1103/PhysRevB.93.121113. URL https://link.aps.org/doi/10.1103/PhysRevB.93.121113.

[16] G. Blatter, M. V. Feigel'man, V. B. Geshkenbein, A. I. Larkin, and V. M. Vinokur. Vortices in high-temperature superconductors. *Rev. Mod. Phys.*, 66:1125–1388, Oct 1994. doi:10.1103/RevModPhys.66.1125. URL https://link.aps.org/doi/10.1103/RevModPhys.66.1125.

[17] P. M. Bonetti. Accessing the ordered phase of correlated Fermi systems: Vertex bosonization and mean-field theory within the functional renormalization group, 2020. URL https://arxiv.org/abs/2007.10661.

[18] S. V. Borisenko, A. A. Kordyuk, V. B. Zabolotnyy, D. S. Inosov, D. Evtushinsky, B. Büchner, A. N. Yaresko, A. Varykhalov, R. Follath, W. Eberhardt, L. Patthey, and H. Berger. Two energy gaps and fermi-surface "arcs" in $NbSe_2$. *Phys. Rev. Lett.*, 102:166402, Apr 2009. doi:10.1103/PhysRevLett.102.166402. URL https://link.aps.org/doi/10.1103/PhysRevLett.102.166402.

[19] P. M. R. Brydon, A. P. Schnyder, and C. Timm. Topologically protected flat zero-energy surface bands in noncentrosymmetric superconductors. *Phys. Rev. B*, 84:020501, Jul 2011. doi:10.1103/PhysRevB.84.020501. URL https://link.aps.org/doi/10.1103/PhysRevB.84.020501.

[20] P. M. R. Brydon, D. F. Agterberg, H. Menke, and C. Timm. Bogoliubov Fermi surfaces: General theory, magnetic order, and topology. *Phys. Rev. B*, 98:224509, Dec 2018. doi:10.1103/PhysRevB.98.224509. URL https://link.aps.org/doi/10.1103/PhysRevB.98.224509.

[21] Y. A. Bychkov and É. I. Rashba. Properties of a 2d electron gas with lifted spectral degeneracy. *JETP lett*, 39(2):78, 1984.

[22] Y. Cao, A. Mishchenko, G. L. Yu, E. Khestanova, A. P. Rooney, E. Prestat, A. V. Kretinin, P. Blake, M. B. Shalom, C. Woods, J. Chapman, G. Balakrishnan, I. V. Grigorieva, K. S. Novoselov, B. A. Piot, M. Potemski, K. Watanabe, T. Taniguchi, S. J. Haigh, A. K. Geim, and R. V. Gorbachev. Quality heterostructures from two-dimensional crystals unstable in air by their assembly in inert atmosphere. *Nano Letters*, 15(8):4914–4921, 08 2015. doi:10.1021/acs.nanolett.5b00648. URL https://doi.org/10.1021/acs.nanolett.5b00648.

[23] Y.-H. Chan, C.-K. Chiu, M. Y. Chou, and A. P. Schnyder. Ca_3P_2 and other topological semimetals with line nodes and drumhead surface states. *Phys. Rev. B*, 93:205132, May 2016. doi:10.1103/PhysRevB.93.205132. URL https://link.aps.org/doi/10.1103/PhysRevB.93.205132.

[24] B. S. Chandrasekhar. A note on the maximum critical field of high-field superconductors. *Applied Physics Letters*, 1(1):7–8, 1962. doi:10.1063/1.1777362. URL https://doi.org/10.1063/1.1777362.

[25] W. Chen, Q. Zhu, Y. Zhou, and J. An. Topological Ising pairing states in monolayer and trilayer TaS_2. *Phys. Rev. B*, 100:054503, Aug 2019. doi:10.1103/PhysRevB.100.054503. URL https://link.aps.org/doi/10.1103/PhysRevB.100.054503.

[26] D. V. Chichinadze, L. Classen, and A. V. Chubukov. Nematic superconductivity in twisted bilayer graphene. *Phys. Rev. B*, 101:224513, Jun 2020. doi:10.1103/PhysRevB.101.224513. URL https://link.aps.org/doi/10.1103/PhysRevB.101.224513.

[27] D. V. Chichinadze, L. Classen, and A. V. Chubukov. Orbital antiferromagnetism, nematicity, and density wave orders in twisted bilayer graphene, 2020. URL https://arxiv.org/abs/2007.00871.

[28] C.-K. Chiu and A. P. Schnyder. Classification of reflection-symmetry-protected topological semimetals and nodal superconductors. *Phys. Rev. B*, 90:205136, Nov 2014. doi:10.1103/PhysRevB.90.205136. URL https://link.aps.org/doi/10.1103/PhysRevB.90.205136.

[29] C.-K. Chiu, H. Yao, and S. Ryu. Classification of topological insulators and superconductors in the presence of reflection symmetry. *Phys. Rev. B*, 88:075142, Aug 2013. doi:10.1103/PhysRevB.88.075142. URL https://link.aps.org/doi/10.1103/PhysRevB.88.075142.

[30] C.-K. Chiu, J. C. Y. Teo, A. P. Schnyder, and S. Ryu. Classification of topological quantum matter with symmetries. *Rev. Mod. Phys.*, 88:035005, Aug 2016. doi:10.1103/RevModPhys.88.035005. URL https://link.aps.org/doi/10.1103/RevModPhys.88.035005.

[31] H. Chono, K. Takasan, and Y. Yanase. Laser-induced topological s-wave superconductivity in bilayer transition metal dichalcogenides. 2020. URL https://arxiv.org/abs/2007.11812.

[32] A. V. Chubukov, M. Khodas, and R. M. Fernandes. Magnetism, superconductivity, and spontaneous orbital order in iron-based superconductors: Which comes first and why? *Phys. Rev. X*, 6:041045, Dec 2016. doi:10.1103/PhysRevX.6.041045. URL https://link.aps.org/doi/10.1103/PhysRevX.6.041045.

[33] L. Classen, R.-Q. Xing, M. Khodas, and A. V. Chubukov. Interplay between magnetism, superconductivity, and orbital order in 5-pocket model for iron-based superconductors: Parquet renormalization group study. *Phys. Rev. Lett.*, 118:037001, Jan

2017. doi:10.1103/PhysRevLett.118.037001. URL https://link.aps.org/doi/10.1103/PhysRevLett.118.037001.

[34] L. Classen, C. Honerkamp, and M. M. Scherer. Competing phases of interacting electrons on triangular lattices in moiré heterostructures. *Phys. Rev. B*, 99:195120, May 2019. doi:10.1103/PhysRevB.99.195120. URL https://link.aps.org/doi/10.1103/PhysRevB.99.195120.

[35] L. Classen, A. V. Chubukov, C. Honerkamp, and M. M. Scherer. Competing orders at higher-order van hove points. 2020. URL https://arxiv.org/abs/2006.14729.

[36] A. M. Clogston. Upper limit for the critical field in hard superconductors. *Phys. Rev. Lett.*, 9:266–267, Sep 1962. doi:10.1103/PhysRevLett.9.266. URL https://link.aps.org/doi/10.1103/PhysRevLett.9.266.

[37] P. Coleman. *Introduction to Many-Body Physics*. Cambridge University Press, 2015. doi:10.1017/CBO9781139020916.

[38] E. Cornfeld and A. Chapman. Classification of crystalline topological insulators and superconductors with point group symmetries. *Phys. Rev. B*, 99:075105, Feb 2019. doi:10.1103/PhysRevB.99.075105. URL https://link.aps.org/doi/10.1103/PhysRevB.99.075105.

[39] V. Cvetkovic, R. E. Throckmorton, and O. Vafek. Electronic multicriticality in bilayer graphene. *Phys. Rev. B*, 86:075467, Aug 2012. doi:10.1103/PhysRevB.86.075467. URL https://link.aps.org/doi/10.1103/PhysRevB.86.075467.

[40] S. C. de la Barrera, M. R. Sinko, D. P. Gopalan, N. Sivadas, K. L. Seyler, K. Watanabe, T. Taniguchi, A. W. Tsen, X. Xu, D. Xiao, and B. M. Hunt. Tuning Ising superconductivity with layer and spin–orbit coupling in two-dimensional transition-metal dichalcogenides. *Nature Communications*, 9(1):1427, 2018. doi:10.1038/s41467-018-03888-4. URL https://doi.org/10.1038/s41467-018-03888-4.

[41] O. V. Dimitrova and M. V. Feigel'man. Phase diagram of a surface superconductor in parallel magnetic field. *Journal of Experimental and Theoretical Physics Letters*, 78(10):637–641, 2003. doi:10.1134/1.1644308. URL https://doi.org/10.1134/1.1644308.

[42] V. Edel'shtein. Characteristics of the Cooper pairing in two-dimensional noncentrosymmetric electron systems. *Soviet Physics-JETP (English Translation)*, 68(6):1244–1249, 1989.

[43] V. M. Edelstein. Magnetoelectric effect in polar superconductors. *Phys. Rev. Lett.*, 75:2004–2007, Sep 1995. doi:10.1103/PhysRevLett.75.2004. URL https://link.aps.org/doi/10.1103/PhysRevLett.75.2004.

[44] V. Fatemi, S. Wu, Y. Cao, L. Bretheau, Q. D. Gibson, K. Watanabe, T. Taniguchi, R. J. Cava, and P. Jarillo-Herrero. Electrically tunable low-density superconductivity in a monolayer topological insulator. *Science*, 362(6417):926–929, 2018. ISSN 0036-8075. doi:10.1126/science.aar4642. URL https://science.sciencemag.org/content/362/6417/926.

[45] R. M. Fernandes and A. V. Chubukov. Low-energy microscopic models for iron-based superconductors: a review. *Reports on Progress in Physics*, 80(1):014503, nov 2016. doi:10.1088/1361-6633/80/1/014503. URL https://doi.org/10.1088%2F1361-6633%2F80%2F1%2F014503.

[46] A. L. Fetter and J. D. Walecka. *Quantum Theory of Many-Particle Systems*. Dover, 2003.

[47] M. H. Fischer, F. Loder, and M. Sigrist. Superconductivity and local noncentrosymmetricity in crystal lattices. *Phys. Rev. B*, 84:184533, Nov 2011. doi:10.1103/PhysRevB.84.184533. URL https://link.aps.org/doi/10.1103/PhysRevB.84.184533.

[48] M. H. Fischer, M. Sigrist, and D. F. Agterberg. Superconductivity without inversion and time-reversal symmetries. *Phys. Rev. Lett.*, 121:157003, Oct 2018. doi:10.1103/PhysRevLett.121.157003. URL https://link.aps.org/doi/10.1103/PhysRevLett.121.157003.

[49] E. Fradkin. *Field Theories of Condensed Matter Physics*. Cambridge University Press, 2 edition, 2013. doi:10.1017/CBO9781139015509.

[50] M. Franz, Z. Tešanović, and O. Vafek. QED_3 theory of pairing pseudogap in cuprates: From d-wave superconductor to antiferromagnet via an algebraic Fermi liquid. *Phys. Rev. B*, 66: 054535, Aug 2002. doi:10.1103/PhysRevB.66.054535. URL https://link.aps.org/doi/10.1103/PhysRevB.66.054535.

[51] P. A. Frigeri, D. F. Agterberg, A. Koga, and M. Sigrist. Superconductivity without inversion symmetry: MnSi versus $CePt_3Si$. *Phys. Rev. Lett.*, 92:097001, Mar 2004. doi:10.1103/PhysRevLett.92.097001. URL https://link.aps.org/doi/10.1103/PhysRevLett.92.097001.

[52] L. Fu and C. L. Kane. Time reversal polarization and a Z_2 adiabatic spin pump. *Phys. Rev. B*, 74:195312, Nov 2006. doi:10.1103/PhysRevB.74.195312. URL https://link.aps.org/doi/10.1103/PhysRevB.74.195312.

[53] P. Fulde and R. A. Ferrell. Superconductivity in a strong spin-exchange field. *Phys. Rev.*, 135: A550–A563, Aug 1964. doi:10.1103/PhysRev.135.A550. URL https://link.aps.org/doi/10.1103/PhysRev.135.A550.

[54] L. P. Gor'kov and E. I. Rashba. Superconducting 2d system with lifted spin degeneracy: Mixed singlet-triplet state. *Phys. Rev. Lett.*, 87:037004, Jul 2001. doi:10.1103/PhysRevLett.87.037004. URL https://link.aps.org/doi/10.1103/PhysRevLett.87.037004.

[55] J. Goryo, M. H. Fischer, and M. Sigrist. Possible pairing symmetries in SrPtAs with a local lack of inversion center. *Phys. Rev. B*, 86:100507, Sep 2012. doi:10.1103/PhysRevB.86.100507. URL https://link.aps.org/doi/10.1103/PhysRevB.86.100507.

[56] M. Greiter. Is electromagnetic gauge invariance spontaneously violated in superconductors? *Annals of Physics*, 319(1):217 – 249, 2005. ISSN 0003-4916. doi:https://doi.org/10.1016/j.aop.2005.03.008. URL http://www.sciencedirect.com/science/article/pii/S0003491605000515.

[57] F. Guinea and B. Uchoa. Odd-momentum pairing and superconductivity in vertical graphene heterostructures. *Phys. Rev. B*, 86:134521, Oct 2012. doi:10.1103/PhysRevB.86.134521. URL https://link.aps.org/doi/10.1103/PhysRevB.86.134521.

[58] A. Hamill, B. Heischmidt, E. Sohn, D. Shaffer, K.-T. Tsai, X. Zhang, X. Xi, A. Suslov, H. Berger, L. Forró, F. J. Burnell, J. Shan, K. F. Mak, R. M. Fernandes, K. Wang, and V. S. Pribiag. Unexpected two-fold symmetric superconductivity in few-layer $NbSe_2$. 2020.

[59] O. Hart, G. Goldstein, C. Chamon, and C. Castelnovo. Steady-state superconductivity in electronic materials with repulsive interactions. *Phys. Rev. B*, 100:060508, Aug 2019. doi:10.1103/PhysRevB.100.060508. URL https://link.aps.org/doi/10.1103/PhysRevB.100.060508.

[60] K. Hashimoto, T. Kimura, and X. Wu. Boundary conditions of Weyl semimetals. *Progress of Theoretical and Experimental Physics*, 2017(5), 05 2017. ISSN 2050-3911. doi:10.1093/ptep/ptx053. URL https://doi.org/10.1093/ptep/ptx053. 053I01.

[61] W.-Y. He and K. T. Law. Magnetoelectric effects in gyrotropic superconductors. *Phys. Rev. Research*, 2:012073, Mar 2020. doi:10.1103/PhysRevResearch.2.012073. URL https://link.aps.org/doi/10.1103/PhysRevResearch.2.012073.

[62] W.-Y. He, B. T. Zhou, J. J. He, N. F. Q. Yuan, T. Zhang, and K. T. Law. Magnetic field driven nodal topological superconductivity in monolayer transition metal dichalcogenides. *Communications Physics*, 1(1):40, 2018. doi:10.1038/s42005-018-0041-4. URL https://doi.org/10.1038/s42005-018-0041-4.

[63] A. Hinojosa, A. V. Chubukov, and P. Wölfle. Effect of pairing fluctuations on the spin resonance in Fe-based superconductors. *Phys. Rev. B*, 90:104509, Sep 2014. doi:10.1103/PhysRevB.90.104509. URL https://link.aps.org/doi/10.1103/PhysRevB.90.104509.

[64] A. Hinojosa, R. M. Fernandes, and A. V. Chubukov. Time-reversal symmetry breaking superconductivity in the coexistence phase with magnetism in Fe pnictides. *Phys. Rev. Lett.*, 113: 167001, Oct 2014. doi:10.1103/PhysRevLett.113.167001. URL https://link.aps.org/doi/10.1103/PhysRevLett.113.167001.

[65] P. J. Hirschfeld, M. M. Korshunov, and I. I. Mazin. Gap symmetry and structure of Fe-based superconductors. *Reports on Progress in Physics*, 74(12):124508, oct 2011. doi:10.1088/0034-4885/74/12/124508. URL https://doi.org/10.1088%2F0034-4885%2F74%2F12%2F124508.

[66] P. Hořava. Stability of Fermi surfaces and K theory. *Phys. Rev. Lett.*, 95:016405, Jun 2005. doi:10.1103/PhysRevLett.95.016405. URL https://link.aps.org/doi/10.1103/PhysRevLett.95.016405.

[67] Y.-T. Hsu, A. Vaezi, M. H. Fischer, and E.-A. Kim. Topological superconductivity in monolayer transition metal dichalcogenides. *Nature Communications*, 8:14985 EP –, 04 2017. URL https://doi.org/10.1038/ncomms14985.

[68] Y.-T. Hsu, W. S. Cole, R.-X. Zhang, and J. D. Sau. Inversion-protected higher order topological superconductivity in monolayer WTe_2. 2019. URL https://arxiv.org/abs/1904.06361.

[69] T. L. Hughes, E. Prodan, and B. A. Bernevig. Inversion-symmetric topological insulators. *Phys. Rev. B*, 83:245132, Jun 2011. doi:10.1103/PhysRevB.83.245132. URL https://link.aps.org/doi/10.1103/PhysRevB.83.245132.

[70] S. Ilić, J. S. Meyer, and M. Houzet. Enhancement of the upper critical field in disordered transition metal dichalcogenide monolayers. *Phys. Rev. Lett.*, 119:117001, Sep 2017. doi:10.1103/PhysRevLett.119.117001. URL https://link.aps.org/doi/10.1103/PhysRevLett.119.117001.

[71] L. Jiao, S. Howard, S. Ran, Z. Wang, J. O. Rodriguez, M. Sigrist, Z. Wang, N. P. Butch, and V. Madhavan. Chiral superconductivity in heavy-fermion metal UTe_2. *Nature*, 579 (7800):523–527, 2020. doi:10.1038/s41586-020-2122-2. URL https://doi.org/10.1038/s41586-020-2122-2.

[72] M. D. Johannes and I. I. Mazin. Fermi surface nesting and the origin of charge density waves in metals. *Phys. Rev. B*, 77:165135, Apr 2008. doi:10.1103/PhysRevB.77.165135. URL https://link.aps.org/doi/10.1103/PhysRevB.77.165135.

[73] M. D. Johannes, I. I. Mazin, and C. A. Howells. Fermi-surface nesting and the origin of the charge-density wave in $Nbse_2$. *Phys. Rev. B*, 73:205102, May 2006. doi:10.1103/PhysRevB.73.205102. URL https://link.aps.org/doi/10.1103/PhysRevB.73.205102.

[74] A. Kamenev. *Field Theory of Non-Equilibrium Systems*. Cambridge University Press, 2011. doi:10.1017/CBO9781139003667.

[75] S. Kanasugi and Y. Yanase. Multiple odd-parity superconducting phases in bilayer transition metal dichalcogenides. 2020. URL https://arxiv.org/abs/2005.13963.

[76] C. L. Kane and E. J. Mele. Quantum spin Hall effect in graphene. *Phys. Rev. Lett.*, 95:226801, Nov 2005. doi:10.1103/PhysRevLett.95.226801. URL https://link.aps.org/doi/10.1103/PhysRevLett.95.226801.

[77] C. L. Kane and E. J. Mele. $\mathbb{Z}_2$ topological order and the quantum spin Hall effect. *Phys. Rev. Lett.*, 95:146802, Sep 2005. doi:10.1103/PhysRevLett.95.146802. URL https://link.aps.org/doi/10.1103/PhysRevLett.95.146802.

[78] J. Kang and O. Vafek. Symmetry, maximally localized wannier states, and a low-energy model for twisted bilayer graphene narrow bands. *Phys. Rev. X*, 8:031088, Sep 2018. doi:10.1103/PhysRevX.8.031088. URL https://link.aps.org/doi/10.1103/PhysRevX.8.031088.

[79] E. Khalaf, H. C. Po, A. Vishwanath, and H. Watanabe. Symmetry indicators and anomalous surface states of topological crystalline insulators. *Phys. Rev. X*, 8:031070, Sep 2018. doi:10.1103/PhysRevX.8.031070. URL https://link.aps.org/doi/10.1103/PhysRevX.8.031070.

[80] M. Khodas and A. V. Chubukov. Orbital order from the on-site orbital attraction. *Phys. Rev. B*, 94:115159, Sep 2016. doi:10.1103/PhysRevB.94.115159. URL https://link.aps.org/doi/10.1103/PhysRevB.94.115159.

[81] A. Y. Kitaev. Unpaired Majorana fermions in quantum wires. *Physics-Uspekhi*, 44(10S): 131–136, oct 2001. doi:10.1070/1063-7869/44/10s/s29. URL https://doi.org/10.1070%2F1063-7869%2F44%2F10s%2Fs29.

[82] S. Kobayashi, S. Sumita, Y. Yanase, and M. Sato. Symmetry-protected line nodes and Majorana flat bands in nodal crystalline superconductors. *Phys. Rev. B*, 97:180504, May 2018. doi:10.1103/PhysRevB.97.180504. URL https://link.aps.org/doi/10.1103/PhysRevB.97.180504.

[83] W. Kohn and J. M. Luttinger. New mechanism for superconductivity. *Phys. Rev. Lett.*, 15: 524–526, Sep 1965. doi:10.1103/PhysRevLett.15.524. URL https://link.aps.org/doi/10.1103/PhysRevLett.15.524.

[84] A. Kormányos, V. Zólyomi, N. D. Drummond, P. Rakyta, G. Burkard, and V. I. Fal'ko. Monolayer MoS_2: Trigonal warping, the Γ valley, and spin-orbit coupling effects. *Phys. Rev. B*, 88:045416, Jul 2013. doi:10.1103/PhysRevB.88.045416. URL https://link.aps.org/doi/10.1103/PhysRevB.88.045416.

[85] E. Lake, C. Webb, D. A. Pesin, and O. A. Starykh. Rashba versus Kohn-Luttinger: Evolution of p-wave superconductivity in magnetized two-dimensional Fermi gases subject to spin-orbit interactions. *Phys. Rev. B*, 93:214516, Jun 2016. doi:10.1103/PhysRevB.93.214516. URL https://link.aps.org/doi/10.1103/PhysRevB.93.214516.

[86] L. D. Landau and E. M. Lifshitz. *Quantum Mechanics: Non-Relativistic Theory*, volume 3. Elsevier, 2013.

[87] A. Larkin and Y. Ovchinnikov. Nonuniform State of Superconductors. *Zh. Eksp. Teor. Fiz.*, 47:1136–1146, 1964.

[88] A. Larkin and A. Varlamov. *Theory of Fluctuations in Superconductors*. Clarendon Press, 2005.

[89] A. Lau and C. Ortix. Novel topological insulators from crystalline symmetries. *The European Physical Journal Special Topics*, 227(12):1309–1321, Dec 2018. ISSN 1951-6401. doi:10.1140/epjst/e2018-800098-y. URL https://doi.org/10.1140/epjst/e2018-800098-y.

[90] P. A. Lee. Amperean pairing and the pseudogap phase of cuprate superconductors. *Phys. Rev. X*, 4:031017, Jul 2014. doi:10.1103/PhysRevX.4.031017. URL https://link.aps.org/doi/10.1103/PhysRevX.4.031017.

[91] C.-S. Lian, C. Si, J. Wu, and W. Duan. First-principles study of Na-intercalated bilayer $NbSe_2$: Suppressed charge-density wave and strain-enhanced superconductivity. *Phys. Rev. B*, 96:235426, Dec 2017. doi:10.1103/PhysRevB.96.235426. URL https://link.aps.org/doi/10.1103/PhysRevB.96.235426.

[92] E. M. Lifshitz and L. P. Pitaevski. *Statistical Physics Part 2*. Butterworth-Heinemann, 1980. ISBN 978-0-08-050350. doi:https://doi.org/10.1016/B978-0-08-050350-9.50003. URL http://www.sciencedirect.com/science/article/pii/B9780080503509500034.

[93] Z.-K. Lin, H.-X. Wang, Z. Xiong, M.-H. Lu, and J.-H. Jiang. Anomalous quadrupole topological insulators in two-dimensional nonsymmorphic sonic crystals. *Phys. Rev. B*, 102:035105, Jul 2020. doi:10.1103/PhysRevB.102.035105. URL https://link.aps.org/doi/10.1103/PhysRevB.102.035105.

[94] C.-X. Liu. Unconventional superconductivity in bilayer transition metal dichalcogenides. *Phys. Rev. Lett.*, 118:087001, Feb 2017. doi:10.1103/PhysRevLett.118.087001. URL https://link.aps.org/doi/10.1103/PhysRevLett.118.087001.

[95] C.-X. Liu, R.-X. Zhang, and B. K. VanLeeuwen. Topological nonsymmorphic crystalline insulators. *Phys. Rev. B*, 90:085304, Aug 2014. doi:10.1103/PhysRevB.90.085304. URL https://link.aps.org/doi/10.1103/PhysRevB.90.085304.

[96] G.-B. Liu, W.-Y. Shan, Y. Yao, W. Yao, and D. Xiao. Three-band tight-binding model for monolayers of group-VIB transition metal dichalcogenides. *Phys. Rev. B*, 88:085433, Aug 2013. doi:10.1103/PhysRevB.88.085433. URL https://link.aps.org/doi/10.1103/PhysRevB.88.085433.

[97] X. Liu, Y. X. Chong, R. Sharma, and J. C. S. Davis. Discovery of a cooper-pair density wave state in a transition-metal dichalcogenide, 2020. URL https://arxiv.org/abs/2007.15228.

[98] J. M. Lu, O. Zheliuk, I. Leermakers, N. F. Q. Yuan, U. Zeitler, K. T. Law, and J. T. Ye. Evidence for two-dimensional Ising superconductivity in gated MoS_2. *Science*, 350(6266): 1353–1357, 2015. ISSN 0036-8075. doi:10.1126/science.aab2277. URL http://science.sciencemag.org/content/350/6266/1353.

[99] A. W. W. Ludwig. Topological phases: classification of topological insulators and superconductors of non-interacting fermions, and beyond. *Physica Scripta*, T168:014001, dec 2015. doi:10.1088/0031-8949/2015/t168/014001. URL https://doi.org/10.1088%2F0031-8949%2F2015%2Ft168%2F014001.

[100] G. D. Mahan. *Many Particle Physics, Third Edition*. Plenum, New York, 2000. doi:10.1007/978-1-4757-5714-9.

[101] S. Maiti and A. V. Chubukov. $s + is$ state with broken time-reversal symmetry in Fe-based superconductors. *Phys. Rev. B*, 87:144511, Apr 2013. doi:10.1103/PhysRevB.87.144511. URL https://link.aps.org/doi/10.1103/PhysRevB.87.144511.

[102] S. Maiti and A. V. Chubukov. Superconductivity from repulsive interaction. *AIP Conference Proceedings*, 1550(1):3–73, 2013. doi:10.1063/1.4818400. URL https://aip.scitation.org/doi/abs/10.1063/1.4818400.

[103] S. Manzeli, D. Ovchinnikov, D. Pasquier, O. V. Yazyev, and A. Kis. 2d transition metal dichalcogenides. *Nature Reviews Materials*, 2:17033 EP –, 06 2017. URL https://doi.org/10.1038/natrevmats.2017.33.

[104] Y. Matsuda and H. Shimahara. Fulde-Ferrell-Larkin-Ovchinnikov state in heavy fermion superconductors. *Journal of the Physical Society of Japan*, 76(5):051005, 2007. doi:10.1143/JPSJ.76.051005. URL https://doi.org/10.1143/JPSJ.76.051005.

[105] S. Matsuura, P.-Y. Chang, A. P. Schnyder, and S. Ryu. Protected boundary states in gapless topological phases. *New Journal of Physics*, 15(6):065001, jun 2013. doi:10.1088/1367-2630/15/6/065001. URL https://doi.org/10.1088%2F1367-2630%2F15%2F6%2F065001.

[106] H. Menke, C. Timm, and P. M. R. Brydon. Bogoliubov Fermi surfaces stabilized by spin-orbit coupling. *Phys. Rev. B*, 100:224505, Dec 2019. doi:10.1103/PhysRevB.100.224505. URL https://link.aps.org/doi/10.1103/PhysRevB.100.224505.

[107] K. Michaeli, A. C. Potter, and P. A. Lee. Superconducting and ferromagnetic phases in $SrTiO_3/LaAlO_3$ oxide interface structures: Possibility of finite momentum pairing. *Phys. Rev. Lett.*, 108:117003, Mar 2012. doi:10.1103/PhysRevLett.108.117003. URL https://link.aps.org/doi/10.1103/PhysRevLett.108.117003.

[108] V. P. Mineev and K. V. Samokhin. Nonuniform states in noncentrosymmetric superconductors: Derivation of Lifshitz invariants from microscopic theory. *Phys. Rev. B*, 78:144503, Oct 2008. doi:10.1103/PhysRevB.78.144503. URL https://link.aps.org/doi/10.1103/PhysRevB.78.144503.

[109] D. Möckli and M. Khodas. s+if pairing in Ising superconductors. *arXiv:1902.02577*. URL https://arxiv.org/abs/1902.02577.

[110] D. Möckli and M. Khodas. Robust parity-mixed superconductivity in disordered monolayer transition metal dichalcogenides. *Phys. Rev. B*, 98:144518, Oct 2018. doi:10.1103/PhysRevB.98.144518. URL https://link.aps.org/doi/10.1103/PhysRevB.98.144518.

[111] D. Möckli and M. Khodas. Ising superconductors: Interplay of magnetic field, triplet channels, and disorder. *Phys. Rev. B*, 101:014510, Jan 2020. doi:10.1103/PhysRevB.101.014510. URL https://link.aps.org/doi/10.1103/PhysRevB.101.014510.

[112] D. Möckli, Y. Yanase, and M. Sigrist. Orbitally limited pair-density-wave phase of multilayer superconductors. *Phys. Rev. B*, 97:144508, Apr 2018. doi:10.1103/PhysRevB.97.144508. URL https://link.aps.org/doi/10.1103/PhysRevB.97.144508.

[113] J. E. Moore and L. Balents. Topological invariants of time-reversal-invariant band structures. *Phys. Rev. B*, 75:121306, Mar 2007. doi:10.1103/PhysRevB.75.121306. URL https://link.aps.org/doi/10.1103/PhysRevB.75.121306.

[114] P. Morel and P. W. Anderson. Calculation of the superconducting state parameters with retarded electron-phonon interaction. *Phys. Rev.*, 125:1263–1271, Feb 1962. doi:10.1103/PhysRev.125.1263. URL https://link.aps.org/doi/10.1103/PhysRev.125.1263.

[115] D. Möckli, M. Haim, and M. Khodas. Magnetic impurities in thin films and 2d Ising superconductors, 2020. URL https://doi.org/10.1063/5.0010773.

[116] Y. Nakamura and Y. Yanase. Odd-parity superconductivity in bilayer transition metal dichalcogenides. *Phys. Rev. B*, 96:054501, Aug 2017. doi:10.1103/PhysRevB.96.054501. URL https://link.aps.org/doi/10.1103/PhysRevB.96.054501.

[117] Y. Nakata, K. Sugawara, S. Ichinokura, Y. Okada, T. Hitosugi, T. Koretsune, K. Ueno, S. Hasegawa, T. Takahashi, and T. Sato. Anisotropic band splitting in monolayer $NbSe_2$: implications for superconductivity and charge density wave. *npj 2D Materials and Applications*, 2(1):12, 2018. doi:10.1038/s41699-018-0057-3. URL https://doi.org/10.1038/s41699-018-0057-3.

[118] S. Nakosai, Y. Tanaka, and N. Nagaosa. Topological superconductivity in bilayer rashba system. *Phys. Rev. Lett.*, 108:147003, Apr 2012. doi:10.1103/PhysRevLett.108.147003. URL https://link.aps.org/doi/10.1103/PhysRevLett.108.147003.

[119] R. Nandkishore, G.-W. Chern, and A. V. Chubukov. Itinerant half-metal spin-density-wave state on the hexagonal lattice. *Phys. Rev. Lett.*, 108:227204, May 2012. doi:10.1103/PhysRevLett.108.227204. URL https://link.aps.org/doi/10.1103/PhysRevLett.108.227204.

[120] R. Nandkishore, L. S. Levitov, and A. V. Chubukov. Chiral superconductivity from repulsive interactions in doped graphene. *Nature Physics*, 8(2):158–163, 2012. doi:10.1038/nphys2208. URL https://doi.org/10.1038/nphys2208.

[121] R. Nandkishore, R. Thomale, and A. V. Chubukov. Superconductivity from weak repulsion in hexagonal lattice systems. *Phys. Rev. B*, 89:144501, Apr 2014. doi:10.1103/PhysRevB.89.144501. URL https://link.aps.org/doi/10.1103/PhysRevB.89.144501.

[122] E. Navarro-Moratalla, J. O. Island, S. Mañas-Valero, E. Pinilla-Cienfuegos, A. Castellanos-Gomez, J. Quereda, G. Rubio-Bollinger, L. Chirolli, J. A. Silva-Guillén, N. Agraït, G. A. Steele, F. Guinea, H. S. J. van der Zant, and E. Coronado. Enhanced superconductivity in atomically thin TaS_2. *Nature Communications*, 7:11043 EP –, 03 2016. URL https://doi.org/10.1038/ncomms11043.

[123] R. Oiwa, Y. Yanagi, and H. Kusunose. Theory of superconductivity in hole-doped monolayer MoS_2. *Phys. Rev. B*, 98:064509, Aug 2018. doi:10.1103/PhysRevB.98.064509. URL https://link.aps.org/doi/10.1103/PhysRevB.98.064509.

[124] R. Oiwa, Y. Yanagi, and H. Kusunose. Time-reversal symmetry breaking superconductivity in hole-doped monolayer MoS_2. *Journal of the Physical Society of Japan*, 88(6):063703, 2019. doi:10.7566/JPSJ.88.063703. URL https://doi.org/10.7566/JPSJ.88.063703.

[125] S. Ok, L. Muechler, D. Di Sante, G. Sangiovanni, R. Thomale, and T. Neupert. Custodial glide symmetry of quantum spin Hall edge modes in monolayer WTe_2. *Phys. Rev. B*, 99: 121105, Mar 2019. doi:10.1103/PhysRevB.99.121105. URL https://link.aps.org/doi/10.1103/PhysRevB.99.121105.

[126] S. Ono, Y. Yanase, and H. Watanabe. Symmetry indicators for topological superconductors. *Phys. Rev. Research*, 1:013012, Aug 2019. doi:10.1103/PhysRevResearch.1.013012. URL https://link.aps.org/doi/10.1103/PhysRevResearch.1.013012.

[127] A. C. Potter and P. A. Lee. Engineering a $p + ip$ superconductor: Comparison of topological insulator and rashba spin-orbit-coupled materials. *Phys. Rev. B*, 83:184520, May 2011. doi:10.1103/PhysRevB.83.184520. URL https://link.aps.org/doi/10.1103/PhysRevB.83.184520.

[128] X.-L. Qi, T. L. Hughes, and S.-C. Zhang. Topological invariants for the Fermi surface of a time-reversal-invariant superconductor. *Phys. Rev. B*, 81:134508, Apr 2010. doi:10.1103/PhysRevB.81.134508. URL https://link.aps.org/doi/10.1103/PhysRevB.81.134508.

[129] X. Qian, J. Liu, L. Fu, and J. Li. Quantum spin Hall effect in two-dimensional transition metal dichalcogenides. *Science*, 2014. ISSN 0036-8075. doi:10.1126/science.1256815. URL https://science.sciencemag.org/content/early/2014/11/19/science.1256815.

[130] N. Read and D. Green. Paired states of fermions in two dimensions with breaking of parity and time-reversal symmetries and the fractional quantum Hall effect. *Phys. Rev. B*, 61:10267–10297, Apr 2000. doi:10.1103/PhysRevB.61.10267. URL https://link.aps.org/doi/10.1103/PhysRevB.61.10267.

[131] R. Roldán, E. Cappelluti, and F. Guinea. Interactions and superconductivity in heavily doped MoS_2. *Phys. Rev. B*, 88:054515, Aug 2013. doi:10.1103/PhysRevB.88.054515. URL https://link.aps.org/doi/10.1103/PhysRevB.88.054515.

[132] S. Ryu, A. P. Schnyder, A. Furusaki, and A. W. W. Ludwig. Topological insulators and superconductors: tenfold way and dimensional hierarchy. *New Journal of Physics*, 12(6): 065010, jun 2010. doi:10.1088/1367-2630/12/6/065010. URL https://doi.org/10.1088%2F1367-2630%2F12%2F6%2F065010.

[133] Y. Saito, Y. Nakamura, M. S. Bahramy, Y. Kohama, J. Ye, Y. Kasahara, Y. Nakagawa, M. Onga, M. Tokunaga, T. Nojima, Y. Yanase, and Y. Iwasa. Superconductivity protected

by spin–valley locking in ion-gated MoS_2. *Nature Physics*, 12:144 EP –, 12 2015. URL https://doi.org/10.1038/nphys3580.

[134] E. Sajadi, T. Palomaki, Z. Fei, W. Zhao, P. Bement, C. Olsen, S. Luescher, X. Xu, J. A. Folk, and D. H. Cobden. Gate-induced superconductivity in a monolayer topological insulator. *Science*, 362(6417):922–925, 2018. ISSN 0036-8075. doi:10.1126/science.aar4426. URL https://science.sciencemag.org/content/362/6417/922.

[135] K. V. Samokhin. Spin susceptibility of noncentrosymmetric superconductors. *Phys. Rev. B*, 76:094516, Sep 2007. doi:10.1103/PhysRevB.76.094516. URL https://link.aps.org/doi/10.1103/PhysRevB.76.094516.

[136] K. V. Samokhin. Upper critical field in noncentrosymmetric superconductors. *Phys. Rev. B*, 78:224520, Dec 2008. doi:10.1103/PhysRevB.78.224520. URL https://link.aps.org/doi/10.1103/PhysRevB.78.224520.

[137] K. V. Samokhin. Symmetry and topology of two-dimensional noncentrosymmetric superconductors. *Phys. Rev. B*, 92:174517, Nov 2015. doi:10.1103/PhysRevB.92.174517. URL https://link.aps.org/doi/10.1103/PhysRevB.92.174517.

[138] K. V. Samokhin and V. P. Mineev. Gap structure in noncentrosymmetric superconductors. *Phys. Rev. B*, 77:104520, Mar 2008. doi:10.1103/PhysRevB.77.104520. URL https://link.aps.org/doi/10.1103/PhysRevB.77.104520.

[139] K. V. Samokhin and B. P. Truong. Current-carrying states in Fulde-Ferrell-Larkin-Ovchinnikov superconductors. *Phys. Rev. B*, 96:214501, Dec 2017. doi:10.1103/PhysRevB.96.214501. URL https://link.aps.org/doi/10.1103/PhysRevB.96.214501.

[140] L. Santos, T. Neupert, C. Chamon, and C. Mudry. Superconductivity on the surface of topological insulators and in two-dimensional noncentrosymmetric materials. *Phys. Rev. B*, 81:184502, May 2010. doi:10.1103/PhysRevB.81.184502. URL https://link.aps.org/doi/10.1103/PhysRevB.81.184502.

[141] L. Santos, T. Neupert, C. Chamon, and C. Mudry. Superconductivity on the surface of topological insulators and in two-dimensional noncentrosymmetric materials. *Phys. Rev. B*, 81:184502, May 2010. doi:10.1103/PhysRevB.81.184502. URL https://link.aps.org/doi/10.1103/PhysRevB.81.184502.

[142] L. H. Santos, Y. Wang, and E. Fradkin. Pair-density-wave order and paired fractional quantum Hall fluids. *Phys. Rev. X*, 9:021047, Jun 2019. doi:10.1103/PhysRevX.9.021047. URL https://link.aps.org/doi/10.1103/PhysRevX.9.021047.

[143] M. Sato and Y. Ando. Topological superconductors: a review. *Reports on Progress in Physics*, 80(7):076501, may 2017. doi:10.1088/1361-6633/aa6ac7. URL https://doi.org/10.1088%2F1361-6633%2Faa6ac7.

[144] M. Sato and S. Fujimoto. Existence of Majorana fermions and topological order in nodal superconductors with spin-orbit interactions in external magnetic fields. *Phys. Rev. Lett.*, 105:217001, Nov 2010. doi:10.1103/PhysRevLett.105.217001. URL https://link.aps.org/doi/10.1103/PhysRevLett.105.217001.

[145] M. Sato, Y. Tanaka, K. Yada, and T. Yokoyama. Topology of Andreev bound states with flat dispersion. *Phys. Rev. B*, 83:224511, Jun 2011. doi:10.1103/PhysRevB.83.224511. URL https://link.aps.org/doi/10.1103/PhysRevB.83.224511.

[146] M. S. Scheurer. Mechanism, time-reversal symmetry, and topology of superconductivity in noncentrosymmetric systems. *Phys. Rev. B*, 93:174509, May 2016. doi:10.1103/PhysRevB.93.174509. URL https://link.aps.org/doi/10.1103/PhysRevB.93.174509.

[147] M. S. Scheurer and J. Schmalian. Topological superconductivity and unconventional pairing in oxide interfaces. *Nature Communications*, 6:6005 EP –, 01 2015. URL https://doi.org/10.1038/ncomms7005.

[148] M. S. Scheurer, D. F. Agterberg, and J. Schmalian. Selection rules for Cooper pairing in two-dimensional interfaces and sheets. *npj Quantum Materials*, 2(1):9, 2017. doi:10.1038/s41535-016-0008-1. URL https://doi.org/10.1038/s41535-016-0008-1.

[149] F. Schindler, A. M. Cook, M. G. Vergniory, Z. Wang, S. S. P. Parkin, B. A. Bernevig, and T. Neupert. Higher-order topological insulators. *Science Advances*, 4(6), 2018. doi:10.1126/sciadv.aat0346. URL https://advances.sciencemag.org/content/4/6/eaat0346.

[150] A. P. Schnyder and P. M. R. Brydon. Topological surface states in nodal superconductors. *Journal of Physics: Condensed Matter*, 27(24):243201, may 2015. doi:10.1088/0953-8984/27/24/243201. URL https://doi.org/10.1088%2F0953-8984%2F27%2F24%2F243201.

[151] A. P. Schnyder and S. Ryu. Topological phases and surface flat bands in superconductors without inversion symmetry. *Phys. Rev. B*, 84:060504, Aug 2011. doi:10.1103/PhysRevB.84.060504. URL https://link.aps.org/doi/10.1103/PhysRevB.84.060504.

[152] A. P. Schnyder, P. M. R. Brydon, and C. Timm. Types of topological surface states in nodal noncentrosymmetric superconductors. *Phys. Rev. B*, 85:024522, Jan 2012. doi:10.1103/PhysRevB.85.024522. URL https://link.aps.org/doi/10.1103/PhysRevB.85.024522.

[153] D. Shaffer, J. Kang, F. J. Burnell, and R. M. Fernandes. Crystalline nodal topological superconductivity and Bogolyubov Fermi surfaces in monolayer $NbSe_2$. *Phys. Rev. B*, 101:224503, Jun 2020. doi:10.1103/PhysRevB.101.224503. URL https://link.aps.org/doi/10.1103/PhysRevB.101.224503.

[154] R. Shankar. Renormalization-group approach to interacting fermions. *Rev. Mod. Phys.*, 66: 129–192, Jan 1994. doi:10.1103/RevModPhys.66.129. URL https://link.aps.org/doi/10.1103/RevModPhys.66.129.

[155] R. Shankar. *Quantum Field Theory and Condensed Matter: An Introduction*. Cambridge University Press, 2017. doi:10.1017/9781139044349.

[156] H. Shapourian, Y. Wang, and S. Ryu. Topological crystalline superconductivity and second-order topological superconductivity in nodal-loop materials. *Phys. Rev. B*, 97:094508, Mar 2018. doi:10.1103/PhysRevB.97.094508. URL https://link.aps.org/doi/10.1103/PhysRevB.97.094508.

[157] W. Shi, J. Ye, Y. Zhang, R. Suzuki, M. Yoshida, J. Miyazaki, N. Inoue, Y. Saito, and Y. Iwasa. Superconductivity series in transition metal dichalcogenides by ionic gating. *Scientific Reports*, 5:12534 EP –, 08 2015. URL https://doi.org/10.1038/srep12534.

[158] K. Shiozaki and M. Sato. Topology of crystalline insulators and superconductors. *Phys. Rev. B*, 90:165114, Oct 2014. doi:10.1103/PhysRevB.90.165114. URL https://link.aps.org/doi/10.1103/PhysRevB.90.165114.

[159] K. Shiozaki, H. Shapourian, K. Gomi, and S. Ryu. Many-body topological invariants for fermionic short-range entangled topological phases protected by antiunitary symmetries. *Phys. Rev. B*, 98:035151, Jul 2018. doi:10.1103/PhysRevB.98.035151. URL https://link.aps.org/doi/10.1103/PhysRevB.98.035151.

[160] M. Sigrist and K. Ueda. Phenomenological theory of unconventional superconductivity. *Rev. Mod. Phys.*, 63:239–311, Apr 1991. doi:10.1103/RevModPhys.63.239. URL https://link.aps.org/doi/10.1103/RevModPhys.63.239.

[161] B. Simon. Holonomy, the quantum adiabatic theorem, and Berry's phase. *Phys. Rev. Lett.*, 51: 2167–2170, Dec 1983. doi:10.1103/PhysRevLett.51.2167. URL https://link.aps.org/doi/10.1103/PhysRevLett.51.2167.

[162] F. Siringo, G. G. N. Angilella, and R. Pucci. Renormalization-group approach to anisotropic superconductors at finite temperature. *Phys. Rev. B*, 53:2870–2881, Feb 1996. doi:10.1103/PhysRevB.53.2870. URL https://link.aps.org/doi/10.1103/PhysRevB.53.2870.

[163] M. Smidman, M. B. Salamon, H. Q. Yuan, and D. F. Agterberg. Superconductivity and spin–orbit coupling in non-centrosymmetric materials: a review. *Reports on Progress in Physics*, 80(3):036501, jan 2017. doi:10.1088/1361-6633/80/3/036501. URL https://iopscience.iop.org/article/10.1088/1361-6633/80/3/036501/meta.

[164] E. Sohn, X. Xi, W.-Y. He, S. Jiang, Z. Wang, K. Kang, J.-H. Park, H. Berger, L. Forró, K. T. Law, J. Shan, and K. F. Mak. An unusual continuous paramagnetic-limited superconducting phase transition in 2d $NbSe_2$. *Nature Materials*, 17(6):504–508, 2018. doi:10.1038/s41563-018-0061-1. URL https://doi.org/10.1038/s41563-018-0061-1.

[165] E. Sosenko, J. Zhang, and V. Aji. Unconventional superconductivity and anomalous response in hole-doped transition metal dichalcogenides. *Phys. Rev. B*, 95:144508, Apr 2017. doi:10.1103/PhysRevB.95.144508. URL https://link.aps.org/doi/10.1103/PhysRevB.95.144508.

[166] D. Sticlet and C. Morari. Topological superconductivity from magnetic impurities on monolayer $NbSe_2$. *Phys. Rev. B*, 100:075420, Aug 2019. doi:10.1103/PhysRevB.100.075420. URL https://link.aps.org/doi/10.1103/PhysRevB.100.075420.

[167] S. Sumita, T. Nomoto, K. Shiozaki, and Y. Yanase. Classification of topological crystalline superconducting nodes on high-symmetry lines: Point nodes, line nodes, and Bogoliubov Fermi surfaces. *Phys. Rev. B*, 99:134513, Apr 2019. doi:10.1103/PhysRevB.99.134513. URL https://link.aps.org/doi/10.1103/PhysRevB.99.134513.

[168] K. Taniguchi, A. Matsumoto, H. Shimotani, and H. Takagi. Electric-field-induced superconductivity at 9.4°K in a layered transition metal disulphide MoS_2. *Applied Physics Letters*, 101 (4):042603, 2012. doi:10.1063/1.4740268. URL https://doi.org/10.1063/1.4740268.

[169] J. C. Y. Teo and C. L. Kane. Topological defects and gapless modes in insulators and superconductors. *Phys. Rev. B*, 82:115120, Sep 2010. doi:10.1103/PhysRevB.82.115120. URL https://link.aps.org/doi/10.1103/PhysRevB.82.115120.

[170] D. J. Thouless, M. Kohmoto, M. P. Nightingale, and M. den Nijs. Quantized Hall conductance in a two-dimensional periodic potential. *Phys. Rev. Lett.*, 49:405–408, Aug 1982. doi:10.1103/PhysRevLett.49.405. URL https://link.aps.org/doi/10.1103/PhysRevLett.49.405.

[171] T. V. Trevisan, M. Schütt, and R. M. Fernandes. Unconventional multiband superconductivity in bulk $SrTiO_3$ and $LaAlO_3/SrTiO_3$ interfaces. *Phys. Rev. Lett.*, 121:127002, Sep 2018. doi:10.1103/PhysRevLett.121.127002. URL https://link.aps.org/doi/10.1103/PhysRevLett.121.127002.

[172] L. Trifunovic and P. W. Brouwer. Higher-order bulk-boundary correspondence for topological crystalline phases. *Phys. Rev. X*, 9:011012, Jan 2019. doi:10.1103/PhysRevX.9.011012. URL https://link.aps.org/doi/10.1103/PhysRevX.9.011012.

[173] M. Tsuchiizu, Y. Yamakawa, S. Onari, Y. Ohno, and H. Kontani. Spin-triplet superconductivity in Sr_2RuO_4 due to orbital and spin fluctuations: Analyses by two-dimensional renormalization group theory and self-consistent vertex-correction method. *Phys. Rev. B*, 91:155103, Apr 2015. doi:10.1103/PhysRevB.91.155103. URL https://link.aps.org/doi/10.1103/PhysRevB.91.155103.

[174] M. M. Ugeda, A. J. Bradley, Y. Zhang, S. Onishi, Y. Chen, W. Ruan, C. Ojeda-Aristizabal, H. Ryu, M. T. Edmonds, H.-Z. Tsai, A. Riss, S.-K. Mo, D. Lee, A. Zettl, Z. Hussain, Z.-X. Shen, and M. F. Crommie. Characterization of collective ground states in single-layer $NbSe_2$. *Nature Physics*, 12:92 EP –, 11 2015. URL https://doi.org/10.1038/nphys3527.

[175] J. W. F. Venderbos, V. Kozii, and L. Fu. Identification of nematic superconductivity from the upper critical field. *Phys. Rev. B*, 94:094522, Sep 2016. doi:10.1103/PhysRevB.94.094522. URL https://link.aps.org/doi/10.1103/PhysRevB.94.094522.

[176] J. Venderley and E.-A. Kim. Evidence of pair-density wave in spin-valley locked systems. *Science Advances*, 5(3), 2019. doi:10.1126/sciadv.aat4698. URL https://advances.sciencemag.org/content/5/3/eaat4698.

[177] G. E. Volovik. *The Universe in a Helium Droplet*, volume 117. Oxford University Press on Demand, 2003.

[178] A. B. Vorontsov, M. G. Vavilov, and A. V. Chubukov. Superconductivity and spin-density waves in multiband metals. *Phys. Rev. B*, 81:174538, May 2010. doi:10.1103/PhysRevB.81.174538. URL https://link.aps.org/doi/10.1103/PhysRevB.81.174538.

[179] L. Wang, T. O. Rosdahl, and D. Sticlet. Platform for nodal topological superconductors in monolayer molybdenum dichalcogenides. *Phys. Rev. B*, 98:205411, Nov 2018. doi:10.1103/PhysRevB.98.205411. URL https://link.aps.org/doi/10.1103/PhysRevB.98.205411.

[180] Q.-Z. Wang and C.-X. Liu. Topological nonsymmorphic crystalline superconductors. *Phys. Rev. B*, 93:020505, Jan 2016. doi:10.1103/PhysRevB.93.020505. URL https://link.aps.org/doi/10.1103/PhysRevB.93.020505.

[181] Y. Wang, S. D. Edkins, M. H. Hamidian, J. C. S. Davis, E. Fradkin, and S. A. Kivelson. Pair density waves in superconducting vortex halos. *Phys. Rev. B*, 97:174510, May 2018. doi:10.1103/PhysRevB.97.174510. URL https://link.aps.org/doi/10.1103/PhysRevB.97.174510.

[182] Y. Wang, M. Lin, and T. L. Hughes. Weak-pairing higher order topological superconductors. *Phys. Rev. B*, 98:165144, Oct 2018. doi:10.1103/PhysRevB.98.165144. URL https://link.aps.org/doi/10.1103/PhysRevB.98.165144.

[183] T. Watanabe, T. Yoshida, and Y. Yanase. Odd-parity superconductivity by competing spin-orbit coupling and orbital effect in artificial heterostructures. *Phys. Rev. B*, 92:174502, Nov 2015. doi:10.1103/PhysRevB.92.174502. URL https://link.aps.org/doi/10.1103/PhysRevB.92.174502.

[184] D. Wickramaratne, S. Khmelevskyi, D. F. Agterberg, and I. I. Mazin. Ising superconductivity and magnetism in $NbSe_2$. 2020. URL https://arxiv.org/abs/2005.05497.

[185] E. Witten. Three lectures on topological phases of matter. *La Rivista del Nuovo Cimento*, 39 (7):313–370, 2016. ISSN 0393697X. doi:10.1393/ncr/i2016-10125-3. URL https://www.sif.it/riviste/sif/ncr/econtents/2016/039/07/article/0.

[186] C. woo Cho, J. Lyu, T. Han, C. Y. Ng, Y. Gao, G. Li, M. Huang, N. Wang, J. Schmalian, and R. Lortz. Distinct nodal and nematic superconducting phases in the 2d Ising superconductor $NbSe_2$. 2020.

[187] X. Xi, Z. Wang, W. Zhao, J.-H. Park, K. T. Law, H. Berger, L. Forró, J. Shan, and K. F. Mak. Ising pairing in superconducting $NbSe_2$ atomic layers. *Nature Physics*, 12:139 EP –, 11 2015. URL https://doi.org/10.1038/nphys3538.

[188] X. Xi, H. Berger, L. Forró, J. Shan, and K. F. Mak. Gate tuning of electronic phase transitions in two-dimensional $NbSe_2$. *Phys. Rev. Lett.*, 117:106801, Aug 2016. doi:10.1103/PhysRevLett.117.106801. URL https://link.aps.org/doi/10.1103/PhysRevLett.117.106801.

[189] D. Xiao, G.-B. Liu, W. Feng, X. Xu, and W. Yao. Coupled spin and valley physics in monolayers of MoS_2 and other group-VI dichalcogenides. *Phys. Rev. Lett.*, 108:196802, May 2012. doi:10.1103/PhysRevLett.108.196802. URL https://link.aps.org/doi/10.1103/PhysRevLett.108.196802.

[190] R.-Q. Xing, L. Classen, and A. V. Chubukov. Orbital order in fese: The case for vertex renormalization. *Phys. Rev. B*, 98:041108, Jul 2018. doi:10.1103/PhysRevB.98.041108. URL https://link.aps.org/doi/10.1103/PhysRevB.98.041108.

[191] J. T. Ye, Y. J. Zhang, R. Akashi, M. S. Bahramy, R. Arita, and Y. Iwasa. Superconducting dome in a gate-tuned band insulator. *Science*, 338(6111):1193–1196, 2012. ISSN 0036-8075. doi:10.1126/science.1228006. URL http://science.sciencemag.org/content/338/6111/1193.

[192] M. Ye and A. V. Chubukov. Itinerant fermions on a triangular lattice: Unconventional magnetism and other ordered states. *Phys. Rev. B*, 97:245112, Jun 2018. doi:10.1103/PhysRevB.97.245112. URL https://link.aps.org/doi/10.1103/PhysRevB.97.245112.

[193] T. Yoshida, M. Sigrist, and Y. Yanase. Topological crystalline superconductivity in locally noncentrosymmetric multilayer superconductors. *Phys. Rev. Lett.*, 115:027001, Jul 2015. doi:10.1103/PhysRevLett.115.027001. URL https://link.aps.org/doi/10.1103/PhysRevLett.115.027001.

[194] N. F. Q. Yuan and L. Fu. Zeeman-induced gapless superconductivity with a partial Fermi surface. *Phys. Rev. B*, 97:115139, Mar 2018. doi:10.1103/PhysRevB.97.115139. URL https://link.aps.org/doi/10.1103/PhysRevB.97.115139.

[195] N. F. Q. Yuan, K. F. Mak, and K. T. Law. Possible topological superconducting phases of MoS_2. *Phys. Rev. Lett.*, 113:097001, Aug 2014. doi:10.1103/PhysRevLett.113.097001. URL https://link.aps.org/doi/10.1103/PhysRevLett.113.097001.

[196] N. F. Q. Yuan, B. T. Zhou, W.-Y. He, and K. T. Law. Ising superconductivity in transition metal dichalcogenides. *arXiv:1605.01847*, 2016. URL https://arxiv.org/abs/1605.01847.

[197] Y. X. Zhao and Z. D. Wang. Topological classification and stability of Fermi surfaces. *Phys. Rev. Lett.*, 110:240404, Jun 2013. doi:10.1103/PhysRevLett.110.240404. URL https://link.aps.org/doi/10.1103/PhysRevLett.110.240404.

[198] F. Zheng and J. Feng. Electron-phonon coupling and the coexistence of superconductivity and charge-density wave in monolayer $NbSe_2$. *Phys. Rev. B*, 99:161119, Apr 2019. doi:10.1103/PhysRevB.99.161119. URL https://link.aps.org/doi/10.1103/PhysRevB.99.161119.

[199] B. T. Zhou, N. F. Q. Yuan, H.-L. Jiang, and K. T. Law. Ising superconductivity and Majorana fermions in transition-metal dichalcogenides. *Phys. Rev. B*, 93:180501, May 2016. doi:10.1103/PhysRevB.93.180501. URL https://link.aps.org/doi/10.1103/PhysRevB.93.180501.

[200] J.-H. Zhou, T. Qin, and J.-R. Shi. Intra-valley spin-triplet p+ip Superconducting pairing in lightly doped graphene. *Chinese Physics Letters*, 30(1):017401, jan 2013. doi:10.1088/0256-307x/30/1/017401. URL https://doi.org/10.1088%2F0256-307x%2F30%2F1%2F017401.